

Die approbierte Originalversion dieser Dissertation ist an der Hauptbibliothek der Technischen Universität Wien aufgestellt (<http://www.ub.tuwien.ac.at>).

The approved original version of this thesis is available at the main library of the Vienna University of Technology (<http://www.ub.tuwien.ac.at/english>).



Vienna University of Technology



DISSERTATION

Nonlinear Terahertz Spectroscopy of Semiconductor Heterostructures

eingereicht von

Dipl.-Phys. (Univ.) Daniel Dietze

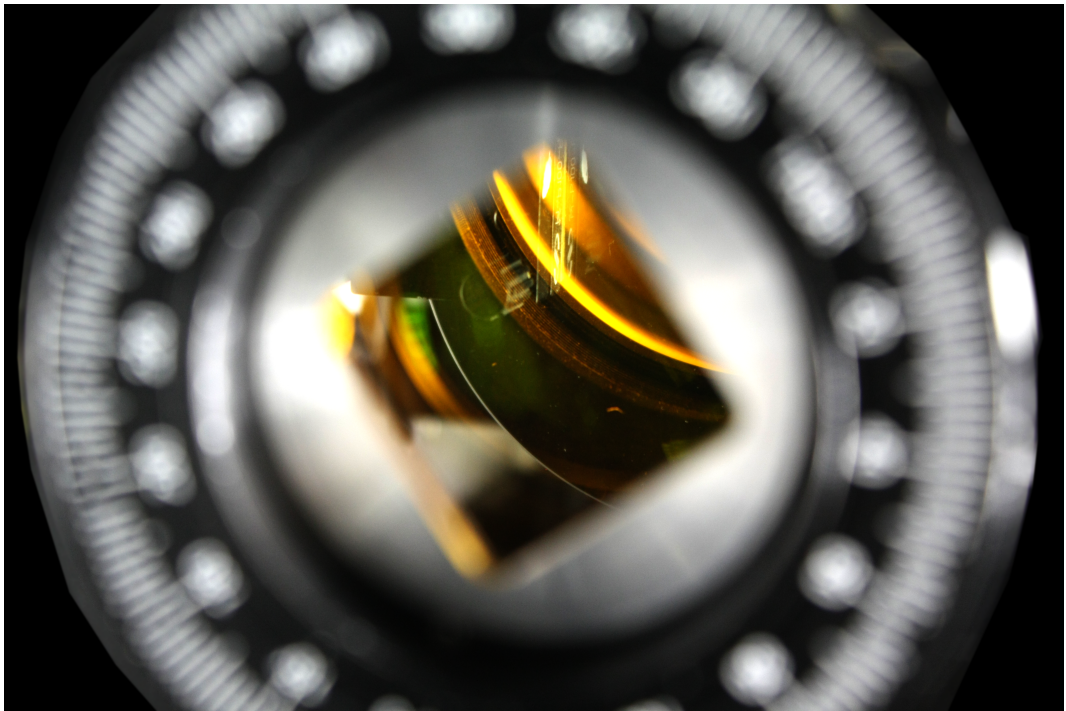
Matr. Nr. 0727841
Tivoligasse 65 / 12
1120 Wien

an der Technischen Universität Wien,
Fakultät für Elektrotechnik und Informationstechnik

zum Zwecke der Erlangung des akademischen Grades eines
Doktors der technischen Wissenschaften

ausgeführt unter der Leitung von
Univ. Prof. Mag. rer. nat. Dr. rer. nat. Karl Unterrainer
und Dipl.-Ing. Dr. techn. Juraj Darmo
am Institut für Photonik (E387)

Wien, Juni 2012



The large area GaP crystal.

Abstract

The main focus of this thesis has been the investigation of the interaction of terahertz (THz) radiation with two-dimensional semiconductor heterostructures beyond the regime of linear optics. The THz spectral region constitutes an especially rich area with many prospects in soft and condensed matter physics. Based on its non-ionizing character and its ability to penetrate a variety of non-conducting materials, THz spectroscopy and imaging techniques face a growing number of industrial and scientific applications. An important milestone in bringing the THz range to the customer has been the invention of the THz quantum cascade laser (QCL) in 2002. Quantum cascade lasers have the potential of being used as miniaturized THz sources in a variety of applications including quality control, environmental monitoring and astronomy. However, room temperature operation, a feature that is highly desired to meet industrial requirements, has not been achieved to date. Recently, THz time-domain spectroscopy (TDS) has been demonstrated to be the perfect tool for an in-depth investigation of the dynamics inside a lasing QCL.

By scaling the incident THz field amplitudes to several tens of kV/cm, the pulses can be used to actively manipulate and control the intersubband excitations, giving rise to non-equilibrium states of matter. From the dynamics following the ultrafast excitation pulse, considerable insight into the microscopic properties of the sample can be gained. Examples of accessible parameters include the identification of dephasing and energy relaxation channels, as well as clarifying the role of multi-photon and collective excitations. During this work, various methods for the generation of intense single-cycle THz pulses have been investigated. Based on the coherent conversion of amplified near infrared laser pulses with pulse energies up to 4 mJ, we have been able to achieve THz peak field strengths up to 40 kV/cm with bandwidths extending over 6 THz. In addition, we have developed several schemes for increasing the THz yield from well-known emitter concepts. These include area sectioning, THz waveguides and dynamic phase-matching.

As a proof-of-principle experiment, we have investigated non-equilibrium dynamics of intersubband (ISB) excitations subject to intense single-cycle THz pulses. The broadband excitation enabled the simultaneous driving of several adjacent transitions. The main results have been the observation of the undressing of collective excitations, coherent population transfer to higher states and the identification of a nonlinear contribution to the refractive index based on parametric multi-photon processes.

An alternative route for probing light-matter interactions beyond the linear regime is provided by cavity quantum electrodynamics. The coupling of ISB transitions to a cavity leads to the formation of so-called ISB cavity polaritons as a new type of elementary excitation. These polaritons are subject to intense research worldwide as they may enable lasing without inversion and the generation of quantum vacuum radiation. To investigate THz ISB polaritons, we have chosen to replace the cavity by a planar THz metamaterial. Thereby, we could prove that the coupling strength between a single parabolic quantum well and the metamaterial is sufficient to open a gap in the polariton dispersion relation, which is a signature of ultrastrong coupling.

Kurzfassung

Der Schwerpunkt der vorliegenden Arbeit lag auf der Untersuchung der nichtlinearen Wechselwirkung zwischen Terahertz (THz) Strahlung und zweidimensionalen Halbleiterheterostrukturen. Das THz Spektrum stellt einen sowohl technologisch als auch wissenschaftlich sehr interessanten Bereich dar. Durch den nichtionisierenden Charakter der Strahlung und die Fähigkeit viele nichtleitende Stoffe zu durchdringen, sieht sich der THz Bereich einer wachsenden Zahl von Anwendungen gegenüber. Ein wichtiger Meilenstein zur weiten Verbreitung der THz Technologie war dabei die Erfindung des THz Quantenkaskadenlasers (QCL) im Jahr 2002. Diese Laser haben ein weitreichendes Potential als miniaturisierte THz Quellen in einer Vielzahl von Anwendungen. Allerdings ist bis heute kein Betrieb bei Raumtemperatur möglich, was jedoch für viele Anwendungen ausschlaggebend wäre. In den vergangenen Jahren hat sich die zeitaufgelöste Spektroskopie mit ultrakurzen THz Pulsen (THz TDS) als ideales Werkzeug für die Untersuchung der internen Vorgänge in THz QCLs profiliert.

Durch die Erhöhung der verfügbaren THz Feldstärke auf mehrere kV/cm können diese Pulse zur aktiven Kontrolle der Intersubbandanregungen verwendet werden. Die Beobachtung der nachfolgenden Ladungsträgerdynamik ermöglicht Rückschlüsse auf die mikroskopischen Eigenschaften der Probe. Beispielsweise können so Zerfallskanäle identifiziert und die Einflüsse von Mehrphotonenprozessen und kollektiven Anregungen geklärt werden. Im Zuge dieser Arbeit wurden verschiedene Methoden zur Erzeugung von intensiven, ultrakurzen THz Pulsen erprobt. Ausgehend von verstärkten Laserpulsen mit Pulsenergien von 4mJ wurden Feldstärken bis zu 40kV/cm und gleichzeitig Bandbreiten von über 6 THz erreicht. Desweiteren konnte die THz Ausbeute durch spezielle Maßnahmen, wie dynamische Phasen Anpassung oder THz Wellenleiter, weiter gesteigert werden.

Diese THz Pulse ermöglichten erstmalig die direkte Messung der Nichtgleichgewichtsdynamik von Intersubbandanregungen in Folge einer breitbandigen Anregung. Die Hauptresultate waren dabei die Beobachtung der Zerstörung kollektiver Anregungen, der kohärente Transfer von Ladungsträgern in höhere Zustände und die Identifikation eines nichtlinearen Beitrags zum Brechungsindex durch parametrische Mehrphotonenprozesse.

Eine alternative Möglichkeit zur Untersuchung von nichtlinearen Licht-Materie-Wechselwirkungen bietet die Quantenelektrodynamik. Die Kopplung von Intersubbandanregungen an einen Resonator führt zur Erzeugung sogenannter Polaritonen als neuen Quasiteilchen. Diese sind Gegenstand aktiver Forschung da sie neuartige Laserquellen sowie die Erzeugung von kohärenter Strahlung aus dem Vakuum ermöglichen könnten. In dieser Arbeit wurden THz Polaritonen untersucht, die durch die starke Kopplung eines THz Metamaterials mit einem einzelnen parabolischen Quantentrog zustande kommen. Dabei konnte gezeigt werden, dass die Kopplungsstärke ausreichend ist, um eine Lücke in der polaritonischen Dispersionsrelation zu öffnen. Diese Lücke gilt als Signatur der sogenannten ultrastarken Kopplung.

To
my wife Michèle
and
my son Nicolas.

Contents

1	Introduction	1
1.1	Terahertz Spectroscopy	1
1.2	Semiconductor Heterostructures and Intersubband Transitions	3
1.3	Terahertz Metamaterials	5
1.4	Nonlinear THz Spectroscopy	6
1.5	Aims and Scope of the Thesis	8
2	Spectroscopy in the Terahertz Frequency Range	11
2.1	Fourier Transform Infrared Spectroscopy	11
2.1.1	Emitters Used For FTIR	14
2.1.2	Detectors Used For FTIR	15
2.2	Terahertz Time-Domain Spectroscopy	16
2.2.1	Terahertz Generation in Photoconductive Antennas	19
2.2.2	Electro-Optic Detection of THz Transients	21
3	THz Metamaterials Coupled To Intersubband Transitions	29
3.1	Optical Properties of Intersubband Transitions in Quantum Wells	29
3.2	Electrodynamics of Terahertz Metamaterials	35
3.3	Strong Light Matter Coupling	46
3.4	Entering the Ultrastrong Coupling Regime	57
3.5	Strong to Weak Coupling Transition	60
4	High Field Terahertz Time-Domain Spectroscopy	65
4.1	High Field THz Time-Domain Spectroscopy Setup	65
4.2	Generation of Intense Terahertz Pulses	73
4.3	Terahertz Emission from Semiconductor Surfaces	75
4.4	Optical Rectification in Nonlinear Crystals	84
4.4.1	Collinear THz Generation in Large Area GaP	85
4.4.2	Dynamically Phase-Matched THz Generation	92
4.5	Large Area Photoconductive Antennas	94
4.6	Four-Wave Mixing in Laser Induced Plasma Filaments	97
4.6.1	Microscopic Polarization Model	100
4.6.2	THz Emission under Tight Focusing Conditions	104

4.6.3	Waveguide-Enhanced THz Emission under Weak Focusing Conditions	107
4.7	Comparison of Methods	112
5	Nonlinear THz Spectroscopy of Intersubband Transitions	115
5.1	First Experimental Results	116
5.2	One-Dimensional FDTD Simulations of Multi-Level QWs	121
5.3	Nonlinear Refractive Index in a Three-Level System	123
5.4	Collective ISB Excitations and Dressed State Effects	125
5.5	Quasi-Thermalization between a QW and a Photon Bath	128
6	Conclusions	133
6.1	Cavity QED with THz Metamaterials	133
6.2	High Field THz Time-Domain Spectroscopy	135
6.3	Quantum Optics Toy Box	136
A	Growth Sheets	143
B	Analytic Expression for Polarizability of a Split-Ring Resonator	151
C	Coupled Pendulums	157
D	Quantum Well Models for FDTD Simulations	163
D.1	Lorentz Model	163
D.2	Maxwell-Bloch Model	165
D.3	Multilevel Maxwell-Bloch Model	168
E	Description of Laser Systems	175
E.1	Er:Fiber Laser	175
E.2	Regenerative Ti:Sapphire Amplifier	180
	Bibliography	183
	Curriculum Vitae	209
	List of Publications	211

Chapter 1

Introduction

1.1 Terahertz Spectroscopy

Ever since the existence of mankind, human curiosity has been a driving force of scientific and technical progress. Born from the wish to understand the basic principles of the world surrounding us, numerous tools and techniques have emerged over the past millennia. One of the most powerful techniques that we have at our disposal is optical spectroscopy, the study of the interaction of light and matter. The field started with the invention of the prism by Sir Isaac Newton (1642 - 1727) in 1666, who showed that sunlight actually consists of a continuous series of colors which he termed *spectrum* [1]. The first quantitative study of the spectrum of the sun was conducted by Joseph von Fraunhofer (1787 - 1826) in 1814, who also invented the transmission grating. He was able to identify 570 dark lines (see Fig. 1.1), which have later been associated to absorption by certain elements in the sun and earth's atmosphere by Gustav Robert Kirchhoff (1824 - 1887) and Robert Bunsen (1811 - 1899). This marked the beginning of modern spectroscopy. Since then, the whole field has made tremendous progress and many branches have emerged that are specialized only to certain wavelength ranges. As spectroscopy is the science of the interaction of light with matter, the wavelength range has to match the elementary excitations of the system under study. In this sense, the terahertz (THz) range of the electromagnetic spectrum is an especially rich area with many prospects in soft and condensed matter physics. Though not consistent throughout literature, it is common practice to define the THz range as the frequency span from $\nu = 0.1$ to 10 THz [2]. This is the domain of phonons in solids [3] and rotational and



Figure 1.1: The spectrum of the sun with the Fraunhofer lines. Stamp printed by the German Federal Mail on the occasion of Fraunhofer's 200th birthday.

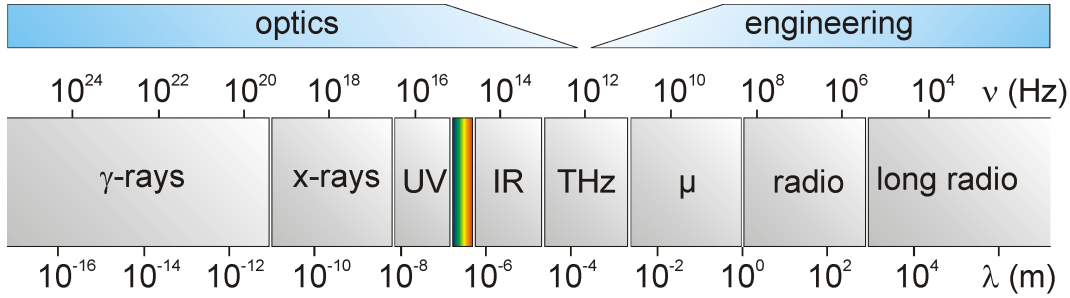


Figure 1.2: Overview over the electromagnetic spectrum. The THz region extends from 1×10^{11} to 1×10^{13} Hz and is situated at the transition region between electrical engineering and optics.

vibrational modes of molecules [4], for instance. The related photon energies $E = h\nu$ are in the range from 0.4 to 40 meV, corresponding to the binding energies of impurities and excitons in semiconductors [3] and Cooper pairs in superconductors [5]. The typical time scale $t = 1/\nu$ is on the order of 1 ps, equivalent to the scattering time of carriers in bulk semiconductors [6] or the spin coherence times in quantum wells [7–9]. The wavelength $\lambda = c/\nu$ ranging from 30 μm to 3 mm and the ability to penetrate non-conducting materials make it an ideal tool for security [10], quality control [11] and art conservation [12]. Due to its non-ionizing character, THz radiation is also of particular interest for medical applications [13].

Despite this strong motivation for spectroscopy in the THz range, this frequency region has long time been unexplored. The reason has been the lack of efficient and powerful sources and detectors [14], which in part can be explained by its unique location within the electromagnetic spectrum (Fig. 1.2). At the low energy side of the THz gap is the domain of electrical engineering where the highest achievable frequencies are set by the RC time constants of the electronic circuits and devices. Typical values are on the order of several hundred GHz [14]. Approaching the THz region from the high energy side, the domain of optics, it is found that the problem is the energy of the THz photons being well below the thermal background and the generally low conversion efficiency from optical to THz frequencies.

However, the exceptional location between the world of engineering and the world of optics also has its advantages. Eventually, it has become evident that the key to success is a combination of concepts from both worlds. A prominent example is the photoconductive emitter [15] which will be discussed in more detail in Chap. 2.2.1. In the past decades, numerous ways to generate and detect THz radiation have been developed. Remarkable examples are the water vapor laser [16, 17] and THz emission from peeling Scotch tape [18]. A good overview over the history and state of the art in THz spectroscopy is found in recent reviews, e.g. [14, 19–22], and textbooks, e.g. [2, 23], for example.

1.2 Semiconductor Heterostructures and Intersubband Transitions

Terahertz spectroscopy in its present form would not have been possible without modern semiconductor technology. For instance, photoconductive emitters and detectors, which mark the beginning of the THz era, rely on semiconductor substrates with a moderate band gap for photoexcitation and a sufficiently high carrier mobility [23]. Materials such as silicon and gallium arsenide with very low defect densities have become available due to recent advances in crystal growth technology [24]. In addition, post-processing techniques have been developed which allow to modify material parameters such as the lifetime of photoexcited carriers. For instance, radiation-damaged silicon films on sapphire substrates have been the first photoconductive emitter substrates that have shown free-space emission of electromagnetic pulses in the THz frequency range [15, 25, 26].

The invention of molecular beam epitaxy (MBE), a technique that allows the deposition of different semiconductor alloys with monolayer precision and very low defect rates [27], has sparked a whole new era in semiconductor device technology. By controlling the growth conditions, photoconductive substrates with unique properties could be created. For example, the growth of GaAs films under very low temperatures, so-called LT-GaAs, leads to a reduction of the carrier lifetime by orders of magnitude to the sub-picosecond range [28, 29], making this material the ideal candidate for high-performance THz emitters (see Chap. 2.2.1).

The capability of MBE to grow monolayers of different semiconductors lattice matched and with a high quality soon triggered the development of lower dimensional structures, such as quantum wells (QW), for instance. There, the strong confinement of the carriers along the growth direction leads to the occurrence of quantum effects [30]. The most important aspect is thereby the formation of subbands within the conduction and valence bands. The energy offset between these subbands and the associated wavefunctions of the carriers can be freely designed by varying the geometry of the heterostructure. In addition, transitions between these subbands, so-called intersubband transitions (ISBTs), can be used to emit and absorb photons in the THz and mid-infrared (MIR) spectral region [31].

Semiconductor laser technology had till then been based solely on optical transitions between the conduction band and the valence band, so-called interband transitions (see for example [32]). The emission frequency is thereby fixed by the band gap of the used material system. In order to develop laser diodes working in the far-infrared (FIR), special materials with a very low band gap would have to be used. Examples include $\text{Hg}_{1-x}\text{Cd}_x\text{Te}$ [33] or bilayer graphene [34]. So far, no working laser has been demonstrated due to huge

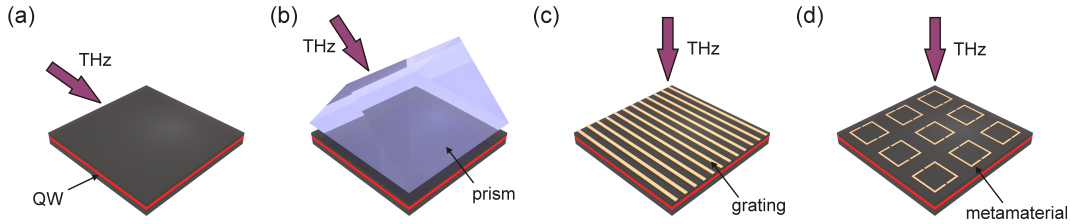


Figure 1.3: Different ways to couple free-space THz radiation to intersubband transitions in a quantum well (red). (a) Waveguide configuration. The THz electric field is oriented parallel to the growth direction. (b) Evanescent field coupling with a prism. The THz pulse has to be TM polarized with respect to the prism. (c) Grating coupling. The THz electric field is perpendicular to the metal stripes. (d) Resonant coupling via a metamaterial resonance. The polarization of the THz pulses depends on the metamaterial geometry.

technological difficulties. Alternatively, interband transitions between light and heavy hole subbands could be utilized, as is the case in the p -Ge laser [35]. However, to observe lasing action in such materials a huge effort, such as high magnetic fields and cryogenic temperatures, is necessary.

In lasers based on ISBTs, the transition strength and frequency are design parameters. In addition, these devices can be based on material systems which are easy to handle and where the processing technology is mature, for example, AlGaAs / GaAs. By using only electrons or holes, multiple photons can be emitted from a single carrier by stacking several emitter sections, so-called cascades. The first working quantum cascade laser has been demonstrated in 1994 in the MIR by Faist *et al.* [36], and eight years later by Koehler *et al.* also in the THz [37].

THz QCLs have the potential of being used as miniaturized THz sources in a variety of applications including imaging, semiconductor inspection and astronomy (see for example [38] and references therein). In addition, a single QCL can be used both as emitter and detector, as has been demonstrated in a compact imaging setup [39]. However, these sources still require significant cooling to function properly. As room temperature operation is a feature that is highly desired to meet industrial requirements, huge efforts are undertaken to meet this goal [38]. THz spectroscopy is thereby the perfect tool for learning more about the physics of semiconductors and especially semiconductor heterostructures.

In order to couple THz pulses to ISBTs, the polarization of the electric field has to fulfill certain polarization selection rules [40]. Only the component polarized parallel to the growth direction of the heterostructure can induce ISBTs. In particular, this states that no coupling of free space radiation and ISBTs is possible under normal incidence. Oblique incidence, especially under Brewster's angle, is in principle possible but very inefficient [31]. This makes

THz spectroscopy on such samples difficult, especially as the thickness of the heterostructure or active zone is usually on the order of just a few microns. There are a few possibilities to still couple light into the heterostructure, for example, by using the substrate as waveguide [41] (Fig. 1.3a), or by using frustrated total internal reflection in prisms [42] (Fig. 1.3b). By fabricating a metallic sub-wavelength grating made from thin metal stripes on top of the sample surface, as shown in Fig. 1.3c, it is even possible under normal incidence to couple broadband THz radiation efficiently to ISBTs [43].

1.3 Terahertz Metamaterials

An alternative way for normal incidence coupling of THz radiation to ISBTs is provided by resonant surfaces made of sub-wavelength metallic structures, so-called metamaterials (MMs, see Fig. 1.3d). Only light with a frequency within a narrow region around the MM resonance is coupled to the heterostructure via the near-field of the resonant mode. Thereby, the enhancement of the electric field amplitude in the vicinity of the MM resonators can be used to improve the interaction between the free-space radiation and the ISBTs.

In recent years, there has been a steadily increasing interest in MMs. The term *metamaterial* denotes an artificial medium with optical properties that cannot be found in nature. A prominent example is negative refraction, i.e. a medium with simultaneously negative permittivity and negative permeability in the same frequency range. The electrodynamics of such a medium have, for the first time, been investigated by Veselago in 1964 [44]. The latest developments in MMs have been sparked by the seminal paper of Pendry published in 2000 [45], where a negative refractive index medium is proposed to serve as perfect lens, i.e. a lens that beats the well-known diffraction limit of conventional optical microscopy.

In the microwave and THz range, the most common way to fabricate such artificial media is based on embedding sub-wavelength-sized inclusions in a dielectric host material. This idea dates back to Lord Rayleigh (1842-1919) [46], and has been used extensively in the middle of the 20th century to build lightweight microwave lenses [47, 48]. Common types of inclusions are small metal spheres or rectangular plates, for example, which show a non-resonant response to the incident electromagnetic radiation. Thus, the optical properties of such media are solely determined by the arrangement of the small scatterers, thereby imitating the crystal lattice of a conventional dielectric. Such media are therefore also denoted by the term *artificial dielectrics*.

The step from artificial dielectrics to modern metamaterials is done by replacing the sub-wavelength scatterers by resonant structures, so-called *meta-atoms*. By carefully selecting the geometry of the meta-atoms, the optical properties of the medium can be tailored at will. For example, it has been

demonstrated in 1852 by Wilhelm E. Weber (1804-1891), that small metallic rings exhibit a diamagnetic response, i.e. a negative permeability, without being made of magnetic material [49]. The magnetic response can be drastically enhanced by introducing an additional capacitor. This observation led to the invention of the well-known split-ring resonator (SRR) [50], which is nowadays the most common shape of meta-atoms.

In addition to the perfect lens, which has been demonstrated experimentally in the optical frequency range in 2005 [51], MMs offer a wealth of applications. These include optical filters [52, 53], perfect absorbers [54, 55], and cloaking devices [56–58], just to name a few. These are all based on the action of the MM as an effective medium. In contrast to this, there are several aspects concerning the individual meta-atoms. For instance, coupling between neighboring meta-atoms can lead to the occurrence of electromagnetically induced transparency (EIT) [59, 60], or single meta-atoms can be strongly coupled to ISBTs in a close by semiconductor quantum well. Thereby, these systems resemble in many respects conventional quantum optics experiments based on atoms, except that they operate at a macroscopic scale and are in many aspects easier to handle experimentally.

Metamaterials are nowadays a very intense field of research in all parts of the electromagnetic spectrum. A good overview over the history and current research activities can be found in [61], for example.

1.4 Nonlinear THz Spectroscopy

Apart from the improved coupling of free-space radiation to semiconductor heterostructures, the aforementioned meta-films can also be used to enhance the electric field in the close vicinity by orders of magnitude [62]. Thereby, the simple linear relationship $P = \epsilon_0 \chi^{(1)} E$ between the material polarization P and the external electric field E may not be a suitable description of light-matter interaction anymore. When the electric field becomes stronger, higher order terms beyond the linear susceptibility $\chi^{(1)}$ become important [63]:

$$\mathbf{P} = \epsilon_0 (\chi^{(1)} \mathbf{E} + \chi^{(2)} \mathbf{E}\mathbf{E} + \chi^{(3)} \mathbf{E}\mathbf{E}\mathbf{E} + \dots). \quad (1.1)$$

The strong electric field created in the vicinity of meta-atoms has already been used for efficient second- and third-harmonic generation of relatively weak incident pulses based on $\chi^{(2)}$ and $\chi^{(3)}$ processes [64–66].

Alternatively, nonlinear optical processes can also be investigated directly using intense pulses with high electric field strengths. To estimate the needed pulse energies, the microscopic origin of the nonlinear terms has to be taken into account. In the THz range, the nonlinearities are mainly related to free carriers [67]. For example, band non-parabolicity and energy dependent scattering rates have a strong impact on the THz susceptibility [68–70]. The

ultrashort duration of the THz pulses allows in addition the study of matter under extreme conditions. Coherent ballistic motion of electrons driven by strong THz fields has been demonstrated by Kuehn *et al.* [71] in *n*-doped GaAs. Thereby, the kinetic energy of the electrons can reach very high values. As a result, efficient intervalley scattering has been observed, for example in GaAs [69, 70, 72, 73] or InAs [74], which leads to a THz induced bleaching of the free carrier absorption. Furthermore, the hot electrons can loose energy via the coherent emission of phonons. Thus, nonlinear THz spectroscopy would give additional insight into fundamental processes and could open the door to a better understanding of the band structure and other parameters relevant to the design of improved semiconductor devices.

To observe, for example, THz induced bleaching in GaAs, the necessary electron kinetic energy is approximately given by the energy offset between the Γ valley and the lowest side valley, the *L* valley, $U_{\text{kin}} = \Delta U_L \approx 0.3 \text{ eV}$ [75]. In order to get a rough estimate on the necessary THz peak field, the electrons can be considered as free particles with effective mass $m_\Gamma = 0.067m_0$, where $m_0 = 9.11 \times 10^{-31} \text{ kg}$ is the free electron mass. Furthermore, the THz field E can be assumed to be constant over the interaction time τ . Thus, the acquired kinetic energy of the electrons is given by

$$U_{\text{kin}} = \frac{1}{2} \frac{e^2}{m} E^2 \tau^2. \quad (1.2)$$

The ballistic acceleration is hindered by scattering with other electrons, holes or phonons. Monte-Carlo simulations suggest that the electrons can reach ballistic velocities only within the first 30 fs before electron-phonon scattering sets in [68, 70]. With $\tau \approx 30 \text{ fs}$, the necessary THz field would be on the order of $E \geq 160 \text{ kV/cm}$. Assuming a homogeneous intensity distribution in the focus, the THz pulse energy can further be estimated from

$$I_{\text{THz}} = \frac{1}{2} n \varepsilon_0 c_0 |E|^2 \quad \text{and} \quad I_{\text{THz}} = \frac{U_{\text{THz}}}{2\tau\pi w^2}, \quad (1.3)$$

to be

$$U_{\text{THz}} = \frac{\pi}{4} \tau w^2 n \varepsilon_0 c_0 |E|^2, \quad (1.4)$$

where $n = 3.6$ is the refractive index of GaAs and w the radius of the focal spot. For a realistic value of $w = 250 \mu\text{m}$, the THz pulse energy would have to be on the order of 5 nJ. Depending on the type of THz emitter used in the experiment, the energy conversion efficiency from the NIR to the THz frequency range is typically on the order of 10^{-6} to 10^{-3} [76, 77]. Thus, it is obvious that a specialized laser system, such as a Ti:Sapphire amplifier, has to be used in order to achieve the desired THz pulse energies.

The generation of such single-cycle THz pulses using table-top systems has been subject to intense research efforts in the past few years. A good overview

can be found in [2, 6, 70], for example. The highest conversion efficiency from the optical to the THz range to date is achieved using tilted pulse front excitation in LiNbO₃ crystals [78–80] and difference frequency mixing of the output of two phase locked optical parametric amplifiers [81, 82]. These methods have yielded record THz peak fields above 1 MV/cm and 100 MV/cm, respectively. However, both methods are limited in the accessible frequency range. In the case of LiNbO₃, the main phonon mode restricts the method to frequencies up to 1.5 THz, while the difference frequency mixing approach is most effective in the mid-infrared spectral range above 10 THz.

Thus, there is a lack of sources for intense and broadband THz pulses in the region between 1.5 and 10 THz, which one could take as the signature of yet another THz gap, the high power THz gap.

1.5 Aims and Scope of the Thesis

The general aim of this thesis has been the investigation of the interaction of THz radiation with two-dimensional semiconductor heterostructures beyond the linear regime. To reach this ambitious goal, two different approaches have been pursued, which is also reflected in the formal organization of this thesis.

In the first part, THz radiation is used as a spectroscopic tool to study the optical properties of intersubband cavity polaritons in the strong coupling regime. Thereby, we have replaced the conventional microcavity usually found in solid state quantum electrodynamics (QED) by THz MMs, which comprise a novel way for coupling free-space radiation to QW systems.

In the second part, we have extended the conventional THz time-domain spectroscopy to use single-cycle THz pulses with high field strengths, thereby filling the aforementioned high power THz gap. These pulses allow the direct access to non-equilibrium ISB dynamics in QWs. The large bandwidth and short duration of the pulses are a key aspect that allows the study of coherent phenomena beyond the textbook two-level atom.

In detail, this thesis is organized as follows. Chapter 2 introduces the basic concepts of spectroscopy in the THz spectral range. Fourier transform infrared spectroscopy and time-domain spectroscopy are shortly presented.

Equipped with these spectroscopic tools, Chap. 3 starts with an introduction of the relevant optical properties of intersubband transitions in quantum wells and the electromagnetic characteristics of THz metamaterials. The remainder of this chapter is devoted to the physics of cavity polaritons, which arise from the combination of these two concepts.

Chapter 4 presents the experimental details of the high field THz TDS setup, which has been developed during this thesis. Several concepts for the generation of broadband THz pulses with high field strengths are discussed and ways for further improvements are pointed out.

These intense single-cycle pulses are then used in Chap. 5 to induce and, at the same time, probe non-equilibrium dynamics in quantum well intersubband excitations. Among the main results are the observation of the undressing of collective excitations, coherent population transfer to higher states and the identification of a nonlinear contribution to the refractive index based on parametric multi-photon processes.

The thesis is completed by a short summary of the key results and some conclusion in Chap. 6.

Chapter 2

Spectroscopy in the Terahertz Frequency Range

In the following chapters, the two major technologies used nowadays for THz spectroscopy, the Fourier transform infrared spectroscopy (FTIR) and the THz time-domain spectroscopy (TDS), will be introduced. As these two techniques have also been used for the experiments presented in this thesis, the underlying concepts will be discussed in more detail.

2.1 Fourier Transform Infrared Spectroscopy

The Fourier transform infrared spectroscopy (FTIR) dates back to the famous interferometer developed by Albert Abraham Michelson (1852 - 1931) [83] and the pioneering work done by Heinrich Rubens (1865 - 1922) and co-workers in Berlin (see [84] for a comprehensive bibliography). FTIR in its present form was then introduced by Peter Berners Fellgett (1922 - 2008) in 1958 [85] during his doctorate in Cambridge. Thereby he realized the great potential of FTIR over other types of spectrometers due to the fact that FTIR uses all wavelengths entering the spectrometer simultaneously for extracting spectral information. In comparison, a monochromator based spectrometer uses only a narrow bandwidth for each frequency. This fact became known as the Fellgett or multiplex advantage. However, only the invention of modern computers and their potential of efficiently calculating the Fourier transformation made FTIR in its present form possible [21].

The basic structure of a FTIR is shown in Fig. 2.1. Although many different interferometer configurations have been designed in the past, the working principle is the same for all. The light from a source is split at a beam splitter in two arms, one of which has a variable length. After the light has been reflected from the end mirrors, it is recombined at the beam splitter and fed to the detector element. The idea is to measure an interferogram $I(\Delta)$ as function of the path difference Δ between the two interferometer

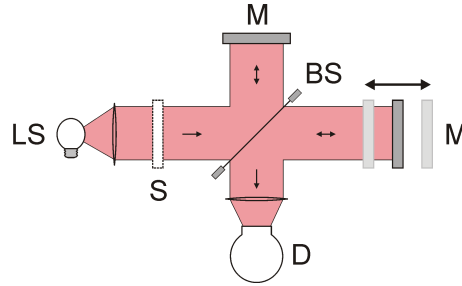


Figure 2.1: Basic setup of a FTIR. The spectrometer is based on a two-beam interferometer, in which the light from a source (LS) is split in two arms after having passed through the sample under study (S). The path length difference between the two arms can be adjusted by displacing one of the two mirrors (M). The reflected light is combined again at the beam splitter (BS) and focused on the detector (D).

arms. Thereby, the interferogram is nothing else but the autocorrelation of the radiation field of the source. The desired radiation spectrum is then obtained by Fourier transformation of the interferogram, hence the name Fourier transform spectroscopy. This shall be derived in the following.

Assuming that the two arms are optically identical up to a path length difference Δ , we can write for the amplitudes in the two arms

$$A_1(\nu) = \sqrt{I(\nu)/2} \quad \text{and} \quad A_2(\nu, \Delta) = \sqrt{I(\nu)/2} e^{i2\pi c_0 \Delta/\nu}, \quad (2.1)$$

where $c_0 = 2.9979 \times 10^8$ m/s is the vacuum speed of light, ν the frequency and $I(\nu)$ the spectrum emitted from the source. In writing (2.1), we have omitted common phase and amplitude factors, for instance caused by the beam splitter or the mirrors [86]. It is convenient to use the wavenumber $\tilde{\nu} = c_0/\nu$ instead of the frequency in the following, as the wavenumber and the path difference Δ constitute a conjugate pair of variables. The radiation of the two arms is finally recombined in the detector, which measures the intensity of the incident radiation integrated over the whole frequency range. For a fixed path difference Δ , the detector signal is thus given by

$$I(\Delta) = \int_{-\infty}^{\infty} |A_1(\tilde{\nu}) + A_2(\tilde{\nu}, \Delta)|^2 d\tilde{\nu}. \quad (2.2)$$

With (2.1), we can rewrite (2.2) to

$$I(\Delta) = \int_{-\infty}^{\infty} I(\tilde{\nu}) [1 + \cos(2\pi\tilde{\nu}\Delta)] d\tilde{\nu}, \quad (2.3)$$

where we have used the fact that the spectrum $I(\tilde{\nu})$ has to be a real quantity. The first term in (2.3) is independent of Δ and therefore attributes to the detector signal just as a constant offset. The second part however is readily

identified as the cosine transform of the spectrum,

$$I'(\Delta) = I(\Delta) - I_\infty = \int_{-\infty}^{\infty} I(\tilde{\nu}) \cos(2\pi\tilde{\nu}\Delta) d\tilde{\nu}. \quad (2.4)$$

Finally, we get the desired spectrum $I(\tilde{\nu})$ directly via the inverse cosine transformation of the measured interferogram,

$$I(\tilde{\nu}) = \int_{-\infty}^{\infty} I'(\Delta) \cos(2\pi\tilde{\nu}\Delta) d\Delta. \quad (2.5)$$

Equations (2.4) and (2.5) can also be written in terms of the continuous Fourier transformation [86].

When a sample S is present in the beam path (Fig. 2.1), the spectrum of the source is modified according to the sample's transmittance, $I'(\tilde{\nu}) = T(\tilde{\nu})I(\tilde{\nu})$, where $T(\tilde{\nu})$ is a function of the angle of incidence, the refractive index and the thickness of the sample [87]. Thus, by measuring the spectrum with and without sample, the transmittance can be extracted by taking the ratio

$$T(\tilde{\nu}) = I'(\tilde{\nu})/I(\tilde{\nu}). \quad (2.6)$$

In the above derivation the two arms have been assumed to be identical up to a path difference, and (2.5) is therefore an even function of $\tilde{\nu}$. Thus, it is sufficient to measure the interferogram single sided, i.e.

$$I(\tilde{\nu}) = 2 \int_0^{\infty} I'(\Delta) \cos(2\pi\tilde{\nu}\Delta) d\Delta. \quad (2.7)$$

In general, the two arms will exhibit a slightly different dispersion or the spectrometer could be designed in the way that the sample is placed only in one of the two arms. In this case, it is necessary to measure the interferogram double sided, i.e. on both sides of the zero-delay position [86].

Figure 2.2 shows a collection of interferogram - spectrum pairs that have been calculated using (2.5) and which shall illustrate the basic relations between the measured interferogram and the associated spectra. If the spectrum consists just of a single frequency, then the interferogram will be a pure cosine, as shown in Fig. 2.2a. When the frequency is large, then the resulting oscillation period in the interferogram is small and vice versa. If the spectrum is broadened, for instance due to a finite coherence length, the interferogram is superimposed by a decaying envelope function. This is shown in Fig. 2.2b for the case of a Gaussian. The larger the bandwidth of the source, the narrower is the interferogram (Fig. 2.2d). When the spectrum consists of two close but isolated frequencies, the interferogram shows a beating pattern (Fig. 2.2c). When the two frequencies are closer together, the position of the minimum is at larger path differences and vice versa. If we would only scan the interferogram up to the

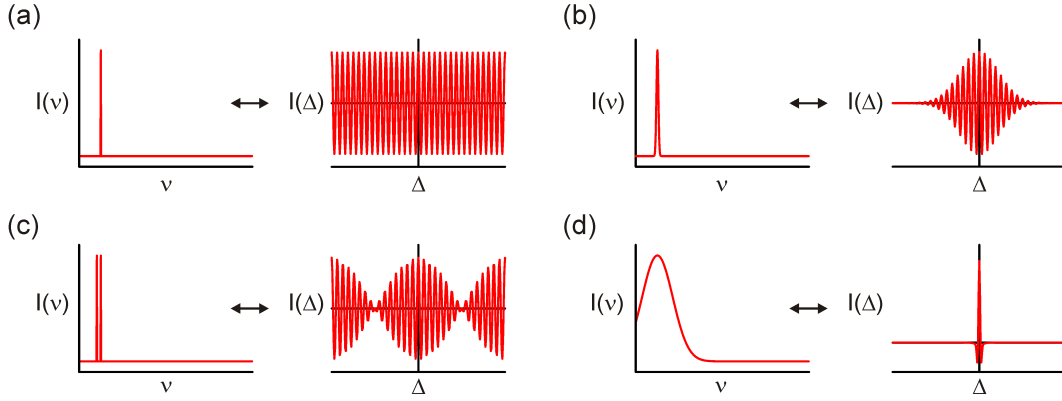


Figure 2.2: Some examples of spectra and associated interferograms calculated using (2.5). See main text for details.

first minimum, then there would be almost no difference to the interferogram of the broadened line (Fig. 2.2b) and we would be unable to distinguish the two cases [88]. Thus, we have to scan at least a full period of the beating signal to be able to completely separate the two lines. From (2.5) it is evident that the spectrum could be measured with infinite frequency resolution, provided that the path difference Δ can be made arbitrarily large. In real spectrometers, the path length is limited by the size of the spectrometer and thus, the spectral resolution is finite. Mathematically, this is expressed by the convolution of the real spectrum $I(\tilde{\nu})$ with the windowing function $w(\tilde{\nu})$ [86],

$$I(\tilde{\nu})_{\text{obs}} = I(\tilde{\nu}) \otimes w(\tilde{\nu}). \quad (2.8)$$

The windowing function is thereby given as the cosine transform of

$$w(\Delta) = \begin{cases} 1 & \text{for } |\Delta| \leq \Delta_{\text{max}} \\ 0 & \text{for } |\Delta| > \Delta_{\text{max}} \end{cases} \quad (2.9)$$

which is

$$w(\tilde{\nu}) = 2\Delta_{\text{max}} \frac{\sin(2\pi\tilde{\nu}\Delta_{\text{max}})}{2\pi\tilde{\nu}\Delta_{\text{max}}}. \quad (2.10)$$

The achievable resolution $\Delta\tilde{\nu}$ is given by the full width at half maximum (FWHM) of the main lobe, $\Delta\tilde{\nu} \approx 1/2\Delta_{\text{max}}$. In practice, the resolution can be improved by multiplying the measured interferogram with another windowing function, which shows a better side lobe suppression and lower FWHM. This method is called apodization and, typically, an increase in resolution by a factor of two is possible [86].

2.1.1 Emitters Used For FTIR

The critical parts for FTIR are the source and the detector. The ideal source would be a high-temperature blackbody, whose emission spectrum is given by

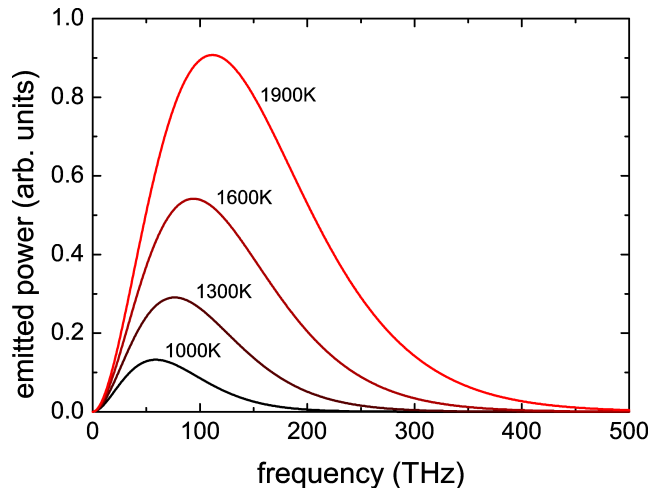


Figure 2.3: Energy spectrum of an ideal blackbody for different temperatures.

Planck's law [89]

$$\rho(\nu) = \frac{8\pi h\nu^3/c_0^3}{e^{h\nu/k_B T} - 1}, \quad (2.11)$$

with $h = 6.6261 \times 10^{-34}$ Js being the Planck constant, $k_B = 1.3807 \times 10^{-23}$ J/K the Boltzmann constant and T the blackbody temperature. The emission spectrum (2.11) for different temperatures is plotted in Fig. 2.3. For increasing temperature, the emission peak shifts to higher frequencies and the total emitted power increases with T^4 [89]. In principle, the temperature should be as high as possible to maximize the signal and hence, the signal-to-noise ratio (SNR). However, lifetime and stability are an issue and it is not possible to seal the blackbody in vacuum as the window transmission is generally poor in the far and mid-infrared region [88]. The most common source in modern FTIRs is a silicon carbide rod (Globar) that is typically heated to about ~ 1300 K [88] and can be used without sealing or water cooling. For far-infrared applications below 6 THz, high pressure mercury arc lamps provide another efficient source [88]. Their equivalent blackbody temperature would be about 4000K [21].

2.1.2 Detectors Used For FTIR

On the detector side, one can distinguish two groups, thermal and quantum detectors. While the latter are based on low band-gap semiconductors, like mercury cadmium telluride (MCT), and are therefore not suited for far-infrared applications [88], thermal detectors are the most common detectors for the THz range. The working principle is based on the absorption of heat and subsequent detection, for example, via the electromotive force (e.g. thermocouples), mechanical movement of a mirror or diaphragm (pneumatic detectors, e.g. the Golay cell), the change of resistance of a conductor (e.g. bolometers) or

the induced polarization in ferroelectric materials (e.g. pyroelectric detector). For the measurements conducted in this thesis, both the bolometer and the pyroelectric detector have been used. The pyroelectric detector senses the absorbed heat by detecting the change of polarization in a ferroelectric crystal sandwiched between two electrodes forming a capacitor. The most common material used nowadays is deuterated triglycine sulfate (DTGS). Due to its high Curie temperature of 49 °C [88], DTGS detectors can be used at room temperature. When the full intensity of the blackbody source is used, the achievable SNR can be as high as $1 : 10^5$ [88]. If the sample aperture is quite small or the transmittance too low, liquid helium cooled bolometers have to be used. The bolometer, which has been invented by Samuel Pierpont Langley (1834 - 1906) in 1880 [90], senses the absorbed heat by a change of resistance in a conductor using, for example, a Wheatstone bridge. While in the original work, metals (especially iron) were used, also superconductors, resistors and thin films have been successfully employed as detector elements [21].

Further information about thermal detectors for THz sensing and their theoretical background can be found in [2], for example. FTIR and its applications are discussed in many textbooks, for instance [86, 88].

2.2 Terahertz Time-Domain Spectroscopy

Another approach to THz spectroscopy is based on the coherent generation and detection of short THz pulses. Thereby, the amplitude and phase of the electric field are directly measured and the spectral information is obtained by Fourier transformation. As these pulses can be as short as a single optical cycle they have a correspondingly broad frequency spectrum.

The pioneering work on THz TDS dates back to Auston *et al.* [15, 91], who have demonstrated in 1984 for the first time free space THz pulses emitted and detected by a photoconductive switch and the electro-optic detection principle for THz transients. The photoconductive switch is therefore also known as the Auston switch. Four years later, in 1988, the first free space guiding of THz pulses has been reported by Fattinger and Grischkowsky [92], who simply used a spherical mirror placed on top of a photoconductive emitter / detector pair. In 1989, van Exter *et al.* then reported the first real THz TDS setup based on off-axis parabolic mirrors for collimation, guiding and focusing of THz pulses [93]. Since then, a large variety of different THz TDS spectrometers has been designed and a complete listing would be beyond the scope of the thesis. However, the working principle is the same and will be shortly introduced in the remainder of this chapter. A good overview is also found in recent textbooks [2, 23].

Figure 2.4 shows a typical THz TDS setup using electro-optic detection (EOD). The TDS principle is based on a pump-probe setup, as is commonly

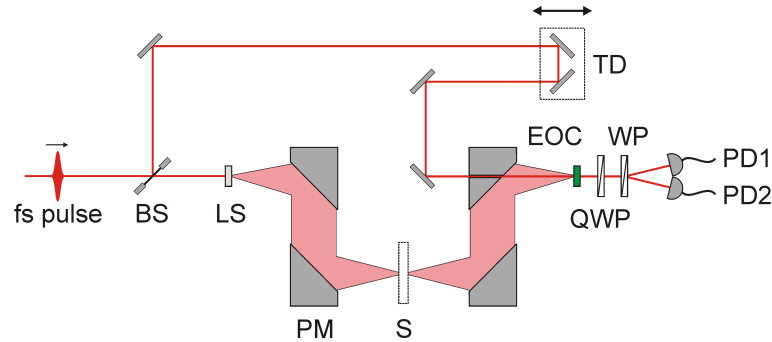


Figure 2.4: Schematic of a THz TDS setup. A fs laser pulse is split at a beam splitter (BS) in two arms, one for generation and one for detection. The generating pulse is then focused on the THz emitter (LS). The THz radiation is collected and guided by a set of off-axis parabolic mirrors (PM). The sample (S) is placed in the intermediate focus. The relative timing between the pump and the probe pulses can be set by a pair of mirrors on a linear translation stage (TD). Finally, the probe pulse is recombined with the THz pulse on the detector crystal (EOC) and passes a quarter wave plate (QWP) and a Wollaston prism (WP) before being detected with a pair of photodiodes (PD1 and PD2).

used in fs-optics. A near-infrared (NIR) laser pulse with a typical length below 100 fs is divided by a beam splitter (BS) in two arms, one for generation and one for detection of the THz pulses. The generation or pump pulse is then focused on the emitter (LS), where the laser pulse is coherently converted to a THz pulse. This photoconverter can be a nonlinear crystal or a photoconductive switch, for example. The emitted THz pulse is then collected and guided by a set of off-axis parabolic mirrors (PM). Compared to THz lenses, these mirrors have the great advantage of a flat reflectivity over the entire THz spectrum and do not suffer from absorption or Fresnel losses at the interfaces. The sample under study (S) is placed in the intermediate focus. The transmitted pulse is finally focused on the electro-optic crystal (EOC) where it is sampled by the probe pulse.

Due to the interaction of the THz pulse and the NIR pulse in the EOC, the polarization state of the probe pulse is changed. This change is sensed by a combination of quarter wave plate (QWP), polarizing beam splitter (WP) and a pair of balanced photo diodes (PD1 and PD2). The detection scheme is discussed in more detail at the end of this chapter. In order to achieve a good SNR, the THz signal is typically modulated and the signal from the balanced photodiodes is detected with a lock-in amplifier. The modulation can be done, for example, electronically by modulating the bias on the photoconductive emitter or optically by using a chopper.

The whole THz transient is reconstructed by changing the relative time delay between the pump and the probe pulse (see Fig. 2.5a). A common way to do this is by moving a pair of mirrors on a linear translation stage

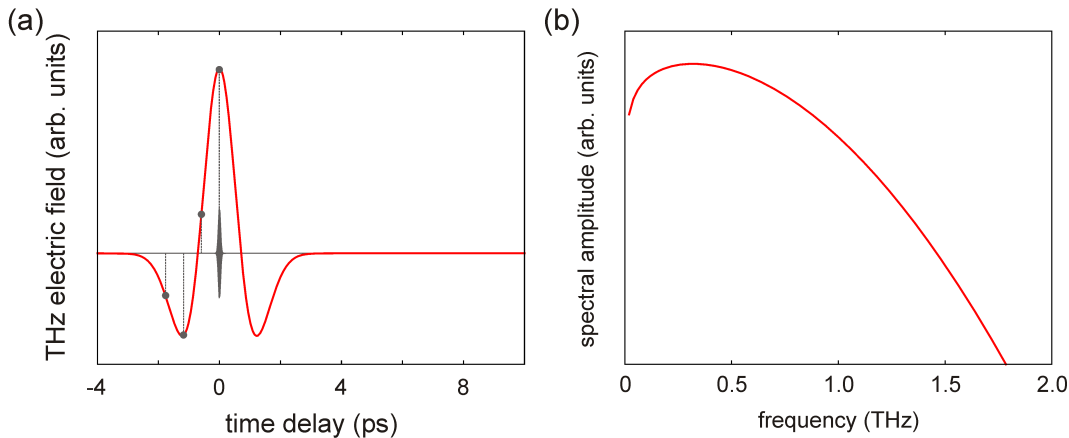


Figure 2.5: (a) Typical THz waveform as obtained with a THz TDS system. The probe pulse (gray) samples the THz electric field (red) at discrete times (circles). (b) The corresponding THz spectrum is obtained by Fourier transformation of the THz transient shown in (a).

(TD) or on a shaking membrane. More sophisticated ways are based on rotating elements [94, 95] or two phase-locked laser oscillators (asynchronous optical sampling, ASOPS [96–98] or electronically controlled optical sampling, ECOPS [99, 100]), thereby achieving scan rates from several hundred Hz to a few 10 kHz. Once the THz electric field $E(t)$ is known, the corresponding spectrum is obtained by Fourier transformation,

$$E(\nu) = \int_{-\infty}^{\infty} E(t)e^{2\pi i\nu t} dt. \quad (2.12)$$

A typical THz transient and its Fourier transform are shown in Figs. 2.5a and 2.5b, respectively. As in the case of FTIR, the maximum length of the scan is limited by the physical dimension of the delay stage. Thus, the same considerations regarding the spectral resolution as in the previous chapter apply also in the case of THz TDS. The limited bandwidth of the THz pulse is additionally given by a combination of the THz emitter and the spectral response of the detector crystal.

If a sample is placed in the beam path, the electric field of the THz pulse is modulated by the complex transmission coefficient of the sample, $E'(\nu) = t(\nu)E(\nu)$. Thereby, $t(\nu)$ contains the transmission through the front and back side of the sample, propagation through the sample, as well as multiple reflections. Experimentally, the transmission coefficient is found by taking the ratio of the spectra with and without sample. As the electro-optic detection principle is directly sensitive to the electric field of the THz pulse, amplitude and phase of the complex transmission coefficient are accessible at the same time, which allows the efficient extraction of material parameters [101].

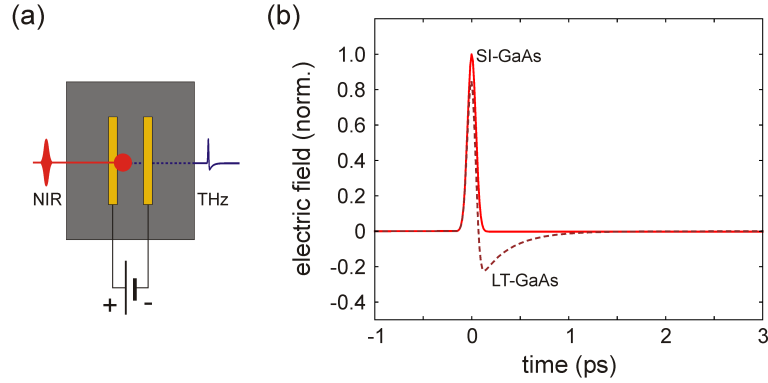


Figure 2.6: (a) Sketch of a typical THz photoconductive antenna. A bias voltage is applied to two metal electrodes. The NIR pump pulse is focused near the positively biased electrode, where it creates an electron-hole plasma. The coherent THz pulse is emitted through the backside of the substrate. (b) Normalized THz electric field transients as calculated from Eq. (2.20) for a pump pulse duration of 100 fs and two values of the carrier lifetime τ_c corresponding to LT-GaAs and SI-GaAs, respectively.

2.2.1 Terahertz Generation in Photoconductive Antennas

Apart from the two examples of photoconverters for THz generation mentioned above, there exists a large variety of physical processes that can be exploited for THz generation. Some examples are surface plasmon oscillations in doped semiconductors [102–105], coherently controlled photocurrents [106, 107], or emission from laser generated plasmas in air [108, 109]. A discussion on these emission mechanisms can be found in Chap. 4. As the photoconductive emitter is by far the most effective for common laser systems with high repetition rate [110], an intuitive description of THz generation in this type of emitter is given in the following.

A schematic of a typical THz antenna is shown in Fig. 2.6a. The antenna is made by deposition of a thick metal layer, e.g. chromium or gold, on a substrate. The substrate should thereby fulfill a number of requirements, such as short carrier lifetime, high mobility and high damage threshold. Furthermore, the band gap has to be in the range of the laser source. For Ti:Sapphire lasers with a center wavelength of 800 nm, often semi-insulating (SI) or low-temperature grown (LT) GaAs is used [23], while for Er-doped fiber lasers (around 1.5 μm), InGaAs/InAlAs heterostructures work very well [111, 112]. Typical values for the carrier lifetime and mobility in SI-GaAs and LT-GaAs are $\tau = 50$ ps and $\mu = 1000$ cm^2/Vs for SI-GaAs and $\tau = 300$ fs and $\mu = 200$ cm^2/Vs for LT-GaAs, respectively [23].

For driving the antenna, a NIR laser pulse with pulse length Δt is focused to a small spot close to the high field region at the positively biased electrode, where it creates free electron-hole pairs in a thin surface layer (the absorption coefficient of GaAs at 800 nm is $\alpha = 13.5 \times 10^3$ cm^{-1} [113]). The two electrodes

can be seen as a pair of ideal back-to-back Schottky barrier diodes [114]. When a voltage is applied, one of the Schottky diodes is reverse biased while the other is forward biased. Most of the applied voltage drops across the depletion region at the reverse biased electrode, thus creating the high field region. This excitation method has been shown to enable sub-picosecond THz transients even in materials with relatively long carrier lifetimes [114, 115]. The drawback, however, is the fast deterioration of the electrode, which can be overcome by a symmetric modulation of the bias voltage [116]. Apart from enhancing the antenna lifetime, this technique has the nice side-effect of also doubling the lock-in signal. For a sufficiently small spot size on the order of a few μm , the field inhomogeneity can be neglected.

Once the carriers have been generated, they are accelerated in the external electric field. The related current density is given by [117]

$$j(t) = -en(t)v(t), \quad (2.13)$$

where $e = 1.6022 \times 10^{-19}$ C is the elementary charge, $n(t)$ the density of free carriers and $v(t)$ their average velocity. The contribution of the holes to the current density has been neglected due to the higher effective mass and the lower mobility. The time evolution of the carrier density obeys the differential equation

$$\frac{d}{dt}n(t) + \frac{n(t)}{\tau_c} = G(t), \quad (2.14)$$

with τ_c being the lifetime of mobile electrons or the electron capture time and

$$G(t) = n_0 e^{-t^2/\Delta t^2} \quad (2.15)$$

the generation rate of carriers [22]. The prefactor n_0 is the carrier density generated at $t = 0$, which is proportional to the energy absorbed in the substrate. In the Drude model, the average velocity of the carriers is determined by the solution of

$$\frac{d}{dt}v(t) + \frac{v(t)}{\tau_s} = -\frac{e}{m}E_{\text{loc}}(t), \quad (2.16)$$

where τ_s is the momentum scattering time, m the effective mass and $E_{\text{loc}}(t)$ the local electric field. The momentum scattering time is related to the electron mobility via $\tau_s = m\mu/e$.

If we neglect any field screening effects, then $E_{\text{loc}}(t) = E_{\text{bias}}$ and (2.16) has the steady state solution

$$v(t) = \text{const.} = -\mu E_{\text{bias}}. \quad (2.17)$$

Insertion of (2.14), (2.15) and (2.17) into (2.13) yields the differential equation

$$\frac{d}{dt}j(t) + \frac{j(t)}{\tau_c} - e\mu n_0 E_{\text{bias}} e^{-t^2/\Delta t^2} = 0, \quad (2.18)$$

which has, for the boundary condition $j(t \rightarrow -\infty) = 0$, the solution

$$j(t) = \frac{\sqrt{\pi}}{2} e \mu n_0 E_{\text{bias}} e^{\Delta t^2 / 4\tau_c^2} e^{-t/\tau_c} \left[1 - \operatorname{erf} \left(\frac{\Delta t^2 - 2t\tau_c}{2\Delta t\tau_c} \right) \right]. \quad (2.19)$$

Thereby, $\operatorname{erf}(x) = (2/\sqrt{\pi}) \int_0^x e^{-t^2} dt$ is the error function [118].

When the spot size of the laser pulse is smaller than the wavelength of the THz radiation, the antenna can be taken as a Hertzian dipole [119]. The emitted far-field is then proportional to $(d/dt)j(t)$ and with (2.19), we finally arrive at an expression for the emitted THz transient,

$$E_{\text{THz}}(t) \propto \mu n_0 E_{\text{bias}} \frac{\Delta t}{\tau_c} \exp \left\{ \frac{\Delta t^2 - 4t\tau_c}{4\tau_c^2} \right\} \times \quad (2.20)$$

$$\times \left[\frac{2\tau_c}{\sqrt{\pi}\Delta t} \exp \left\{ -\frac{(\Delta t^2 - 2t\tau_c)^2}{4\Delta t^2\tau_c^2} \right\} + \operatorname{erf} \left(\frac{\Delta t^2 - 2t\tau_c}{2\Delta t\tau_c} \right) - 1 \right].$$

Figure 2.6b shows typical waveforms for SI-GaAs and LT-GaAs substrates calculated with $\Delta t = 100$ fs. The largest contribution to the THz pulse comes from the fast carrier injection due to the absorption of the pump pulse and, hence, it is possible to observe sub-picosecond THz pulses even with long carrier lifetimes [114].

In this simple picture, the peak field is directly proportional to the applied bias, the incident pump power and the carrier mobility, and the temporal shape of the pulse is only dependent on the duration of the pump pulse and the carrier lifetime. Of course, space-charge and radiation screening effects are important factors in the THz emission process, as has been shown by several authors (see for example [117, 120–123]). The local electric field should be replaced by a superposition of the applied bias field E_{bias} , the induced space-charge polarization due to a separation of charges and the radiation screening field induced by the magnetic field of the THz currents [123]. Additionally, the geometry of the antenna structure plays an important role and more details on this and further aspects can be found, for example, in [23].

2.2.2 Electro-Optic Detection of THz Transients

The photoconductive antenna can also be used for the coherent detection of THz pulses. Instead of the external bias voltage, the THz electric field is used to drive a photocurrent, which is then measured by a lock-in amplifier. In fact, this has been one of the first detection methods employed in THz TDS [15, 92] and a detection bandwidth of up to 60 THz has been reported [124].

Another method for sampling coherent THz transients is electro-optic detection (EOD). Its use in THz TDS has been pioneered by Valdmanis *et al.* [125, 126] and Auston *et al.* [91]. Due to the inherently higher detection bandwidth [127] and the possibility of shot-noise limited detection [128, 129],

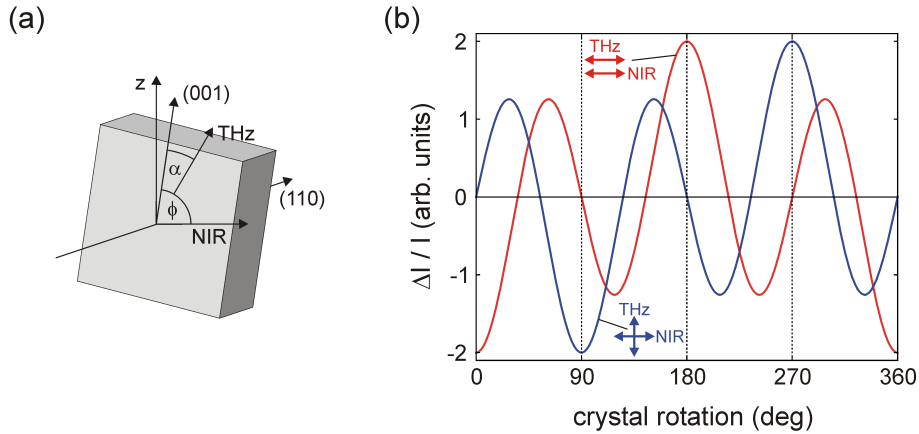


Figure 2.7: (a) Coordinate system used for the derivation of Eq. (2.26). The THz and the probe pulse propagate along the (110) direction of the electro-optic crystal. The laboratory z -axis is used to define vertical polarization. (b) The calculated intensity modulation $\Delta I/I$ for the case of vertical (blue) and horizontal (red) polarization of the THz field as function of the crystal rotation relative to the laboratory z -axis. The probe light is in both cases horizontally polarized.

EOD soon became the mostly used detection method for THz TDS. In the following, a short summary of the method is presented.

The working principle is based on the Pockels effect [63], the change of the refractive index of a nonlinear crystal upon applying an electrical field. In the case of EOD, the electric field is provided directly by the THz transient. A schematic of the detection setup is shown in Fig. 2.4. The linearly polarized probe pulse is collinearly combined with the THz transient in the EOC. The induced change of polarization is detected with a quarter-wave plate (QWP), a polarizing beam-splitter (WP) and a pair of balanced photodiodes (PD1 and PD2) [128, 130]. In this configuration, any common-mode noise of the laser and the optical components in the setup is canceled and the minimum detectable intensity modulation is on the order of 10^{-8} [128]. A clearly defined linear polarization of the probe pulse is essential and, typically, an additional polarizer is used in front of the EOC. As polarizing beam-splitter, a Wollaston prism is often used, which yields contrast ratios as high as $1 : 10^5$.

The material of choice for the EOC are covalent crystals with a zinc-blende-type lattice due to their low index mismatch between NIR and THz, their moderate electro-optic coefficients and no intrinsic birefringence [128]. Typical examples are GaP and ZnTe for Ti:Sapphire lasers and GaAs for Er:Fiber lasers.

A derivation of the intensity modulation $\Delta I/I = (I_{PD1} - I_{PD2}) / (I_{PD1} + I_{PD2})$ for ZnTe has been given by Planken *et al.* [130] as function of the polarization of probe and THz pulses relative to the crystal z -axis. The coordinate system used for the derivation is shown in Fig. 2.7a. The THz light and the probe

light are assumed to be monochromatic plane waves propagating along the (110) direction. The angle between the THz electric field and the crystal z -axis is denoted by α , the angle between the electric field of the probe pulse and the z -axis by ϕ , respectively.

After a suitable coordinate transformation, the refractive indices along the new z'' and y'' axes are given by [130]

$$n_{y''}(\alpha) \approx n + \frac{n^3}{2} E_{\text{THz}} r_{41} [\cos(\alpha) \sin^2(\theta) + \cos(\alpha + 2\theta)], \quad (2.21)$$

$$n_{z''}(\alpha) \approx n + \frac{n^3}{2} E_{\text{THz}} r_{41} [\cos(\alpha) \cos^2(\theta) - \cos(\alpha + 2\theta)], \quad (2.22)$$

where n is the NIR refractive index of the crystal, r_{41} the electro-optic coefficient, E_{THz} the THz electric field amplitude and

$$2\theta = -\tan^{-1}(2 \tan(\alpha)) - m\pi \quad (2.23)$$

with

$$\left(m - \frac{1}{2}\right) \pi \leq \alpha < \left(m + \frac{1}{2}\right) \pi, m = 0, 1, \dots \quad (2.24)$$

From Eqs. (2.21) and (2.22), it is evident that the field components of the probe light along the y'' and z'' direction acquire different phases and the probe beam will become elliptically polarized. The intensity modulation detected at the balanced diodes reads

$$\Delta I/I = \sin(2\phi - 2\theta) \sin\left(\frac{\omega L}{c_0} [n_{y''}(\alpha) - n_{z''}(\alpha)]\right), \quad (2.25)$$

where $\omega = 2\pi c_0/\lambda$ is the angular frequency of the probe light and L the crystal thickness. If the THz field is weak, i.e. the induced refractive index change is small compared to the linear refractive index, the second sine can be developed as a series. Just keeping the first term of the expansion leads to the simplified expression

$$\Delta I/I = \frac{\omega n^3 E_{\text{THz}} r_{41} L}{2c_0} [\cos(\alpha) \sin(2\phi) + 2 \sin(\alpha) \cos(2\phi)]. \quad (2.26)$$

Thus, the detected signal is directly proportional to the amplitude of the THz electric field. This allows the absolute determination of the field strength and will be used extensively in Chap. 4.

The dependence of the observable intensity modulation on the polarizations of the THz and the probe fields is plotted in Fig. 2.7b for two configurations commonly encountered in the experiment. In both cases, the probe light is assumed to be horizontally polarized, i.e. with the electric field parallel to the table plane. The two curves for the THz field polarized horizontally (red) and

vertically (blue) are offset by 90° with respect to each other. At certain rotation angles, the signal for one configuration vanishes, while it is maximized for the other configuration. Thus, by a suitable choice of the crystal orientation, it is possible to selectively detect only light with horizontal or vertical polarization, respectively.

Until now, we have dealt with phase matched plane waves. In reality, both THz and NIR pulses have a large bandwidth and dispersion becomes important. The extension to short pulses is done by replacing all parameters by their frequency dependent counterparts. Also, the THz and the NIR pulse typically travel with different velocities. This effect is known as the group velocity mismatch (GVM). The velocity of the NIR pulse is thereby given by the group refractive index

$$n_g(\lambda) = n(\lambda) - \lambda \frac{dn(\lambda)}{d\lambda}. \quad (2.27)$$

The achievable SNR is strongly dependent on a velocity matched propagation of the two pulses through the crystal. To estimate this effect on the detector response, we approximate the probe pulse by a delta-function centered at λ and the THz pulse by a monochromatic plane wave $E_{\text{THz}}(t) = E_{\text{THz}}^0(\Omega) \exp(i\Omega t)$. The detected THz spectrum can then be calculated by convolution of the detector response function with the THz field transient.

After propagation through the EOC with length L , the NIR pulse and the THz plane wave have acquired an accumulated GVM time of [129]

$$\delta(\Omega) = \frac{n_g(\lambda) - n_{\text{THz}}(\Omega)}{c_0} L, \quad (2.28)$$

where $n_{\text{THz}}(\Omega)$ is the THz refractive index. When we neglect any multiple reflections of the THz pulse inside the EOC, the frequency response function of the detector is obtained from Eq. (2.26) by averaging over $\delta(\Omega)$ and taking into account the frequency-dependent transmission of the crystal facet. This yields [128],

$$G(\Omega) = A \frac{r_{41}(\Omega)t_{12}(\Omega)}{\delta(\Omega)} \int_0^{\delta(\Omega)} e^{i\Omega t} dt \quad (2.29)$$

$$= A r_{41}(\Omega)t_{12}(\Omega) \frac{e^{i\Omega\delta(\Omega)} - 1}{i\Omega\delta(\Omega)}, \quad (2.30)$$

where

$$t_{12}(\Omega) = \frac{2}{1 + n_{\text{THz}}(\Omega)} \quad (2.31)$$

is the THz transmission coefficient of the crystal front-facet and

$$A = \frac{\omega n^3 L}{2c_0} [\cos(\alpha) \sin(2\phi) + 2 \sin(\alpha) \cos(2\phi)] \quad (2.32)$$

	ZnTe	GaP	GaAs
$n(\lambda = 800 \text{ nm})$	2.8529	3.1911	-
$n(\lambda = 1.55 \text{ }\mu\text{m})$	2.7332	3.0541	3.3737
$n_g(\lambda = 800 \text{ nm})$	3.2387	3.6151	-
$n_g(\lambda = 1.55 \text{ }\mu\text{m})$	2.8071	3.1431	3.5422
ε_∞	6.7 ^a	9.075 ^a	10.86 ^b
ω_{TO} [$2\pi \times 10^{12}\text{s}^{-1}$]	5.31 ^a	11.01 ^a	8.05 ^b
ω_{LO} [$2\pi \times 10^{12}\text{s}^{-1}$]	6.18 ^a	12.08 ^a	8.75 ^b
γ [$2\pi \times 10^{12}\text{s}^{-1}$]	0.09 ^a	0.13 ^a	0.08 ^b
C	-0.07 ^a	-0.47 ^c	-0.59 ^d
$r_{41}(\Omega = 0)$ [pm/V]	3.9 ^e	0.98 ^f	1.5 ^d
r_e [pm/V]	4.19	1.85	3.65

Table 2.1: Material parameters used for the calculation of the frequency response function of the EOD. The values for n_g are from the references mentioned in the text. The electronic part of the electro-optic coefficient is calculated using (2.35). Further values are taken from ^(a) Ref. [133], ^(b) Ref. [134], ^(c) Ref. [135], ^(d) Ref. [136], ^(e) Ref. [130], and ^(f) Ref. [137].

an amplitude factor.

The effect of different detector configurations, including those with reflections from the crystal backside, have been discussed by Wu *et al.* [128]. Even if the GVM time would be zero, the reflection of the THz pulse from the backside distorts the measured spectrum significantly. In the experiment, it is therefore advisable to circumvent any reflections by using anti-reflection coatings [116,131] or a thick (100) substrate, which is not electro-optically active.

The frequency dependence of the electro-optic coefficient $r_{41}(\Omega)$ has been derived by Faust and Henry [132]. In the THz frequency range, it shows a strong dispersion due to the transverse optical (TO) phonon resonance of the crystal lattice. With the TO phonon frequency ω_{TO} , the electro-optic coefficient is given by [132,133]

$$r_{41}(\Omega) = r_e \left[1 + C \left(1 - \frac{(\hbar\Omega)^2 - i\hbar\Omega\gamma}{(\hbar\omega_{TO})^2} \right)^{-1} \right], \quad (2.33)$$

where γ is the lattice damping, C the Faust-Henry coefficient, which is related to the ratio of the ionic and electronic part of the electro-optic coefficient and r_e the electronic contribution, which is assumed to be constant.

The parameters for GaP, ZnTe and GaAs are listed in Tab. 2.1. The THz refractive index of zinc-blende crystals is, in addition to ω_{TO} and γ , determined

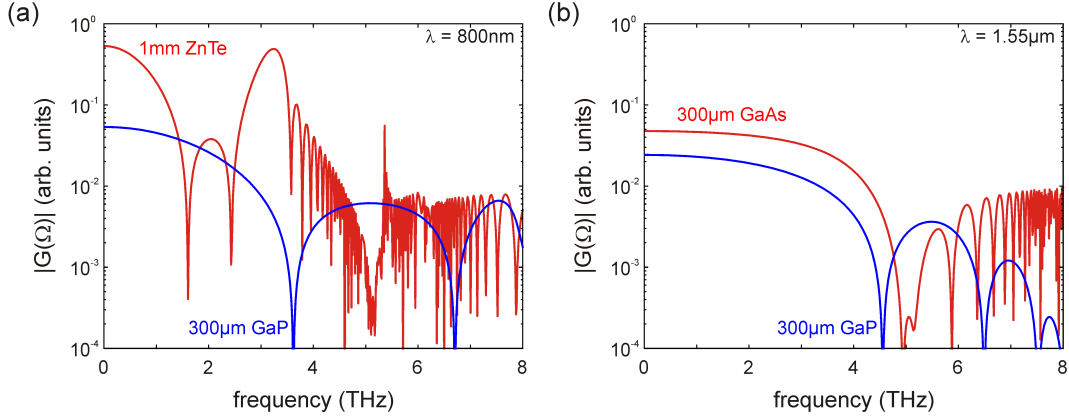


Figure 2.8: Frequency response function of different crystal / wavelength combinations as calculated using Eq. (2.29). (a) Response function of 1 mm thick ZnTe (red) and 300 μm thick GaP (blue) for $\lambda = 800\text{ nm}$. (b) Response function of 300 μm thick GaAs (red) and GaP (blue) for $\lambda = 1.55\ \mu\text{m}$.

by the longitudinal optical (LO) phonon frequency [3],

$$n_{\text{THz}}(\Omega) = \sqrt{\varepsilon_{\infty} \left(1 + \frac{\omega_{LO}^2 - \omega_{TO}^2}{\omega_{TO}^2 - \Omega^2 + i\Omega\gamma} \right)}. \quad (2.34)$$

The group index of the probe pulse has been calculated using Eq. (2.27) from the refractive index, which is often given in form of a Sellmeier equation. The NIR refractive indices for GaP, ZnTe and GaAs are found, for example, in [138], [139] and [140], respectively. The electronic contribution to the electro-optic coefficient is given by the static electro-optic coefficient $r_{41}(\Omega = 0)$ and the Faust-Henry coefficient C as

$$r_e = \frac{r_{41}(\Omega = 0)}{1 + C}, \quad (2.35)$$

which has been derived from (2.33) by letting $\Omega = 0$.

Figure 2.8 shows the frequency response function of four EOC / wavelength combinations that have been used in this thesis. For Ti:Sapphire lasers with a center wavelength around 800 nm, a 1 mm thick ZnTe crystal and a 300 μm thick GaP crystal have been employed (see Fig. 2.8a). For frequencies below $\approx 1.5\text{ THz}$, the ZnTe crystal yields an up to ten times higher signal than the GaP crystal. Around 3 THz, it could in principle also be used for an efficient narrow-band detection. For higher frequencies, the GaP is better suited for EO detection due to the higher lying phonon frequencies, which allow a broadband detection (see Tab. 2.1). In combination with an Er:Fiber laser, GaP and GaAs crystals, each with a thickness of 300 μm have been used. From Fig. 2.8b, it is evident that GaAs is the better choice, both in terms of achievable signal and bandwidth.

In the simplified discussion so far, two effects have been left out, that may have some influence on the detector response function. One effect is the finite width of the probe pulse, which could be taken into account by averaging Eq. (2.29) over its spectrum. This would have two consequences. First, the sharp minima of the response function are washed out, i.e. become less pronounced and, second, the signal amplitude falls off towards higher frequencies. For a 100 fs long pulse, however, this effect does not play a significant role.

The second effect are two-phonon resonances below the reststrahlen band, which lead to a high absorption of the THz pulse. In the case of ZnTe, there are two broad absorption bands centered around 1.6 THz and 3.7 THz, respectively, with the 3.7 THz band being the strongest [141]. Thus, the ZnTe EOC shown in Fig. 2.8a is effectively only usable up to ≈ 2.5 THz.

The dominant modes in GaP are weaker than those in ZnTe. They are centered around 2.2 THz, 3 THz, and 4.3 THz [142, 143], leading to a staircase-like absorption spectrum. The decrease of the response curve for higher frequencies is thus steeper than shown in Figs. 2.8a and 2.8b.

In the case of GaAs, the relevant resonances are at 2.4 THz and 4.6 THz, respectively [144]. While the 2.4 THz mode is relatively weak and has little influence on the response function, the absorption in the higher one is very strong. Luckily, this resonance coincides with the first minimum of the detector response function for the case shown in Fig. 2.8b and does not corrupt the detector efficiency below 4.5 THz.

Chapter 3

THz Metamaterials Coupled To Intersubband Transitions

The following chapters introduce the basic theory underlying optical properties of intersubband transitions (ISBTs) in semiconductor quantum wells (QWs) and the electrodynamics of metamaterials (MM), both subjects that present an interesting field of research on their own. In the subsequent chapters, effects arising from the close contact of QWs with a regular array of meta-atoms are discussed. It is demonstrated that the coupling between ISBTs and the MM leads to the occurrence of the so-called normal mode splitting, which is an indicator for light-matter interaction in the strong coupling regime. In the THz spectral range, the coupling strength can even approach the transition energy, a regime which is referred to as ultrastrong coupling [145,146]. The experimental signature is the opening of a so-called polaritonic gap in the anti-crossing diagram of the normal mode frequencies [147–150]. We present experimental evidence of ultrastrong coupling between a MM and QW ISBTs and, finally, some theoretical indications of a possible THz-field-induced strong-to-weak coupling transition.

3.1 Optical Properties of Intersubband Transitions in Quantum Wells

The following chapter is devoted to the derivation of basic optical properties of ISBTs in QWs as these form the basis for understanding the coupling between MMs and intersubband (ISB) excitations in general. Intersubband transitions are transitions between different subbands of the conduction band of a semiconductor that arise from a strong confinement of the electronic wavefunction along one dimension.

The whole topic has been started with the invention of molecular beam epitaxy, a technique that allows the growth of semiconductor heterostructures

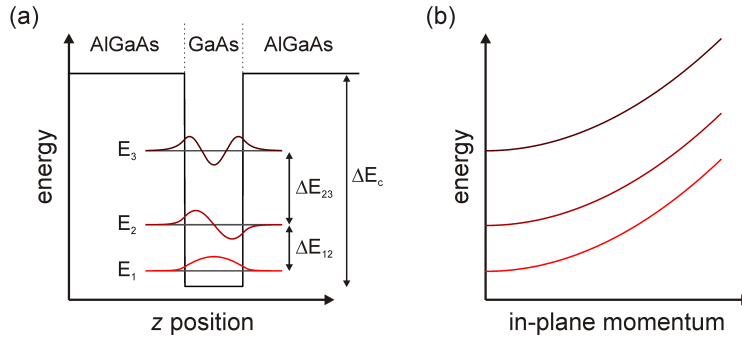


Figure 3.1: (a) Conduction band structure of a thin GaAs quantum well embedded between two semi-infinite AlGaAs barriers. The confinement along the z axis leads to discrete bound states. (b) The bound electrons behave as free particles in the quantum well plane and show a quadratic dispersion relation. Therefore, the transition energy between different subbands is independent of the wavevector.

with atomic precision [27]. Thereby, an important aspect is to achieve lattice matching between different semiconductor layers in order to fabricate high quality interfaces. A model system in this respect is AlGaAs / GaAs, for example, which has been used in the very first experiments that demonstrated the existence of quantized states in semiconductor heterostructures [151]. At room temperature, $\text{Al}_x\text{Ga}_{1-x}\text{As}$ has a direct band gap of $E_{g,\text{AlGaAs}} = (1.424 + 1.274x)$ eV for aluminum concentrations below 45% [152], which is larger than the band gap of GaAs, $E_{g,\text{GaAs}} = 1.424$ eV. The AlGaAs / GaAs system forms a type-I band structure, i.e. AlGaAs forms a barrier for both electrons and holes. The further discussion is limited to electrons in the conduction band only¹. The barrier height for the electrons is determined by the conduction band offset, ΔE_c , which is 62% of the total band gap difference $\Delta E_g = E_{g,\text{AlGaAs}} - E_{g,\text{GaAs}}$ [153]. For an aluminum concentration of $x = 0.3$, for example, the conduction band offset is $\Delta E_c = 0.24$ eV.

The conceptually simplest heterostructure is a quantum well, i.e. a very thin layer of GaAs sandwiched between two semi-infinite layers of AlGaAs. The conduction band profile is sketched in Fig. 3.1a for the case of a $L = 15$ nm wide GaAs layer. The coordinate system is chosen such that the growth direction is given by the z axis and the quantum well lies in the x - y plane. The confinement potential of the QW can be written as

$$V(\mathbf{r}) = V(z) = \begin{cases} 0 & \text{for } -L/2 \leq z \leq L/2 \\ \Delta E_c & \text{elsewhere} \end{cases} \quad (3.1)$$

The strong confinement of the electron wavefunction in the GaAs well along the growth direction leads to the occurrence of quantization effects, whereas the electrons behave as free particles along the x and y directions, respectively.

¹The theory is however equally valid for holes in the valence band.

The optical properties of the QW are reflected in the ISB absorption coefficient α , which is usually defined via Beer's law,

$$\frac{d}{dz}I(z) = -\alpha I(z), \quad (3.2)$$

and the intensity I of the optical beam. In a QW, the absorption of photons is associated with the excitation of electrons. Thus, the absorption coefficient is proportional to the total transition probability W_t of electrons from lower to higher states, which is obtained by summing over the transition rates between all possible initial and final states weighted by the statistical occupation numbers, i.e. $W_t \propto \sum_{if} W_{if} f(E_i) [1 - f(E_f)]$ [30].

To calculate the transition rate W_{if} from an initial state $|i\rangle$ to a final state $|f\rangle$, we make use of Fermi's golden rule²:

$$W_{if} = \frac{2\pi}{\hbar} |\langle f | H_{\text{int}} | i \rangle|^2 \delta(E_f - E_i - \hbar\omega), \quad (3.3)$$

where the δ -function ensures energy conservation, and $H_{\text{int}} = -e\mathbf{r}\mathbf{E}$ is the interaction Hamiltonian in the dipole approximation. Thereby, the electric field of the incident wave is denoted by $\mathbf{E} = \hat{\mathbf{e}}E_0$, where E_0 is the amplitude of the wave and $\hat{\mathbf{e}}$ its polarization vector. In order to determine the matrix element

$$\langle f | H_{\text{int}} | i \rangle = -eE_0 \int_V \Psi_f^*(\mathbf{r}) \mathbf{r} \hat{\mathbf{e}} \Psi_i(\mathbf{r}) d\mathbf{r}, \quad (3.4)$$

which is the central term in Eq. (3.3), we first need to calculate the electron wavefunctions. To simplify the algebra, we use the envelope function approach in the effective mass approximation for the electron wavefunctions [40]. Taking into account only the conduction band, we can assume that the lattice-periodic part of the wavefunction, the so-called Bloch function [3], is the same in both well and barrier. Thus, only the envelope wavefunction, $\Psi_n(\mathbf{r})$, has to be considered in the following.

In each layer, the wavefunction of the n -th bound state has to satisfy the Schrödinger equation [40]

$$-\frac{\hbar^2}{2m_{\text{eff}}} \nabla^2 \Psi_n(\mathbf{r}) + V(\mathbf{r}) \Psi_n(\mathbf{r}) = E_n \Psi_n(\mathbf{r}), \quad (3.5)$$

with the effective mass m_{eff} and the energy eigenvalue E_n . In view of (3.1), a natural choice for the envelope wavefunction is the Ansatz

$$\Psi_n(\mathbf{r}) = \psi_n(x, y) \varphi_n(z). \quad (3.6)$$

²Named after Enrico Fermi (1901 - 1954). It dates back to the initial work of Paul Dirac (1902 - 1984) [154].

The in-plane part $\psi_n(x, y)$ is directly solved by a plane wave,

$$\psi_n(x, y) = \psi(\mathbf{r}_{\parallel}) = \frac{1}{\sqrt{A}} e^{ik_{\parallel}\mathbf{r}_{\parallel}}, \quad (3.7)$$

while the z dependent part can be solved using the following continuity relations at an interface between layers A and B [40]:

$$\varphi_n^A(z_0) = \varphi_n^B(z_0) \quad (3.8)$$

$$\frac{1}{m_{\text{eff}}^A} \frac{\partial \varphi_n^A}{\partial z}(z_0) = \frac{1}{m_{\text{eff}}^B} \frac{\partial \varphi_n^B}{\partial z}(z_0). \quad (3.9)$$

The latter can be done very efficiently using a transfer matrix approach [155]. The prefactor in (3.7) is a normalization factor with A being the sample area. As an example, the z dependent wavefunctions of the three bound states of the 15 nm wide QW are shown in Fig. 3.1a.

Once the energy eigenvalues E_n are found, the total energy of the n -th subband can be written as

$$E_{n,k_{\parallel}} = E_n + \frac{\hbar^2 k_{\parallel}^2}{2m_{\text{eff}}}. \quad (3.10)$$

The quadratic in-plane dispersion is shown in Fig. 3.1b. Note that neither k_{\parallel} nor m_{eff} depend on the subband index and that the energy difference between two subbands is thus independent of the in-plane wavevector k_{\parallel} . As a consequence, the transitions between two subbands appear as distinct absorption lines in the spectra.

For the further discussion, it is instructive to consider the simple case of an infinite QW, i.e. $\Delta E_c \rightarrow \infty$, where the z dependent part of the wavefunction has to vanish at the interfaces $z = \pm L/2$. The total envelope wavefunction of the n -th level is found to be given by [156]:

$$\Psi_n(\mathbf{r}) = \sqrt{\frac{2}{V}} \sin\left(\frac{n\pi}{L}z + \frac{n\pi}{2}\right) e^{ik_{\parallel}\mathbf{r}_{\parallel}}, \quad n \geq 1, \quad (3.11)$$

with the normalization volume $V = AL$. Thus, the wavefunctions of different subbands are orthogonal to each other, i.e. $\langle \Psi_n | \Psi_m \rangle = 0$ for $n \neq m$. Furthermore, the wavefunctions associated to subsequent levels have opposite polarity and the in-plane coordinates x and y enter only via the phase term $\exp(ik_{\parallel}\mathbf{r}_{\parallel})$.

We can separate the matrix element (3.4) into three terms according to the three coordinate axes:

$$\langle \Psi_f | \mathbf{r}\hat{\mathbf{e}} | \Psi_i \rangle = \langle \Psi_f | x | \Psi_i \rangle + \langle \Psi_f | y | \Psi_i \rangle + \langle \Psi_f | z | \Psi_i \rangle. \quad (3.12)$$

Due to the rotational symmetry around the growth axis, the matrix elements $\langle \Psi_f | x | \Psi_i \rangle$ and $\langle \Psi_f | y | \Psi_i \rangle$ have to be equal. As the coordinates x and y enter

only via a phase, it is obvious that light polarized in the QW plane can never contribute to intersubband transitions. For light polarized along the z axis, however, the matrix element $\langle \Psi_f | z | \Psi_i \rangle$ is non-zero provided that the polarity of the wavefunctions of the initial and final states is different.

By taking into account not only absorption but also stimulated emission and replacing the δ -function by a Lorentzian line shape, the intersubband absorption coefficient is found after integrating over $k_{||}$. For frequencies ω close to the transition frequency $\omega_{nm} = (E_m - E_n)/\hbar$, the final result reads [40]:

$$\alpha = \frac{e^2 k_B T L}{2\varepsilon_0 c_0 n_0 \hbar} \sum_{n,m} f_{nm} \ln \left(\frac{1 + e^{(E_F - E_n)/k_B T}}{1 + e^{(E_F - E_m)/k_B T}} \right) \frac{\Gamma/(2\pi)}{(\omega_{nm} - \omega)^2 + \Gamma^2/4}, \quad (3.13)$$

where E_F is the Fermi energy, T the temperature, n_0 the background refractive index and Γ the full width at half maximum linewidth of the transition. Furthermore, we have introduced the so-called oscillator strength [40],

$$f_{nm} = \frac{2m_{\text{eff}}\omega_{nm}}{\hbar} |\langle m | z | n \rangle|^2, \quad (3.14)$$

which obeys the sum rule $\sum_{nm} f_{nm} = 1$. The replacement of the δ -function by the Lorentzian line shape follows from the inclusion of relaxation processes in the density matrix formalism and is well justified by experimental observations [40, 89]³.

The position of the Fermi level is determined by the doping and the number of free carriers in the structure. In general, the doping is chosen such that at zero temperature, only the lowest subband is filled. In this case, only the transition between the first and the second subband is important, and Eq. (3.13) can be simplified to [40]

$$\alpha = \frac{e^2 n_{2d} L}{2\varepsilon_0 c_0 n_0 m_{\text{eff}}} f_{12} \frac{\Gamma/2}{(\omega_{12} - \omega)^2 + \Gamma^2/4}, \quad (3.15)$$

where n_{2d} is the areal electron density. This expression is formally equivalent to the absorption coefficient derived from the classical Lorentz model of a two-level system [89]. Therefore, we will use the Lorentz model for the simulation of quantum wells in finite-difference time-domain calculations (FDTD) in Chap. 3.3.

The doping also influences the band structure and has to be taken into account in the calculation of the energy levels and the transition frequencies by solving the Schrödinger and Poisson equations self-consistently [40]. For high electron densities, many body effects start to play a role in the optical properties

³This line shape is strictly valid only for parallel subbands, all electrons in the ground state and weak optical driving fields. A discussion of corrections to the Lorentzian line shape can be found in [157].

of QWs. Especially in the THz range, the so-called depolarization shift can lead to a quite significant modification of the absorption frequency [40]:

$$\tilde{\omega}_{12} = \omega_{12}\sqrt{1 + \Delta}, \quad (3.16)$$

where

$$\Delta = \frac{2e^2 n_{2d}}{\varepsilon \varepsilon_0 \hbar \omega_{12}} S, \quad (3.17)$$

with

$$S = \int_{-\infty}^{\infty} dz \left[\int_{-\infty}^z dz' \Psi_2(z') \Psi_1(z') \right]^2. \quad (3.18)$$

The electrons do not feel the incident electric field, but rather a field screened by the remaining two-dimensional electron gas. Exposing the system to radiation not only excites electrons into higher subbands, but changes at the same time the charge density. This gives rise to a restoring force, which leads to collective oscillations of the electrons. Thus, Eq. (3.16) can alternatively be written in terms of a three-dimensional plasma frequency [40]

$$\tilde{\omega}_{12} = \sqrt{\omega_{12}^2 + f_{12}\omega_p^2}, \quad (3.19)$$

with $\omega_p = \sqrt{n_{2d}e^2/\varepsilon\varepsilon_0 m_{\text{eff}} L_{\text{eff}}}$, and $L_{\text{eff}} = \hbar f_{12}/2m_{\text{eff}} S \omega_{21}$. In the case of the infinite QW, $S = (5/9\pi^2)L$ and $L_{\text{eff}} = 3f_{12}/5L$ for the transition between the ground and first excited state. Equation (3.17) is strictly valid only for two-level systems and an extension to more levels can be found in Ref. [158], for example.

For increasing temperature, electrons are thermally excited and also the higher subbands become occupied. As a consequence, the absorption strength of the lower transitions decreases. Thus, for too high values of T , no ISBTs will be observable. An intuitive argument for the maximum allowed temperature is that the transition energy should be larger than the thermal energy, i.e. $E_2 - E_1 > k_B T/2$ [156]. For a transition at 1 THz, for example, this criterion yields a maximum temperature of 96 K. In general, an increased temperature is accompanied by an increase of the linewidth due to enhanced scattering. Thus, the temperature dependence of the transmission through a quantum well structure constitutes a simple way of identifying ISBTs in semiconductor heterostructures. We will make use of this fact in Chap. 3.3. Another experimental technique to detect the relatively weak ISB absorption is to modulate the electron density inside the quantum well by applying an external bias voltage [159]. This amounts to a variation of the Fermi level and allows to switch the ISBT on and off, while keeping all other experimental parameters unchanged. This is the preferred way of measuring THz ISBTs due to its selectivity and will be used extensively in Chap. 5.

To summarize, we have derived the basic optical properties of ISBTs in QWs. The most important aspect is that only light polarized parallel to the growth

direction of the heterostructure can induce ISBTs. This polarization selection rule limits the ability to couple free space radiation efficiently into the QW. In the following chapter, we introduce THz metamaterials, which present an excellent way to overcome this limitation.

3.2 Electrodynamics of Terahertz Metamaterials

This chapter gives a short overview over the electrodynamic properties of metamaterials as far as these are needed for the understanding of the coupling of ISBTs and metamaterials. The term *metamaterial* denotes an artificial medium in the general sense with optical properties that cannot be found in nature. A special class of MM is thereby the so-called metasurface or metafilm [160], a two-dimensional arrangement of scattering particles or meta-atoms showing a resonant electric and / or magnetic polarizability. Such metafilms are technologically easy to implement and hence represent the largest sub-group within the family of metamaterials. In the following discussion, which deals solely with two-dimensional metafilms, we use both terms, metafilm and metamaterial, synonymously.

An exotic example of a metafilm is shown in Fig. 3.2a, which consists of a regular array of the Japanese character (kanji) for *husband* fabricated by physical vapor deposition (PVD) of gold on a GaAs substrate. In principle, there is no limitation on the geometrical shape of the meta-atoms making up the metamaterial, as long as the typical length scale fulfills a certain size criterion. Based on this criterion, analytic models for the optical properties of metamaterials use the so-called effective medium approach. The rather complex geometry of the metamaterial is replaced by effective material parameters, which allow to model the metamaterial as a bulk medium [48], or via averaged transition conditions for the electromagnetic field [160, 161].

Under the assumption that the typical size of the scatterers is much smaller than the wavelength, $R \ll \lambda$, the external electromagnetic field can be taken as homogeneous across the particle⁴. The scattered field can then be described in a multipole expansion. If the spacing of the particles, a , is larger than twice the particle size, $a > 2R$, the contributions from higher terms become negligible and the metasurface can be approximated as an array of dipole scatterers. Neglecting the coupling between neighboring meta-atoms, the electric and magnetic polarization densities induced by the incident wave can be approximated by

$$\begin{pmatrix} \mathbf{P} \\ \mathbf{M} \end{pmatrix} = N\bar{\alpha} \begin{pmatrix} \mathbf{E} \\ \mathbf{B} \end{pmatrix}, \quad (3.20)$$

⁴For plane waves under normal incidence, the phase front is constant across the sample and the size limit on the scatterer is not so critical.

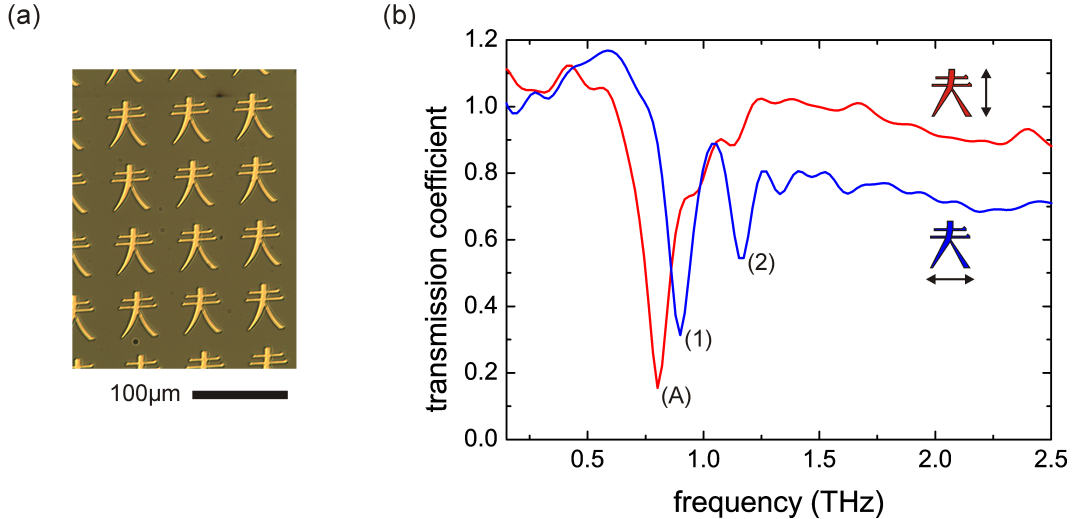


Figure 3.2: Metamaterial based on the Japanese kanji for *husband*. (a) Microscope image of the processed metamaterial. (b) Measured transmission spectra under normal incidence. The electric field polarization is indicated by the black arrows. The resonances can be attributed to (1) the long horizontal bar, (2) the short horizontal bar and (A) the vertical bars.

where $N = 1/a^2$ is the average areal density of the particles and $\bar{\alpha}$ the polarizability tensor. The elements of $\bar{\alpha}$ can be calculated analytically for some basic shapes using, for instance, antenna theory [162], or equivalent circuit models [163, 164].

However, the above stated criterion is only partially fulfilled in most metamaterials. In the case of the Japanese kanji metafilm shown in Fig. 3.2a, for example, the unit cell size is similar to the incident wavelength. Additionally, the typical feature size of the meta-atoms is often on the order of

$$R \approx \lambda / (2\bar{n}) \quad (3.21)$$

to be resonant with the incident wave. Thereby, \bar{n} is the effective refractive index of the surrounding medium [165],

$$\bar{n} = \sqrt{\bar{\epsilon}\bar{\mu}}, \quad (3.22)$$

where

$$\bar{\epsilon} = \frac{1}{2} (\epsilon_1 + \epsilon_2), \quad \text{and} \quad \bar{\mu} = \left[\frac{1}{2} (\mu_1^{-1} + \mu_2^{-1}) \right]^{-1}, \quad (3.23)$$

respectively, and the indices 1 and 2 denote the two half-spaces enclosing the meta-atom. For a GaAs substrate, for example, $\bar{n} = 2.64$. Figure 3.2b shows the transmission coefficient of the structure that has been measured using a THz TDS setup under normal incidence. The orientation of the electric field of the THz pulses with respect to the metasurface is indicated by the black arrows.

The transmission coefficient, which is essentially flat in the entire frequency range, exhibits sharp resonances depending on the polarization. Using the resonance criterion postulated above, these can be associated to the long (1) and short (2) horizontal bars and the body (A) of the kanji.

Due to this only marginal fulfillment of the homogenization requirements, the analytic treatment in the effective medium picture becomes much more involved [166]. Furthermore, there exist almost no closed analytic expressions for the polarizabilities of general meta-atom geometries. Therefore, it is common practice to switch to fully numerical methods, such as the finite-difference time-domain method⁵, for example [168]. Furthermore, these methods allow to study the quite complex interaction between single meta-atoms and ISBTs in a QW underneath the metasurface with relatively low additional effort and are thus ideally suited for our purposes.

The computational space we are using for the three-dimensional full-wave calculations is shown in Fig. 3.3a. The metasurface is placed at the boundary between vacuum in the upper half-space and the substrate in the lower half-space. By using periodic boundary conditions (PBC) at the four side walls, it is sufficient to just consider a single unit cell. For simplicity, we consider the THz pulses to be normally incident from the top, which leads to an especially simple formulation of the PBCs:

$$\mathbf{F}(i, j, k) = \mathbf{F}(i + N_x, j, k) \quad (3.24)$$

$$\mathbf{F}(i, j, k) = \mathbf{F}(i, j + N_y, k), \quad (3.25)$$

where \mathbf{F} represents some field variable, $N_x \times N_y$ is the number of grid cells making up a unit-cell and i, j , and k are grid cell indices. At the top and bottom boundary, we use first-order Engquist-Majda absorbing boundary conditions (ABC) [169,170], together with the so-called total-field / scattered-field approach to reduce the load on the ABCs [170,171]. We use a plane wave excitation source to simulate a single-cycle THz pulse with a Gaussian envelope. The substrate is taken into account as frequency independent and lossless dielectric with a constant refractive index n . This simplified treatment is sufficient for most substrate materials and frequencies far from the phonon resonance. In GaAs, for example, this is the case for frequencies below 5 THz. However, the extension to a more realistic, dispersive medium would be straightforward [167]. The FDTD algorithm is based on the standard Yee grid and the leapfrog method for spatial and temporal staggering of the electric and magnetic field components [172]. The temporal step size Δt is related to the spatial grid size Δr by $c_0 \Delta t = \mathcal{C} \Delta r$, where $\mathcal{C} = 0.5$ is the Courant number. To ensure stable computation, the Courant number should be smaller than $1/\sqrt{3}$ for three-dimensional simulations [167]. The spatial step size has to be chosen according

⁵In the FDTD method, Maxwell's equations are solved by replacing the partial derivatives by finite-differences and solving for the new field values at the next time step. An excellent introduction is found in [167], for example.

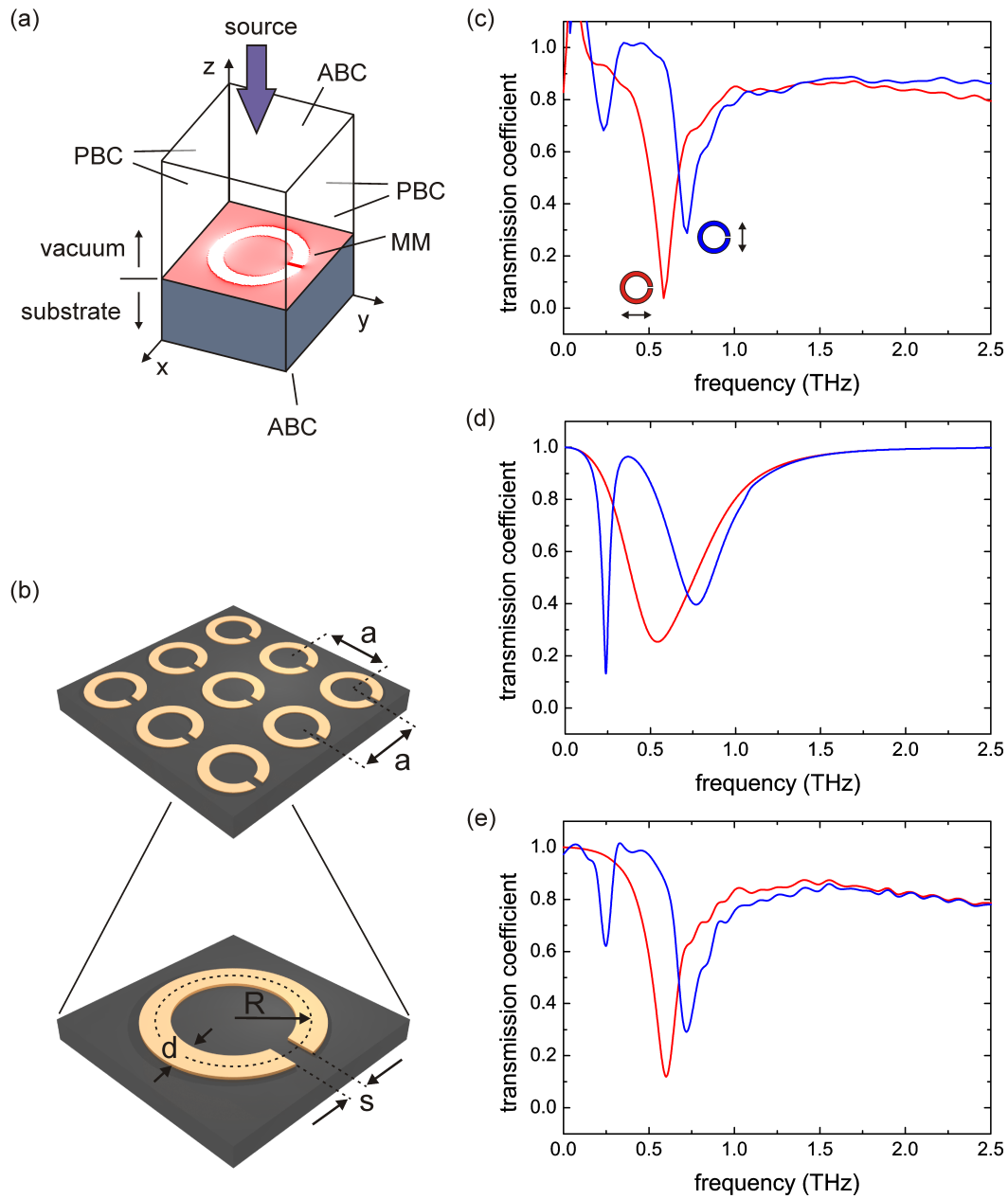


Figure 3.3: (a) Sketch of the FDTD domain used for the simulations. The metamaterial (MM) separates vacuum and substrate. The THz pulses are incident from the vacuum side. The top and bottom face is bounded by Mur absorbing boundary conditions (ABC), while the sides use periodic boundary conditions (PBS). (b) Metamaterial based on split-ring resonators. The unit cell size is $a \times a$. The rings have a radius R and a thickness d , the split width is s . (c) Measured transmission coefficients for the polarizations indicated by the black arrows under normal incidence. (d) Calculated transmission coefficients using the analytic model. (e) Calculated transmission coefficients using the FDTD code.

to the smallest feature sizes of the meta-atom. Typically, we use a step size of $\Delta r = 1 \mu\text{m}$, unless otherwise noted. To minimize staircasing errors introduced by approximating rounded contours of the meta-atoms by rectangular grid cells, we use the diagonal split-cell method [167]. The meta-atoms themselves are simulated as perfect electric conductors by fixing the components of the electric field along the x and y direction in the respective grid-cells to zero. Thereby, the meta-atoms have an effective height of half a grid cell. Using a perfect metal is a very good approximation in the THz frequency range, where Ohmic losses in the metal can usually be neglected (see below).

To illustrate the performance of the FDTD code, Figs. 3.3c to 3.3e show the transmission coefficient of a split-ring resonator (SRR) based metasurface. The SRR can be considered the archetype of any modern metamaterial. Its popularity dates back to the seminal paper by Pendry *et al.* [173], where it has been mentioned as a constituent of magnetic metamaterials. Its original proposal dates back to Schelkunoff and Friis [50], who stated that the diamagnetic response of a metallic ring could be strongly enhanced by introducing a load capacitance in form of a slit. The SRR is nowadays probably the most often used MM building block and the ideal model system to illustrate the electrodynamics of metamaterials. The geometry of the SRR MM is sketched in Fig. 3.3b. The SRRs are arranged on a regular array with a lattice period of $a = 120 \mu\text{m}$. They have a mean radius of $36 \mu\text{m}$ and a thickness of $d = 12 \mu\text{m}$. The split width is chosen as $s = 5 \mu\text{m}$.

For the experimental realization, the MM has been fabricated by physical vapor deposition (PVD) of a 10 nm titan adhesion layer followed by 180 nm gold on a GaAs substrate. The transmission has been measured under normal incidence with a THz TDS setup using two different polarizations of the incident wave. To obtain the frequency dependent transmission coefficient, the transmission signal with the metasurface has been normalized to the transmission of a bare GaAs substrate. The orientation of the electric field is indicated by the black arrows in Fig. 3.3c. When the electric field is oriented parallel to the slit (red), there appears a single resonance around 0.6 THz. In the perpendicular case (blue), the resonance is split into a narrow one around 0.26 THz and a broader one at 0.73 THz. The details of the resonant modes will be discussed below.

The SRR is one of the few cases for which a closed analytic form of the polarizability tensor $\bar{\alpha}$ exists (see Appx. B). Figure 3.3d shows the calculated transmission coefficients based on the analytic model outlined above. The position and qualitative shape of the resonances are well reproduced. However, the absolute width of the transmission minima is overestimated and the relative amplitudes are different. These deviations from the simple model can be attributed to a mutual coupling between neighboring unit cells, which has been neglected in the analytical calculations⁶.

⁶There exist several ways in which the coupling can be taken into account. See for

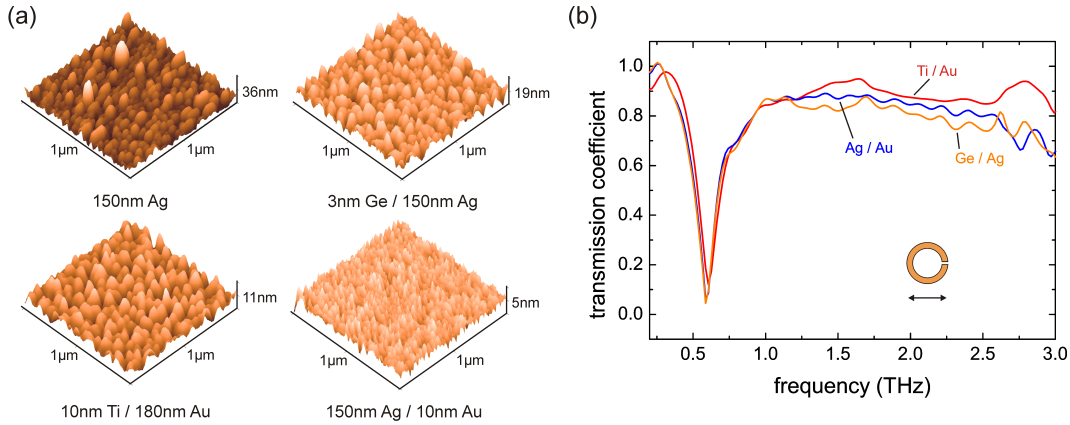


Figure 3.4: Effect of different metalizations on the metamaterial performance. (a) AFM images showing the surface profile of different metalizations. The smoothest surface with the smallest grains is achieved by a combination of Ag/Au. (b) Measured transmission coefficient of a SRR based metamaterial fabricated with different metalizations. The influence of the metal is visible for frequencies above 1.2 THz with Ti/Au showing the highest transmission.

Finally, Fig. 3.3e shows the simulated transmission coefficients using the FDTD code. For the simulations, we have used a computational domain consisting of $60 \times 60 \times 400$ grid cells with a simulation time of 20 ps and a spatial step size of $\Delta r = 2 \mu\text{m}$. There is an excellent agreement to the experimental results shown in Fig. 3.3c. The simulation predicts not only the exact position, but reproduces both the amplitude and correct width of the resonances. This confirms the validity of the assumptions made for the substrate material and especially for the MM metalization.

To further investigate the role of the metalization, we have fabricated the same SRR MM with different combinations of metals by PVD on GaAs substrates. For the metalizations, we have chosen primarily silver (150 nm) and gold (180 nm) due to their high bulk conductivities [175, 176]. To improve the adhesion of gold on GaAs, a 10 nm thick Ti layer is usually deposited beforehand. As evaporated silver films tend to oxidize quickly in the ambient atmosphere, we have also tested the use of a thin Au protection layer (10 nm) on top of the Ag film. Finally, we have evaporated Ag on a very thin Ge wetting layer (3 nm), as this combination is expected to produce extremely smooth silver surfaces [177].

Figure 3.4a shows atomic-force microscope (AFM) images of $1 \times 1 \mu\text{m}^2$ -sized patches of the SRR surface. These images allow to evaluate properties such as typical grain size and surface roughness, which are mainly responsible for the THz conductivity of the metal films [178]. The highest value of the surface roughness is found for the silver film. The peak-to-valley distance of 36 nm and the root-mean square (rms) roughness of 4 nm agree with reported values [177].

example [48, 174].

The use of Ge as wetting layer brings an improvement by roughly a factor of two (peak-to-valley: 19 nm, rms: 2.5 nm). Thus, for the thickness of the Ag layers we are using, the Ge film does not work as well as for thin films with thicknesses about 10-15 nm [177]. The Ti/Au layer shows a peak-to-valley distance of 11 nm and a rms roughness of 1.5 nm. Thereby, it exhibits the largest grains with diameters ranging from 70 nm to 160 nm. By far the smoothest surface is achieved by capping the Ag film with a protective Au layer (peak-to-valley: 6 nm, rms: 0.7 nm). The achieved roughness values are similar to the *ultrasmooth* silver films reported in [177]. At the same time, this sample shows the smallest grains with diameters between 20 and 40 nm.

To evaluate the performance of the different metalizations, we have measured the transmission coefficient of the SRR MM for the electric field of the incident pulse oriented parallel to the slit. The results for Ti/Au, Ag/Au and Ge/Ag are shown in Fig. 3.4b. Unfortunately, no transmission data is available for the case of pure silver⁷. For frequencies below 1.2 THz, there is practically no difference between the three samples, while for higher frequencies, the curves start to deviate. The Ti/Au layer shows the highest transmission, followed by Ag/Au and Ge/Ag. The difference in the transmission coefficients is thereby on the order of a few percent. The measured results contradict the aforementioned role of the surface roughness in the THz conductivity of metal layers, at least regarding the height variations. The slightly better performance of the gold layer, might be attributed to the larger (lateral) grain size which favors ballistic motion on the time scale of a THz cycle [179].

The comparably small differences of the transmission coefficients measured with different metalizations support the approximation made in the FDTD simulations regarding the use of a perfect metal, especially as they are smaller than the typical spread induced by geometrical variations and fabrication imperfections. The remaining discussion of the properties of MMs will be based on the results of the FDTD simulations.

In order to determine the microscopic origin of the well-defined resonances shown in Figs. 3.3c to 3.3e, we have performed a Fourier analysis of the z field component in the grid plane directly underneath the MM. To this end, the z field profile over the x - y plane has been stored every 66.7 fs for a time interval of 20 ps. This yields a time domain trace for every grid cell, which can be transformed to the frequency domain by applying the fast Fourier transformation (FFT). Finally, one obtains the two-dimensional energy density profile associated with the z field component by taking the absolute square for every frequency in the FFT spectrum. The mode profiles for the three fundamental SRR resonances are shown in Fig. 3.5 for the orientation of the electric field as indicated by the black arrow. For parallel polarization of the incident field, the SRR shows only a single resonance, which can be

⁷The silver layer shown in the AFM images has been used for a different MM geometry and can therefore not be compared to the SRR transmission.

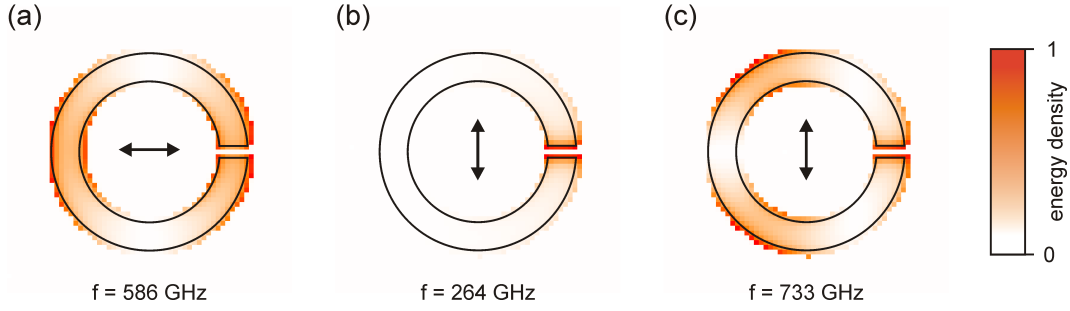


Figure 3.5: Normalized energy density of the fundamental modes of a SRR associated with the z field component for different orientations of the incident field (black arrows). (a) Fundamental dipole mode of a plain ring. (b) LC resonance. (c) Hybridized dipole mode of the SRR.

attributed to the electric dipole mode of the entire ring (Fig. 3.5a). Electrons are accelerated by the electric field of the THz pulse, which leads to a current flowing along the metal wire. When the incident field is oriented parallel to the slit, the currents flow symmetrically in the upper and lower half of the ring, leading to a dipole-like charge distribution. In this case, the slit has no influence on the movement of the charges and the resonance equals the fundamental resonance of the bare ring.

The situation is different for perpendicular polarization. Figure 3.5b shows the resonant mode around 0.26 THz. The induced currents can flow only in the left half of the SRR, while in the right half, the slit hinders the free movement of the charges. This leads to a redistribution of charges from one side of the slit to the other leading to a charge accumulation with opposite polarity on both sides of the slit. The slit acts as a capacitance, while the remaining ring takes the role of an inductance. Therefore, this resonance is often denoted as LC resonance [61]. As can be seen from Fig. 3.5b, the electric field of the mode is localized to the close vicinity of the slit. For completeness, we note that the asymmetric current flow induced by the electric field generates a magnetic dipole moment oriented along the z axis, which gives rise to a cross-polarizability between electric and magnetic dipole moments and fields. Vice versa, the resonance can also be effectively excited by applying a time varying magnetic field perpendicular to the MM plane. Therefore, the LC resonance is also referred to as magnetic resonance [61]. There is another resonance for the same polarization of the incident field, which can be attributed again to the electric dipole mode of the bare ring (Fig. 3.5c). The presence of the slit leads to a hybridization with the LC resonance due to the mode overlap around the slit position. This hybridization manifests itself in a repulsion of the resonance frequencies, i.e. the dipole resonance is shifted to a higher frequency (0.73 THz) compared to the dipole mode of the bare ring (0.6 THz, see Fig. 3.5c).

From Fig. 3.5, it is evident that part of the energy of the incident THz

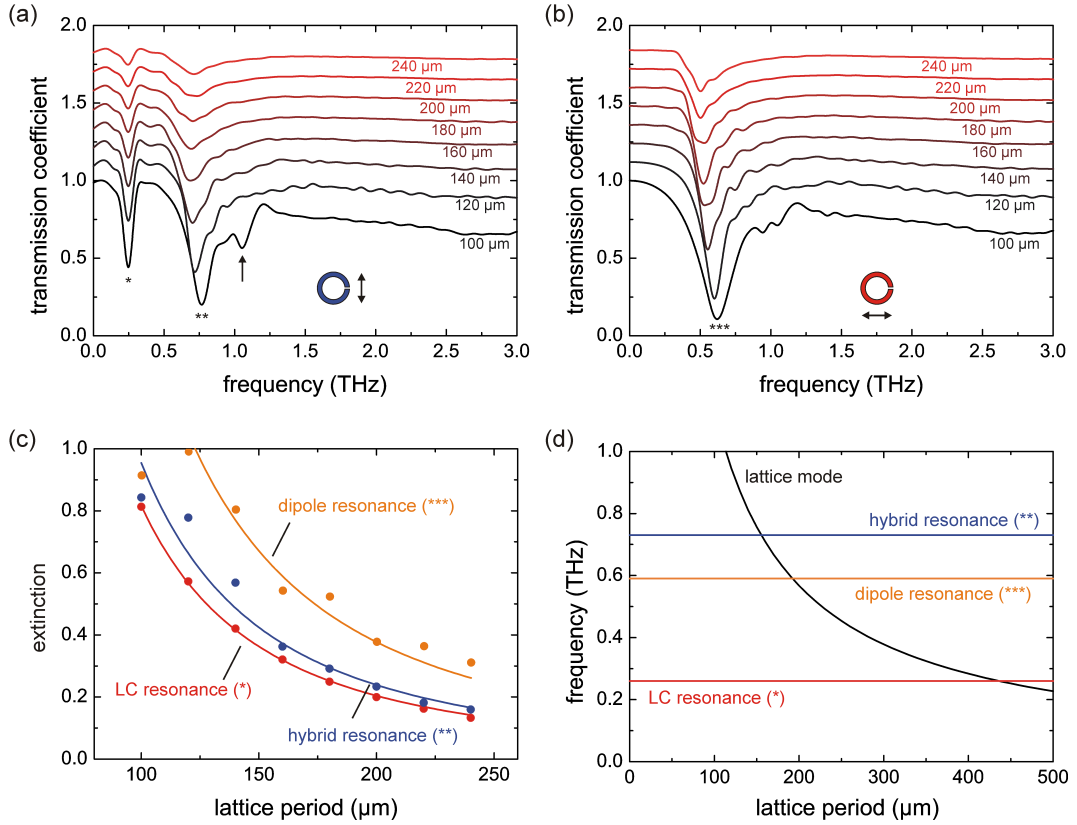


Figure 3.6: (a) Effect of lattice spacing on the LC (*) and hybrid (**) resonance of a SRR for the electric field polarized across the slit. At a lattice spacing of 100 μm , an additional resonance dip appears (black arrow). The curves are offset for clarity. (b) Same for the dipole (***) resonance excited with the electric field polarized parallel to the slit. (c) The extinction, $1 - t(\nu)$, as function of the lattice spacing. The solid lines show a $1/a^2$ - fit to the simulated data. (d) Dispersion relation of the fundamental lattice mode (black). Hybridization of the meta-atom resonance and the lattice mode is expected at the crossing points.

pulse is stored in the meta-atom, which acts like a THz antenna. The stored energy is subsequently re-emitted at the resonance frequency, but with opposite phase compared to the incident wave. This explains the observed minima in the amplitude transmission despite the fact that both the metal and the substrate are taken to be lossless. The absorption and re-emission of energy is an important concept, which finds application in many areas of physics. Especially, it will become useful for the discussion of the coupling between MMs and ISBTs in Chap. 3.3.

Another important parameter for the optical properties of metasurfaces is the lattice spacing. If there would be no interaction between neighboring meta-atoms, the simple relation (3.20) would predict a linear scaling of the resonance amplitude with the areal density N . Thus, the deviation from this simple

scaling rule can be used to determine the degree of mutual influence between different resonators. Figures 3.6a and 3.6b show the simulated transmission coefficients of the SRR metafilm for different values of the lattice spacing, a , ranging from 100 μm to 240 μm . The electric field is polarized perpendicular (Fig. 3.6a) and parallel (Fig. 3.6b) to the slit giving rise to the LC and the hybrid resonance (marked by * and **), and the pure dipole resonance (marked by ***), respectively.

As expected from Eq. (3.20), the modulation depth increases for both resonances as the meta-atoms are arranged on a tighter lattice. For a more quantitative analysis, the extinction $1 - t$, where t is the amplitude transmission, is shown in Fig. 3.6c as function of the unit cell size. The simulated data is shown as dots. The solid curves are the result of a least squares fit $\propto 1/a^2$ to the data. As can be seen, there is an excellent agreement for the LC resonance for the entire range of lattice spacings. Thus, in the case of the LC resonance, there seems to be no sign of mutual coupling between neighboring unit cells. This is supported by the fact that both shape and position of the LC resonance are barely influenced by the lattice spacing (Fig. 3.6a). A possible reason is the magnetic origin of this resonance. Efficient coupling between neighboring cells can only be mediated via a mutual inductance, and the lattice mode consequently by magneto-inductive surface waves. In the planar geometry, the induced inductance changes are on the order of a few percent [61].

In the case of the hybrid resonance, however, the extinction deviates from the simple scaling law when $a < 150 \mu\text{m}$, indicating an additional influence of the entire array on the optical properties of the meta-atoms. This is also seen from Fig. 3.6a. For smaller lattice spacings, the resonance appears to be narrower and being shifted to higher frequencies. A similar behavior is observed for the pure electric dipole mode shown in Fig. 3.6b. In this case, the interaction between the meta-atoms seem to be effective over an even wider distance, which is obvious from the poor quality of the fitted $1/a^2$ -dependence. A useful measure in this respect is the so-called quality or Q factor, which is defined as the ratio

$$Q = \frac{\Delta\nu}{\nu} \quad (3.26)$$

of the spectral width $\Delta\nu$ and the resonance position ν . Thus, for smaller lattice spacings, the Q factor of the dipole resonances is strongly enhanced. This enhancement has been attributed to the efficient scattering of electromagnetic energy into lattice modes, i.e. collective excitations of the entire MM array [180–182]. Thereby, less energy is radiated into free space, reducing the radiative losses of the MM. A similar reduction of coupling to free-space radiation can be achieved by breaking the symmetry of the meta-atoms, which leads to a comparable enhancement of the Q factor [183].

The enhancement of the Q factor by collective modes is maximized when

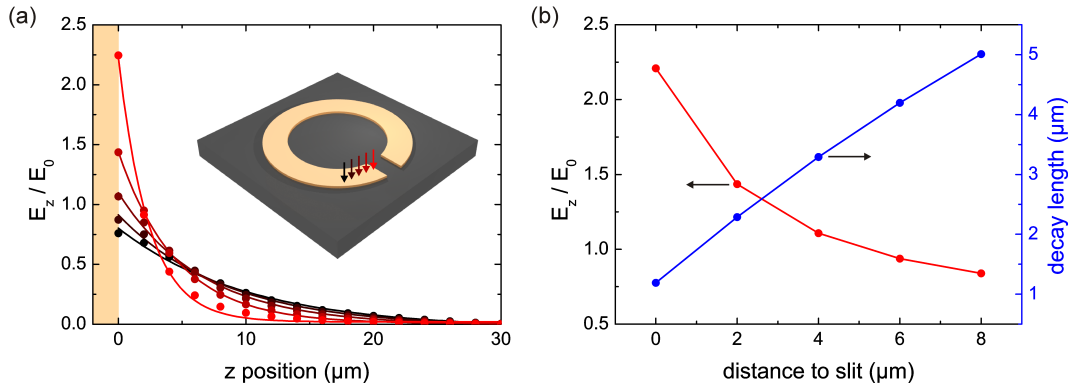


Figure 3.7: (a) Dependence of the z field amplitude in the substrate as function of distance to the metal surface of a SRR. The solid lines represent exponential fits to the simulated data. The field profiles have been taken at the positions indicated by the arrows. (b) Dependence of the field enhancement and the decay length into the substrate as function of the in-plane distance to the slit.

the meta-atom resonance coincides with the lattice resonance:

$$\nu = \frac{c_0}{a\bar{n}}, \quad (3.27)$$

where \bar{n} is the effective refractive index (3.22). For the dipole resonance at 0.73 THz, the crossover appears at a lattice spacing of 155 μm (see Fig. 3.6d). The coupling between the localized and the collective mode leads to an avoided crossing which manifests itself in the observed frequency shift of both hybrid and dipole resonance [181]. For a lattice spacing of 100 μm , there appears an additional minimum around 1.1 THz, which is indicated by the vertical arrow in Fig. 3.6a. This frequency coincides with the frequency of the fundamental lattice mode as given by Eq. (3.27), which supports the use of the effective refractive index (3.22) for the calculation of the lattice modes⁸. Far from the avoided crossing, the amplitudes of the lattice modes are in general much smaller than the amplitudes of the MM resonances and are therefore barely visible [181].

Of special interest is the decay of the z field into the substrate and the magnitude of the field enhancement that can be achieved in the vicinity of the metal. Figure 3.7a presents the normalized z -field amplitude in the substrate as function of the distance to the SRR. The field has been normalized to the peak amplitude of the incident field in vacuum times the Fresnel transmission coefficient of the GaAs substrate ($t = 0.43$) and represents the achievable field enhancement in the structure. The simulation has been performed for the incident field oriented perpendicular to the slit. The arrows in the inset show

⁸In [182], the authors explicitly use the refractive index of the substrate, and in [181], the authors do not state which refractive index should be used.

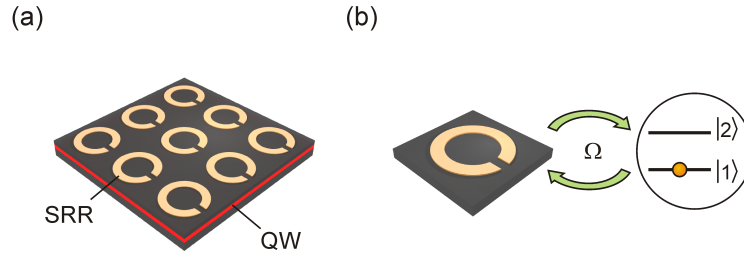


Figure 3.8: (a) Sketch of the sample. A planar MM is fabricated on top of a QW sample. No additional metalization is used for confinement of the electromagnetic field. (b) Energy can be exchanged at a rate Ω between the MM and the ISBTs in the QW via the electric field along the z axis associated with the resonant mode of the meta-atoms.

the positions on the SRR for which the z field profile has been extracted. The lateral distance between subsequent profiles is $2\ \mu\text{m}$.

The simulated data (dots) can be reasonably well fitted by an exponential, $A \exp(-z/z_0)$, with decay length z_0 and peak amplitude A , shown by the solid lines⁹. The quality of the fit degrades for smaller distances to the slit, which is a sign for the increasing distortion of the field lines due to an enhanced localization. This can also be seen in the high field enhancement and small decay length of the field. Figure 3.7b shows the extracted amplitude and decay length as function of the distance to the slit, with the origin aligned with the grid cell right next to it. The achievable field enhancement in this structure is approximately 2.3 and decreases exponentially with increasing distance. At the same time, the decay length varies linearly with a minimal value of $1\ \mu\text{m}$ at the slit position.

For an efficient coupling of the MM to ISBTs, this decay length has to be compared to the depth and thickness of the semiconductor heterostructure. Especially, the exponential decay of the field has important implications for the use of multi-QW structures. These considerations are subject of the following chapter.

3.3 Strong Light Matter Coupling

In the following, the optical properties of the coupled system sketched in Fig. 3.8a will be discussed. The sample consists of a thin QW grown on a semiconductor substrate. A MM is fabricated on top of the sample, which is resonant with the ISBT in the QW. As has been presented in the preceding

⁹Based on the exponential decay of the z field and the restricted geometry in the x - y plane, the term *localized plasmons* is sometimes used to describe the resonant modes of meta-atoms.

chapter, two-dimensional metafilms can be used to efficiently convert part of the incident electromagnetic energy into an electric field oriented parallel to the growth direction of the heterostructure. Thereby, the electric field fulfills the polarization selection rules and can induce ISBTs in the QW. In contrast to other coupling methods, such as subwavelength gratings, the meta-atoms constitute electromagnetic resonators that can periodically exchange energy with the electrons in the QW (see Fig. 3.8b). The main results of this chapter have also been published in Dietze *et al.*, *Opt. Express* **19**, 13700 (2011).

As is often the case in physics, appreciable insight into the properties of complicated systems can be gained by considering a simple analogy from classical mechanics. In the present case, the analogy is a pair of coupled pendulums (see Appx. C). Many (but not all!) characteristic features of strongly coupled systems can be derived from this classical model¹⁰, thereby giving an intuitive picture of the underlying phenomena [185]. In the geometry shown in Fig. 3.8a, the electromagnetic field of the incident THz pulse interacts directly only with the metafilm due to the polarization selection rules. Thus, without coupling to the QW, the transmission coefficient is expected to show a single dip belonging to the studied MM resonance (compare to previous chapter).

When the coupling between the MM and the QW is switched on, the eigenstates of the individual systems, characterized by the eigenvalues ω_{MM} and $\tilde{\omega}_{12}$, represent no longer the eigenstates of the coupled system. Neglecting damping, the new eigenfrequencies are given by [186]

$$\omega_{\pm} = \frac{1}{2} \left(\tilde{\omega}_{12} + \omega_{MM} \pm \sqrt{(\tilde{\omega}_{12} - \omega_{MM})^2 + 4\Omega_R^2} \right), \quad (3.28)$$

in analogy to Eq. (C.12) of the coupled pendulum. The use of $\tilde{\omega}_{12}$ instead of ω_{12} is a consequence of the MM resonance coupling to the ISB plasmon rather than to the single electron ISBT [187]. Furthermore, the coupling strength is determined by the so-called vacuum Rabi frequency Ω_R , which will be discussed in more detail later on. This effect is known as normal mode coupling [188, 189], and results in a splitting of the MM transmission minimum into two minima that are separated by a frequency $\Omega = 2\Omega_R$, when the two systems are resonant. This frequency determines the rate of energy exchange between the MM and the ISBT (Fig. 3.8b). Normal mode splitting in solid state systems has been observed so far in a number of experiments including QW excitons in dielectric mirror cavities [186, 190], ISB polaritons in dielectric cavities [147] and structured microcavities [191, 192], meta-films coupled to optical phonons [193] or to a cyclotron resonance of a two-dimensional electron gas [150]. As is shown in Appx. C, normal mode splitting can be observed only

¹⁰In the weak coupling limit, there is even a one-to-one correspondence between the classical mode amplitudes and the quantum mechanical creation and annihilation operators, and thus, the classical picture yields all information contained in the quantum system [184].

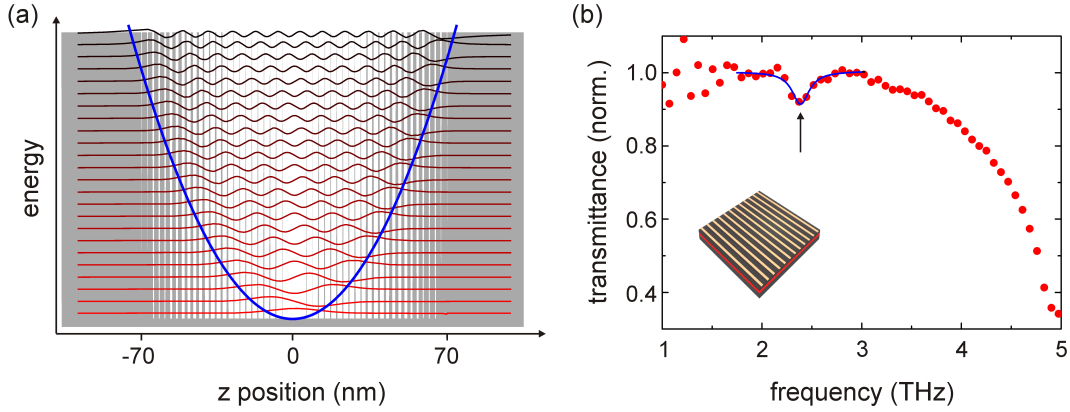


Figure 3.9: (a) Level scheme of the parabolic quantum well (G334, G424) calculated with the transfer matrix method. The actual heterostructure profile is indicated in gray. The thick blue curve represents the effective parabolic potential. (b) Normalized transmittance of the PQW measured with a grating coupler at $T = 5$ K. The solid line is a Lorentzian fit to the ISB absorption dip.

if Ω is larger than the damping rates. Thus, an experimental observation of the normal mode splitting would be a clear indication for strong coupling between the MM and the ISBTs.

However, this simple picture is valid only if a single resonant mode of the meta-atom couples to a single ISBT of the QW. Otherwise, the energy would be distributed among all participating modes and any characteristic feature of this normal mode coupling would remain hidden. The necessary selectivity can be achieved by requiring that the frequency spacing between different resonant modes of the MM is much larger than the linewidth of each mode. The same is equally true for the ISBTs in the QW. The latter can be realized by introducing a large energy separation between the first and second excited state, for example, by using coupled quantum wells.

An alternative geometry, namely the parabolic quantum well (PQW), is shown in Fig. 3.9a. The PQW imitates the confinement potential of a harmonic oscillator (thick blue line). Consequently, there is a constant energy spacing between subsequent levels, leading to a single isolated ISBT. Due to the parity selection rules, the next allowed transition is at three times higher frequency, which is well outside of the observation window. This makes the PQW the ideal system to investigate the coupling between a metafilm and ISBTs. The energy spacing between subsequent levels is approximately given by [194]

$$\Delta E = \hbar \sqrt{\frac{8\Delta E_c}{L^2 \bar{m}_{\text{eff}}}}, \quad (3.29)$$

where ΔE_c is the conduction band offset between the GaAs wells and the

Al_xGa_{1-x}As barriers, and

$$\bar{m}_{\text{eff}} = \frac{1}{L} \int_{-L/2}^{L/2} m_{\text{eff}}(z) dz, \quad (3.30)$$

is the effective mass averaged over the entire QW structure. In addition, the optical transition frequency is directly given by Eq. (3.29) and is independent of electron-electron interactions, such as the depolarization shift (3.16), and the number of carriers in the well [195, 196]. This is a consequence of the generalized Kohn's theorem [197], which states that long wavelength radiation ($\lambda \gg L$) couples only to the center of mass coordinates of the electron wavefunction in the parabolic potential. Thus, $\tilde{\omega}_{12} = \omega_{12}$, and we drop the tilde in the following.

For the experiments, we have used two nominally identical structures, one modulation-doped (G334) and one without doping (G424). The samples have been grown by stacking GaAs and Al_xGa_{1-x}As layers with varying thicknesses (digital alloy). The width, L_i , and center position, z_i , of the i -th layer of Al_xGa_{1-x}As measured from the middle of the well have been chosen as [194]

$$L_i = \left[\frac{2}{N} \left(i - \frac{1}{2} \right) \right]^2 \frac{L}{N}, \quad (3.31)$$

$$z_i = \left(i - \frac{1}{2} \right) \frac{L}{N}, \quad (3.32)$$

where N is the total number of Al_xGa_{1-x}As barriers and L the total width of the PQW. The minimum layer thickness is typically set to $\approx 10 \text{ \AA}$ to ensure a good quality of the interfaces [198]. The grown layer sequence is indicated in Fig. 3.9a by the shaded area. The distance of the well to the sample surface has been 185 nm. The effective carrier density in the doped well has been determined by Hall measurements to be $n_{2d} = 5 \times 10^{11} \text{ cm}^{-2}$ at 240 K and $n_{2d} = 3.8 \times 10^{11} \text{ cm}^{-2}$ at 20 K, respectively [196].

For a well thickness of $L = 140 \text{ nm}$ and $x = 0.3$, the averaged effective mass becomes $\bar{m}_{\text{eff}} = 0.074m_0$ and Eq. (3.29) yields a transition frequency of $\omega_{12} = 2\pi \times 2.4 \text{ THz}$. This value corresponds to the calculated transition frequencies using the transfer-matrix method [155]; it is however different from the values reported in Refs. [196, 199, 200]. This discrepancy is probably due to a different value for the effective mass. Using the results of the transfer-matrix method for the wavefunctions (shown as red curves in Fig. 3.9a) and Eq. (3.14), the oscillator strength of the fundamental transition between the ground state and the first excited state has been calculated to $f_{12} = 1.08$.

Figure 3.9b shows the measured intensity transmittance through sample G334 at $T = 5 \text{ K}$ obtained using a commercial FTIR spectrometer (Bruker V80). The transmittance has been normalized to the value at 2 THz to emphasize the transmission minimum due to the ISBT. In order to couple light under normal incidence to the PQW, a subwavelength ($8 \mu\text{m}$ metal / $8 \mu\text{m}$ gap)

grating has been fabricated by PVD of 150 nm Ag / 10 nm Au on top of the sample. The roll-off of the transmittance at higher frequencies is associated to the first lattice resonance of the grating at $\nu = 7$ THz, as given by Eq. (3.27). The ISBT is visible as a dip in the transmittance indicated by the black arrow. Approximately 9% of the incident intensity gets absorbed by the PQW. We have extracted the center frequency and the FWHM linewidth from a Lorentzian fit to the data (black solid line). The experimental value of $\omega_{12} = 2\pi \times 2.39$ THz matches the calculated transmission frequency using Eq. (3.29), which supports the use of the averaged effective mass (3.30). The linewidth $\Delta\omega = 2\pi \times 0.21$ THz equals the value obtained from intersubband plasmon emission measurements on the same structure [199]. The corresponding dephasing time, $\tau = 2/\Delta\omega = 1.5$ ps, is a bit lower than the reported value of 2.5 ps obtained from THz TDS measurements of the free induction decay [200]. For the FDTD simulations, we will use the latter value.

When the sample is heated to room temperature, the ISBT dip disappears from the transmittance spectrum. Thus, the comparison between the 5 K and RT data presents a possibility to identify effects caused by the presence of ISBTs. Another possibility is the comparison between the doped and the undoped sample, which allows to discern effects caused by the presence of electrons in the structure.

For efficient coupling between the metafilm and the PQW, the meta-atoms have to be resonant with the ISBT. One possibility to tune the resonance frequency of the MM is to isotropically scale the entire structure. For the SRR based MM presented in Chap. 3.2, for instance, the dimensions would have to be reduced by almost a factor of ten. For such small feature sizes the fabrication becomes technically demanding. An alternative way is to additionally change the meta-atom geometry.

Figure 3.10a shows the fundamental building block of the metafilm used in the following. It consists of a rectangular doubly-split-ring resonator (dSRR) with a side length of $28 \mu\text{m}$ and a wire thickness of $2 \mu\text{m}$. The dSRRs are arranged in a regular array with a lattice constant of $40 \mu\text{m}$. By using two $2 \mu\text{m}$ wide slits on opposite faces of the ring, the total capacitance is almost doubled compared to a conventional SRR. Thus, the LC mode, which will be used for the coupling, shows a twice higher resonant frequency. A microscope image of the finished sample is shown in Fig. 3.10b. The meta-atoms have been fabricated by PVD of 150 nm Ag capped by 10 nm Au in a single optical lithography step.

The transmission coefficients of the structure fabricated on the undoped sample G424 have been measured using a THz TDS setup with linearly polarized THz pulses. There is an excellent agreement between the measured transmission coefficients and the results from FDTD simulations as shown in Figs. 3.10e and 3.10f. Depending on the orientation of the incident field, there are two distinct resonances. The normalized energy density associated with the z component

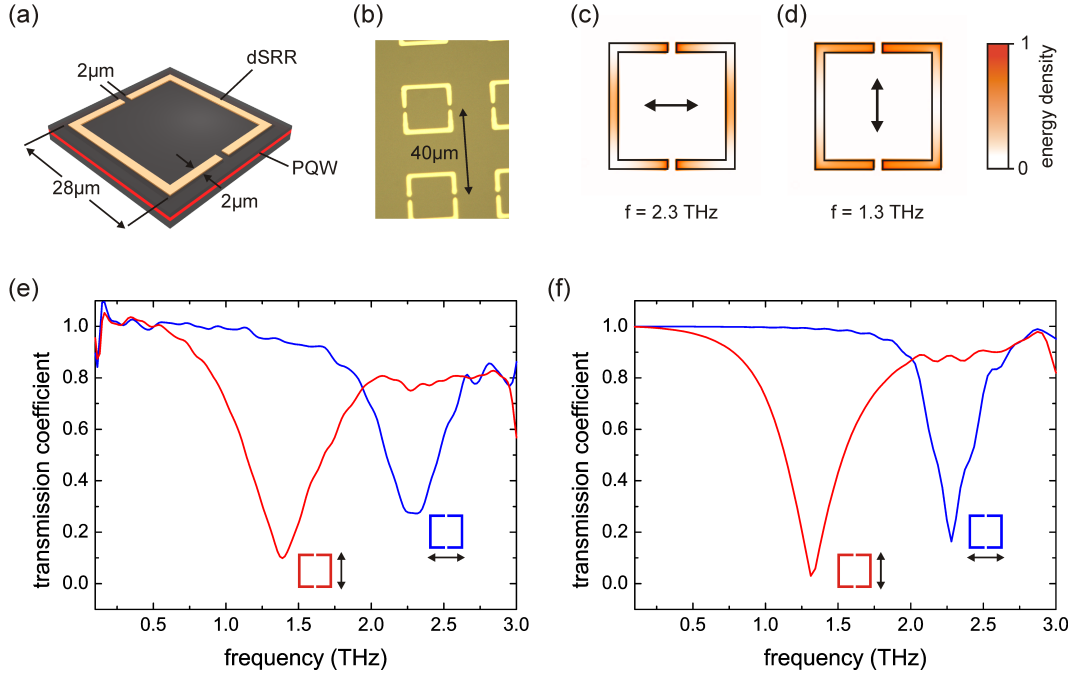


Figure 3.10: (a) Unit cell of the doubly-split-ring resonator MM. The wire thickness and gap size are $2\ \mu\text{m}$, the edge length is $28\ \mu\text{m}$. (b) Microscope image of the fabricated structure. The lattice period is $40\ \mu\text{m}$. (c, d) Normalized energy density associated to the electric field along the z axis for the polarization of the incident field indicated by the black arrow. (e) Measured transmission coefficients of the dSRR MM for two different orientations of the incident field [201]. The dipole resonance of the ring is around $1.3\ \text{THz}$, while the LC resonance is at $2.3\ \text{THz}$. (f) Transmission coefficients obtained from FDTD simulations [201].

of the electric field is plotted for both resonances in Figs. 3.10c and 3.10d, respectively. The LC resonance around $2.3\ \text{THz}$ is excited when the incident field is oriented perpendicular to the slits. The z component of the electric field shows thereby a similar field enhancement as has been observed for the conventional SRR (Fig. 3.7). At a distance of $250\ \text{nm}$ from the metal, the z field is about ten times stronger than the incident peak field.

In view of the importance of the linewidth of the MM resonance for the possible observation of normal mode splitting, we have extracted the center frequency and width of the experimental and simulated transmission minima by fitting a Lorentzian line shape. For the simulated data, we obtain $\omega_{MM} = 2\pi \times 2.3\ \text{THz}$ and $\Delta\omega_{MM} = 2\pi \times 0.27\ \text{THz}$ (FWHM), giving a Q-factor of 8.5. The experimental data yields $\omega_{MM} = 2\pi \times 2.28\ \text{THz}$ and $\Delta\omega_{MM} = 2\pi \times 0.46\ \text{THz}$, giving a Q-factor of 4.9. The slightly lower Q factor obtained in the experiment is probably due to variations of the gap capacitance as the feature size of the slit is close to the resolution limit of the laser writer used for the optical lithography step (compare to Fig. 3.10b).

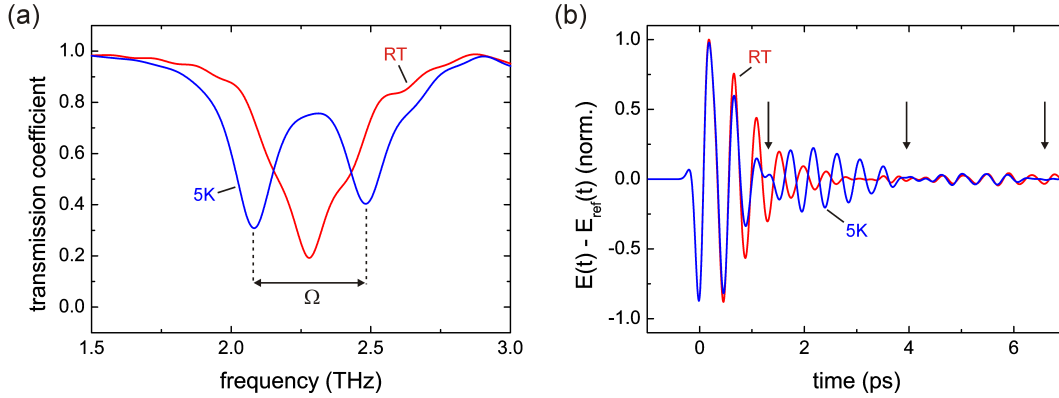


Figure 3.11: (a) Simulated transmission coefficients for the dSRR MM coupled to a PQW with (blue) and without (red) electrons [201]. The normal mode splitting of the MM resonance is clearly observable. (b) In the time domain data, the normal mode coupling is visible as beating of the free induction decay. Phase flips by π indicate periodic absorption and emission of energy by the QW ISBT (marked by arrows).

The simulated transmission coefficient of the combined system is shown in Fig. 3.11a (blue)¹¹ along with the response of the bare MM (red). The latter corresponds to the expected signal at room temperature or from the undoped sample G424, respectively. The QW has been simulated using the simple Lorentz model for the z component of the electric field (see Appx. D.1). We expect this model to be adequate for isolated transitions and weak electric fields. Both assumptions are fulfilled in the present case.

When the ISBT in the QW is switched on, the transmission coefficient shows a very pronounced splitting of the plain MM resonance. Thus, this splitting is associated to the presence of electrons in the QW layer. By fitting the data with a sum of two Lorentzians, the frequency separation has been determined to $\Omega = 2\pi \times 0.34$ THz. As this value is larger than both the linewidths of the MM resonance ($2\pi \times 0.27$ THz) and of the ISBT ($2/\tau = 2\pi \times 0.13$ THz), respectively, we attribute the observed mode splitting to the strong coupling between the PQW and the planar metafilm¹². This conclusion is further supported by an analysis of the linewidths of the doublet, which should be equal to the averaged linewidths of the two coupled systems at zero detuning, i.e. 0.20 THz (see Appx. C). The simulated normal modes have FWHM linewidths of 0.18 THz and 0.17 THz, respectively, in close agreement to the theoretical prediction. The symmetry of the linewidths suggests that the detuning of the MM from the ISBT in the QW is negligible.

¹¹For the simulations, a spatial step size of $1 \mu\text{m}$, an areal density of $n_{2d} = 2.5 \times 10^{11} \text{ cm}^{-2}$ and a transition frequency of $2\pi \times 2.2$ THz have been used.

¹²This is more conservative criterion for strong coupling than the one using the coupled normal mode linewidths.

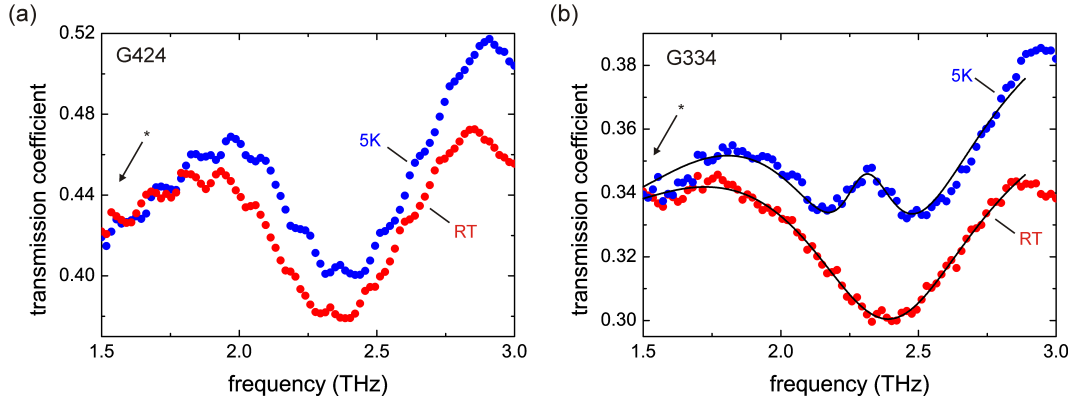


Figure 3.12: Transmission coefficients of (a) G424 and (b) G334 at RT (red) and 5K (blue) obtained with a FTIR spectrometer [201]. The asterisk (*) indicates the dipole resonance of the ring at 1.3 THz. A sum of multiple Lorentzians is fitted to the data to extract resonance parameters. The splitting of the resonance occurs only at 5 K for the doped structure.

According to the simple pendulum analogy (Appx. C), the observation of the normal mode splitting is related to a periodic energy exchange between the two coupled systems. Figure 3.11b shows the free induction decay in the time domain obtained by subtracting the transient of the reference pulse from the transmitted pulse. The reference has been recorded for the same substrate but without MM. In the case of the plain MM (red), the free induction decay shows a pronounced oscillation with an exponential envelope. When the ISBT is switched on (blue), there is a clear beating observable. Furthermore, at the times marked by the black arrows, the phase of the free induction decay changes by π relative to the bare MM case. This is a clear indication for the aforementioned periodic exchange of energy (see also [202]). The time difference between these phase jumps is approximately 2.7 ps, which corresponds closely to the inverse of the normal mode frequency splitting.

To support the model results from the FDTD simulations, we have also performed measurements on the doped and undoped PQW samples, G334 and G424, respectively. The measurements have been performed using the Bruker IFS113V FTIR spectrometer with the internal glowbar emitter and a helium cooled bolometer detector. The sample chamber could be evacuated to suppress the disturbing influence of residual absorption by atmospheric water vapor. The samples have been mounted in a flow cryostat at an intermediate focus. To suppress Fabry-Perot fringes due to multiple reflections, the samples have been slightly wedged under an angle of 2° and double side polished. To reduce any effects related to in-plane movement of free carriers in the QW, the first 400 nm of the sample have been removed by reactive ion etching (RIE). Thereby, the MM metalization has been directly used as etch mask without further processing. As both the wedging and the RIE etching have been done

after the fabrication of the top metalization, this has led to a significant degradation of the MM performance.

Figure 3.12a shows the measured transmission coefficients of the undoped sample G424 for two different temperatures¹³. As the light in the FTIR is unpolarized, the transmission coefficient shows both the dipole resonance of the entire ring (marked by asterisk) and the LC resonance of the slits at the same time. This circumstance has to be considered in the analysis of the data. As has been expected for the undoped structure, there is no significant difference between the results obtained at room temperature and at 5 K. The situation is different in the case of the doped sample G334, shown in Fig. 3.12b. While at room temperature (red), only the MM resonance is visible, the 5 K data shows a clear splitting. The data can be excellently fitted by a sum of two (three) Lorentzians, respectively, where one represents the dipole resonance at 1.3 THz (shown as solid lines). The bare MM resonance is shifted to a center frequency of 2.4 THz and shows a FWHM of 0.79 THz. The reduced Q-factor of only 3 (compared to 4.9) is due to the aforementioned treatment of the sample. At 5 K, the normal mode doublet shows a frequency splitting of 0.41 THz, which is slightly larger than expected from the FDTD simulations. The linewidths associated to the two modes are 0.31 THz and 0.58 THz, respectively, which is comparable to the expected averaged linewidth of 0.5 THz. The asymmetry is probably an artifact caused by the distortion of the transmission coefficient due to the dipole resonance. The condition (C.20) is, however, barely fulfilled. Thus, the successful observation of the normal mode coupling can be mainly attributed to the high frequency resolution and dynamic range of the FTIR. This might be the reason why we have not yet been able to observe the strong coupling also in a THz TDS spectrometer.

The high values of the frequency splitting Ω obtained both from the FDTD simulations and the FTIR measurements demonstrate the quality of the MM resonators and the excellent coupling to the QW ISBTs. Especially, no additional field confinement, such as provided by a cavity, is necessary to observe the normal mode coupling. This concept has also been applied with great success to optical phonons [193] and to cyclotron resonances in a 2d electron gas [150]. In these cases, the strong in-plane field enhancement has been used to provide an efficient coupling to the quantum systems. However, for higher frequencies only weak coupling between metasurfaces and QWs has been reported so far [203, 204]. Therefore, we will shortly discuss the dependence of the coupling strength on various parameters of the QWs.

In the *classical* case of N_{QW} QWs embedded in an optical (micro-) cavity, the normal mode splitting for zero detuning is determined by the expression

¹³The transmission coefficients have been obtained by taking the square root of the transmittance to facilitate comparison with the FDTD data.

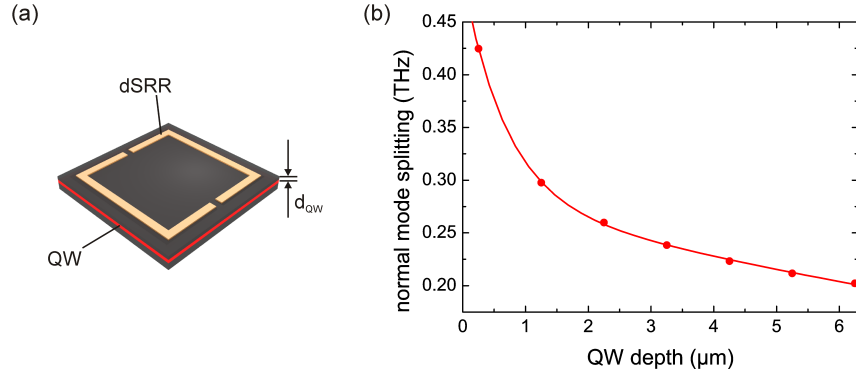


Figure 3.13: (a) The effective cavity parameters that determine the normal mode splitting are the meta-atom geometry and the distance between the MM and the QW, d_{QW} . (b) Results of FDTD simulations for the PQW parameters as used in Fig. 3.11 for different values of d_{QW} (dots). The solid line is a fit of Eq. (3.35) to the data.

[145, 191]

$$\Omega = 2\Omega_R = \sqrt{\frac{e^2}{\varepsilon_0 \varepsilon m_{\text{eff}}} \frac{f_{12} N_{QW} n_{2d}}{L}}, \quad (3.33)$$

where ε is the dielectric constant of the substrate material, L the size of the cavity, and n_{2d} the sheet carrier density in the QW. Thereby, it is assumed that all electrons are in the ground state and that the electric field is homogeneous over the entire volume of the cavity. If, instead, the field is confined by a planar metafilm, it becomes difficult to define an effective mode volume. As has been shown in Chap. 3.2 the z field decays exponentially away from the metalization. In addition, there is a strong lateral variation of the electric field strength.

This exponential variation of the electric field has also implications for multi-QW systems, as each well experiences a different field amplitude. Thus, N_{QW} has to be replaced by an effective number of wells [205]:

$$\tilde{N}_{QW} = e^{-2z/\zeta} \left(\frac{1 - e^{-2\Delta z N_{QW}/\zeta}}{1 - e^{-2\Delta z/\zeta}} \right), \quad (3.34)$$

where z is the distance of the first well to the MM and Δz the spacing between subsequent wells. The parameter ζ is an effective decay length of the coupling strength, i.e. at a distance ζ to the MM, the frequency splitting Ω has dropped to $1/e$. It is solely determined by the meta-atom geometry and the dielectric constant of the substrate material. For a single QW, the second term of Eq. (3.34) becomes unity and the frequency splitting should scale as $\Omega \propto \exp(-z/\zeta)$.

We have performed a series of FDTD simulations to test the validity of this model for the dSRR MM used in our experiments. By changing the distance z between the QW and the MM in the FDTD simulations, we found that the

normal mode splitting could best be fitted by a bi-exponential decay law

$$\Omega = \Omega_1 e^{-z/\zeta_1} + \Omega_2 e^{-z/\zeta_2}, \quad (3.35)$$

where $\Omega_{1,2}$ is the extrapolated frequency splitting for direct contact to the metasurface (see Fig. 3.13). This result can be understood by taking a look at Figs. 3.5b and 3.10c, which show the energy density associated with the z component of the electric field for a simple SRR and the dSRR meta-atoms at the respective LC resonance frequency. In the case of the SRR, the resonant mode is localized only at the slit, showing a single effective decay behavior. In the case of the dSRR, the resonant mode is localized at two different positions along the wire (at the slit and in the center of the connecting bar) with two different decay constants of the electric field into the substrate. The part of the field at the slit is much more localized, showing a much higher value of the field enhancement and a faster decay. The two parts of the resonant mode will interact in slightly different ways with the QW, which explains the bi-exponential decay law. By equating Eq. (3.33) with the amplitudes $\Omega_{1,2}$, we can extract effective cavity lengths, $L_{1,2,\text{eff}}$, from the fit results:

$$L_{1,2,\text{eff}} = \frac{e^2}{\varepsilon_0 \varepsilon m_{\text{eff}}} \frac{f_{12} N_{\text{QW}} n_{2d}}{\Omega_{1,2}^2}. \quad (3.36)$$

For the dSRR MM of Fig. 3.10a, we find $\zeta_1 = 0.69 \pm 0.06 \mu\text{m}$, $L_{1,\text{eff}} \approx 10 \mu\text{m}$, $\zeta_2 = 18 \pm 2 \mu\text{m}$, and $L_{2,\text{eff}} \approx 6 \mu\text{m}$, respectively.

Summarizing all terms, Eq. (3.33) takes the form

$$\Omega = 2\Omega_R = \sqrt{\frac{e^2 f_{12} n_{2d}}{\varepsilon_0 \varepsilon m_{\text{eff}}}} \left[\sum_i \sqrt{\frac{1}{L_{i,\text{eff}}} \left(\frac{1 - e^{-2\Delta z N_{\text{QW}}/\zeta_i}}{1 - e^{-2\Delta z/\zeta_i}} \right)} e^{-z/\zeta_i} \right] \quad (3.37)$$

for a general metafilm coupled to QW ISBTs. Under the assumption that $\zeta_{1,2}$ and $L_{1,2,\text{eff}}$ are independent of the resonant frequency, we can directly compare the expected normal mode splitting using the dSRR metafilm to the measured splitting in a microcavity using published QW parameters.

For example, Todorov *et al.* measured a splitting of $\Omega = 2\pi \times 0.8 \text{ THz}$ using $N_{\text{QW}} = 15$ periods of 32 nm wide GaAs wells separated by 20 nm AlGaAs barriers in a metal-dielectric-metal microcavity. Thus, the Rabi frequency is 11.4% of $\omega_{12} = 2\pi \times 3.5 \text{ THz}$. Substituting their published values, $n_{2d} = 5 \times 10^{10} \text{ cm}^{-2}$, $f = 0.96$, and $m_{\text{eff}} = 0.067m_0$, we would expect a normal mode splitting of $\Omega = 2\pi \times 0.49 \text{ THz}$ using the dSRR metafilm. Geiser *et al.* achieved a splitting of $\Omega = 2\pi \times 0.96 \text{ THz}$ with $N_{\text{QW}} = 8$ GaAs / AlGaAs PQWs in a LC resonator with double metal confinement. The Rabi frequency is 13.7% of the ISBT frequency $\omega_{12} = 2\pi \times 3.51 \text{ THz}$. Taking their published parameters, $n_{2d} = 1.1 \times 10^{11} \text{ cm}^{-2}$, $f = 1$, $L_{\text{tot}} = 0.8 \mu\text{m}$, and $m_{\text{eff}} = 0.067m_0$, we calculate a theoretical value of $\Omega = 2\pi \times 0.55 \text{ THz}$. These high values of Ω demonstrate again the excellent coupling between planar metafilms and QW ISBTs.

Reference	ω_{12} (THz)	Ω_R/ω_{12} (%)	System
Scalari <i>et al.</i> [150]	0.5	58	Cyclotron transition with SRR
Geiser <i>et al.</i> [149]	3.9	27	PQWs in <i>LC</i> microcavity
Todorov <i>et al.</i> [191]	3.0	23.5	MQWs in 0d MDM microcavity
Jouy <i>et al.</i> [148]	27	20.9	MQWs in MDM microcavity
Shelton <i>et al.</i> [193]	31.4	14.2	Phonons with SRR
Geiser <i>et al.</i> [192]	3.51	13.6	PQWs in <i>LC</i> microcavity
Todorov <i>et al.</i> [191]	3.5	11.4	MQWs in MDM microcavity
Anappara <i>et al.</i> [207]	37	10.8	MQWs in dielectric waveguide
Günter <i>et al.</i> [147]	27	9.0	MQWs in dielectric waveguide
Dietze <i>et al.</i> [201]	2.4	8.5	PQW with dSRR

Table 3.1: Listing of recent reports on (ultra-) strong coupling involving ISBTs (not necessarily complete, MDM = metal-dielectric-metal).

3.4 Entering the Ultrastrong Coupling Regime

When the vacuum Rabi frequency, Ω_R , is a significant fraction of the ISBT frequency of the QW, ω_{12} , the light-matter interaction enters a new regime, the so-called *ultrastrong coupling regime* [145]. While in the weak and strong coupling regimes, characterized by the condition $\Omega_R/\omega_{12} < 0.01$, the anti-resonant terms in the interaction Hamiltonian are small and are therefore usually being neglected by making the rotating-wave approximation, these terms become important in the ultrastrong coupling regime and result in the occurrence of new quantum phenomena [145]. One example is the generation of correlated photon pairs out of vacuum by the nonadiabatic modulation of the vacuum Rabi frequency [206].

After the first report of experimental signatures of ultrastrong coupling in a dielectric ISB microcavity by Anappara *et al.* [207], there has been a steady increase of the number of experimental observations. Table 3.1 gives an overview over the experiments and the achieved Ω_R/ω_{12} ratios. Using the values for Ω and ω_{12} from the previous chapter, we find a ratio of $\Omega_R/\omega_{12} = 0.085$ for the dSRR MM coupled to the single PQW. This value is however just an approximation, as the observed splitting is not necessarily the minimum splitting which is related to the vacuum Rabi frequency [145]. Nevertheless, it emphasizes the extreme good coupling between the systems and suggests that our experiment is indeed in or close to the ultrastrong coupling regime.

The primary signature of ultrastrong coupling is the opening of a gap in the polariton dispersion diagram [146]. The frequencies of the two polariton branches are given by the eigenvalue equation [187]

$$(\omega^2 - \tilde{\omega}_{12}^2) (\omega^2 - \omega_{MM}^2) = 4\Omega_R^2 \omega_{MM}^2, \quad (3.38)$$

which takes the role of the characteristic equation (C.11) from the classical

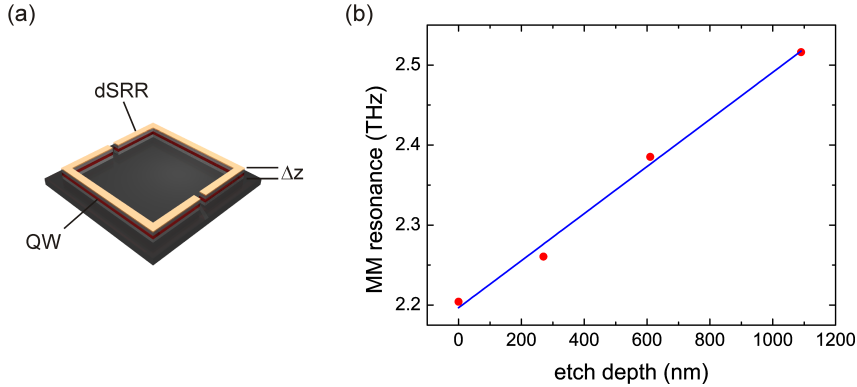


Figure 3.14: (a) Schematic view of etched sample. The metalization of the MM is used a etch mask. (b) Tuning of MM resonance frequency by RIE etching. The solid line is a linear fit to the data.

analog. The overlap factor between the cavity mode and the QW, which appears on the right-hand side of Eq. (3.38) as given in Ref. [187], is already included in the vacuum Rabi frequency Ω_R from Eq. (3.37). In Eq. (3.38), we use $\tilde{\omega}_{12}$ instead of ω_{12} to emphasize the fact that the MM couples to the ISB plasmon rather than to the bare ISBT. It has been shown that Kohn's theorem still applies for PQWs in the ultrastrong coupling regime [149], and, thus $\tilde{\omega}_{12} = \omega_{12}$.

The resulting normal mode frequencies are given by:

$$\omega_{\pm} = \sqrt{\frac{1}{2}(\omega_{MM}^2 + \omega_{12}^2) \pm \sqrt{\frac{1}{4}(\omega_{MM}^2 - \omega_{12}^2)^2 + 4\omega_{MM}^2\Omega_R^2}}, \quad (3.39)$$

where ω_+ denotes the upper and ω_- the lower polariton branch. To identify the aforementioned polaritonic gap, we take the limits $\lim_{\omega_{MM} \rightarrow 0} \omega_+ = \omega_{12}$ and $\lim_{\omega_{MM} \rightarrow \infty} \omega_- = \sqrt{\omega_{12}^2 - 4\Omega_R^2}$. Thus, there appears a forbidden frequency region with a size of¹⁴ [187]:

$$\Delta\omega = \omega_{12} - \sqrt{\omega_{12}^2 - 4\Omega_R^2} \approx 2\Omega_R^2/\omega_{12}. \quad (3.40)$$

Experimentally, the polariton dispersion is usually measured by tuning the bare cavity frequency by varying suitable parameters. Examples include the angle of incidence [207], the magnetic field [150], or the geometry [191, 192].

In the following, we pursue another approach, which is based on Eq. (3.21). The resonant frequency of a given meta-atom geometry is inversely proportional to the effective refractive index of the surrounding medium. Thus, by lowering the index, the resonant frequency is shifted to higher values. One way of doing

¹⁴Note, that a similar gap appears also in the case of strong coupling (3.28), but as $\Omega_R \ll \omega_{12}$, it is usually negligible.

so is to etch part of the sample away, as shown schematically in Fig. 3.14a. By removing a thin layer of thickness Δz , substrate material with a refractive index of $n = 3.6$ is replaced by air with a refractive index of $n = 1$.

To test this idea, we have performed a series of subsequent etch steps on the very same sample using a uniform dry etching process (RIE). By using the metalization of the meta-atoms directly as an etch mask, there is no need for any further lithography steps. Due to the high quality of the etch profile in the RIE, there is almost no under etching, and the QW underneath the MM, where the main part of the resonant z field is located, remains unperturbed. The final etch depth has been measured using a Dektak profilometer.

The used sample is similar to the one presented in the previous chapter (dSRR on G334). The lattice spacing for this sample has been chosen as $51 \mu\text{m}$ to match the resonant frequency with the lattice mode. The meta-atoms have been fabricated by PVD of Ti / Au (10 nm / 180 nm) after defining the structures by standard optical lithography. To allow multiple etch steps on a single sample, the sample has not been wedged. In order to remove interferences due to multiple reflections in the sample, we have applied a numerical filtering algorithm after calculating the transmittance [208]. The measurements have been performed in a Bruker V80 FTIR spectrometer with a helium cooled bolometer detector and the internal glowbar source. To isolate the LC resonance, a wire grid polarizer has been used to clean the incident polarization. The sample chamber has been purged with dry air to minimize the absorption by residual water vapor.

Figure 3.14b shows the measured center frequency of the LC resonance as function of the etch depth Δz . The resonance frequencies have been extracted by fitting a Lorentzian line shape to the measured transmittance data. The MM resonance shifts nearly linear with Δz . The solid line is a least squares fit to the data, giving a slope of $0.29 \pm 0.02 \text{ THz}/\mu\text{m}$. Thus, the modification of the effective refractive index by RIE etching presents a simple way to effectively tune the MM resonance in a single post processing step.

For mapping the polariton dispersion relation, we have *switched on* the interaction with the ISBTs by cooling the sample to 5 K in an optical flow cryostat. The resulting transmittance curves are shown in Fig. 3.15a (points). In all cases, the normal mode splitting is clearly observable. The solid lines show results of a fit of a sum of two Lorentzians to the measured data. From these fits, we have extracted the coupled normal mode frequencies, which are plotted against the bare MM resonances in Fig. 3.15b (dots).

The gray dots represent the results for the unetched sample, while the red ones show the normal mode frequencies of the remaining etch steps. The first etch step opens the QW layer, thereby altering the coupling efficiency to the MM. We attribute this to trapping of free carriers at surface defects, which reduces the effective number of carriers in Eq. (3.37). As a result, the gray and red datasets cannot be compared directly. For the remaining discussion, we

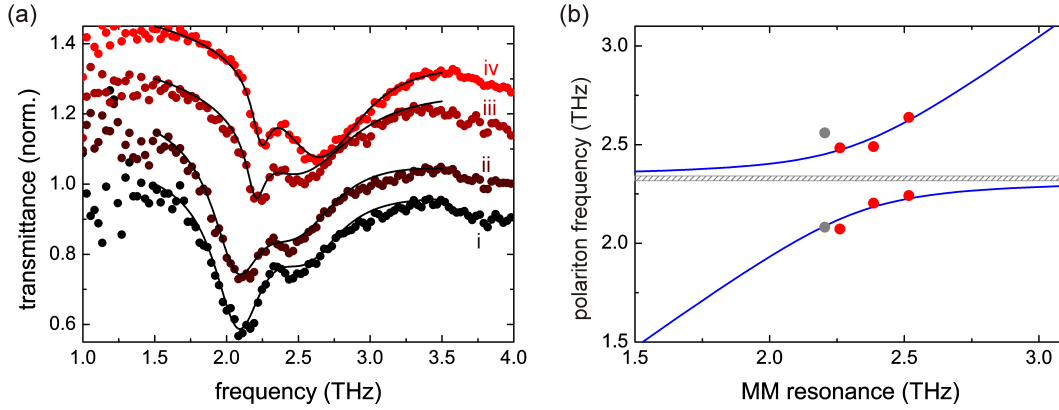


Figure 3.15: (a) Measured transmittance at 5K for: (i) as grown, (ii) $\Delta z = 270$ nm, (iii) $\Delta z = 610$ nm, and (iv) $\Delta z = 1090$ nm etched. Curves are offset for clarity and normalized to the transmittance at 1 THz. (b) Cavity polariton frequencies versus bare MM resonance. The gray dots correspond to the unetched sample. The solid lines represent a fit of Eq. (3.39) to the etched data (red dots). The ruled area represents the polaritonic gap.

use only the normal mode frequencies of the etched samples (red).

The blue solid curves show a least squares fit of Eq. (3.39) to the data. The best fit was obtained for $\omega_{12} = 2\pi \times 2.34 \pm 0.05$ THz and $\Omega_R = 2\pi \times 0.17 \pm 0.03$ THz. Both values agree well with the results from the previous chapter. The vacuum Rabi frequency makes 7.3% of the QW ISBT frequency. This value is lower but still close to the estimated value of 8.5%. From Eq. (3.40), the polaritonic gap would be $\Delta\omega = 2\pi \times 25 \pm 9$ GHz, which makes roughly 1% of the ISBT frequency (shown as ruled area in Fig. 3.15b). The relative values for the polaritonic gap and the Rabi frequency are comparable to the results of Jouy *et al.* for multiple QWs in metal-dielectric-metal microcavities in the MIR spectral range [148].

Thus, we have used the modification of the effective refractive index by RIE etching to tune the MM resonance using just a single sample. By fitting the eigenfrequencies, obtained in the ultrastrong coupling regime, to the data, we found a polaritonic gap of 1% of the ISBT frequency. Therefore, the coupling efficiency between a planar metafilm and QW ISBTs is even sufficient to enter the ultrastrong coupling regime.

3.5 Strong to Weak Coupling Transition

In the discussion so far, we have neglected any effects that are directly connected to the field strength of the incident THz light. As long as the field is sufficiently weak, as in the case of FTIR, for example, this is a reasonable approximation. However, in view of the achievable field enhancement in the vicinity of the

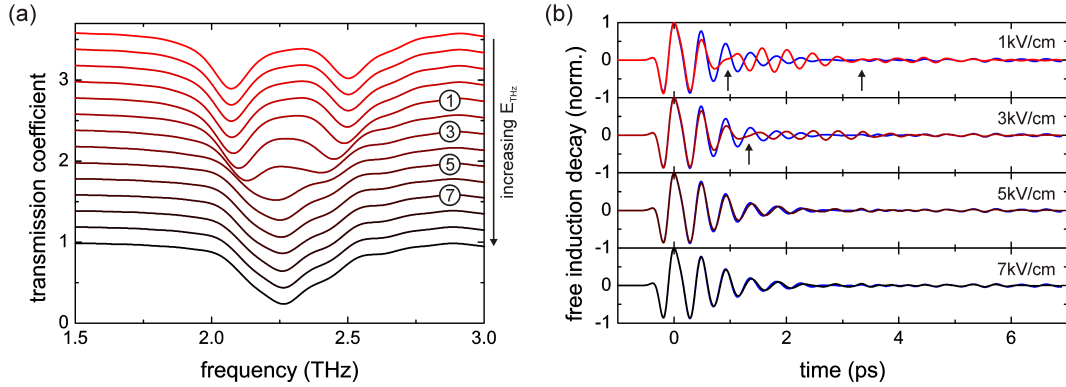


Figure 3.16: (a) Simulated transmission coefficients of dSRR MM coupled to PQW for different peak field strengths of the incident THz pulse ranging from 10 V/cm to 10 kV/cm. The disappearance of the normal mode splitting for higher field strengths is clearly visible. The curves have been offset for clarity. Labels 1 to 7 correspond to the field strengths shown in Fig. 3.16b. (b) Time-domain transients of free induction decay associated to various values of the incident peak field amplitude. The blue curve shows the free induction decay of the bare MM.

metalization this might not hold for the moderate field strengths available in standard THz TDS setups (see Chap. 2.2).

To study the influence of the electric field amplitude in the FDTD simulations, we have replaced the simple Lorentz model by the optical Bloch equations for a two-level system. The finite-difference implementation for solving the coupled set of Maxwell-Bloch equations is based on Ref. [209] with the time discretization scheme adopted from Ref. [210]. The chosen formulation of the problem leads to a full decoupling of the Maxwell-Bloch equations, as is derived in Appx. D.2. Both the sample properties, including the meta-atom geometry, and the simulation parameters have been chosen equal to the ones used in Fig. 3.11. The simulated transmission coefficients for different field strengths of the incident THz pulse are shown in Fig. 3.16a. As expected for weak fields, the transmission coefficients equal the results of Chap. 3.3 obtained with the Lorentz model. The normal mode splitting is clearly visible. For increasing field strengths, the two transmission minima start to merge into a single resonance dip. The transmission coefficient for high THz fields resembles thereby the result obtained for the bare metafilm (see Fig. 3.11a). This transition from strong to weak coupling occurs for peak amplitudes roughly between 2 and 4 kV/cm.

The free induction decay for field strengths of 1, 3, 5 and 7 kV/cm is shown in Fig. 3.16b. The blue curve represents the bare MM case. In the case of 1 kV/cm, the energy exchange between the metafilm and the QW is clearly visible as a beating. The arrows indicate the times where the phase of the free induction decay changes sign. For 3 kV/cm, this phase change appears at a

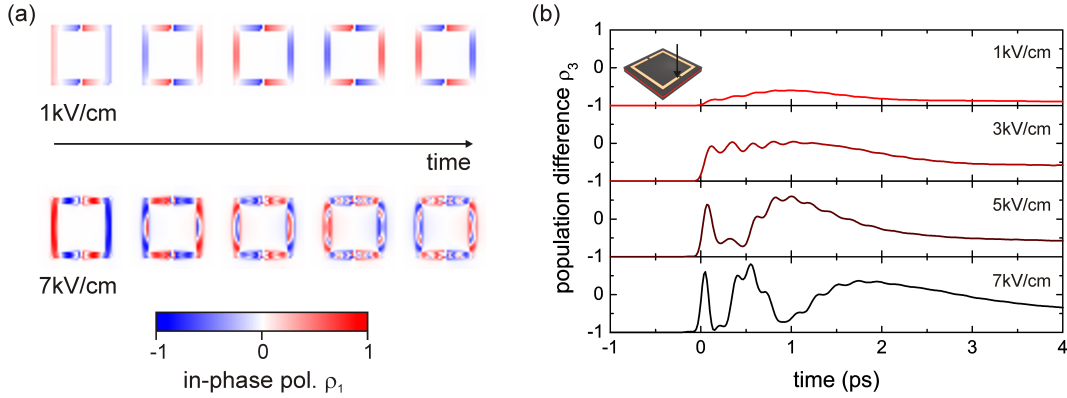


Figure 3.17: (a) Simulated in-phase component, ρ_1 , of the Bloch vector in the QW plane as function of time for different values of the incident peak field. The time step between subsequent images is 235 fs. For a peak field of 7 kV/cm, the polarization pattern does not match the resonant mode of the MM. (b) Fractional population difference, ρ_3 , at the grid cell indicated by the black arrow in the inset as function of time.

later time and, in addition, only a single nodal point is visible. For higher fields, the free induction decay is almost equal to the MM reference. This is a clear sign that no energy is coupled back to the meta-atoms. However, the presence of the QW still alters the system response. Thus, the combined system is now in the weak coupling limit.

To find the physical reason behind this field dependence, it is necessary to take a look at the components of the Bloch vector describing the two level system. Figure 3.17a shows the in-phase polarization component, ρ_1 , across the QW plane as function of time for two different field amplitudes. According to Eq. (D.20), this quantity is proportional to the polarization density of the QW and is out of phase with the electric field by 90° . To achieve a good coupling between the MM and the QW, the spatial profile of the QW polarization has to fit to the resonant mode of the meta-atom. In other words, the overlap integral over the QW plane between the z field below the MM and the electric field emitted by the QW polarization has to be different from zero. From a comparison of Figs. 3.10c and 3.17a, it is obvious that this condition is well fulfilled for weak driving fields. Above the strong-to-weak coupling transition, however, the QW polarization looks completely different. While at early times, there is still some resemblance to the MM mode, at later times, it shows a very fine grained pattern. The overlap integral between the resonant mode of the meta-atom and the QW polarization becomes zero.

The origin of this pattern becomes obvious by looking at the population difference between the upper and lower QW level. Figure 3.17b shows the temporal evolution of the fractional population difference, ρ_3 , for the QW grid-cell indicated by the black arrow in the inset. For $\rho_3 = -1$, the electrons

are in the ground state, while for $\rho_3 = 1$, the electrons are in the excited state. For incident fields below 3 THz, the population is partly transferred to the upper state during the duration of the THz pulse. When the pulse has passed, the electrons relax back to the ground state. The small oscillations that overlay the curves are due to the fast oscillations of the electric field at the carrier (resonance) frequency¹⁵. For higher peak amplitudes, the population starts to oscillate between the upper and lower level of the QW. These fast oscillations are caused by carrier-wave Rabi oscillations [211]. Both the amplitude and the Rabi frequency are thereby proportional to the local value of the instantaneous electric field component parallel to the growth direction, $|E_z|$. As has been discussed in Chap. 3.2, the z field underneath a meta-atom is spatially localized and shows strong variations over the cross-section of the resonant mode (compare to Fig. 3.7). These variations are directly mapped to the Rabi oscillations and, hence, to the spatial profile of the QW polarization.

The above simulations have been based on the parameters used in Chap. 3.3, for which we found also a reasonable agreement with the experiment. To observe the strong-to-weak coupling transition experimentally, the incident field strengths would have to be on the order of a few kV/cm. This is out of reach for standard THz TDS setups. However, the use of amplified laser systems opens new possibilities for the generation of intense THz pulses, which is subject to the remainder of this thesis.

¹⁵These are not visible in the slowly-varying envelope approximation that is usually employed in the optical frequency range.

Chapter 4

High Field Terahertz Time-Domain Spectroscopy

In the previous chapter, a series of experiments has been presented, that showed a very special kind of light-matter interaction going beyond the linear optics regime. However, the use of the term *nonlinear* in optics usually refers to very high field strengths. In the following chapters, the high power THz TDS setup, that has been built in the course of this thesis, will be introduced. After a detailed presentation of the experimental realization of the TDS scheme, various methods for the generation of intense few-cycle THz pulses will be discussed. The main focus thereby has been the generation of broadband radiation in order to bridge the high-power THz gap mentioned in Chap. 1.4.

4.1 High Field THz Time-Domain Spectroscopy Setup

Figure 4.1 shows a scheme of the laser system that has been used for the high power THz TDS setup. The heart of the system is an Er:Fiber laser (Menlo Systems C-Fiber Sync 780 Custom) with a center wavelength of 1560 nm. The oscillator output is split in two parts, one is frequency doubled to 780 nm and the other is amplified in a fiber amplifier stage. The 780 nm pulse is used to seed the regenerative Ti:Sapphire amplifier (Spectra Physics Spitfire XP 4W). The pump energy for the Ti:Sapphire amplifier is delivered by a 30 W green pump laser (Spectra Physics Empower). The amplifier output and the 1560 nm light from the fiber laser are then both used for the THz TDS setup. The working principle of the two lasers as well as the technical data are discussed in detail in Appx. E. Part of the light generated by the Er:Fiber laser is detected by two fast photodiodes (PD1 and PD2). These signals are used to synchronize the regenerative amplifier and the detection electronics.

The high power THz TDS setup is very similar to the general TDS setup

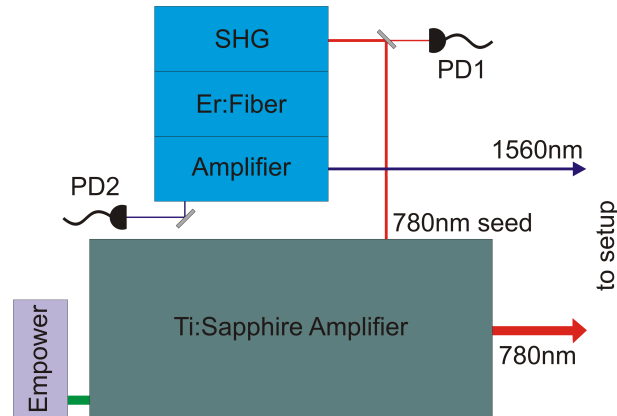


Figure 4.1: Schematic of the arrangement of the laser sources used for the generation of high power THz transients. The pulses from an Er:Fiber laser are frequency doubled and then used to seed a regenerative Ti:Sapphire amplifier. The second part of the pulses are amplified in a fiber amplifier and are then used for probing the THz transient. The Empower pump laser provides the energy for the regenerative amplifier. The two photodiodes PD1 and PD2 are used to generate a 80 MHz reference signal for the amplifier and the detection electronics.

that has been presented in Chap. 2.2. Therefore, only the differences are discussed in the following. The schematic of the setup is shown in Fig. 4.2. The main difference between the two setups is that the high-power version uses two different lasers to provide the pump and the probe pulses, whereas in a common setup, both pulses are split off from the same laser. This requires a precise timing with a very high stability but shows many advantages compared to the common setup when used with amplified pulses. For instance, there is no need for additional modulation of the THz pulse.

Another difference is the high pulse energy of the pump pulse, which allows to use a large area emitter for the generation of the THz pulses. The phase front of the generated pulses equals thereby the phase front of the pump pulse and, therefore, the THz pulse is already collimated. This reduces the number of parabolic mirrors (PM) used for guiding and focusing of the THz light. Additionally, the high pump energy allows to use completely new concepts for THz generation. In order to get a tight focus at the sample position, the first PM is chosen to have a focal length of $f = 50$ mm. To still be able to use an optical cryostat, the second mirror has to have a focal length of at least 100 mm. Thus, the first two parabolic mirrors form a 1:2 telescope. When a large area emitter is used for THz generation, part of the energy will be lost before detection due to the finite aperture of the collecting mirror (2"). Thus, the detected electric field strength and pulse energy will be underestimated. This issue becomes important later on for the discussion of the various THz generation principles.

The laser system used for the high-power THz TDS is different from the light

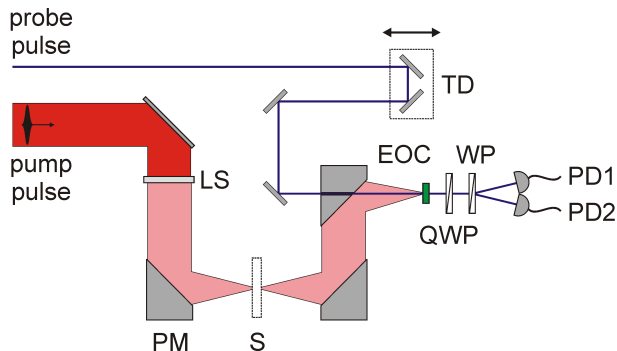


Figure 4.2: Schematic of the THz TDS setup as used with the laser system presented in Fig. 4.1. The 780 nm pump light generates THz pulses on a large area emitter (LS). The collimated beam is focused on the sample and is then recollimated by a second parabolic mirror (PM). For detection, the pulses are overlapped with the 1560 nm probe light on an electro-optic crystal (EOC). The change in probe polarization is sensed by a combination of quarter-wave plate (QWP), Wollaston prism (WP) and balanced photo diodes (PD1 and PD2).

sources usually employed for THz TDS in several aspects. The most important aspect is the reduced repetition rate of the THz pulses of only 1 kHz compared to the 80 MHz of the probe pulses. Conventional lock-in techniques do not work in this regime, as only one pulse out of 80 000 contributes to the signal. As a consequence, the detection chain has to measure on the repetition rate of the probe laser and pick only the relevant pulses. Basically, there are two ways to achieve this. First, by the use of a pulse picker, e.g. a fast Pockels cell, that reduces the 80 MHz repetition rate to 2 kHz, and the subsequent use of slow detection electronics. Or, second, by the use of fast digitizers, that allow the detection and processing at the full rate of 80 MHz. The detection setup built in this thesis is based on the latter.

In a conventional THz TDS setup, the relative modulation signal $\Delta I/I$ of the electro-optic detector is typically on the order of 10^{-8} to 10^{-3} . To ensure a high dynamic range and good SNR, the balanced detector circuit usually uses a low-noise preamplifier with a gain of 500 to 1000 at a relatively low bandwidth of a few 10 kHz [116]. However, for the reasons mentioned above, the balanced detector used for the high-power THz TDS setup has to be fast enough to detect single probe pulses at a rate of 80 MHz. In this frequency range, it already becomes difficult to build a preamplifier with enough gain which shows excellent noise characteristics at the same time. The high energy of the THz pulses in the present setup leads to modulation signals of several percent in the electro-optic detection crystal, and thus, to expected modulation signals in the range from 10^{-3} to 10^{-1} , which is easily measurable with modern digitizers.

This in mind, the electronic circuit of the balanced detector should be kept

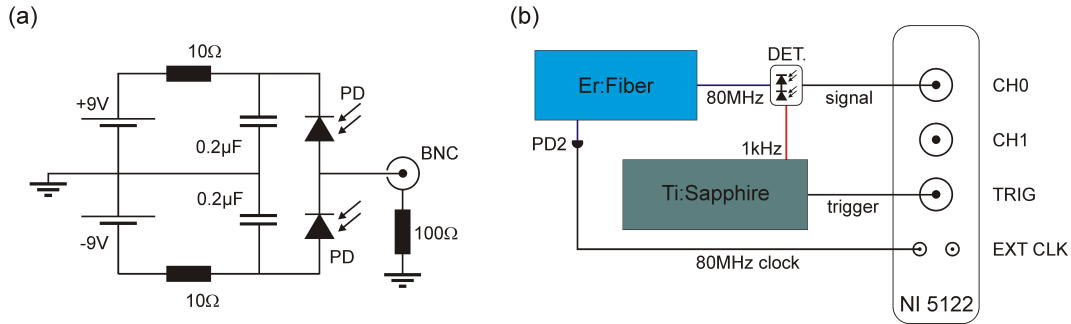


Figure 4.3: (a) Circuit diagram of the balanced detector for the high-power THz TDS setup. The detector is based on two fast InGaAs photodiodes (PD) that are reverse biased by two 9 V batteries. The generated differential photocurrent leads to a voltage drop over the $100\ \Omega$ termination resistor, which is detected by the fast digitizer (BNC). (b) Connection diagram of the detection chain. The fast digitizer is triggered from the Ti:Sapphire amplifier at a rate of 1 kHz (TRIG). The 80 MHz signal from a fast photodiode (PD2) serves as external clock signal (EXT CLK). The THz signal from the balanced detector is fed to one of the two digitizer channels (CH0). The second channel (CH1) is free to be used for modulation measurements, for example.

as simple as possible to reduce any spurious noise. Figure 4.3a shows the electronic circuit diagram of the final detector layout. Two biased InGaAs diodes (Hamamatsu Photonics G8376-05) are placed in series and the differential photocurrent is measured as voltage drop over a $100\ \Omega$ resistor. To improve high speed operation, the bias voltage is provided by two $0.2\ \mu\text{F}$ capacitors that are charged by two 9 V batteries over two $10\ \Omega$ resistors. The two batteries are connected in series to form a virtual ground. By using batteries, the detector is decoupled from the usual 50 Hz noise from the AC-power line. The amplitude of the measured signal can be increased by using higher values of the termination resistor. However, the signal gain is accompanied by a reduction of the bandwidth at the same rate. We found a value of $100\ \Omega$ to be a good compromise.

The full diode signal I , i.e. the sum of the signals obtained for one diode blocked, can be adjusted by varying the power of the probe beam. This value should be as high as possible, to be well above the noise floor caused by the electronics and digitization errors. For values above 8 V, however, the diodes start to behave nonlinearly. Typically, we use $I = 6\ \text{V}$, leading to a modulation signal ΔI in the range from 6 mV to 600 mV.

This signal from the balanced detector is then detected using a fast digitizer (National Instruments NI 5122) with a resolution of 14 bit at a vertical range of $-200 \dots 200\ \text{mV}$ to $-10 \dots 10\ \text{V}$. The connection diagram is shown in Fig. 4.3b. The digitizer has two equivalent input channels (CH0 and CH1), which can be configured separately. The input voltages are read and converted by a fast

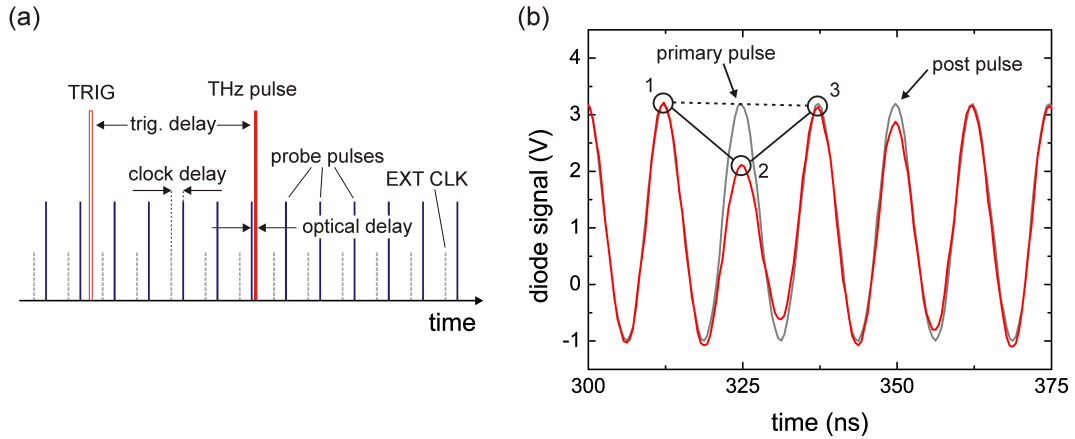


Figure 4.4: (a) Timing scheme of the two laser sources and the detection chain. The different lines denote the THz pulse (red bar), the trigger signal (TRIG, empty red bar), the probe pulses (blue lines), and the external clock (EXT CLK, gray dashed lines). The signals are offset by the clock delay and an optical delay. For details see main text. (b) Real-time signal of the balanced detector with one diode blocked for the pump-probe geometry used to determine the temporal overlap. Additionally to the main pulse, two post pulses are visible roughly 25 ns and 50 ns later. See main text for details.

analog-to-digital converter at a maximum rate of 105 MS/s real-time or 2 GS/s equivalent-time. In both cases, the data is continuously stored in a ring buffer until a trigger pulse arrives from the regenerative amplifier (TRIG). The ring buffer enables real pre-triggering, i.e. to read values that arrived immediately before the trigger pulse, even if the trigger is not periodic in time.

The digitizer can be used either free running or with an external sample clock (EXT CLK). The external clock allows to synchronize the digitizer with the probe pulses. To this end, the secondary output of the fiber laser is recorded using a fast amplified InGaAs photodiode (Thorlabs PDA10CF, PD2 in Fig. 4.1) resulting in a 80 MHz signal that is phaselocked to the Er:Fiber laser. The exact timing synchronization is discussed below in more detail.

The recorded data is stored in the device memory until a certain number of samples has been recorded. Then, the data is transferred to a computer via a PCI Express interface card. This delayed sending is necessary due to the limited data transfer speed of the interface. As indicated in Fig. 4.3b, the electro-optic modulation signal is only fed to CH0 and, thus, CH1 can be used for secondary signals. Examples include trigger pulses for double modulation experiments or the power level of the amplifier for signal normalization.

Compared to a conventional lock-in-based THz TDS setup (see Chap. 2.2), the high-power THz TDS setup presented above depends crucially on the right timing between the THz pulses, the probe pulses and the detection electronics. The basic situation is depicted in Fig. 4.4a. The THz pulse (red bar) arrives

at the detector 300 ns to 400 ns after the trigger signal (TRIG, empty red bar), depending on the alignment of the amplifier cavity and the timing of the Pockels cells. The probe pulses from the fiber laser (blue lines) have a repetition rate of 80 MHz and, thus, arrive every 12.5 ns at the balanced detector. The signal is sampled by the fast digitizer at the time instances defined by the external clock pulses from the fast InGaAs diode (EXT CLK, gray dashed lines). In general, the external clock will not coincide with the signal peak from the detector. To achieve a temporal coincidence, an additional clock delay has to be introduced. The simplest and most effective way is to vary the length of the BNC cable from the InGaAs diode to the EXT CLK input of the digitizer. A cable length of 20 cm corresponds thereby to a delay of roughly 1 ns (for PTFE dielectric).

Additionally, there is a non-negligible offset between the THz pulse and the probe pulses, which has to be compensated by the optical path on the laser table. Despite the fact that both the Ti:Sapphire and the fiber amplifier are seeded with the same laser pulse from the fiber oscillator (see Fig. 4.1), the optical paths of the pulses inside each amplifier are quite different. Thus, it is not possible to use two pulses that have been derived from a common seed pulse, but rather the probe pulse closest in time to the THz pulse has to be used. In order to determine the temporal overlap between one of the probe pulses and the pump pulse from the amplifier, a pump-probe setup can be used.

The transmission of the 1560 nm pulse through a GaAs wafer is monitored using the balanced detector with one diode blocked, while the pump pulse is incident on the GaAs surface. As its wavelength of 780 nm is well above the band gap of GaAs, the pump pulse creates a dense electron-hole plasma which acts as a plasma mirror for the 1560 nm probe pulse. Thus, the transmission of the probe pulse will be reduced when the two pulses arrive at the same time on the GaAs surface. The pump power has to be reduced to below 100 mW, and a larger focal spot on the order of several millimeters has to be used to prevent damage of the GaAs surface. A typical time trace is shown in Fig. 4.4b. The signal has been recorded using the equivalent-time mode of the digitizer with 2 GS/s and the time axis is relative to the trigger signal.

The optical path of the probe pulse is then varied until a modulation of one of the probe pulses becomes visible (pulse 2). The maximum variation of the path, that might be necessary, is 3.75 m corresponding to the repetition rate of the probe pulses. In the time trace shown in Fig. 4.4b, additional modulation of subsequent pulses (25 ns and 50 ns later) is observable. This modulation is due to post pulses from the amplifier and should not be confused with the modulation due to the main pulse. Once the time overlap has been found, it remains constant until the alignment of the amplifier or the timing of the Pockels cells has to be changed.

In order to measure the weak modulation signal ΔI caused by the THz field with a good SNR, some sort of referencing to the background signal without THz field is necessary. In a conventional lock-in based setup, this is achieved

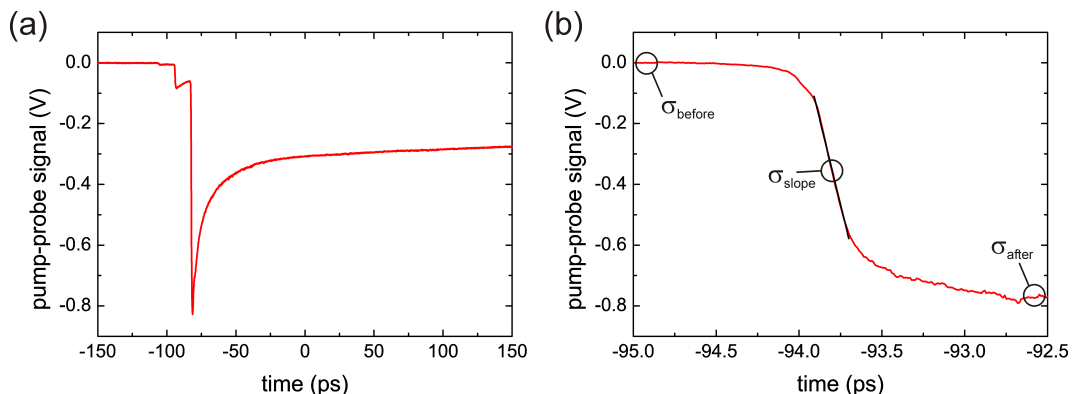


Figure 4.5: Results of a 780 nm pump - 1560 nm probe measurement on a piece of undoped GaAs. (a) The strong pump pulse generates a free carrier plasma which leads to a change in transmission of the 1560 nm probe pulse. (b) Noise measurements around the overlap position allow the estimation of the relative timing jitter between the pump and the probe pulses. See main text for details.

by either modulating the THz source (antenna) or by optically chopping the pump beam. In the present setup, this is done by using the signal from the two probe pulses right before and after the main pulse (pulses 1 and 3). From Fig. 4.4b it is evident that these pulses are not affected by the pump pulse even with regard to the long carrier lifetimes in the pump-probe measurement. Thus, a single measurement point is obtained from three subsequent probe pulses ΔI_1 to ΔI_3 centered around a THz pulse via

$$\Delta I = \Delta I_2 - \frac{\Delta I_1 + \Delta I_3}{2}. \quad (4.1)$$

Figure 4.5a shows the pump-probe signal on GaAs that has been recorded using this method as function of the relative delay between pump and probe pulses. For early times, the probe pulse arrives before the pump pulse, and thus, no modulation is visible. When the two pulses coincide, the transmission signal shows a step-like decrease. The width of this step is thereby mainly determined by the cross-correlation of the two pulses. Additionally, there are two minor steps located 12 ps and 24 ps before the main step which are related to reflections in the probe path, probably from a neutral density filter. The slow recovery of the transmission at later times is finally related to the free carrier lifetime in GaAs.

An important aspect in such a dual laser setup is the relative timing jitter between the laser pulses used for generation and detection of the THz field. In conventional THz TDS setups, pump and probe pulses are derived from the same laser pulse and are therefore inherently stable in time. In the setup presented in this chapter, pump and probe are derived from laser pulses that have made a different number of cavity roundtrips in the fiber laser and may be subject to strong timing fluctuations. Such timing jitter is not only source of

additional noise but effectively reduces the bandwidth of the THz TDS setup. Thus, for a good performance, these fluctuations should be as low as possible.

The pump-probe measurement on GaAs presents a simple way of determining this timing jitter. Figure 4.5b shows a close-up on the main step. The timing jitter can be estimated by noise measurements for three distinct values of the relative delay, just before the overlap, just after the overlap and directly in the middle of the step. To this end, $N = 1000$ measurements of ΔI have been made over a time span of several seconds according to (4.1), resulting in a standard deviation

$$\sigma = \sqrt{\frac{1}{N} \sum_{i=1}^N (\Delta I_i - \mu)^2}, \quad (4.2)$$

with μ being the mean value. The standard deviation before the overlap, σ_{before} , consists of electronic noise of the detection chain and pulse-to-pulse fluctuations of the pulse energy of the fiber laser. The corresponding value after the overlap, σ_{after} , contains also pulse-to-pulse fluctuations of the regenerative amplifier.

For the measurements taken in the middle of the step, there is an additional contribution to the noise due to timing fluctuations Δt , leading to

$$\sigma_{\text{slope}} = \sqrt{\frac{1}{N} \sum_{i=1}^N (\Delta I_i + \beta \Delta t_i - \mu)^2}. \quad (4.3)$$

The slope of the step has been determined by a linear fit (black line in Fig. 4.5b) to $\beta = -2.23 \text{ V/ps}$. Under the assumption that the timing jitter σ_{timing} is not correlated to the laser noise, (4.2) and (4.3) can be solved for

$$\sigma_{\text{timing}} = \frac{1}{|\beta|} \sqrt{\sigma_{\text{slope}}^2 - \sigma_{\text{laser}}^2}. \quad (4.4)$$

The noise from the two lasers and the detection chain right on the step has been approximated by the average value, $\sigma_{\text{laser}} \approx (\sigma_{\text{before}} + \sigma_{\text{after}})/2$. From the experimentally determined values for $\sigma_{\text{laser}} = 8.495 \text{ mV}$ and $\sigma_{\text{slope}} = 8.99 \text{ mV}$, a timing jitter of only $\sigma_{\text{timing}} = 1.3 \text{ fs}$ has been calculated.

This small value proves the excellent timing stability of the combination of fiber laser and regenerative amplifier used for the high-power THz TDS setup. An analog analysis has been presented in [212] for a combination of Ti:Sapphire oscillator and amplifier based on the noise figures in a MIR pulse trace. They found a value for the timing jitter of only 1 fs. This good value can be explained by the shorter measurement time compared to our analysis and suggests an even better performance of our system in real THz TDS measurements.

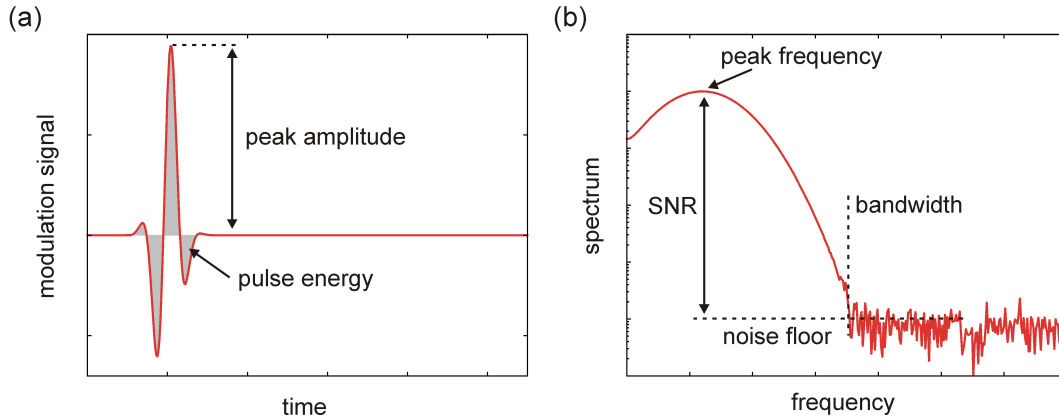


Figure 4.6: Some common parameters that can be used for characterizing THz pulses (a) in the time domain, and (b) in the frequency domain.

4.2 Generation of Intense Terahertz Pulses

As has been mentioned in Chap. 1.4, the state-of-the-art of high field THz sources at the moment are tilted pulse front excitation in LiNbO₃ [78, 80], and difference frequency mixing using two phase-locked optical parametric amplifiers [81, 82]. As those sources are limited in the accessible wavelength range, new ways of generating intense THz pulses in the frequency range between 1.5 and 10 THz are highly desirable, especially, as this frequency range is most interesting for nonlinear spectroscopy of THz semiconductor devices based on intersubband transitions.

Motivated by the lack of efficient emitters, various different approaches for the generation of high field THz pulses have been investigated in the course of this thesis to reach this ambitious goal. These include THz emission based on coherent plasma oscillations, optical rectification in large area crystals, photoconductive antenna arrays and four-wave mixing in dual-color laser filaments. The general aim has been the generation of ultrashort pulses with a large bandwidth above 5 THz. Thereby, we achieved peak electric field strengths on the order of 40 kV/cm.

In order to be able to quantitatively compare the different methods, various parameters, such as bandwidth or peak amplitude, can be used. These parameters will be defined in the following and apply then to all subsequent chapters. An exemplary THz transient and the corresponding spectrum are shown in Figs. 4.6a and b, respectively. In the time domain, the important parameters are peak amplitude and pulse area. From the measured modulation signal $\Delta I/I$ the detected electric field strength can be calculated using Eq. (2.25), thereby keeping the second sine term. Under the assumption that the angular orientation of the EO crystal is optimized according to Fig. 2.7b, the

first sine term is unity and we can solve (2.25) for the THz field amplitude,

$$E_{\text{THz}}^{\text{det.}} = \frac{c_0}{\omega n^3 r_{41} L} \sin^{-1}(\Delta I/I) = \eta \sin^{-1}(\Delta I/I). \quad (4.5)$$

For a 300 μm thick crystal and $\lambda = 1.56 \mu\text{m}$, the prefactor η has the value $\eta = 287 \text{ kV/cm}$ for GaAs and $\eta = 593 \text{ kV/cm}$ for GaP, respectively. If the modulation amplitude is below $\approx 10\%$, the arcsine can be replaced by its argument, thereby introducing only an error below 10^{-3} . The superscript used for $E_{\text{THz}}^{\text{det.}}$ shall indicate that this is the field value inside the EO crystal. To eliminate the influence of the detection crystal, the field value has to be corrected by the Fresnel transmission coefficient [87],

$$t_{\text{EOC}} = \frac{2}{n_{\text{THz}} + 1} \quad (4.6)$$

with n_{THz} being the THz refractive index of the crystal. For simplicity, the frequency dependence of both the transmission coefficient and the detector response function has been neglected. Using Eq. (2.34) with the values given in Tab. 2.1 and $\Omega = 1 \text{ THz}$ yields $t_{\text{EOC}} \approx 0.44$ for GaAs and $t_{\text{EOC}} \approx 0.46$ for GaP, respectively. For some generation methods it is necessary to block the NIR pump light by placing a silicon wafer in the beam path to prevent damage of the EO crystal. The THz amplitude is then reduced by

$$t_{\text{Si wafer}} = \frac{4n_{\text{Si}}}{(n_{\text{Si}} + 1)^2} \approx 0.7, \quad (4.7)$$

with the refractive index of silicon taken as $n_{\text{Si}} = 3.4$, when the wafer is placed under normal incidence in the beam path. For incidence under 45° , $t_{\text{Si wafer}} = 0.82$. The peak field amplitudes given in the following chapters are all corrected in the manner described above.

The second important parameter extracted from the time domain data is the pulse energy. Assuming a Gaussian beam profile in the focus, the pulse energy can be estimated from the corrected THz transient $E_{\text{THz}}(t)$ using the expression

$$U_{\text{THz}} = \frac{\pi}{4} w^2 \varepsilon_0 c_0 \int |E_{\text{THz}}(t)|^2 dt, \quad (4.8)$$

that has been derived using (1.3). The spot size w , defined as the $1/e^2$ radius of the intensity, can in principle be estimated by calculating the spectrally-weighted mean-square radius [213]

$$w^2 = \frac{\int_0^\infty |w_0(\nu) E_{\text{THz}}(\nu)|^2 d\nu}{\int_0^\infty |E_{\text{THz}}(\nu)|^2 d\nu}, \quad (4.9)$$

where $E_{\text{THz}}(\nu)$ is the Fourier transform of the THz transient. Using Gaussian beam optics, $w_0(\nu)$ can be calculated from the focal length, $f = 50 \text{ mm}$, and

the diameter, $D = 50$ mm, of the last focusing mirror according to [32]

$$w_0(\nu) = \frac{c_0}{\pi\nu} \frac{2f}{D}. \quad (4.10)$$

However, Eq. (4.9) assumes ideal focusing conditions and gives the minimal achievable spot size. In reality, the beam waist will be larger, and also the collection efficiency of the imaging optics will be less than unity. Thus, the pulse energy determined in this way represents a lower bound on the generated THz pulse energy. Alternatively, the THz beam waist can also be measured by scanning the focusing mirror over the probe laser spot using a linear translation stage [80, 214]. Under the assumption that the probe spot size is negligible, the beam waist is then found by fitting a Gaussian $\propto \exp(-x^2/w^2)$ to the measured electric field profile. The conversion efficiency from the optical to the THz frequency range is then determined by taking the ratio of the pulse energies,

$$\kappa = \frac{U_{\text{THz}}}{U_{\text{pump}}}. \quad (4.11)$$

Again, this value gives a lower bound for the conversion efficiency.

In the frequency domain, the parameters used for characterizing the THz pulses are the center frequency, the bandwidth and the SNR (see Fig. 4.6b). We take the center frequency ν_{max} to be defined as the frequency of the spectral maximum. It is related to the center wavelength via $\lambda_{\text{max}} = c_0/\nu_{\text{max}}$. The bandwidth is the frequency range over which the spectrum has an amplitude above the noise floor. In the example shown in Fig. 4.6b, the bandwidth extends from zero to the point where the signal hits the noise floor, indicated by the vertical dashed line. The SNR of the pulse is finally defined as the ratio of the amplitude at the center frequency to the amplitude of the noise floor, i.e. the SNR of the pulse is the maximum SNR of the spectrum.

4.3 Terahertz Emission from Semiconductor Surfaces

Terahertz emission from semiconductor surfaces illuminated by ultrashort laser pulses has first been observed by Zhang *et al.* in 1990 [215], shortly after the invention of THz TDS. Depending on the type of semiconductor and the associated band structure, different physical mechanisms contribute to the generation of THz radiation. The most important mechanisms are depicted in Figs. 4.7a to 4.7c and can be separated into surface field and photo-Dember field related effects.

The surface field is a consequence of the depletion layer at the semiconductor to vacuum interface that builds up due to Fermi level pinning to surface or

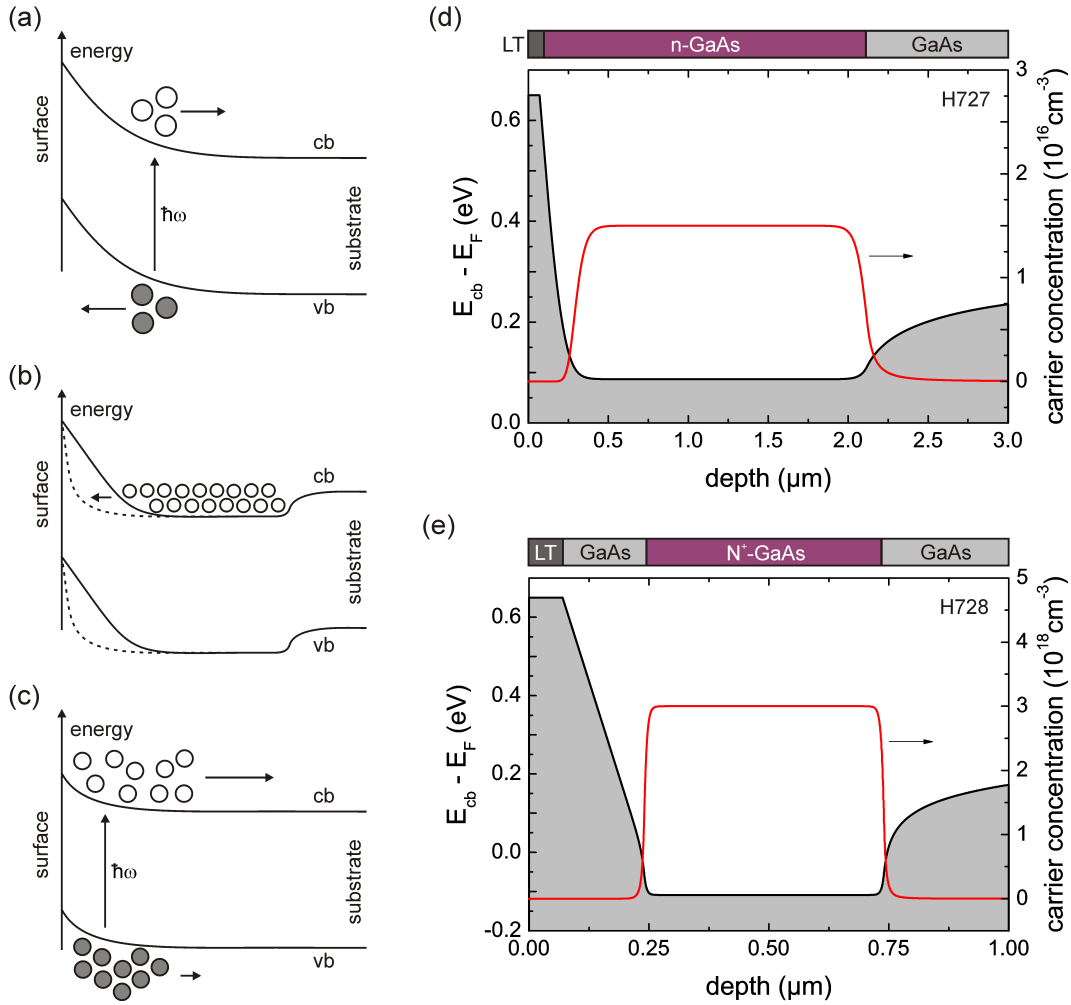


Figure 4.7: Working principle of THz generation from semiconductor surfaces illuminated by ultrashort laser pulses. (a) Electrons and holes are generated within the depletion layer of an intrinsic semiconductor and are accelerated due to the built-in field in different directions. The charge separation leads to a restoring force which causes the carriers to oscillate at the plasma frequency (so-called coherent plasma oscillations). (b) Photogenerated carriers screen the surface potential of a doped semiconductor (dashed line). The cold electrons are then no longer in their equilibrium position and start to oscillate at the plasma frequency (so-called cold plasma oscillations). (c) If the Fermi level pinning is weak, carrier transport is dominated by diffusion away from the surface. Due to the different diffusion constants, electrons move faster, leading to a charge separation (so-called Dember effect). (d, e) Layer structure, conduction band diagram and carrier concentration for emitter structures H727 (d) and H728 (e).

defect states. The width of this space-charge layer and the associated built-in field are given by the Schottky model [216]

$$w_{\text{dep.}} = \sqrt{\frac{2\varepsilon_0\varepsilon}{eN_D}}\phi_b, \quad (4.12)$$

$$E_b(z) = -\frac{eN_D}{\varepsilon_0\varepsilon}(w_{\text{dep.}} - z), \quad (4.13)$$

where ε is the dielectric constant of the semiconductor, N_D the doping density, and $\phi_b = (E_{F,\text{pin.}} - E_F)/e$ the built-in potential due to the difference of surface and bulk Fermi levels, $E_{F,\text{pin.}}$ and E_F . In GaAs, the surface Fermi level is pinned approximately 0.65 eV below the conduction band minimum [217]. The amplitude of the built-in field and the thickness of the depletion layer are both dependent on the doping density. For typical doping levels, the depletion layer width is on the order of a few tens of nanometers and the built-in field reaches several tens of kV/cm.

When an ultrashort laser pulse with photon energy above the band gap strikes a semiconductor surface, electron-hole pairs are generated within the absorption length (see Fig. 4.7a). In GaAs, the absorption coefficient at 780 nm is $\alpha = 10^4 \text{ cm}^{-1}$ giving an $1/e^2$ absorption length of $2 \mu\text{m}$ [218]. The electrons and holes are then accelerated in the built-in field $E_b(z)$ resulting in a current flow normal to the interface. The increasing separation of the charges creates a restoring force which screens the surface potential and finally leads to an oscillatory movement of the electrons. The contribution of the holes can be neglected due to their higher effective mass. The natural frequency of these oscillations is given by the screened plasma frequency [102],

$$\omega_p = \sqrt{\frac{n_0 e^2}{m\varepsilon_0\varepsilon}}. \quad (4.14)$$

The electron density n_0 is directly proportional to the energy of the pump pulse, and is given as a function of z by the relation

$$n_0(z) = \frac{\Phi_\gamma}{(hc_0/\lambda)}(1 - R) \frac{1 - e^{-\alpha z}}{z}, \quad (4.15)$$

where $\Phi_\gamma = U_{\text{pump}}/A_{\text{pump}}$ is the pump fluence, λ the pump wavelength, and R the reflectivity of the semiconductor. For GaAs, $R \approx 0.3$ at 780 nm under normal incidence [219]. Using this value with Fresnel's equations, $R \approx 4 \times 10^{-4}$ for incidence under Brewster's angle and TM polarized light [87].

For higher doping densities and a significant overlap of the doped region with the surface depletion layer, the situation changes to the one depicted in Fig. 4.7b. The separation of photogenerated electron-hole pairs leads to an ultrafast screening of the surface potential [220]. The electron distribution in

the doped region of the semiconductor does not correspond to the equilibrium distribution anymore. This results in the electrons pushing towards the surface followed by a subsequent oscillation around the new equilibrium position at the screened plasma frequency (4.14) [103, 104]. The significant electron density is in this case the doping density, $n_0 = N_D$, and thus, the THz center frequency is independent of the pump fluence. The initial current burst from the cold plasma oscillations is oriented in the opposite direction as compared to the previous case of Fig. 4.7a. Therefore, the initial polarity of the emitted THz pulse will also be different. This property will be important later-on for the discrimination of the different emission processes.

If the semiconductor does not exhibit significant Fermi level pinning, these two mechanisms cannot account for the observed THz emission. Instead, it has been shown by Dekorsy *et al.* [220, 221] that the THz emission in this case can be attributed to the so-called photo-Dember effect, named after its discoverer Harry Dember (1882-1943) [222]. The spatial distribution of the electron-hole plasma after ultrafast optical excitation is highly non-uniform. This density gradient gives rise to a fast diffusion of hot carriers away from the surface (see Fig. 4.7c). Due to different mobilities and effective temperatures of electrons and holes and, therefore, different diffusion constants, electrons and holes separate spatially giving rise to a photo-Dember field. This abrupt switch-on of the internal electric field within a few hundred femtoseconds after optical excitation leads to the emission of an intense THz pulse [221]. The polarity of the THz transient emitted by the photo-Dember effect is thereby the same as that of the THz pulse emitted by charge acceleration in the built-in surface-field (Fig. 4.7a). It has been demonstrated by Heyman *et al.* [223] that even in semiconductors with large Fermi level pinning, the photo-Dember effect can become the dominant emission process when the excess energy of the electrons (and therefore their temperature) is sufficiently high. In their experiment, they used optical excitation with different photon energies, however, this finding applies also to THz emission using high optical fluences.

To evaluate the performance of these types of emitters for the generation of intense THz pulses, we have fabricated two different structures using molecular beam epitaxy. Sample H727 consists of 50 nm LT GaAs (230 °C, annealed for 10 min at 600 °C) on 2 μm Si-doped n -GaAs ($N_D = 1.5 \times 10^{16} \text{ cm}^{-3}$), sample H728 of 70 nm LT GaAs (230 °C, annealed for 10 min at 600 °C) on 170 nm intrinsic GaAs followed by 500 nm Si-doped N^+ -GaAs ($N_D = 3 \times 10^{18} \text{ cm}^{-3}$). Both samples have been grown on single-side polished semi-insulating (100)-oriented GaAs wafers. One drawback of these emitters is their relatively low saturation fluence [214, 224]. To circumvent this problem, we have used 3'' wafers to maximize the illuminated area [110]. The LT GaAs capping layer has been used to enhance the band bending at the surface ($E_{cb} - E_{F,\text{pin.}} = 0.75 \text{ eV}$) and to ensure a firm pinning of the Fermi level due to the large density of defect states (up to 10^{20} cm^{-3}) [105].

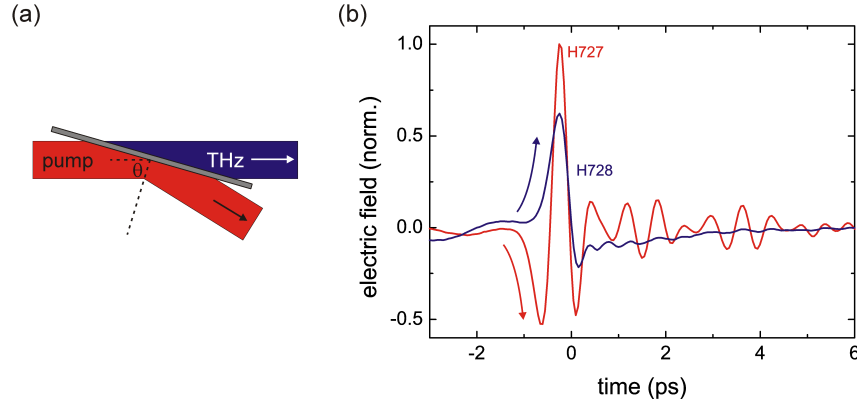


Figure 4.8: (a) Quasi-transmission THz generation scheme. The pump pulse is incident on the polished surface of the wafer under the Brewster angle θ . The generation mechanism preserves the curvature of the phase front and thus, the THz pulse is emitted in forward direction. (b) Normalized transients of surface plasmon emitters H727 (red) and H728 (blue) recorded for low excitation power (to scale). The arrows indicate the polarity of the initial THz burst.

Figures 4.7d and 4.7e show the conduction band diagrams of the two emitter structures calculated using a 1D Poisson solver [225, 226]. In sample H727 (Fig. 4.7d), the surface depletion layer extends 300 nm into the n -doped region. According to the aforementioned arguments, we expect the THz emission process in this structure to be based mainly on cold plasma oscillations as indicated in Fig. 4.7b.

In the case of sample H728, the 170 nm thick intrinsic GaAs layer leads to an extension of the depletion layer width, despite the higher doping level of the adjacent N^+ -doped region, and to the creation of a homogeneous electric field. The thickness of this spacer layer and the doping concentration have been chosen to give a constant built-in field of 40 kV/cm over the first 200 nm of the structure. This field amplitude corresponds to the critical field in GaAs at which the drift velocity of the electrons saturates [227, 228]. The THz emission process is thus expected to be based on the acceleration of photogenerated electron-hole pairs in the built-in field as depicted in Fig. 4.7a.

The experimental geometry for efficient outcoupling of the THz radiation is shown in Fig. 4.8a. As the displacement currents flow perpendicular to the surface, the excitation has to occur under an angle. The maximum emission in forward direction is observed when the pump beam is incident on the sample surface under Brewster's angle, $\theta = \tan^{-1}(n_{\text{GaAs}}/n_{\text{air}}) = 74.5^\circ$ [215]. The phase front curvature of the THz pulse is given by the phase front of the incident pump beam. Therefore, this scheme is also referred to as quasi-transmission. The emitted THz pulse is TM polarized, i.e. the electric field vector is parallel to the plane of incidence.

To validate the theoretical expectations, we have first performed measure-

ments under low optical fluence using 800 nm laser pulses from an 80 MHz Ti:Sapphire oscillator (Spectra Physics Tsunami). The pump beam had a diameter of 3 mm and an average power of 360 mW, resulting in a pump fluence of $\Phi_\gamma = 0.017 \mu\text{J}/\text{cm}^2$. The measured THz transients from the two emitter structures are shown in Fig. 4.8b. The strong oscillations after the main pulse for sample H727 are due to residual water vapor in the sample compartment. The two transients differ significantly, both in temporal shape and frequency content, indicating that different generation mechanisms are responsible for THz emission. First, the polarity of the initial THz burst, indicated by the two curved arrows, is opposite for the two samples. This is expected from the above discussion and supports the assumptions made for the underlying emission processes. Further, from the Fourier transform of the transients (not shown), the center frequencies are determined to $\nu_{\text{max,H727}} \approx 1.23 \text{ THz}$ and $\nu_{\text{max,H728}} \approx 0.2 \text{ THz}$, respectively. The theoretical center frequency for H727 is calculated from (4.14) to $\omega_p = 2\pi \times 1.2 \text{ THz}$, where the doping concentration $N_D = 1.5 \times 10^{16} \text{ cm}^{-3}$ has been used. For H728, only the carriers generated within the first $z = 200 \text{ nm}$ contribute to the THz emission process. Using this value together with Eq. (4.15), we estimate the density of photogenerated carriers to $n_0 = 6.2 \times 10^{14} \text{ cm}^{-3}$. The center frequency is thus expected around $\omega_p = 2\pi \times 240 \text{ GHz}$. The close agreement between the experimental and theoretical values for the center frequencies is a further indication for the validity of the models.

For the high-power experiments, the wafers have been placed under Brewster's angle in the collimated beam section (see Fig. 4.2) with the (01 $\bar{1}$)-facet of the wafer aligned horizontally (primary flat). The pump beam diameter has been increased to 35 mm using a beam expander consisting of a pair of 2'' planoconcave and planoconvex lenses ($f_1 = -100 \text{ mm}$ and $f_2 = 250 \text{ mm}$) to avoid the creation of a filament at an intermediate focus. For detection of the THz transients, we have used a 300 μm thick (110)-GaAs crystal attached to a 500 μm thick piece of (100)-cut GaAs. The response function of the crystal is essentially flat up to 4.5 THz (see Fig. 2.8b). During the experiment, the pump pulse energy has been varied from 50 μJ to 1 mJ corresponding to optical fluences between $\Phi_\gamma = 1.4 \mu\text{J}/\text{cm}^2$ and $27.8 \mu\text{J}/\text{cm}^2$. These fluences are considerably higher than the fluence used for the measurements shown in Fig. 4.8b and we expect this to have a significant impact on the THz generation process.

For the characterization of the THz pulses, we have additionally measured the beam waist at the detector crystal by vertically scanning the last focusing mirror. The beam waists ($1/e^2$ radius of the intensity) have been determined to $w_{\text{H727}} = 250 \mu\text{m}$ and $w_{\text{H728}} = 256 \mu\text{m}$, respectively. Using the measured THz transients and Eq. (4.9), the diffraction limited beam waists are calculated to $\bar{w}_{\text{H727}} = 192 \mu\text{m}$ and $\bar{w}_{\text{H728}} = 250 \mu\text{m}$, respectively. The discrepancy in the case of sample H727 is most likely due to a slight misalignment of the parabolic

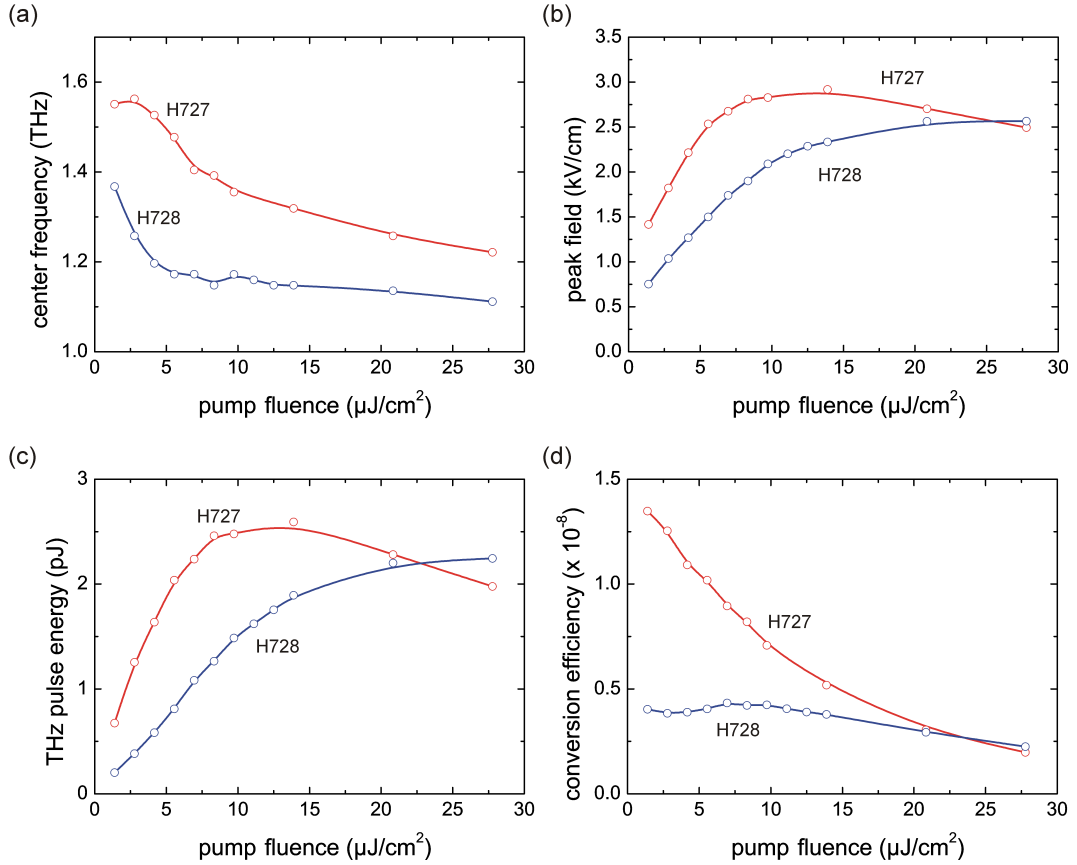


Figure 4.9: Dependence of (a) center frequency, (b) peak electric field, (c) pulse energy, and (d) optical-to-THz conversion efficiency as function of the pump fluence for emitters H727 (red) and H728 (blue).

mirrors used for imaging the THz pulse to the detector. For sample H728, there is a good correspondence. We have used the experimentally measured values for the calculation of the pulse energies in the following.

Figure 4.9a shows the dependence of the center frequencies of both emitters as function of the pump fluence. Neither curve corresponds to the theoretical expectations. At the lowest pump fluence, $\Phi_\gamma = 1.4 \mu\text{J}/\text{cm}^2$, the expected center frequency for emitter H728 is calculated to $\nu_{\text{max,H728}} \approx 2.2 \text{ THz}$. Instead, the measured value is around 1.4 THz. Also, the center frequency should rise as the square root of the pump fluence. Emitter H727 should emit at $\nu_{\text{max,H727}} \approx 1.2 \text{ THz}$, independent of the pump power. However, the measured value is between 1.5 THz and 1.6 THz and decreases for increasing fluence. For fluences above $10 \mu\text{J}/\text{cm}^2$, the two emitters behave almost similar with the center frequency approaching a value of 1.2 THz. This can be seen as a first indication that at these high fluences a different generation mechanism is dominating.

The measured peak amplitudes for both emitters are shown in Fig. 4.9b.

H727 exhibits the highest peak field strength of 3 kV/cm for a fluence around 15 $\mu\text{J}/\text{cm}^2$. For higher fluences, the field amplitude decays again. Emitter H728 saturates between 20 $\mu\text{J}/\text{cm}^2$ and 25 $\mu\text{J}/\text{cm}^2$ at a slightly lower peak amplitude around 2.5 kV/cm. Compared to the results of other groups [214, 224, 229], the saturation fluence is in our case significantly higher. This might be explained by the lower repetition rate of our laser giving the photogenerated carriers more time to recombine. This results in a lower background carrier density and a less effective screening of the built-in electric field [229]. The increased saturation fluence of H728 compared to H727 can be related to the higher doping density and the consequently higher number of photogenerated carriers necessary for efficient screening. The slightly worse performance of H728 in terms of peak amplitude is then simply related to an increased THz absorption due to the higher doping level [215].

The same behavior is also found in the dependence of the THz pulse energy on the pump power, as shown in Fig. 4.9c. The pulse energies have been calculated using the measured beam waists and the electro-optic transients according to (4.8). The highest pulse energies are thereby on the order of 2.5 pJ. The optical-to-THz conversion efficiencies are plotted in Fig. 4.9d as function of the pump fluence. Especially at lower fluences, H727 is almost two times more efficient than H728. At high fluences, however, the conversion efficiency drops to 2×10^{-9} for both emitters. The order of magnitude of the pulse energy corresponds to numerical simulations, however, for smaller excitation spot sizes [224].

Possible reasons for this discrepancy might be found in the neglect of the group velocity mismatch in the detection crystal and the related limited detection bandwidth (see Fig. 2.8), Ohmic losses due to carrier-carrier scattering or the surface roughness of the emitter backside. Another factor is the finite aperture of the collecting mirror after the intermediate focus. Only part of the generated THz pulse energy is actually detected. The ratio of emitted to collected energy can be estimated from the relation

$$U_{\text{coll.}} = U_{\text{emit.}} \left(1 - e^{-2r^2/w^2} \right), \quad (4.16)$$

where r is the mirror radius. Using $w = 2 \times 17.5 \text{ mm}$ and $r = 25 \text{ mm}$, yields a ratio $U_{\text{coll.}}/U_{\text{emit.}} = 64\%$.

Additionally, competing THz generation mechanisms could interact destructively and effectively reduce the amplitude of the emitted THz field. For instance, surface-field mediated optical rectification (OR) has been observed to be the dominant emission mechanism from (100) and (111)-cut InP [230] and (100)-cut InAs [231] under high excitation fluences. Thereby, the surface depletion field breaks the inversion symmetry of the (100) or (111) face of the semiconductor leading to a second-order nonlinearity $\chi^{(2)}(\Omega; -\omega, \omega + \Omega) = \chi^{(3)}(\Omega; 0, -\omega, \omega + \Omega)E_b$ [230]. The polarity of the OR signal depends on the sign of the surface depletion field and equals the polarity of case Fig. 4.7a.

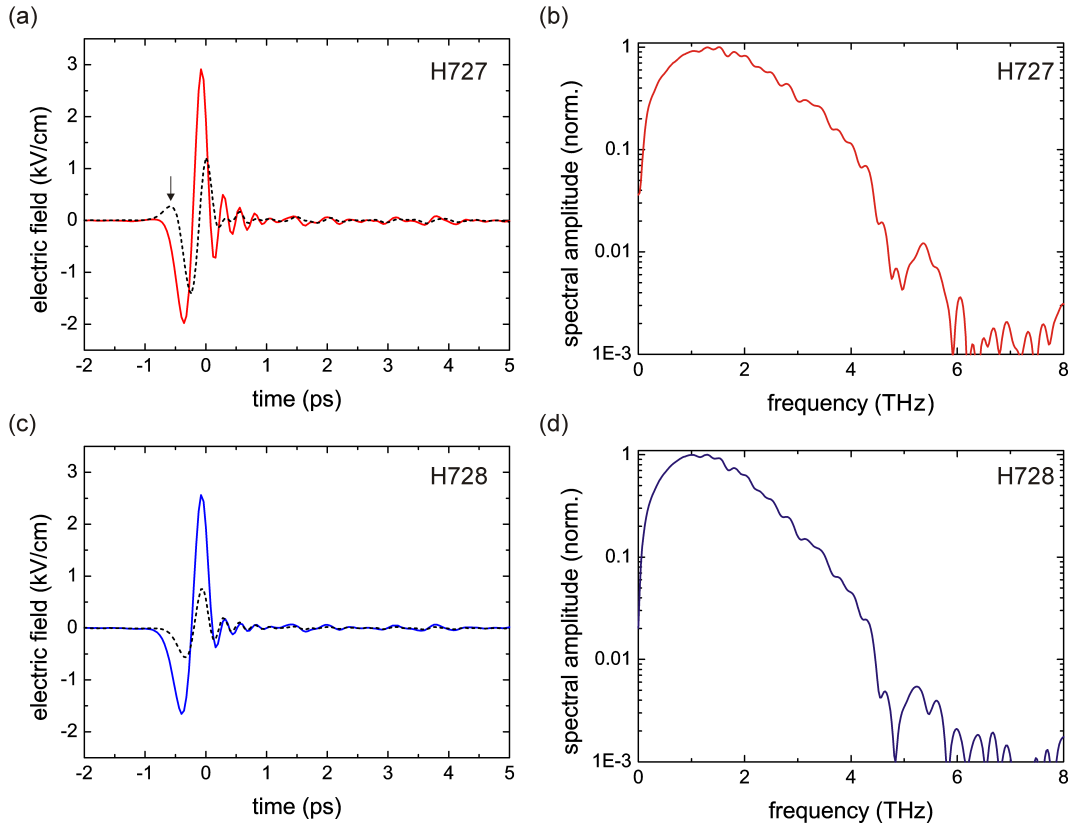


Figure 4.10: Experimental transients and spectra obtained for emitter structures H727 (a,b) and H728 (c,d) in the amplifier setup under optimal pump fluences. The dashed lines indicate the transients obtained for the lowest pump fluence.

A measurement of the THz peak amplitude as function of crystallographic orientation of H728 for $3.9 \mu\text{J}/\text{cm}^2$ excitation fluence (not shown) showed an amplitude modulation of $\pm 15\%$ with a twofold rotational symmetry, which is a clear indication for OR. Also, the aforementioned photo-Dember effect could play a role. It becomes dominant for higher excess energies of the photogenerated carriers, which are easily acquired in the ponderomotive potential of the intense pump pulse. The polarity of the emitted THz pulse is equal to the polarity of the OR signal and the polarity of case Fig. 4.7a.

In both cases, the polarity is opposite to the polarity from the cold plasma oscillations, i.e. the polarity emitted from H727 at low pump fluences, but equal to the polarity of H728. This is clearly seen from the experimental transients taken at the lowest (dashed line) and optimal (solid line) pump fluences as shown in Fig. 4.10. While for H727 (Fig. 4.10a), the polarity of the transient changes sign when going to higher fluences (indicated by the black arrow), no such thing is observed for H728. The polarity for both emitters is equal for high pumping, which is a clear indication for an additional, dominating generation mechanism such as OR.

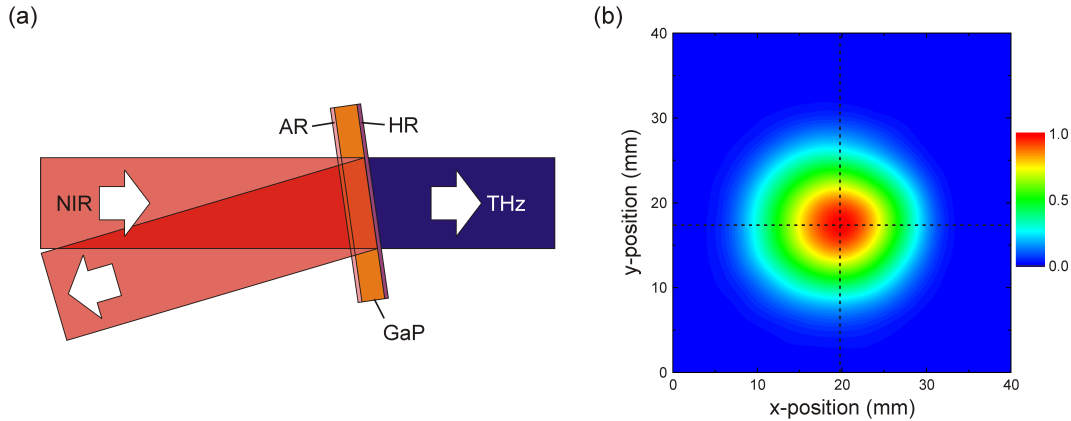


Figure 4.11: (a) Schematic view of the GaP emitter. The crystal has been coated for 780 nm with an anti-reflection layer on the front facet and a high-reflection layer on the back facet. Only the THz pulse is transmitted in forward direction. To allow dumping of the NIR energy, the crystal is slightly tilted ($< 2^\circ$). (b) THz beam profile after the emitter crystal measured by scanning the beam with a 7 mm metal aperture. The dashed lines indicate the cut-planes for determination of the beam waists along the x and y axes.

The spectra for both emitters are shown in Figs. 4.10b and 4.10d, respectively. The bandwidth extends in both cases to 6 THz with a dip between 4.5 and 5 THz, which is related to the response function of the GaAs detector crystal. The SNR is almost 1000 at the maximum and, for H727, the SNR is still above 100 up to 4 THz. The moderate field strength and the relatively low power consumption make this emitter the ideal source of probe pulses in a THz pump-THz probe configuration.

4.4 Optical Rectification in Nonlinear Crystals

Optical rectification (OR) of short laser pulses in electro-optic crystals has been among the very first techniques used for the generation of pulsed radiation in the far-infrared region [26, 91, 232]. Classically, the term OR is related to a dc electric polarization that is induced by an intense laser beam in a nonlinear medium [233]. In the context of THz generation, the polarization shows a time-dependence according to the pulsed nature of the excitation, which emits coherent radiation [234]. Mathematically, the description is similar to difference-frequency mixing [63]. Depending on the type of phase matching that can be achieved between THz and optical frequencies, several emission modes can be distinguished. These include THz emission in a Čerenkov-like cone [26, 91, 235], surface emission [230, 236] (see Chap. 4.3), forward emission by collinear phase matching [129, 237–240], and tilted-pulse front generation [241]. While the latter has been proven as efficient source of high-intensity THz pulses using LiNbO₃-

crystals [78, 80], THz generation by collinear phase matching in (110)-cut zinc-blende crystals is the simplest technique to implement experimentally.

In conjunction with Ti:Sapphire laser systems, ZnTe is the most often used crystal as it allows phase-matched generation at 2 THz [240] and exhibits a comparatively large nonlinearity $d_{\text{eff}} = 68.5 \text{ pm/V}$ [78]. By using large crystal areas, the saturation of the THz yield due to two-photon absorption can be avoided [110], and THz pulse energies up to $1.5 \mu\text{J}$ with peak fields of 49 kV/cm have been demonstrated [242]. However, the accessible bandwidth is effectively limited to approximately 3.3 THz due to the fundamental phonon resonance in ZnTe around 5.3 THz and additional two-phonon resonances at 1.7 THz and 3.3 THz, respectively [141].

A possible alternative to ZnTe is GaP, where the Reststrahlen band lies near 11 THz [243]. In addition, the bandgap is larger than the bandgap of ZnTe, which results in a significant reduction of two-photon absorption [244]. The drawback, however, is the smaller nonlinearity of only $d_{\text{eff}} = 24.8 \text{ pm/V}$ and, more important, the higher index mismatch between THz and optical frequencies.

In the following, we first discuss THz generation in the conventional collinear geometry and compare theoretical predictions with our measurements using large area GaP crystals. For higher pump pulse energies, the measured data deviates from the theoretical prediction. This is then shown in the subsequent chapter to be related to dynamic phase matching. We show that dynamic phase-matching is a novel way of extending the achievable pulse energy and bandwidth from GaP crystals when pumped by amplified Ti:Sapphire laser pulses. The key results of the following chapters have also been published in Dietze *et al.*, *Opt. Lett.* **37**, 1047 (2012).

4.4.1 Collinear THz Generation in Large Area GaP

The experimental geometry is depicted in Fig. 4.11a. The pump beam waist is expanded by a factor 2.5 to 17.5 mm using a beam expander consisting of a pair of 2" planoconcave and planoconvex lenses ($f_1 = -100 \text{ mm}$, and $f_2 = 250 \text{ mm}$) to avoid the creation of a filament at an intermediate focus. The pump pulse energy has been varied from $50 \mu\text{J}$ to above 3 mJ , which is the maximum energy available at the crystal position. This pump energy corresponds to averaged optical fluences between $\Phi_\gamma = 5 \mu\text{J/cm}^2$ and $300 \mu\text{J/cm}^2$. The pulse is incident on the crystal under almost normal incidence. The crystal is a (110)-cut, double side polished GaP crystal (MolTech, Berlin) with $30 \times 30 \text{ mm}$ clear aperture and a thickness of $400 \mu\text{m}$. To increase the pump energy inside the crystal and minimize the amount of light transmitted into the setup, the front-facet is coated with a broadband anti-reflection (AR) layer for 740-820 nm, while the backside is coated with a high reflective (HR) layer. The residual pump light is then blocked by a double side polished Si wafer. We have confirmed by THz

TDS measurements that the two coating layers have no detrimental impact on the emitted THz pulse. The crystal is slightly tilted ($< 2^\circ$) to allow efficient dumping of the reflected pump beam. For detection of the THz transients, we have used a 300 μm thick (110)-GaAs crystal attached to a 500 μm thick piece of electro-optically inactive (100)-cut GaAs. The response function of the detection crystal is plotted in Fig. 2.8b.

The incident electric field of the pump pulse, E_L , creates a nonlinear polarization [245]

$$P^i(\Omega) = \frac{1}{2}\epsilon_0 \int_{-\infty}^{\infty} \sum_{j,k} \chi_{ijk}^{(2)}(\Omega; \omega_0, -\omega_0 + \Omega) E_L^j(\omega_0) E_L^{k*}(\omega_0 - \Omega) d\omega_0 \quad (4.17)$$

inside the GaP crystal, where i , j , and k refer to the crystallographic axes, ω_0 to the center frequency of the pump pulse, Ω to the THz frequency, and $\chi_{ijk}^{(2)}$ to the second-order nonlinear susceptibility. The asterisk denotes the complex conjugate and the prefactor 1/2 comes from the fact that $P^i(\Omega)$ is a real valued quantity. The nonlinear polarization is related to the THz electric field via the wave equation [245]

$$\left(\nabla^2 - \frac{\epsilon}{c_0^2} \frac{\partial^2}{\partial t^2} \right) E_{\text{THz}}(t, \mathbf{r}) = \frac{1}{\epsilon_0 c_0^2} \frac{\partial^2}{\partial t^2} P(t, \mathbf{r}), \quad (4.18)$$

where

$$P(t) = \frac{1}{2\pi} \int P(\Omega) e^{i\Omega t} d\Omega, \quad (4.19)$$

$$E(t) = \frac{1}{2\pi} \int E(\omega) e^{i\omega t} d\omega. \quad (4.20)$$

From (4.17) and (4.18), it is apparent that the THz field scales as $E_{\text{THz}} \propto |E_L|^2 \propto I_L$, or $I_{\text{THz}} \propto I_L^2$. The beam waist of the generated THz pulse is thus expected to scale as $w_{\text{THz}} \propto w_L/\sqrt{2}$. Figure 4.11b shows the normalized electric field profile of the THz pulse 10 cm after the emitter crystal. To this end, we have scanned a 7 mm diameter copper aperture across the beam and recorded the transmitted peak signal. The profile is almost circular with a Gaussian cross-section. The measured beam waists ($1/e^2$ radius of intensity) along the x and y direction are 8.2 mm and 7.5 mm, respectively. The deviation from the theoretical value of 12.4 mm can be attributed to clipping of the THz beam at the collecting mirror after the intermediate focus, i.e. the limited field of view of the detection (1:2 telescope, see Chap. 4.3).

To simplify further discussion, we adopt in the following the contracted notation $d_{il} = d_{ijk} = \frac{1}{2}\chi_{ijk}^{(2)}$ for the second-order nonlinearity [63]. GaP has cubic crystal structure with symmetry group $\bar{4}3m$. Thus, the only non-vanishing nonlinear coefficients are $d_{14} = d_{25} = d_{36}$ [63]. The dependence of the generated polarization on the crystal orientation can be included in an effective

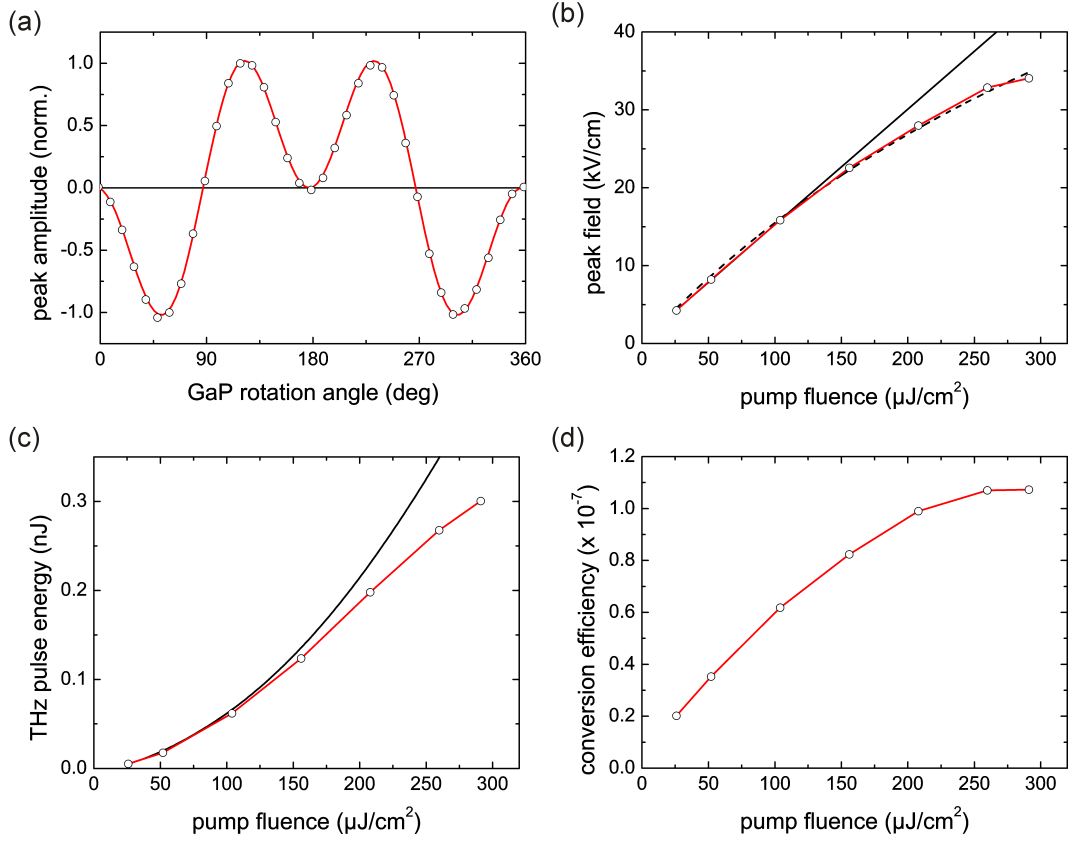


Figure 4.12: (a) Normalized THz peak amplitude as function of the rotation angle of the GaP crystal around the optical axis. The circles are experimental results and the solid line is a fit of Eq. (4.21). (b) THz peak electric field as function of pump fluence (red). The black solid line is a linear fit to the first three data points, the dashed curve is a fit of Eq. (4.23). (c) THz pulse energy as function of pump fluence (red). The black line is a quadratic fit to the first three data points. (d) Energy conversion efficiency versus pump fluence.

nonlinearity [237]

$$d_{\text{eff},\parallel} = d_{14} (\cos 3\theta - \cos \theta), \quad (4.21)$$

$$d_{\text{eff},\perp} = \frac{1}{3} d_{14} (3 \cos 3\theta + \cos \theta), \quad (4.22)$$

where \parallel (\perp) refers to the emitted THz polarization parallel (perpendicular) to the incident pump field polarization and θ is the azimuthal angle of the crystal. Case (4.21) corresponds to our experimental situation. A comparison of measured data (circles) and Eq. (4.21) (solid line) is shown in Fig. 4.12a for a pump fluence of $100 \mu\text{J}/\text{cm}^2$. The excellent agreement shows that the THz generation is solely due to OR.

At higher pump fluences, the THz yield starts to saturate. This is illustrated in Figs. 4.12b and 4.12c. In Fig. 4.12b, the measured peak electric field is

plotted as function of the pump fluence. From the above discussion, we would expect a linear scaling with the pump energy. This is indicated by the black line which shows the result of a linear fit to the data points up to a fluence of $100 \mu\text{J}/\text{cm}^2$. For higher fluences, saturation sets in. This behavior is excellently described by [214, 246]

$$E_{\text{peak}}(\Phi_\gamma) = \frac{E_{\text{sat}}\Phi_\gamma}{\Phi_\gamma + \Phi_{\text{sat}}}, \quad (4.23)$$

where E_{sat} is the saturated peak field amplitude and Φ_{sat} the saturation fluence. From a least squares fit to the data (shown as dashed line), we find $E_{\text{sat}} = 100 \pm 9 \text{ kV}/\text{cm}$ and $\Phi_{\text{sat}} = 0.55 \pm 0.07 \text{ mJ}/\text{cm}^2$. This result shows that the THz yield may still be increased by using a smaller pump beam waist, unless two photon absorption sets in.

For the determination of the pulse energy, we have measured the THz beam waist at the detector crystal by vertically scanning the last parabolic mirror with a linear translation stage. From a Gaussian fit, we have extracted a beam waist of $w = 250 \mu\text{m}$. At the same conditions the diffraction limited spot size calculated from Eq. (4.9) would have been $\bar{w} = 180 \mu\text{m}$. The pulse energy can now be estimated using Eq. (4.8) and is plotted in Fig. 4.12c as function of pump fluence. For fluences above $100 \mu\text{J}/\text{cm}^2$, the curve deviates again from the expected quadratic dependence, which is plotted as black solid line. The highest pulse energies are around 0.3 nJ , which gives an energy conversion efficiency from the visible to the THz of almost 1.1×10^{-7} (plotted in Fig. 4.12d). This value compares well with the results of [110] in the case of ZnTe when the thinner crystal and the lower nonlinearity are taken into account. In contrast to the THz peak field, the conversion efficiency saturates already around $250 \mu\text{J}/\text{cm}^2$ and stays constant for higher fluences. This behavior has also been observed for OR in large area ZnTe crystals [242].

To proceed with the theoretical discussion of collinear phase matched THz generation, we substitute d_{eff} into Eq. (4.17), which is then reduced to

$$P(\Omega) = \varepsilon_0 \int_{-\infty}^{\infty} d_{\text{eff}} E_L(\omega_0) E_L^*(\omega_0 - \Omega) d\omega_0. \quad (4.24)$$

At this point, several simplifications can be made [245]. As the thickness of the crystal is much smaller than both the lateral dimension and the Rayleigh length of the collimated pump beam, we can make a plane-wave approximation and reduce the wave equation (4.18) to a one-dimensional equation. Furthermore, we neglect absorption of the NIR light in the crystal as well as pump depletion. Finally, if the effective nonlinearity has no resonances in the frequency range of the pump beam, we can treat it as independent of the pump pulse frequency and pull it out of the convolution integral in (4.24). With these assumptions and Eqs. (4.17), (4.19) and (4.20), the wave equation (4.18) becomes [245]

$$\left(\frac{\partial^2}{\partial z^2} - \frac{\varepsilon(\Omega)}{c_0^2} \frac{\partial^2}{\partial t^2} \right) E_{\text{THz}}(t, z) = \frac{d_{\text{eff}}(\Omega)}{c_0^2} \frac{\partial^2}{\partial t^2} |E_L(t, z)|^2. \quad (4.25)$$

The pump pulse electric field, $E_L(t, z)$, is given by the expression

$$E_L(t, z) = \frac{1}{2} E_0 e^{-(t-z/v_g)^2/\Delta t^2} e^{-i(\omega_0 t - k_0 z)} + c.c. \quad (4.26)$$

where E_0 is the (real) peak amplitude, $k_0 = \omega_0 n(\omega_0)/c_0$ the wavevector, $n(\omega)$ the refractive index for the pump light,

$$v_g = c_0 \left(n(\omega_0) + \omega_0 \frac{\partial n(\omega)}{\partial \omega} \right)^{-1} \quad (4.27)$$

the group velocity and Δt the $1/e^2$ pulse length of the intensity envelope. The pulse length is taken as constant over the thickness of the GaP crystal.

To find an analytic solution to the wave equation, we substitute (4.26) into (4.25) and take the Fourier transform [245],

$$\begin{aligned} \left(\frac{\partial^2}{\partial z^2} + \frac{\varepsilon(\Omega)}{c_0^2} \Omega^2 \right) E_{\text{THz}}(\Omega, z) = & \quad (4.28) \\ & - \sqrt{\frac{\pi}{2}} \frac{d_{\text{eff}}(\Omega) \Omega^2 \Delta t}{4c_0^2} e^{-\frac{1}{8}\Omega^2 \Delta t^2} e^{-i\Omega z/v_g} E_0^2. \end{aligned}$$

This equation can be integrated with respect to z using the initial conditions

$$E_{\text{THz}}(\Omega, z=0) = 0 \quad \text{and} \quad \frac{\partial}{\partial z} E_{\text{THz}}(\Omega, z=0) = 0 \quad (4.29)$$

which state that no THz field is present at the entrance face of the crystal. The solution is finally found to be given by [245]

$$\begin{aligned} E_{\text{THz}}(\Omega, z) = & \frac{\sqrt{2\pi}}{8} \frac{d_{\text{eff}} \Delta t E_0^2}{n_{\text{THz}}^2 - n_g^2} e^{-\frac{1}{8}\Omega^2 \Delta t^2} \left[\frac{1}{2} \left(1 - \frac{n_g}{n_{\text{THz}}} \right) e^{i\Omega n_{\text{THz}} z/c_0} \right. \\ & \left. + \frac{1}{2} \left(1 + \frac{n_g}{n_{\text{THz}}} \right) e^{-i\Omega n_{\text{THz}} z/c_0} - e^{-i\Omega n_g z/c_0} \right], \quad (4.30) \end{aligned}$$

where we have used the abbreviations $n_{\text{THz}} = \sqrt{\varepsilon(\Omega)}$ and $n_g = c_0/v_g$.

The generated THz field consists of three parts represented by the three terms in the parentheses. The first two terms $\propto \exp(in_{\text{THz}}z/c_0)$ and $\propto \exp(-in_{\text{THz}}z/c_0)$ represent the freely propagating THz pulses in backward and forward direction, respectively, and the third term $\propto \exp(-in_g z/c_0)$ the part of the THz pulse driven by the pump pulse. The amplitude of the backward propagating wave scales as $(n_{\text{THz}} - n_g)/(n_{\text{THz}} + n_g)$ compared to the forward propagating one and vanishes for perfect phase matching. The factor $\exp(-\frac{1}{8}\Omega^2 \Delta t^2)$, which accounts for the finite length of the pump pulse envelope, shows that shorter pump pulses allow the generation of spectrally broader THz pulses. The signal in the time domain is finally obtained by taking the inverse

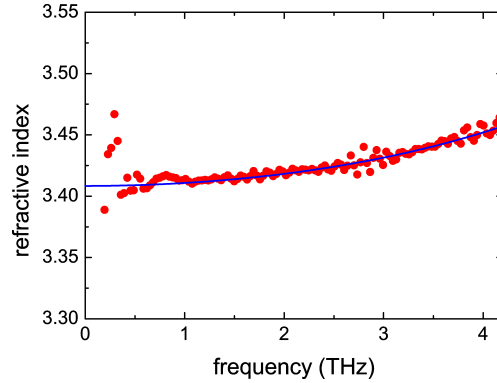


Figure 4.13: THz refractive index of GaP. The solid line is a fit of Eq. 4.33 to the experimental data.

Fourier transform of Eq. (4.30). This is best done after transforming to the center-of-mass frame of the pump pulse.

The refractive index of GaP in the visible spectral region is given by the Sellmeier equation [138]

$$n_{\text{NIR}}^2 = 4.1705 + \frac{4.9113}{1 - 0.1174/\lambda^2} + \frac{1.9928}{1 - 756.46/\lambda^2}, \quad (4.31)$$

where λ is the wavelength in μm . The group refractive index is related to n_{NIR} via

$$n_g(\lambda_0) = n_{\text{NIR}}(\lambda_0) - \lambda_0 \left. \frac{\partial n_{\text{NIR}}(\lambda)}{\partial \lambda} \right|_{\lambda_0}. \quad (4.32)$$

At the carrier frequency $\lambda_0 = 780\text{nm}$, we have $n_0 = 3.20$ and $n_g = 3.66$.

The permittivity of GaP in the THz region is modeled as a single Lorentzian oscillator,

$$\varepsilon(\Omega) = \varepsilon_\infty + \frac{\varepsilon_\infty(\omega_{LO}^2 - \omega_{TO}^2)}{\omega_{TO}^2 - \Omega^2 + i\gamma\Omega} \quad (4.33)$$

where ε_∞ is the high-frequency permittivity, ω_{LO} and ω_{TO} the longitudinal and transversal optical phonon frequencies, and γ the phonon damping rate.

We use the values as given in Ref. [133] as starting point, $\varepsilon_\infty = 9.075$, $\omega_{TO} = 2\pi \times 11.011\text{ THz}$, $\omega_{LO} = 2\pi \times 12.082\text{ THz}$, and $\gamma = 2\pi \times 0.129\text{ THz}$. In general, the data obtained in the visible region is more reliable compared to the permittivity found in the THz region. This becomes obvious when one compares the various values for $\varepsilon(\Omega)$ given in literature [3, 133, 134, 138, 247–250]. The main reason for these variations can be attributed to variations in the crystal quality and background impurities. Thus, we take the NIR refractive index as given and use our experimental data to determine the THz refractive index.

As both the exact thickness L and the refractive index $n_{\text{THz}}(\Omega) = \sqrt{\varepsilon(\Omega)}$ of the GaP crystal are unknown, we have performed an additional THz transmission measurement. This yields independent data which allows us in conjunction

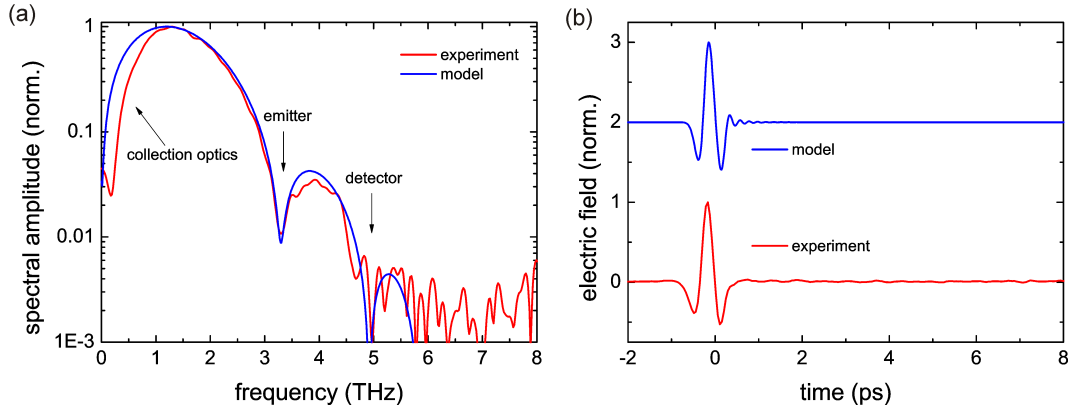


Figure 4.14: Comparison of theoretical (blue) and experimental (red) THz spectra (a) and transients (b) obtained for the lowest pump fluence. The spectral dip around 3.3 THz is due to the velocity mismatch between THz and pump pulses. The THz transients have been offset for clarity.

with the emission spectrum to unambiguously determine both thickness and refractive index. The frequency dependence of the experimentally determined refractive index data is thereby in excellent agreement with Eq. (4.33). Thus, we retain the frequency dependent part and add just an offset by adjusting the high frequency dielectric constant.

The procedure is as follows. For a given initial crystal thickness, we determine the THz refractive index of the crystal using the equations from Ref. [251]. Then, we vary the high frequency dielectric constant ϵ_∞ to obtain the best fit to the experiment. Now, both values are used in Eq. (4.30) to calculate the theoretical THz emission spectrum, which is then compared with the experimental spectrum obtained for the lowest pump fluence. The phase matching dip in the emission spectrum is very sensitive to both thickness and refractive index of the crystal and only the correct choice of L and $\epsilon(\Omega)$ yields a perfect match to both datasets. We have obtained the best fit for a crystal thickness of $L = 412.5 \mu\text{m}$ and a high frequency dielectric constant of $\epsilon_\infty = 9.075 + 0.575 = 9.65$. The resulting THz refractive index is shown in Fig. 4.13 together with the experimental data.

Figure 4.14a shows a comparison between normalized THz spectra obtained from experiment (red) and calculations (blue). The experimental emission spectrum has been recorded for the lowest pump fluence. There is also an excellent agreement in the slope of the spectrum for a pulse length of $\Delta t = 130$ fs. The low frequency cut-off is attributed to aperture effects in the THz imaging setup. The two spectral dips at 3.3 THz and around 5 THz are attributed to velocity mismatch in the GaP crystal and the GaAs detector crystal, respectively.

The normalized THz transients are compared in Fig. 4.14b. The theoretical curve has been differentiated once with respect to time to account for the transfer function of the optical setup. Based on the excellent agreement

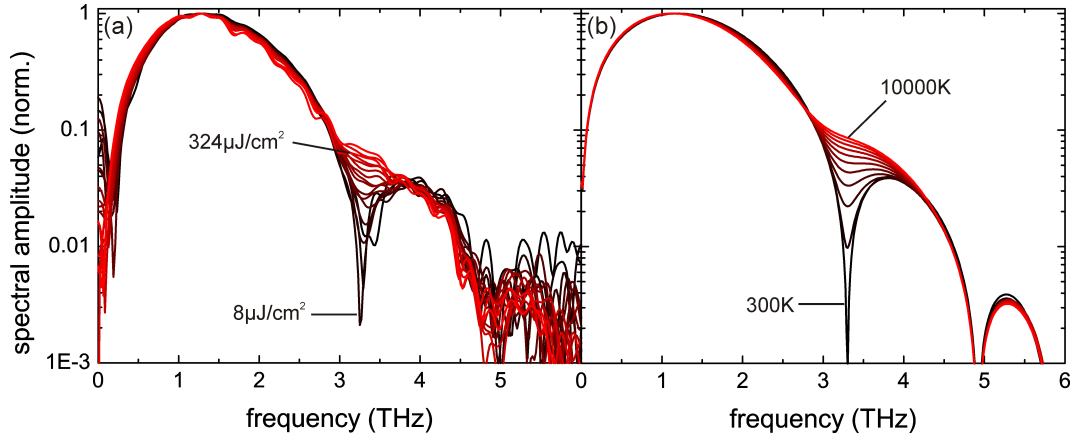


Figure 4.15: (a) Normalized THz spectra for different pump fluences from $8 \mu\text{J}/\text{cm}^2$ to $324 \mu\text{J}/\text{cm}^2$. The spectral dip at 3.3 THz disappears for increasing pump fluences. (b) Model spectra for various effective phonon temperatures from 300 K to 10 000 K.

between theory and experiment, we conclude that the model correctly describes the THz generation process in GaP under low excitation fluences.

4.4.2 Dynamically Phase-Matched THz Generation

When the optical pump power is increased, the situation becomes different from the collinear phase-matched THz generation discussed above. Nonlinear effects start to play a role, which lead to an enhanced efficiency in the THz generation process as compared to the conventional case.

Figure 4.15a shows normalized THz emission spectra for different pump fluences ranging from $8 \mu\text{J}/\text{cm}^2$ to $324 \mu\text{J}/\text{cm}^2$. The most prominent effect of the increased pump power is the disappearance of the spectral dip at 3.3 THz, which has been attributed to the velocity mismatch between the THz and the pump pulse. Its disappearance is a clear indication for an improved phase matching, which can be related to an increase of the THz refractive index. As this effect is a function of the pump power, it is solely connected to the presence of the pump pulse and is thus a temporal effect. Such a transient improvement of the phase matching is referred to as *dynamic phase matching* [252].

To find the physical origin of this dynamic phase matching, we have compared the experimental results with model calculations. Thereby, we could exclude any nonlinear optical effects connected with the second- and third-order nonlinear susceptibilities of the GaP crystal, respectively.

In the following, a model is presented which is based on the coherent generation of phonons by the pump pulse and the connected increase of the optical phonon decay rates. The generation of phonons leads basically to a change of the effective phonon temperature. The temperature dependence of the THz permittivity is reflected in a temperature dependence of the high frequency

dielectric constant, of the phonon frequencies and of the phonon lifetimes. The first two effects are a direct consequence of the thermal expansion of the crystal lattice [253] (thermal equilibrium). We argue that these effects take place on time scales which are long compared to the duration of the pump pulse and can therefore be neglected in the further discussion. The latter effect, however, is directly connected to the density of coherently generated phonons [254, 255].

In GaP, the main decay channel for the infrared active TO phonons is the decay into two acoustic phonons, LA(X) and TA(X), at the zone boundary via a third-order anharmonic interaction [254]. The optical phonon decay rate is then expected to have the temperature dependent form [254]

$$\gamma(T) = \gamma_0 [n(\omega_{LA(X)}) + n(\omega_{TA(X)}) + 1], \quad (4.34)$$

where $n(\omega)$ are the Bose-Einstein occupation numbers for phonons with energy $\hbar\omega$,

$$n(\omega) = (e^{\hbar\omega/k_B T} - 1)^{-1}, \quad (4.35)$$

with Boltzmann constant k_B . The frequencies of the two acoustic phonon modes have been determined by neutron scattering to $\omega_{LA(X)} = 2\pi \times 7.46$ THz and $\omega_{TA(X)} = 2\pi \times 3.21$ THz, respectively [256]. We use the room temperature value of the phonon decay rate to calculate the value of the scaling constant $\gamma_0 = 2\pi \times 0.0441$ THz. The temperature which appears in the phonon occupation numbers is thereby an effective phonon temperature and is not to be confused with the temperature of the crystal lattice.

Figure 4.15b shows calculated THz spectra for various phonon temperatures ranging from 300 K to 10 000 K. The dominant effect of an increased phonon temperature is the disappearance of the spectral dip around 3.3 THz. Apart from a slight narrowing of the spectra for higher temperatures, the overall shape of the spectra is almost not affected by the increased phonon linewidth. The excellent agreement between the experimental and theoretical spectra clearly shows that the proposed model captures the essential physics underlying the dynamic phase matching in GaP.

Finally, in Figs. 4.16a and 4.16b, a typical THz transient and spectrum for high pump fluence ($324 \mu\text{J}/\text{cm}^2$) is shown. The peak field strength of the single cycle THz pulse reaches values up to 40 kV/cm and could be further increased by using lower beam expansion ratios (see Fig. 4.12). The spectrum extends to 6 THz and is mainly limited by the response function of the GaAs detector crystal. The high field strength together with the good SNR and the simple experimental handling make the GaP crystal the ideal workhorse for nonlinear THz transmission experiments. The GaP emitter has also been used for most of the experiments presented in this thesis.

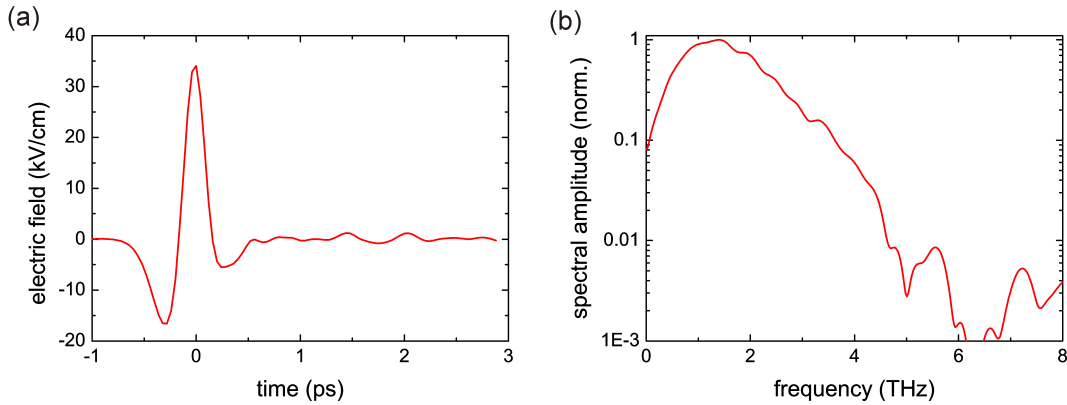


Figure 4.16: Example of a THz transient (a) and spectrum (b) for 2.8 mJ pump pulse energy. For this pump energy, the emission process is dynamically phase matched.

4.5 Large Area Photoconductive Antennas

Terahertz emission from semiconductors by the acceleration of free carriers in an electric field has been demonstrated in Chap. 4.3. There, the electric field has been the static electric field provided by the surface potential of the semiconductor itself. Thus, the THz generation efficiency has been limited by the value of the built-in field and the complicated emission geometry. These limitations can be overcome in a natural way by applying an external bias field along the surface of the semiconductor by using electrodes. This forms the basic principle of the photoconductive (PC) antenna, which has already been presented in Chap. 2.2.1.

The THz electric field emitted from such an antenna, given by Eq. (2.20), is thereby proportional to the density of photogenerated carriers and the applied bias field. Thus, to increase the THz output power, both quantities should be maximized. The maximum bias field that can be applied is limited by the breakdown voltage of the semiconductor substrate. In the case of LT-GaAs, for example, the breakdown occurs for a static electric field of 200 kV/cm when applied under dark conditions [257]. However, a combination of Ohmic and optical heating strongly reduce this value when the antenna is illuminated [258]. Additionally, higher bias fields increase the scattering rate of electrons to satellite valleys with higher effective mass leading to a saturation of the THz generation process [259]. The density of carriers, on the other hand, can be increased to values above 10^{18} cm^{-3} by using higher optical pump powers. For excitation densities above $\approx 3 \times 10^{17} \text{ cm}^{-3}$, however, carrier screening effects lead again to a saturation of the THz pulse amplitude [259].

Like in the previous chapters, the solution is to increase the emission area in order to increase the total number of carriers while keeping their density below the saturation limit. The easiest way is to fabricate two electrodes on a

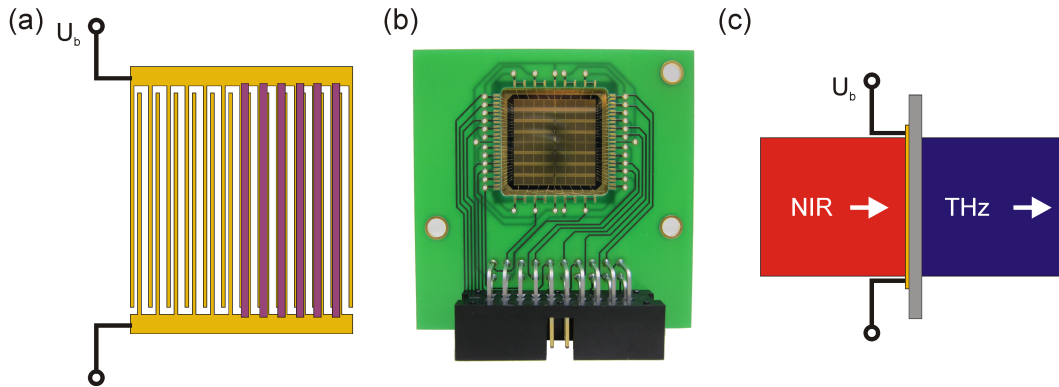


Figure 4.17: (a) Scheme of PC antenna with interdigitated electrodes. A bias voltage U_b is applied to the antenna electrodes. Every second gap is masked due to the opposite orientation of the biasing field. (b) Photograph of the finished PC emitter matrix with 16x16 interdigitated antenna pixels. Four neighboring pixels are connected to form a bigger emitter resulting in a 4x4 antenna array. (Courtesy of D. Bachmann [262].) (c) Quasi-transmission scheme for THz generation from PCA emitter.

large area GaAs wafer, for example, using ordinary silver paint. The electrode spacing is usually on the order of a few cm. This scheme has been applied very successfully leading to peak fields well above 100 kV/cm [260, 261]. The drawback is the high supply voltage that is necessary to generate the needed bias electric fields. Typically, several tens of kV have to be applied, which leads to strong heating of the antenna due to the residual dark current. In pulsed operation, heating effects can be reduced, but the fast switching of the voltage supply leads to strong electrical disturbances.

To circumvent these problems, we have decided to use an alternative antenna design based on interdigitated electrodes, which can be scaled easily to large areas [262, 263]. The main work (including design and sample fabrication) has been done by D. Bachmann and is published in Ref. [262]. Therefore, the present chapter is limited to a short presentation of the key results.

A sketch of such an antenna element is shown in Fig. 4.17a. The small spacing between the electrodes allows to reach high acceleration fields with a low voltage of only a few V. The bias voltage is applied to the top and bottom electrode. Upon illumination, the carriers are accelerated in the horizontally oriented electric field between the fingers of the two electrodes. To avoid destructive interference of THz emission from neighboring gaps (the electric field in every second gap is oriented in the opposite direction), every second gap is covered with a metallic shadow mask (shown as pink bars in Fig. 4.17a).

The electrodes have been fabricated by PVD of 10 nm Ti / 180 nm Au on a 2 μm thick LT-GaAs layer on a 3" SI-GaAs substrate using standard optical lithography techniques [262]. The electrode width is 10 μm with the

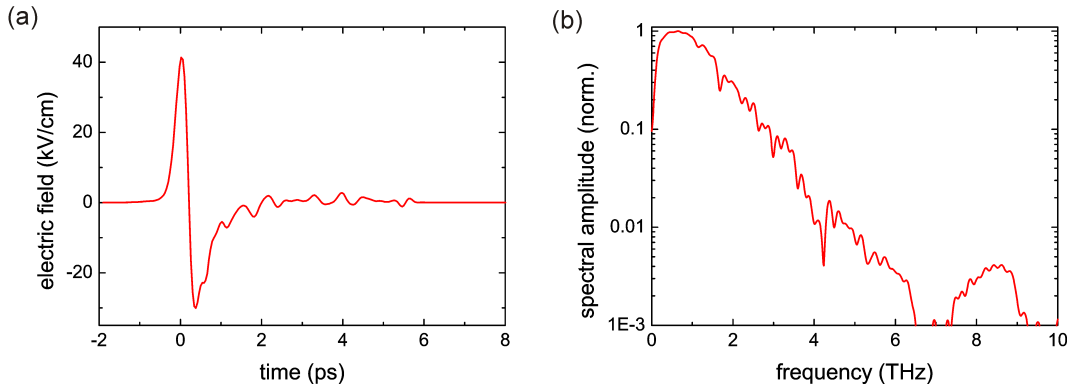


Figure 4.18: Example of a typical THz transient (a) and spectrum (b) for a bias voltage of 45 V and a pump fluence of $90 \mu\text{J}/\text{cm}^2$. The spectrum peaks at around 500 GHz and extends to roughly 6 THz. The dip around 4 THz is attributed to the response function of the GaAs detector crystal. (Adopted from [262].)

gap widths being $20 \mu\text{m}$ and $10 \mu\text{m}$ for the open and covered gaps, respectively. This asymmetry helps to increase the illuminated area and hence the THz yield. However, a too large asymmetry limits the applicable bias voltage as the breakdown field strength is first reached in the shadowed gap. An applied voltage of 50 V corresponds thereby to an electric field of 25 kV/cm in the emission gap and 50 kV/cm in the shadow gap, respectively. The shadow mask has been fabricated by vapor deposition of 10 nm Ti / 180 nm Au on a 850 nm thick layer of Si_3N_4 , which acts both as insulation layer and anti-reflection coating for the 780 nm pump light [262]. The emitter area is around $1.8 \times 1.8 \text{mm}^2$.

Figure 4.17b shows the finished PC array emitter (PCA) after mounting and connecting the antenna. It consists of an array of 64 basic emitter units (pixels) giving a total emitter area of $15 \times 15 \text{mm}^2$. Thereby, four neighboring pixels are connected to form one bigger pixel. By splitting the antenna in several subunits, problems which arise from fabrication imperfections (e.g. shortcuts) are greatly reduced. Additionally, the pixels can be biased separately which might be used for beam steering and compressive imaging, for example [262].

The THz generation scheme is shown in Fig. 4.17c. The pump beam is first expanded to a beam diameter of approximately 20 mm in order to cover the whole emitter area and is then normally incident on the PCA. The THz pulses are then emitted under quasi-transmission, i.e. the phase front of the THz pulse resembles the phase front of the pump pulse. The THz beam is well collimated and exhibits a Gaussian beam profile with a $1/e$ radius of 12.5 mm [262]. The biasing is done using a specialized control circuit that allows independent biasing of each pixel [262]. In the following, all pixels are equally biased. The bias voltage is applied as a 1 kHz square wave that is synchronized with the amplifier pulses.

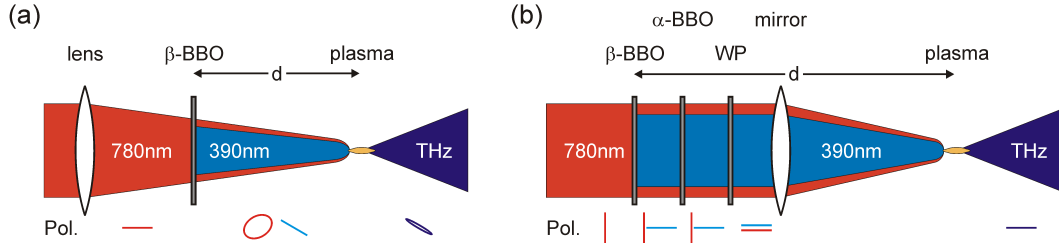


Figure 4.19: Schematic view of typical setups used for THz generation from two-color plasma filaments. The polarizations of the fundamental, second-harmonic and THz pulses are indicated at the bottom. (a) The pump beam is focused by a lens through the β -BBO crystal to generate the second-harmonic. This allows short distances d between the BBO and the plasma spot, but leads to elliptical polarization of the THz pulse. (b) The polarization and the relative pulse delay can be optimized using an α -BBO and a dual-color wave plate (WP). In this case, a mirror has to be used for focusing.

Figure 4.18 shows a typical THz transient (a) and spectrum (b) obtained for a pump fluence of $90 \mu\text{J}/\text{cm}^2$ and an applied bias voltage of 45 V. The THz peak field reaches values around 40 kV/cm with the spectrum extending up to 6 THz. The prominent dip around 4 THz is attributed to the response function of the GaAs detector crystal, that has been used for the measurements. The spectrum peaks around 0.5 THz and decreases exponentially for higher frequencies (linear decrease in the log-plot). This is a typical spectral feature of LT-GaAs PC emitters and is in contrast to the more round shape found from the surface emitters (Chap. 4.3) or the optical rectification sources (Chap. 4.5). We have not measured the THz beam waist at the detector position, but we can use the THz spectrum and Eq. (4.9) to calculate the spectrally-weighted beam waist, $\bar{w} = 450 \mu\text{m}$. The resulting THz pulse energy of 3 nJ corresponds to an optical to THz conversion efficiency of 1.5×10^{-5} . This is the highest THz pulse energy we have measured in this thesis.

To increase the THz peak field amplitude further, larger emitter structures would have to be fabricated. Additionally, the PCA can be electrically modulated, which makes this emitter an ideal source in a THz-pump / THz-probe type of experiment targeting the spectral region below 1 THz.

4.6 Four-Wave Mixing in Laser Induced Plasma Filaments

Up to now, the presented high-power THz emitters have all been based in some form on a THz emitter used in conventional TDS setups and scaling of the pump power. This upscaling has been achieved in most cases by using large excitation areas or splitting of the emitter in sub-sections. In contrast, THz

emission from laser induced filaments constitutes a novel type of THz source, that cannot be realized using high repetition rate laser systems. In this chapter, the prospects of using two-color laser filaments for the generation of intense THz pulses is investigated.

The use of gas plasmas as THz emitter has attracted considerable attention after the first reports by Hamster *et al.* in the early 1990s [108, 264]. Few years later, Cook and Hochstrasser found a significant increase in emitted THz power by mixing fundamental and frequency doubled laser pulses [109]. Their setup is sketched in Fig. 4.19a. The pump laser pulse is focused by a lens through a β -BBO crystal into ambient air. In the BBO, a frequency doubled pulse is generated by a second-order nonlinear process [63]. Close to the focus point, the two pulses undergo self-focusing due to the third-order optical nonlinearity of air [265]. Once the field strength reaches the threshold for ionization, a plasma filament is formed from which an intense single-cycle THz pulse emanates. The microscopic origin of the THz emission is discussed later. In this configuration, electric peak field strengths of 400 kV/cm and high bandwidths up to 75 THz have been reported [266, 267]. Using higher pump energies and proper system design, field amplitudes even over 1 MV/cm are anticipated [268].

Despite the seemingly simple setup, the usability of the plasma source is limited by the complexity of the emission process. The β -BBO crystal is typically cut for type-I phase matching, i.e. the highest conversion efficiency is achieved when the fundamental and second-harmonic polarizations are orthogonal. However, in this configuration, no THz radiation is generated from the plasma. The optimal rotation angle of the BBO crystal is found to be close to 55° between the crystal z -axis and the fundamental polarization [269, 270]. After passing the BBO crystal, the initially linearly polarized fundamental pulse is almost circularly polarized, as indicated in Fig. 4.19a. This results in an elliptically polarized THz pulse whose orientation is additionally a function of the pump power and of the distance between the BBO crystal and the filament [270].

Another parasitic effect of a varying pump power is the dependence of the position of the plasma filament due to self-phase modulation in the lens material [271]. Thus, by changing the pump power, the THz source moves along the optical axis which in turn changes the focusing of the THz pulse on the detector crystal. Furthermore, the plasma filament constitutes an extended source of THz radiation, which emits over its entire length. Hence, an important issue is the efficient imaging of the emitted radiation both onto the sample under study and the detector. Usually, only a small portion of the THz light around the focal plane of the collimating optics is collected efficiently, which limits the achievable peak field strengths. Both issues can be overcome by enclosing the filament in a THz waveguide [272]. Alternatively, an off-axis parabolic mirror with short focal length can be used. The focal length should be short enough to limit the filament length to a value which is still efficiently detected (approximately 25 mm in our setup [272]).

Based on these considerations, we have decided to use the setup shown in Fig. 4.19b for our experiments. The collimated pump pulse is thereby passing through a combination of β -BBO, α -BBO and a dual-color wave plate before it is focused by an off-axis parabolic mirror into ambient air. This combination of crystals is referred to as phase-compensation unit [273, 274]. Its purpose is to maximize the second-harmonic and THz yield by properly setting the involved polarizations and to optimize the relative time delay between fundamental and second-harmonic pulses. First, the second-harmonic of the pump pulse is generated in the 100 μm thick β -BBO (cut angle 29.9°), which is rotated by 90° for highest conversion efficiency. The polarizations of the pulses are again indicated in Fig. 4.19b. While the relative phase between the fundamental and second-harmonic pulses is fixed to $\pi/2$ [63], the pulse envelopes are offset by approximately 20 fs due to the different group velocities. To obtain a maximum THz signal, the polarization of the fundamental pulse has to be rotated by 90° . This is accomplished by a 570 μm thick quartz plate, which acts as a half-wave plate for 780 nm and as full-wave plate for 390 nm. The quartz plate leads to an additional time delay between the two pulses of 110 fs. Propagation of the two pulses through air adds another 8.6 fs per 10 cm propagation distance to the total time delay [275]. This time offset can be compensated by an α -BBO crystal (cut angle 90°), which has the unique property that the group velocity of the second-harmonic is higher than that for the fundamental pulse [274]. In our case, the crystal has a thickness of 800 μm , which compensates a time delay of 200 fs. The optimal distance of the β -BBO to the focus is thus between 40 cm and 70 cm. All crystals have a clear aperture of 1" and are anti-reflection coated for 780 nm and 390 nm. The setup shown in Fig. 4.19b differs from the original proposal in [274] in the fact that we do not use a wedge pair to control the relative phase between the fundamental and second-harmonic pulses. In our case, this is done by moving the β -BBO relative to the plasma position and using the different propagation velocities in air [267, 270]. As focusing mirrors we have used off-axis parabolas with effective focal lengths between 50 mm and 150 mm. The mirrors have been coated either by gold or by aluminum, which shows a higher reflectivity for the second-harmonic light.

Apart from technological issues, THz emission from two-color filaments is itself a highly complex process. In addition to the strong signal in forward direction, there are numerous mechanisms contributing to the total THz emission from the plasma. Examples include ponderomotive forces [264] or Čerenkov emission from the laser wake field [276]. However, these processes do not contribute to the measured THz signal in our experimental configuration due to the polarization selection rules of the electro-optic detection scheme and will not be investigated further. The microscopic origin of this strong forward THz emission has a long time been unknown. In early reports, the authors explained their findings by a phenomenological four-wave mixing model [109, 266, 269, 277, 278]. The necessary third-order nonlinearity has first been attributed to air and later

to the plasma itself. Sparked by this uncertainty and other deviations from experimental observations, a microscopic polarization (MP) model has been brought forward by Kim *et al.* [267, 279] and Thomson *et al.* [213]. It has been adopted from an equivalent model used for the description of higher harmonics generation from plasmas [280]. In addition, the hypotheses of this model are supported by particle-in-cell simulations [281] and fully quantum-mechanical calculations [282, 283].

4.6.1 Microscopic Polarization Model

The idea behind the MP or current surge model is that electrons, which are created by strong-field ionization of neutral gas molecules, are accelerated in the combined electric field of the fundamental and second-harmonic pulses. The electrons wobble around the positive ions, which are stationary on the time scale of the pulse duration. When the two fields are added with the correct relative phase, the electrons do not return to their respective origin after the laser pulses have passed. This leads to the formation of a non-vanishing polarization and the associated current burst gives rise to the emission of an intense half-cycle THz pulse. In the following, we derive the basic equations describing THz emission from two-color plasma filaments based on the MP model. Any polarization dependence is neglected and the model is purely one-dimensional. This reflects the experimental configuration shown in Fig. 4.19b. In addition, neither scattering processes nor THz absorption in the plasma are taken into account as this leads to an especially simple analytic expression for the emitted THz field. Despite these simplifications, the model still reflects the main properties of the plasma emitter and shows good agreement with experimental results. Part of the results obtained in this chapter and a further discussion of the different models for THz generation in dual-color filaments have been published in Dietze *et al.*, *J. Opt. Soc. Am. B* **26**, 2016 (2009).

The incident two-color laser pulse is modeled as

$$E(t) = A_0 \sin(\omega_0 t) e^{-t^2/2\Delta t^2} + \sqrt{\eta} A_0^2 \sin(2\omega_0 t + \Phi) e^{-(t-\tau)^2/\Delta t^2}, \quad (4.36)$$

where A_0 is the fundamental peak field amplitude, ω_0 its angular frequency, $\Delta t = T_{\text{FWHM}}/2\sqrt{\ln 2}$ the intensity pulse width, η the energy conversion efficiency of the second-harmonic generation process, Φ the relative phase between the two pulses and τ the relative time delay between the two pulse envelopes. Note that the value of Φ for maximum THz emission depends on the choice of sine or cosine in Eq. (4.36). In our formulation, maximum THz emission occurs for $\Phi = 0$. The peak field amplitude

$$A_0 = \sqrt{\frac{\sqrt{2}U_0}{\pi^{3/2}\epsilon_0 c_0 w_0^2 \Delta t}} \quad (4.37)$$

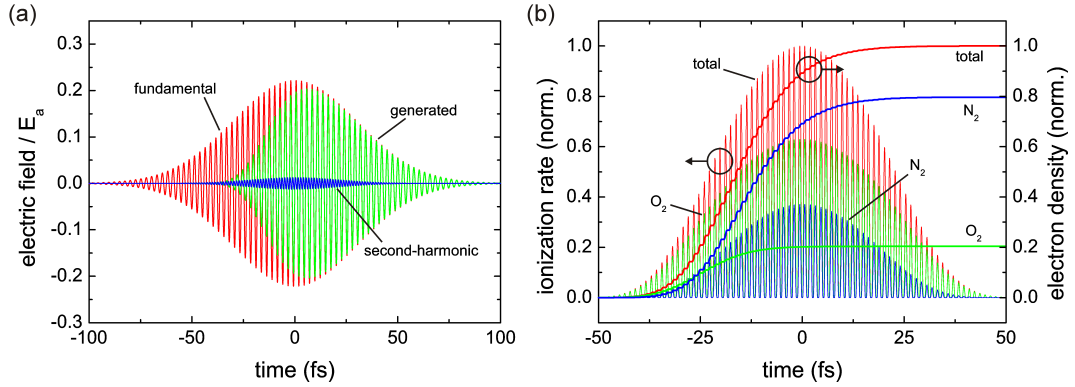


Figure 4.20: (a) Electric field of the fundamental and second-harmonic pulses for a pulse length of 50 fs in units of the atomic field strength E_a . The emitted field calculated from the microscopic polarization model is shown in green (curve not to scale). (b) Ionization rate and electron density for atmospheric oxygen and nitrogen as calculated from the static tunneling model. The abundances of O_2 and N_2 in air have been taken as 20% and 80%, respectively.

is in turn determined by the pulse energy U_0 , Δt and the beam waist in the focus $w_0 = \lambda f / \pi w_{in}$, where f is the focal length of the focusing optics and w_{in} the input beam waist. In this formulation, intensity clamping effects in the filament are neglected. This seems to be a valid assumption for tight focusing conditions [213]. An example of a two-color driving pulse is shown in Fig. 4.20a for $U_0 = 3$ mJ, $T_{FWHM} = 50$ fs, $\lambda_0 = 780$ nm and $\eta = 0.0625$.

The density of electrons at time t can be described by the differential equation

$$\frac{d}{dt}n(t) = W(t)(n_{bg} - n(t)), \quad (4.38)$$

where n_{bg} is the background density of neutral atoms and $W(t)$ the ionization rate. In using this expression, we neglect any recombination effects which would reduce the number of electrons. This is acceptable on the time scale of the THz emission process. For hard focusing conditions, the ionization process is dominated by tunneling ionization [213], i.e. the strong electric field of the laser pulse deforms the confinement potential of the electron in the atom so strongly, that the electron can escape. The simplest form of the ionization rate is given by the static tunneling model [284–286]:

$$W(t) = 4\omega_a \left(\frac{U_i}{U_H} \right)^{5/2} \frac{E_a}{|E(t)|} \exp \left\{ -\frac{2}{3} \left(\frac{U_i}{U_H} \right)^{3/2} \frac{E_a}{|E(t)|} \right\}, \quad (4.39)$$

where U_i is the ionization potential of the neutral gas molecule (12.1 eV for O_2 and 15.6 eV for N_2 [287]), $U_H = 13.6$ eV the ionization potential of hydrogen,

$$\omega_a = \frac{1}{(4\pi\epsilon_0)^2} \frac{me^4}{\hbar^3} \quad (4.40)$$

the atomic frequency unit and

$$E_a = \frac{1}{(4\pi\epsilon_0)^3} \frac{m^2 e^5}{\hbar^4} \quad (4.41)$$

the atomic field unit. For the boundary condition $n(t \rightarrow -\infty) \equiv 0$, Eq. (4.38) has the analytic solution [213, 288]

$$n(t) = n_{bg} e^{-\int_{-\infty}^t W(t') dt'} \int_{-\infty}^t e^{\int_{-\infty}^{t'} W(t'') dt''} W(t') dt'. \quad (4.42)$$

which can be simplified to

$$n(t) = n_{bg} \left(1 - e^{-\int_{-\infty}^t W(t') dt'} \right). \quad (4.43)$$

Figure 4.20b shows the total ionization rate and electron density (red) as function of time, split according to the contributions of both O₂ (green) and N₂ (blue). For the calculations, the driving pulse shown in Fig. 4.20a has been used and the relative abundances of the two species have been taken as 20% for O₂ and 80% for N₂, respectively. The ionization of the gas occurs mainly during the leading half of the driving pulse, while at later times, the electron density barely changes.

For the later derivations, we need the number of electrons that are created at time t_0 , $\dot{n}(t_0)$, which can be written as

$$\dot{n}(t_0) = \left. \frac{d}{dt} n(t) \right|_{t=t_0} dt. \quad (4.44)$$

Once an electron is born, it feels a driving force due to the combined electric field of the two laser pulses. Under the assumption that electrons are created at rest, i.e. $v(t_0, t_0) \equiv 0$, the velocity of an electron born at time t_0 can be written as

$$v(t, t_0) = -\frac{e}{m} \int_{t_0}^t E(t') dt' \quad \text{with } t_0 < t, \quad (4.45)$$

where e is the electron charge and m its mass. If we assume that electrons that have been created at the same time move at the same speed, we can write the contribution to the current from electrons created at time t_0 as

$$j(t, t_0) = -e \dot{n}(t_0) v(t, t_0). \quad (4.46)$$

The total current at time t is thus obtained by integrating (4.46) over all times t_0 ,

$$j(t) = \int_{-\infty}^t j(t, t_0) dt_0 = -e \int_{-\infty}^t \dot{n}(t_0) v(t, t_0) dt_0. \quad (4.47)$$

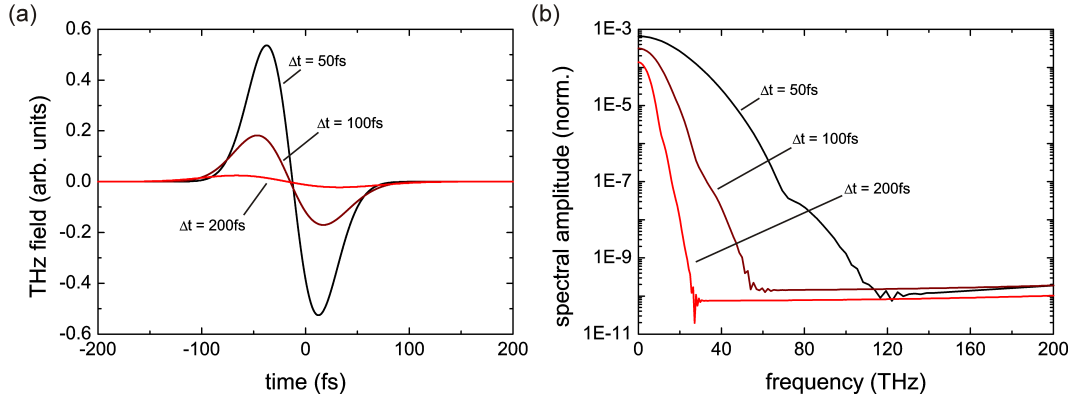


Figure 4.21: THz transients (a) and spectra (b) calculated with the microscopic polarization model for different pump pulse lengths from 50 fs to 200 fs. The time domain data has been differentiated once to account for the transfer function of the optical setup. For shorter pulses, both the peak field and the bandwidth of the THz pulses increases.

Note that the time t appears both in the integrand and the integration limit. Equation (4.47) is equivalent to the formulation given in Ref. [279]. The authors use the expression $N_e(t')$ for the electron density created at time t' , which corresponds to (4.44) in our picture.

As the lateral emission spot size is usually small compared to the THz wavelength, the emission spot can be treated as Hertzian dipole. Then, the THz field E_{THz} is proportional to $(d/dt)j(t)$, i.e.

$$E_{\text{THz}} \propto \frac{d}{dt}j(t) = -e \frac{d}{dt} \int_{-\infty}^t \dot{n}(t_0)v(t, t_0)dt_0. \quad (4.48)$$

This expression can be simplified by using the relation [289, p. 476]

$$\begin{aligned} \frac{d}{dy} \int_{\alpha(y)}^{\beta(y)} f(x, y)dx &= \int_{\alpha(y)}^{\beta(y)} \frac{\partial f(x, y)}{\partial y} dx \\ &+ \frac{\partial \beta(y)}{\partial y} f(\beta(y), y) - \frac{\partial \alpha(y)}{\partial y} f(\alpha(y), y). \end{aligned} \quad (4.49)$$

From (4.48), we get

$$\frac{d}{dt}j(t) = -e \int_{-\infty}^t \dot{n}(t_0) \frac{\partial v(t, t_0)}{\partial t} dt_0 - e \dot{n}(t_0)v(t, t), \quad (4.50)$$

where $v(t, t) \equiv 0$ by definition. With the relation [289, p. 458]

$$\frac{d}{dy} \int_y^a f(x)dx = f(y) \quad (4.51)$$

and the definition of the velocity (4.45), the result reads

$$\frac{d}{dt}j(t) = \frac{e^2}{m} \int_{-\infty}^t \dot{n}(t_0)E(t)dt_0 = \frac{e^2}{m} E(t) \int_{-\infty}^t \dot{n}(t_0)dt_0 = \frac{e^2}{m} E(t)n(t), \quad (4.52)$$

where the electric field $E(t)$ could be pulled out of the integral as it is independent of t_0 . Using the fact that the integral over the rate of change of the electron density is nothing else but the total electron density at time t , Eq. (4.52) is reduced to the appealingly simple result

$$E_{\text{THz}} \propto E(t)n(t). \quad (4.53)$$

For the above parameters, the emitted electric field (4.53) is shown in Fig. 4.20a (green). Apart from the THz signal, it contains also components at the fundamental and second-harmonic frequencies, as well as higher harmonics. To compare the model predictions to our experimental results, we have applied a low-pass filter with cut-off frequency 10 THz and a time-derivation step to account for the transfer function of the THz setup [270]. The obtained THz transients are shown in Fig. 4.21a for different pulse lengths of the fundamental pulse. The associated spectra before low-pass filtering are shown in Fig. 4.21b. The MP model predicts the generation of extremely broadband THz pulses with continuous spectra extending up to several tens of THz. Both the bandwidth and the electric peak field are significantly increased by using shorter pump pulses. Both aspects could be confirmed experimentally using an air-biased-coherent-detection scheme (ABCD) [74]. Note that the accessible frequency range in our experiment is limited to 0 to 10 THz.

4.6.2 THz Emission under Tight Focusing Conditions

Figure 4.22 shows the dependence of the THz peak field on various experimental parameters. Thereby, the default values that have been used for the calculations are indicated by the two vertical arrows. The aforementioned strong dependence of the THz peak field on the pump pulse width is also reflected in Fig. 4.22a (solid line). The open circles represent experimental data that has been measured using the setup of Fig. 4.19b and a 150 mm focal length aluminum mirror. To obtain a best fit to the model the data has been multiplied by a scaling constant. During the experiment, the pulse length has been set by controlling the internal compressor of the Spitfire XP and has been measured using a self-built autocorrelator based on two-photon absorption in a GaAsP photodiode. The resulting chirp of the pulse has not been taken into account in the model. However, it has been observed that negatively chirped pulses lead to slightly higher THz peak fields compared to positively chirped pulses with the same pulse length.

The dependence of the peak field on the pump pulse energy is shown in Fig. 4.22b for different pulse lengths of the driving pulse. In all cases, a typical

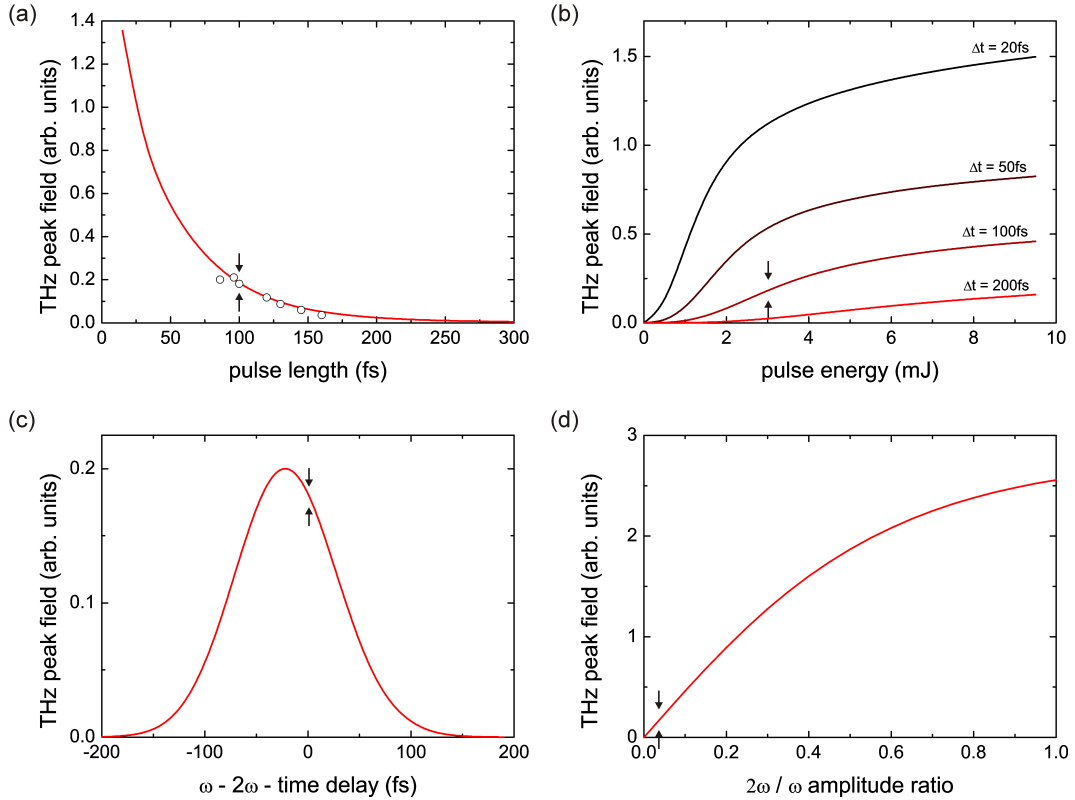


Figure 4.22: Calculated dependence of the THz peak field on pulse length (a), pulse energy (b), relative time delay between fundamental and second-harmonic (c), and ratio of fundamental and second-harmonic peak field strengths (d), respectively. The arrows indicate the default parameters used in the calculations. The open circles in (a) shows experimental data. Figures (a) to (d) are to scale.

saturation behavior is visible. For shorter pump pulses, the saturated THz field amplitude is increased while the saturation energy is reduced. This can be understood from Fig. 4.20b and Eq. (4.53). Only the part of the pump pulse during which the electron density is changing contributes to the emitted THz field. Thus, the electric field of shorter pulses is used more efficiently for THz generation than that of longer pulses. To achieve the smallest possible pulse length in the experiment, we had to remove the half-wave plate and the polarizing beam splitter, which we have used in the previous chapters to control the pump power. Thus, we have measured the THz peak field for 3.35 W and 1.67 W using a thin 50:50 beam splitter with negligible effect on the pulse length. The ratio of the peak amplitudes has been 2.2, which is significantly lower than the theoretical value of 4 (see Fig. 4.22b). This discrepancy can be related to a more complicated energy dependence than is predicted by the simple model. In reality, the pump pulse energy dependence will exhibit additional oscillations due to changes of filament length and the resulting phase walk off between fundamental and second-harmonic pulses (so-called Maker fringes) [270, 290].

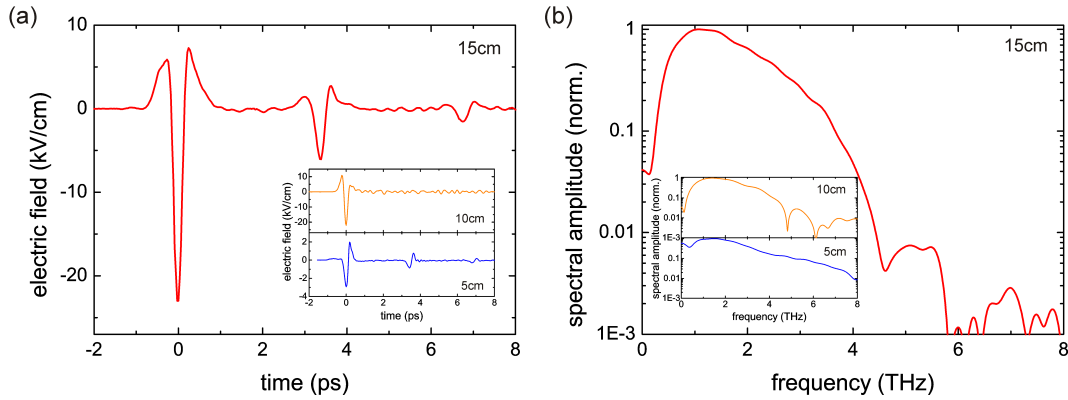


Figure 4.23: THz transient (a) and spectrum (b) obtained using an aluminum mirror with 15 cm focal length and optimized parameters. The insets show results obtained with a gold mirror with 10 cm focal length and an aluminum mirror with 5 cm focal length, respectively.

The same argument applies also to the peak field dependence on the relative time delay between the second-harmonic and the fundamental pulse envelopes, as shown in Fig. 4.22c. The ionization of air is mainly linked to the fundamental pulse envelope, while the THz emission relies on the coherent addition of both fields. By overcompensating the group velocity delay of the second-harmonic pulse, the overlap of the dual color driving field with the ionization period can be optimized. For the given parameters, the maximum THz emission occurs when the second-harmonic pulse advances the fundamental pulse by approximately 20 fs, which corresponds to a shortening of the distance between the β -BBO and the focus by 23 cm (see above).

Finally, the dependence of the THz peak amplitude on the ratio of the second-harmonic field amplitude to the fundamental field amplitude is shown in Fig. 4.22d. For small conversion efficiencies of the β -BBO, there is an almost linear relationship. For increasing field strengths of the second-harmonic pulse, the peak amplitude saturates. This saturation is due to an increasing ionization rate due to the second-harmonic pulse, which cancels the effect of the coherent addition of the two laser pulses (electrons are now also created at the "wrong" phase).

Taking into account these dependencies of the THz peak field on experimental parameters and after further optimization of the pump pulse energy [291], we obtained the THz transients and spectra shown in Fig. 4.23. These have been recorded for three different values of the focal length of the focusing mirror. The effect of the focusing on the density and geometry of the plasma is not included in the model calculations. The highest peak field strength of 23 kV/cm has been achieved with an effective focal length of 150 mm and a filament length of approximately 1 cm. The spectrum shows a bandwidth up to approximately 6 THz. For detection, we have used a 150 μ m thick GaP crystal, which shows

a larger detection bandwidth compared to the 300 μm thick GaAs crystal used so far. The echoes around 3.5 ps and 7 ps are due to reflections in the detection crystal. For the calculation of the THz spectrum, only the main pulse has been taken into account.

The insets of Fig. 4.23 show the results obtained for mirrors with 100 mm (orange) and 50 mm (blue) effective focal length, respectively. The peak field amplitudes have been measured to 22 kV/cm and 3 kV/cm, respectively. This decrease in peak amplitude is probably related to an increased THz absorption in the plasma. The use of shorter focal lengths is equivalent to tighter focusing. The filament length is reduced and the plasma density is increased. For the 100 mm mirror, we have used the 300 μm thick GaAs crystal for detection. Despite the smaller detection bandwidth, the THz spectrum extends to slightly higher frequencies and shows a less pronounced roll-off compared to the case of the 150 mm mirror. For even shorter focal lengths, the bandwidth extends to over 8 THz. To our knowledge, this dependence of the spectral width on focusing conditions has not been reported so far.

Finally, we have determined the THz pulse energy obtained with the 150 mm focusing mirror. To this end, the THz beam waist at the detector crystal has been measured by vertically scanning the last focusing mirror across the probe beam. Equation (4.8) together with the waist size of 158 μm yields a THz pulse energy of 56 pJ and an optical to THz conversion efficiency of 1.7×10^{-8} . The theoretical waist size calculated from Eq. (4.9) would be 184 μm , which is larger than the measured value. This may be due to the extended filament length and the resulting emission character of a line source, which leads to a more complex beam profile at the detector (see Chap. 4.6.3). Using the theoretical waist size, the THz pulse energy is calculated to 75 pJ, which gives an optical to THz conversion efficiency of 2.2×10^{-8} . These values are lower than reported literature values (see for example [213] and references therein), which we attribute mainly to the small detection bandwidth of our setup as compared to the totally emitted bandwidth (see Fig. 4.21b). From Figs. 4.22a and 4.22d, a possible way to increase the THz peak field and thus the THz energy would be to use shorter pulses and to improve the second-harmonic generation efficiency. The latter could be done by using smaller beam waists at the β -BBO crystal and by increasing the crystal thickness.

4.6.3 Waveguide-Enhanced THz Emission under Weak Focusing Conditions

Based on the results of the preceding chapter, one limiting factor for the THz emission from the filament seems to be strong absorption in the dense plasma column [267]. The plasma density can be reduced, for example, by using longer focal length optics, thereby creating a longer filament. However, as has been mentioned in the introductory paragraph, the filament constitutes an extended

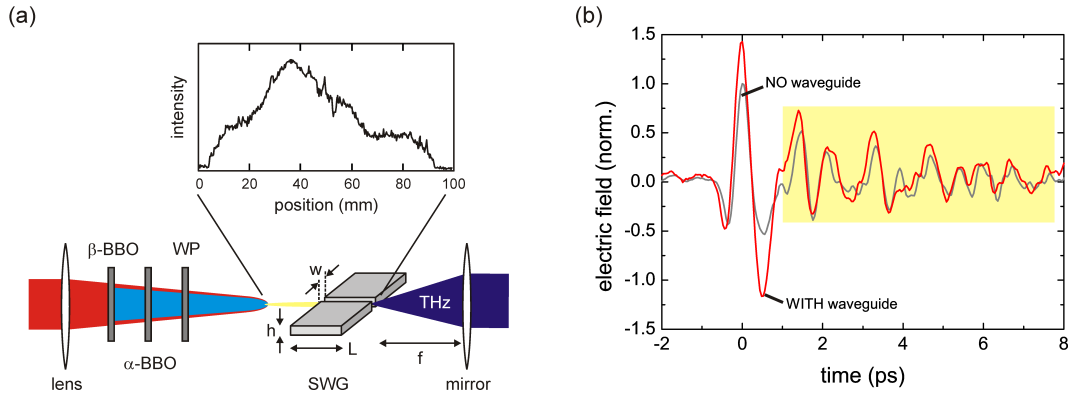


Figure 4.24: (a) Experimental realization of waveguide enhance THz emission. A long focal length lens is mounted in front of the phase compensation unit. A parallel plate waveguide comprised of two polished copper plates (length L , height h and separation w) encloses the filament. The inset shows the luminescence profile of the filament. Partly adopted from [272]. (b) Typical THz transient with and without the waveguide installed. The data is normalized to the case without waveguide. The strong oscillations are due to water vapor, as the waveguide assembly has been mounted outside of the purge chamber (yellow area).

source of radiation, which has to be imaged efficiently onto the sample and the detector. A possible solution would be to enclose the entire filament in a THz waveguide, which collects and guides the THz radiation. The end facet of the waveguide then acts as a point-like source, which can easily be refocused by the existing optics. The results of this chapter have also been published in Dietze *et al.*, *Appl. Phys. Lett.* **100**, 091113 (2012).

Figure 4.24a shows a sketch of the experimental assembly. For enclosing the filament, we have chosen to use a slot waveguide (SWG), which is relatively easy to realize experimentally. The SWG consists of two $h = 2$ mm thick and $L = 20$ mm long copper plates with polished facets (using a $1 \mu\text{m}$ diamond paste) to reduce scattering losses [292]. The plates are mounted horizontally on two separate kinematic mounts with a variable separation d . The SWG is vertically and horizontally centered around the filament with the THz electric field being polarized in the waveguide plane.

To create the filament, we have used a 500 mm focal length lens. To ensure a reasonable temporal overlap between the fundamental and second harmonic pulses, the lens has to be placed in front of the phase compensation unit. By varying the optical pulse energy, we have first maximized the THz peak amplitude before installing the waveguide. The created filament thereby had a length of 95 mm, as has been extracted from the length of the luminescence profile (shown in the inset of Fig. 4.24a). The position of the lens along the optical axis has been adjusted such that the visible part of the plasma column ends exactly at the focal plane of the collecting mirror. We have used a 150 mm

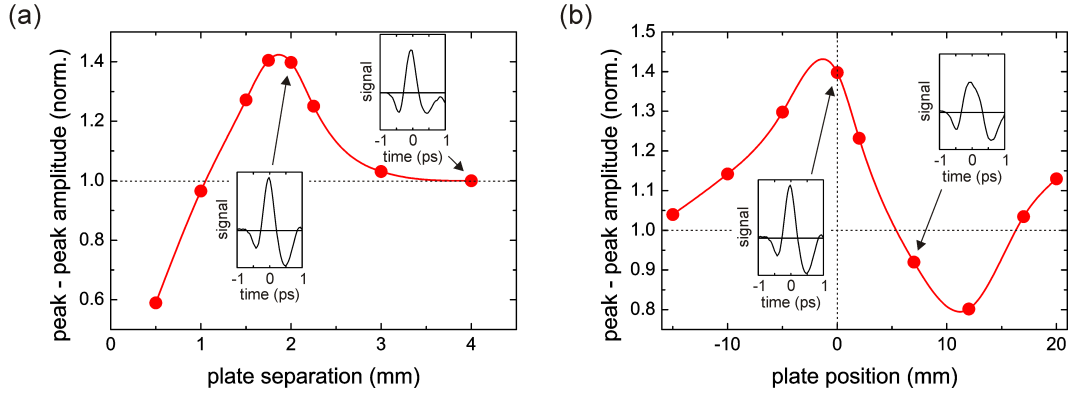


Figure 4.25: Measured peak-to-peak amplitude of the THz transients as function of (a) plate separation and (b) plate position relative to the focal plane of the collecting mirror. The data is normalized to the case without waveguide. The insets show the effect of the waveguide on the THz transients. Adopted from [272].

focal length off-axis parabolic mirror for this purpose. To separate the visible and THz pulses, we have used a Si wafer under 45° . From a comparison of the luminescence profiles with and without SWG, we ensured that the waveguide has no detrimental effects on the plasma filament for the used plate separations (down to $500 \mu\text{m}$).

Due to the size of the assembly, we could not enclose it in the purge chamber. Thus, the experimental data has been recorded under humid conditions. Figure 4.24b shows typical THz transients recorded with and without the waveguide. The water vapor free induction decay is strongly visible (yellow area) and, hence, the further discussion is restricted to the main pulse only. The measured THz peak amplitudes in the two cases have been 3.2 kV/cm without SWG and 4.5 kV/cm with waveguide. The THz field with the SWG is thus increased by 40% compared to the case without waveguide. For the measurement, we used a plate separation of 2 mm, and the SWG has been mounted with the end facet aligned with the focal plane of the collecting mirror.

To study the influence of these two parameters on the detected THz field, we have made a series of measurements. Figure 4.25a shows the peak-to-peak amplitude of the recorded transients as function of the plate separation. The SWG has been aligned with the focal plane of the collecting mirror. The values have been normalized to the value without waveguide. For decreasing separation, the peak-to-peak amplitude increases until it reaches a maximum around $w = 2 \text{ mm}$. For this plate separation, $w = h$, the SWG is impedance matched to free space which yields minimized reflection losses at the end facet [292]. The maximum field enhancement that has been achieved is over 40% compared to the case without waveguide. Reducing the plate separation further leads to a drastic decrease of the measured signal. We attribute this to worse imaging of the electric field onto the detector due to strong diffraction, and

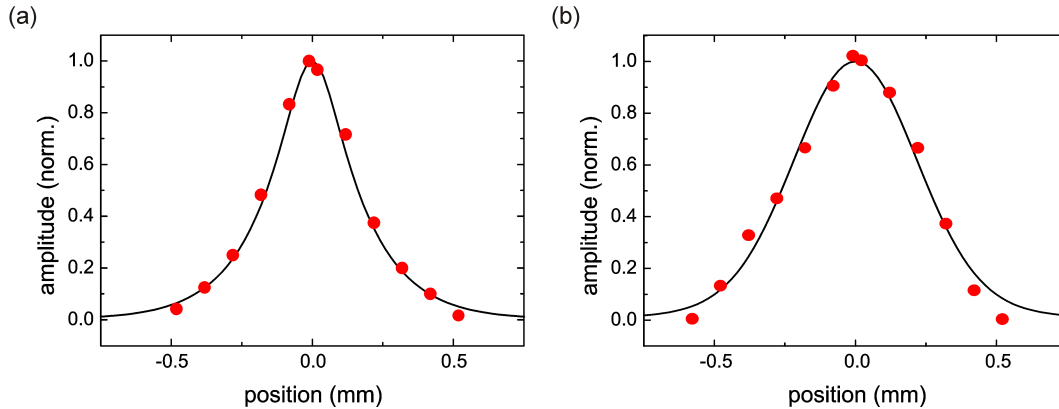


Figure 4.26: Transversal beam profile at detector position (a) without and (b) with waveguide installed (red dots). The solid line shows the calculated profile using the model described in the text. Adopted from [272].

enhanced absorption due to a higher overlap of the waveguide mode with the plasma filament. For separations above 2 mm, the waveguide had a negligible effect on the pulse dispersion, as can be seen from the insets in Fig. 4.25a.

For a plate separation of 2 mm, Fig. 4.25b shows the measured peak-to-peak amplitude as function of position relative to the focal plane of the parabolic mirror. Negative values correspond thereby to positions closer to the mirror. The focal plane separates two distinct regimes. For shorter distances, the overlap between the filament and the waveguide reduces. In addition, the image of the source is also translated out of the focal plane of the last focusing mirror. Thus, the signal quickly decays. For longer distances, respectively, the detected signal is the coherent addition of the radiation emitted from the SWG end facet and the radiation emitted along the part of the filament protruding the waveguide. The observed oscillation is a consequence of the interference of the two parts. From the data, we could estimate a half-period of 22 mm, which corresponds roughly to the periodicity created by the temporal walk-off between the fundamental and second-harmonic pulses in air (see [270], for example). This hypothesis is also supported by the recorded field transients (shown in the insets of Fig. 4.25b), which show a clear shoulder for larger distances to the mirror.

The presence of the SWG should also have a significant impact on the THz beam profile at the detector as it modifies the radiation characteristics of the filament from a line source to a point-like source. Figure 4.26 shows the measured beam profiles without and with waveguide, respectively. The profiles have been recorded by vertically translating the last focusing mirror to scan the THz beam across the probe beam. For the measurements, the SWG has been aligned with the focal plane of the collecting mirror and the chosen plate separation has been 2 mm.

As is expected for an extended THz source, the beam profile shown in Fig.

4.26a for the case without waveguide is highly non-Gaussian. To understand the detailed shape of the profile, we have adopted a simple model based on Gaussian beam propagation using the ABCD matrix formalism [293]. The model is conceptually similar to the one proposed by Zhong *et al.* [294], which is based on the coherent addition of spherical waves emitted along the filament. However, in contrast to their work, our model allows to include the frequency dependent transfer function of the optical setup, and, thus, to calculate the expected beam profile at the detector crystal. The generation spot of the THz light is taken as the beam waist position, z_0 , of an emanating Gaussian beam relative to the focal plane of the collecting mirror. The waist size, w_0 , is initially frequency independent, which accounts for the fact that the emission spot size is given by the filament diameter. By application of the ABCD-matrix method for each frequency of the generated THz spectrum, ω , we can derive the new beam waist $w(\omega, z_0)$ at the position of the detector crystal [293]. In the calculations, the finite aperture size of the 2" THz optics is explicitly taken into account (see [295]). The radial beam profile at the detector position is then obtained by

$$E_{\text{det}} \propto \int_{-L_{\text{fil}}}^0 dz_0 \int_0^\infty d\omega e^{-r^2/w(\omega, z_0)^2}, \quad (4.54)$$

where L_{fil} is the effective length of the filament contributing to the detected signal and r the radial distance to the optical axis. Thereby, we have neglected any phase-mismatch and temporal walk-off between THz, fundamental and second-harmonic pulses. This results in an effective filament length, which combines the effects of real filament length, optical depth of focus and phase-matching length (see [270], for example).

The solid line in Fig. 4.26a shows a best fit of our model to the data. The effective filament length has been estimated to 25 mm, which is only one-third of the total filament length. This shows that a large portion of the generated THz signal is actually lost in the conventional imaging setup. Apart from the limited depth of view of the optical setup, the limiting factors are mainly temporal walk-off of the pump pulses and strong diffraction of the emitted radiation. As typical filament diameters are on the order of a hundred micrometers [265], the generated THz radiation is emitted in a large solid angle and the detected signal is finally aperture limited. This is expressed by the fact that the model calculation shown in Fig. 4.26a does not change for beam waists below $\approx 200 \mu\text{m}$. Based on the excellent agreement with the experimental data, we conclude that the proposed model correctly describes the origin of the measured beam profiles.

In the case with the waveguide installed, as shown in Fig. 4.26b, we have found a best match for a single emission spot, i.e. $L_{\text{fil}} = 0$, and an initial beam waist of 1.8 mm. The latter corresponds roughly to the used plate separation and the slight discrepancy might be related to the exact shape of

the field distribution of the guided mode. From $L_{\text{fil}} = 0$, we conclude that the waveguide successfully changed the emission characteristics from a line source to a point-like emitter.

Finally, we have estimated the detected pulse energy in both cases by temporally integrating over the transient squared (including the water vapor free induction decay). Without the waveguide, we have measured the beam waist to be around $150\ \mu\text{m}$, leading to a pulse energy of approximately $9\ \text{pJ}$. The beam waist in the case with SWG is approximately $320\ \mu\text{m}$, despite the fact that the detected peak field is larger by 40%. The pulse energy in this case is calculated to $38\ \text{pJ}$. Thus, the waveguide efficiently increases the detected pulse energy by a factor 4.3.

In summary, we have found a significant increase in both the detected pulse energy and peak field emitted from a long filament under weak focusing conditions by using a slot waveguide. However, the achieved peak field strength is still a factor of four lower than what has been achieved under the strong focusing conditions without waveguide (see preceding chapter).

4.7 Comparison of Methods

The general aim of the preceding chapters has been the generation of broadband THz pulses with as high as possible peak field strengths. To reach this ambitious goal, various different approaches for the generation of high field THz pulses have been investigated. These included THz emission based on coherent plasma oscillations, optical rectification in large area crystals, photoconductive antenna arrays and four-wave mixing in dual-color laser filaments.

All presented methods have shown a bandwidth in excess of $5.5\ \text{THz}$, which has been mainly limited by the used detector crystal. The highest bandwidth has been achieved with the two-color laser induced filament, which extended up to $8\ \text{THz}$ (under hard focusing conditions).

All methods, except the plasma emitter, reached a maximum SNR of almost 1:1000. The low SNR of 1:200 in the case of the two-color filament is due to the highly nonlinear processes involved in the filament formation and THz emission, which amplifies the pulse-to-pulse fluctuations of the pump pulse energy. The surface plasmon emitter reached the highest SNR at $4\ \text{THz}$ (1:100), closely followed by the large area GaP crystal. The THz spectrum generated by the photoconductive antenna array showed the typical shape of any GaAs based PCA emitter. Thus, the use of the PCA array is limited to frequencies below approximately $2\ \text{THz}$.

The highest pulse energy has been achieved with the PCA array ($3\ \text{nJ}$), followed closely by the GaP emitter ($0.3\ \text{nJ}$). Both methods thereby achieved a similar peak field strength of almost $40\ \text{kV/cm}$. Thus, by improved imaging of the antenna emission onto the detector, even higher field strengths should be

obtainable.

In the case of the two-color filament, the achieved peak field strengths have been much lower than what has been expected based on reports from other groups (see for instance [266, 268]). We attribute this discrepancy mainly to differences in the used pump pulse lengths. Using 35 fs pulses instead of 100 fs would yield at least a four times enhancement in the THz peak field (compare to Fig. 4.22a).

The field strength obtained from the surface plasmon emitters has been limited to below 5 kV/cm. However, the broad frequency content and the high SNR make this type of emitter an excellent choice for generating THz probe pulses in a THz pump / THz probe configuration.

Based on the simplicity of the experimental setup accompanied by an excellent SNR and a high peak field amplitude, the large area GaP crystal has been chosen as the workhorse for further nonlinear experiments. Especially the high stability of the emitted radiation and the Gaussian beam profile make it attractive for high power THz spectroscopy of intersubband excitations in semiconductors. First results on THz induced non-equilibrium dynamics in rectangular QWs are subject to the following chapter.

Chapter 5

Nonlinear THz Spectroscopy of Intersubband Transitions

The following chapter is devoted to the study of coherent dynamics of intersubband transitions subject to intense few-cycle THz pulses. Rabi oscillations, the periodic exchange of energy between a two-level system and an electromagnetic radiation field, are probably the most prominent example of coherent dynamics in quantum systems [296]. However, the ideal two-level atom, in general, represents a too simplified model of real world solid state systems. To study light-matter interactions beyond textbook models, QWs provide the ideal experimental test bed, as the number of subbands, their energy spacing and the transition dipole moments can be engineered at the growth stage [40] (see also Chap. 3.1).

The use of ultra short pulses allows time-resolved spectroscopy on picosecond time scales and the observation of coherence phenomena despite the short dephasing times usually found in solid state systems [211]. However, this requires a solid theoretical description that goes beyond the commonly made approximations, such as the slowly-varying envelope approximation (SVE) and the rotating wave approximation (RWA) [89]. In addition, the large bandwidth of single-cycle THz pulses can be used to couple adjacent QW levels, which allows to study quantum interference phenomena [297], or to coherently control ISBTs [147, 298, 299].

The spectroscopy of ISB excitations in quantum wells subject to intense THz radiation has been mainly based on optical probing of intraband transitions [300–303], or has been limited to the mid-infrared spectral region [147, 202, 297, 304]. Thereby, most THz experiments have been conducted using narrowband radiation from free-electron lasers delivering THz powers on the order of several kW. In the following, we present, to our knowledge, the first results on direct measurements of the complex dynamics of ISBTs subject to intense single-cycle THz pulses. Due to the complicated nature of the underlying processes, we can give only a qualitative discussion on a few dominant effects. Part of the results

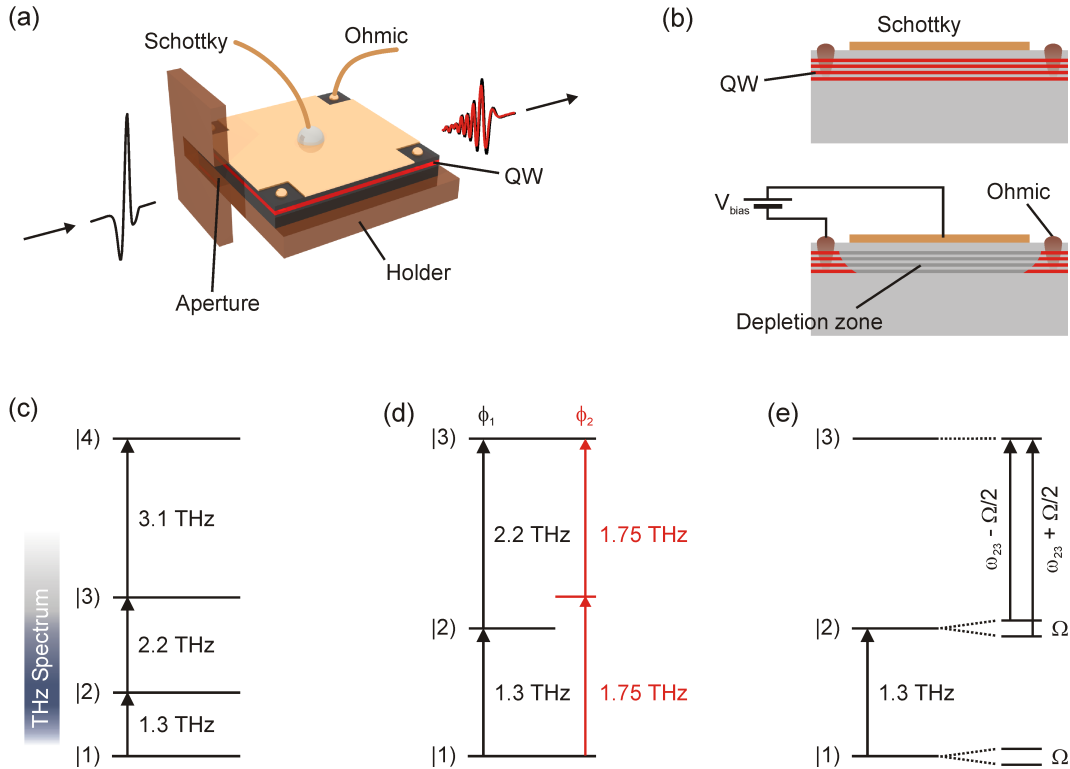


Figure 5.1: Scheme of the experiment. (a) The multiple QW sample is mounted on a copper holder with a narrow aperture to block any bypassing THz light. (b) The QWs can be depleted by applying a negative bias voltage to the Schottky gate. (c) The four lowest energy levels of the QW. At 5 K all electrons are in the ground state. The THz spectrum peaks around the first transition and extends up to the second excited level. (d) Direct single photon transitions to the second excited level are dipole forbidden, but there are two distinct two-photon transitions possible, which might lead to interference phenomena due to different accumulated phases ϕ_1 and ϕ_2 . (e) Strong driving of the primary transition leads to a level splitting, which can be probed by the $|2\rangle \rightarrow |3\rangle$ transition. Adopted from [305].

presented in the following have also been submitted to Nat. Photonics (2012).

5.1 First Experimental Results

Figure 5.1a shows a sketch of the experiment. Intense single-cycle THz pulses are tightly focused onto the facet of a 5 mm long multiple QW sample (UKQW, see Appx. A) which is mounted on a copper holder with a $500 \mu\text{m} \times 5 \text{mm}$ aperture to block any bypassing THz light. The substrate is thereby used as a dielectric waveguide for the THz pulses, which are polarized parallel to the growth direction of the heterostructure in order to fulfill the optical selection rules. The sample is held in a flow cryostat with silicon windows and is cooled

to 5 K during the measurements.

The THz pulses are generated by dynamically phase matched optical rectification in a large area (110)-cut GaP crystal [252]. The electric peak field strength incident on the sample is estimated to 20 kV/cm for an optical pump energy of 3.3 mJ. The spectrum peaks around 1.3 THz and extends up to 5.5 THz. The details of the generation process are given in Chap. 4.4. The transmitted signal is finally detected using electro-optic sampling based on a 300 μm thick (110) GaAs crystal. After transmission through the sample, the THz peak amplitude is about 10% of the incident peak field. This is due to significant dispersion in the GaAs waveguide in addition to distorted imaging of the end facet to the detector crystal¹.

The QWs are directly contacted by Ge/Au Ohmic contacts. On the surface, an aluminum Schottky contact has been fabricated by physical vapor deposition. Thus, by applying a negative bias voltage of -10 V to the Schottky gate, the electrons are pushed out of the area underneath the top contact (see Fig. 5.1b). This allows electrical modulation of the electron density and yields a selective way of measuring the ISB polarization (see also Chap. 3.1). In the experiment, the electron density is modulated by applying a 500 Hz square signal to the sample, which is phase locked to the 1 kHz trigger signal from the regenerative amplifier. The detection electronics stores both transients, depleted and non-depleted, simultaneously. This allows to directly calculate the modulation signal induced by the intersubband polarization via:

$$\Delta E = E_{\text{sig}} - E_{\text{ref}}, \quad (5.1)$$

where E_{ref} denotes the transmission signal through the depleted sample and E_{sig} the transmission through the non-depleted sample, respectively. The achieved modulation signal is almost 12% of the transmitted reference field with a SNR of about 1:100.

The sample itself consists of ten symmetrically modulation doped, 52 nm wide GaAs QWs separated by 160 nm thick $\text{Al}_{0.3}\text{Ga}_{0.7}\text{As}$ barriers grown on a semi-insulating GaAs wafer. From capacitance-voltage measurements, the average sheet density in the wells has been determined to $n_{2d} = 2.55 \times 10^{10} \text{ cm}^{-2}$ at a sample temperature of 5 K [306]. From the ten wells, only seven are actually contacted and can be depleted. Figure 5.1c shows the theoretical level structure obtained using the transfer matrix method (see Chap. 3.1). The calculated transition frequencies are not corrected for the depolarization shift, which becomes quite important in rectangular QWs at THz frequencies [40]. Using the above carrier density, Eq. (3.16) yields the corrected transition frequencies $\tilde{\omega}_{12} = 2\pi \times 1.56 \text{ THz}$, $\tilde{\omega}_{23} = 2\pi \times 2.44 \text{ THz}$, and $\tilde{\omega}_{34} = 2\pi \times 3.31 \text{ THz}$. The blue bar indicates the extend of the THz spectrum. At 5 K all electrons can be

¹The emission spot is offset by 5 mm from the original focus position, and the metallic holder extends another few mm behind the sample, which leads to an asymmetric far field pattern.

assumed to be in the ground state. Therefore, only the fundamental transition $|1\rangle \rightarrow |2\rangle$ is directly possible, which coincides with the peak of the driving spectrum.

The second excited level $|3\rangle$ can be populated only via two one-photon transitions over the first excited state, or via a two-photon transition over a virtual state (see Fig. 5.1d). The accumulated phase of the electron wavefunction of the second excited level is different for the two coherent paths, which can lead to quantum interference phenomena reminiscent of electromagnetically induced transparency [297]. The peak of the pump spectrum coincides with the first transition from the ground state to the first excited state. For high enough THz field strengths we expect a dressing of the involved energy levels due to Rabi oscillations (see Fig. 5.1e). In the frequency domain, this dressing manifests itself as level splitting, which can be probed via the (weakly driven) $|2\rangle \rightarrow |3\rangle$ transition. This is known as the Autler-Townes effect² [307]. The level splitting also leads to the occurrence of sidebands on the strongly driven transition, the so-called Mollow triplet³ [308].

The occurrence of these coherent effects is thereby strongly dependent on the electric field amplitude of the THz driving pulse. Figure 5.2 shows the measured modulation signal, ΔE , for different values of the pump power incident on the GaP crystal. For the chosen experimental parameters, the THz peak field scales almost linearly with the optical pulse energy (see Chap. 4.4). At the lowest pump energy of $125\ \mu\text{J}$, shown in Fig. 5.2a, the THz peak field incident on the sample is estimated to be $0.8\ \text{kV/cm}$. The modulation signal consists of two parts, a leading pulse (yellow area) followed by a damped, almost monochromatic oscillation. The first part consist of the coherently driven response of the QW as the electrons essentially try to follow the incident electric field, while the second part represents the free induction decay of the ISB polarization [200]. From a fit of a damped sinus to the free induction decay part (not shown), we could extract a center frequency of $1.5\ \text{THz}$ and a dephasing time of $2.3\ \text{ps}$. The latter corresponds to a FWHM linewidth of $0.14\ \text{THz}$ and is in good agreement with the modulation spectrum obtained by Fourier transformation (shown in Fig. 5.2b). Thus, for weak driving, the multiple QW behaves as a two-level system. The measured transition frequency fits to the calculated frequency corrected for the depolarization shift, as is expected in square wells.

When the THz electric field amplitude is increased, there is a gradual appearance of a beating pattern, indicated by the black arrows in Fig. 5.2c. The data has been taken for $750\ \mu\text{J}$ pump pulse energy corresponding to $4.5\ \text{kV/cm}$ incident electric field. This beating is a clear indication for a second frequency component in the spectrum. We attribute this to an increased occupation of the first excited level, which *activates* the next higher transition

²Named after Stanley H. Autler (1922-1991) and Charles H. Townes (born 1915).

³Named after Benjamin Mollow.

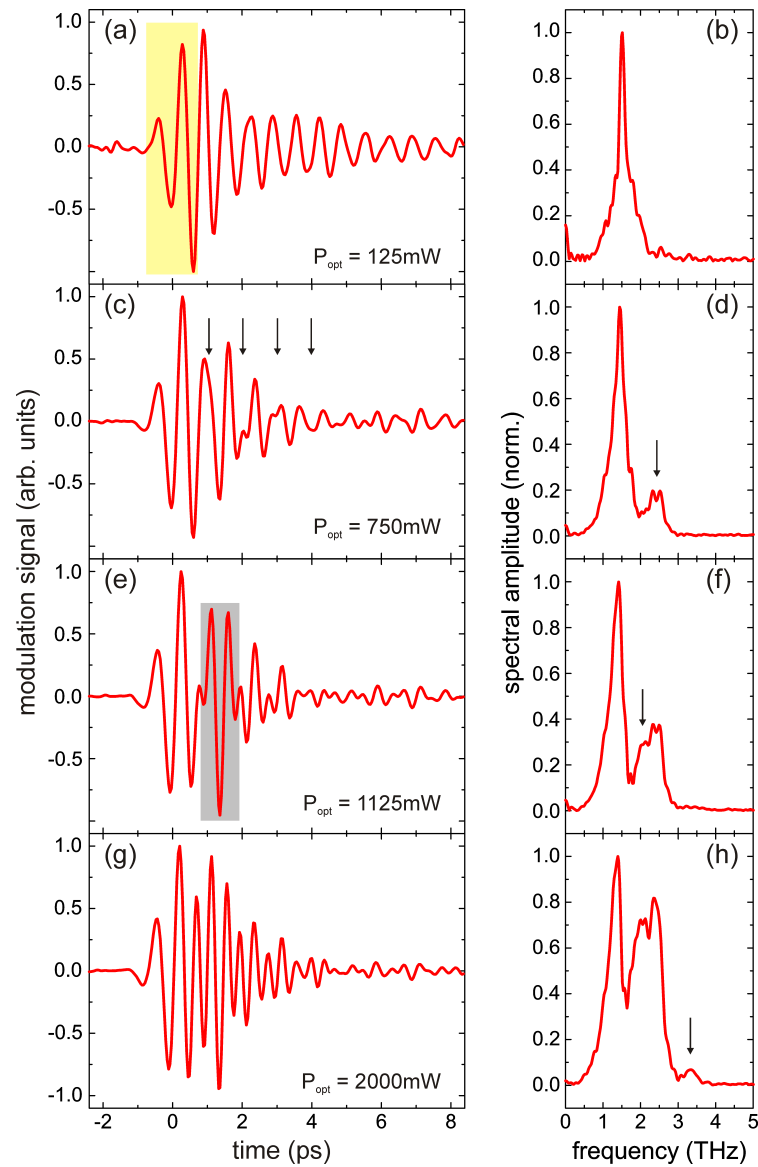


Figure 5.2: Modulation signal obtained for different THz pulse energies. (a) Modulation signal in the time domain for 125 mW of optical pump power. The signal consists of the free induction decay of the QW system and a residual part of the driving pulse due to refractive index changes (yellow area). (b) Spectrum associated to Fig. 5.2a. (c) Same as Fig. 5.2a for 750 mW. There is a beating indicated by the black arrows. (d) Spectrum associated to Fig. 5.2c. There appears a second peak (black arrow). (e) Same as Fig. 5.2a for 1125 mW. The free induction decay acquires a pulse-like structure (gray area). (f) Spectrum associated to Fig. 5.2e. There appears a broad feature between the two distinct peaks (black arrow). (g) Same as Fig. 5.2a for 2000 mW. The signal contains higher frequencies. (h) Spectrum associated to Fig. 5.2g. A third peak appears (black arrow). Partly adopted from [305].

$|2\rangle \rightarrow |3\rangle$. In addition, the decay of the modulation signal becomes faster, which indicates an additional loss mechanism compared to the two-level case. The shape of the beating suggests that the two frequency components have different decay times, whereby the second frequency probably decays faster. In the modulation spectrum, shown in Fig. 5.2d, a second peak appears around 2.4 THz (indicated by black arrow), which corresponds to the depolarization shifted value of the $|2\rangle \rightarrow |3\rangle$ transition frequency. The peak appears to be splitted into a doublet, which might be a first sign of the Autler-Townes effect. The first transition peak is broadened compared to the weakly driven case. This is either due to an additional loss channel or an indication of the appearance of the Mollow triplet [308].

Around 1125 mW of optical pump power (6.8 kV/cm), shown in Fig. 5.2e, the beat pattern gets more pronounced and resembles the photon echoes produced by the free-induction decay in water molecules, for example [4]. This pulse-like structure is an indication for a broadened modulation spectrum which contains many frequency components. In the Fourier domain, these additional frequencies appear as a broad feature between the first and second transition (indicated by black arrow). The $|1\rangle \rightarrow |2\rangle$ peak becomes asymmetric with the wing facing the broad feature being steeper. This asymmetric line shape is a signature of a Fano resonance⁴, which involves interference between a discrete transition and a continuum [309]. Similar signatures are obtained from the interference of an ISBT with the ponderomotive current induced by an in-plane electric field component [310]. In the present configuration, however, the ponderomotive current does not play a role as the electric field is perpendicular to the QW plane. The microscopic origin of this broad feature will be discussed below in more detail.

Figure 5.2g shows the modulation signal for an optical pump energy of 2 mJ corresponding to an incident peak field strength of approximately 12 kV/cm. Both the oscillation period and the decay time are faster than in the previous cases. The modulation spectrum shows the appearance of a third peak centered around 3.3 THz (indicated by black arrow in Fig. 5.2h). This peak can be associated to the $|3\rangle \rightarrow |4\rangle$ transition, as the frequency fits to the calculated value including the depolarization shift. The appearance of this transition requires a significant electronic population in the second excited state. As the sample is held at 5 K, the population transfer is solely accredited to the strong THz pulse and, thus, has to take place within the pulse duration. From the modulation transient, we know that the dephasing times of the ISBTs are longer than the THz pulse length. Hence, the population transfer is a coherent process similar to the Rabi oscillation in a two-level system. We conclude that the broad band THz pulse creates a phase-locked population in all (accessible) energy levels of the QW. The population transfer will be treated below in more

⁴Named after Ugo Fano (1912-2001).

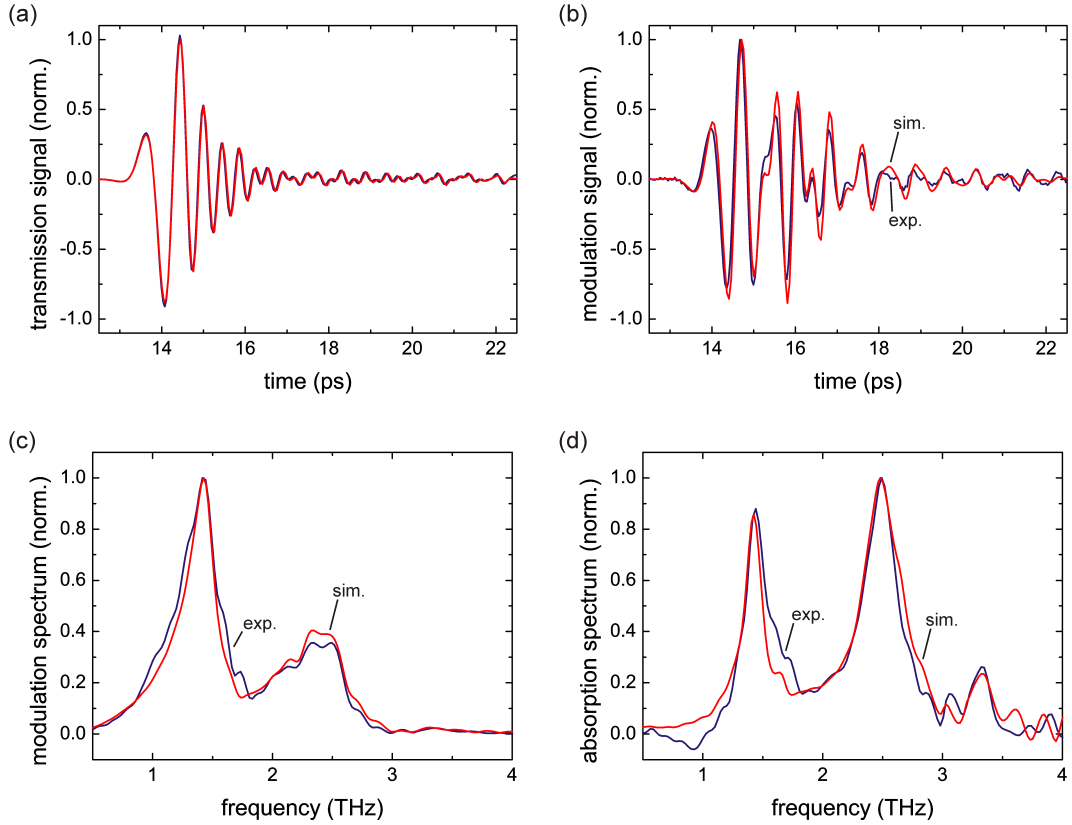


Figure 5.3: Comparison of measured (blue) and simulated (red) data. The measured data has been obtained with $P_{\text{opt}} = 1000 \text{ mW}$. (a) The THz pulse transmitted through the depleted sample has been used as input for the FDTD code. (b) Modulation signal in the time domain. (c) Modulation spectra. (d) Absorption spectra.

detail. Finally, we note the appearance of a sharp minimum between the broad feature and the second transition peak. In combination with the asymmetric line shape of this peak, this is a signature of a second Fano resonance.

5.2 One-Dimensional FDTD Simulations of Multi-Level QWs

In order to get a rough understanding of the multitude of effects taking place in the strongly driven QW system, we attempted a theoretical description in terms of the Maxwell-Bloch equations for multilevel systems [89]. The equations present an extension of the two-level Maxwell-Bloch model treated in Chap. 3.5 and Appx. D.2. To simulate the complex interaction of the incident few-cycle THz pulse with the extended sample, we combined the multilevel Maxwell-Bloch equations with a one-dimensional FDTD code [167].

The QW sample is simulated as a homogeneous slab embedded in vacuum, whereby the semiconductor substrate is included as a lossless dielectric with a constant refractive index $n = 3.6$. The computational space is bounded by Engquist-Majda ABCs, which are exact in 1d [169, 170]. The spatial grid size is chosen as $\Delta z = 1 \mu\text{m}$, which ensures a resolution of at least 10 grid cells per wavelength. The details of the finite difference implementation of the Maxwell-Bloch equations are given in Appx. D.3. The treatment is based on a single-electron picture, i.e. collective effects such as the depolarization shift are not included. In addition, the electron momentum is neglected since the electric field is oriented perpendicular to the quantum well plane and the subband dispersion is assumed to be parabolic. Thus, our model does not include a ponderomotive in-plane current [310].

The dispersion, the THz pulse experiences upon transmission through the waveguide, is taken into account by using the transient transmitted through the depleted sample as input waveform for the FDTD simulation (similar to Ref. [299]). The waveform obtained for an optical pump energy of 1 mJ is shown in Fig. 5.3a. We have applied a window function to the experimental data to reduce the noise introduced by an abrupt switch on of the electric field at the beginning of the simulation. This particular pump power has been chosen as it represents an intermediate driving strength with the free induction decay already showing contributions from all three ISBTs.

By iteratively changing the QW parameters for the simulation, we could obtain an excellent agreement between the experimental data and the simulation results, as is shown in Figs. 5.3b to 5.3d. For the simulation, the transition dipole moments have been taken from the transfer matrix calculations of the wavefunctions: $\mu_{12} = 9 \text{ nm}$, $\mu_{23} = 10 \text{ nm}$, and $\mu_{34} = 11 \text{ nm}$, respectively. The transition frequencies have been determined as $\nu_{12} = 1.44 \text{ THz}$, $\nu_{23} = 2.49 \text{ THz}$, and $\nu_{34} = 3.31 \text{ THz}$. The best correspondence between the simulated and measured FWHM linewidths and relative amplitudes of the absorption peaks has been obtained for the following dephasing times and population decay rates: $\tau_{12} = 2 \text{ ps}$, $\tau_{23} = 1 \text{ ps}$, $\tau_{34} = 1.3 \text{ ps}$, and $\Gamma_{13} = 3 \times 10^{11} \text{ s}^{-1}$. The population decay rate describes the (possibly non-radiative) transfer of population from the upper to the lower level. Its main effect is to reduce the relative amplitude of the absorption line associated to the $|3\rangle \rightarrow |4\rangle$ transition. The excellent agreement shows that our simple model captures the essential physics, and we will discuss some aspects of this complicated light-matter interaction in the remainder of this chapter.

For the following simulations, we have chosen to rather use a model pulse, that imitates the experimental transient, than the experimental data itself. In this way, we get rid of noise that is always present in the experiment. The input pulse of Fig. 5.3a could be best approximated using

$$E_{\text{THz}}(t) = E_0 \cos(\omega_0 t + ct^2 + \phi_0) e^{-(4 \ln 2)t^2/\Delta t^2}, \quad (5.2)$$

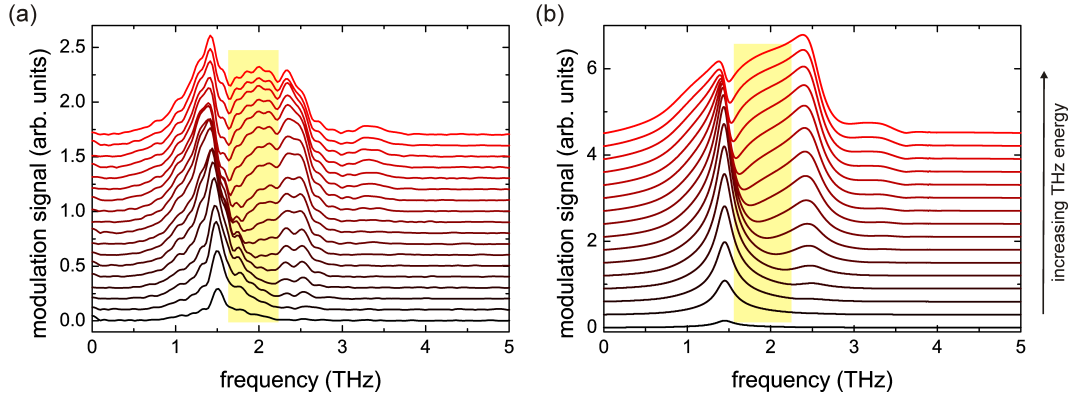


Figure 5.4: Measured (a) and simulated (b) modulation spectra for different THz pulse energies. The simulation reproduces the broad feature between the first and second transition (yellow area). Partly adopted from [305].

with E_0 being the peak amplitude, $\omega_0 = 2\pi \times 1.35$ THz the center frequency, $c = 3 \times 10^{24} \text{ s}^{-2}$ the linear chirp, $\phi_0 = -1.3$ the phase offset, and $\Delta t = 1.8$ ps the FWHM pulse length.

5.3 Nonlinear Refractive Index in a Three-Level System

Figure 5.4 shows the measured and simulated modulation spectra for increasing values of the THz pulse energy. In the experiment, the optical pump power has been varied from $125 \mu\text{J}$ to 3.3 mJ , while, in the simulation, the peak amplitude E_0 incident on the sample has been varied from 0.1 kV/cm to 6.1 kV/cm . From the good correlation between the two datasets, we conclude that the effective electric field interacting with the QWs inside the sample lies between approximately 0.1 kV/cm and 2.7 kV/cm ⁵.

As can be seen from Fig. 5.4, the FDTD simulations reproduce the power dependent appearance of the three ISBTs and, especially, reproduce the broad feature between the first and second transition peak (indicated by yellow area). Thus, the ponderomotive current can be eliminated as physical origin of the continuum leading to the observed Fano resonances as it is explicitly excluded from the model. Furthermore, no electronic transition apart from the QW ISBTs does play a role since this broad feature is absent in the absorption spectra [310] (see Fig. 5.6).

⁵These values have been derived using the Fresnel transmission coefficient of the vacuum-GaAs interface. The electric field in the simulation is related to the field which has an actual overlap with the electronic wavefunctions of the multiple QW sample and does not necessarily coincide with the real peak amplitude in the GaAs waveguide.

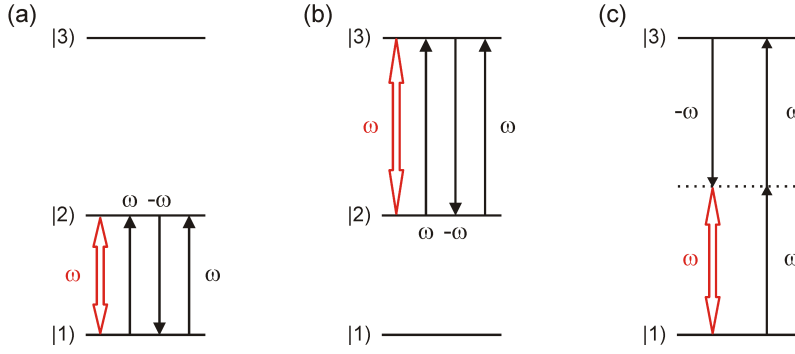


Figure 5.5: Energy level diagram of four-wave mixing processes in a three level system. The red arrow indicates the frequency of the resulting polarization. (a) Four-wave mixing by saturation-type nonlinearity on the $|1\rangle \rightarrow |2\rangle$ transition. (b) Same for the $|2\rangle \rightarrow |3\rangle$ transition. (c) Two-photon absorption nonlinearity associated to the $|1\rangle \rightarrow |3\rangle$ transition.

Therefore, it has to be related to a coherent modification of the refractive index, caused, for example, by self- or cross-phase modulation. Figure 5.5 summarizes the possible contributions to this nonlinear refractive index modification in a three-level QW. The dominant contribution comes from a one-photon resonant driving of two adjacent levels of the QW, as shown in Figs. 5.5a and 5.5b. This process is often described by $\chi^{(3)}(\omega; \omega, -\omega, \omega)$ to emphasize its triply resonant nature. The nonlinearity stems in this case from the saturation of the two-level absorption, which is why it is also called saturation-type nonlinearity [63]. This results in a modification of the refractive index in the vicinity of the (one-photon) transition frequencies $\tilde{\omega}_{12}$ and $\tilde{\omega}_{23}$, respectively. As a consequence, the modulation signal shows a pedestal around the ISBT peaks, as seen in Fig. 5.4a, which is absent in the absorption spectra (shown in Fig. 5.6a).

In addition to the saturation-type nonlinear refractive index, there is a two-photon absorption nonlinearity as sketched in Fig. 5.5c. This four-wave mixing process, denoted by $\chi^{(3)}(\omega; -\omega, \omega, \omega)$, is resonantly enhanced for frequencies close to or less than half the ISBT frequency ω_{13} [311]. Due to the parity selection rules, this two-photon nonlinearity is restricted to the $|1\rangle \rightarrow |3\rangle$ transition and cannot be observed for the other two transitions. Furthermore, there is a connected parametric interaction of the type $\chi^{(3)}(\omega_a; -\omega_b, \omega, \omega)$, which describes cross-phase modulation between weak optical fields of frequencies ω_a and ω_b provided that $\omega_a + \omega_b \approx 2\omega$ [312]. Hence, the spectral width of the nonlinearity associated to the two-photon absorption is sufficient to explain the large bandwidth of the observed feature.

In the simulation, the two-photon resonance should appear around $\omega_{2\gamma} = 2\pi \times 1.95$ THz, which agrees with the center frequency of the broad feature as shown in Fig. 5.4b. As has been mentioned earlier, the simulation is based on

a one-electron picture and thus neglects the effect of the depolarization shift on the ISBT frequencies. Using the bare ISBT frequencies for ω_{12} and ω_{23} , the two-photon resonance in the experiment should appear centered around $\omega_{2\gamma} = 2\pi \times 1.75$ THz, or around $\omega_{2\gamma} = 2\pi \times 2.0$ THz when the depolarization shift is included. As can be seen from Fig. 5.4a, the position of the broad feature complies with the corrected frequencies, which fits to the results of Heyman *et al.* on ISB second- and third-harmonic generation in QWs [313].

According to Khurgin *et al.* [311], the one-photon saturation-type nonlinearity should completely dominate the nonlinear refractive index and mask any signs of the two-photon absorption nonlinearity. Especially, this should be the case in ordinary rectangular QWs, such as the one we are using in our experiment. To circumvent this issue, they have proposed to use special types of QW structures, where the one-photon resonance cannot interfere with the two-photon transition [311]. One possible explanation, why we can see signatures of the two-photon absorption nonlinearity in rectangular QWs, is based on the fact that the saturation-type nonlinearity suffers from huge absorption losses, which limits the achievable nonlinearity [311]. In contrast, there is no linear absorption associated with the two-photon nonlinearity, why its amplitude does barely saturate with higher driving fields. For strong enough driving fields, the two-photon nonlinear refractive index will eventually dominate the spectrum (at least far from the ISBT frequencies).

5.4 Collective ISB Excitations and Dressed State Effects

Figure 5.6a shows the measured absorption spectra for different values of the THz pulse energy. The total absorption of the sample has been calculated via [310]:

$$\alpha(\omega) \propto \text{Im} \left(-i \frac{\Delta E(\omega)}{E_{\text{ref}}(\omega)} \right), \quad (5.3)$$

which is valid for the single-pass transmission under the assumption that $|\Delta E(\omega)| \ll |E_{\text{ref}}(\omega)|$ and the substrate is non-absorbing⁶. Part of the spectra is shaded in gray and is excluded from the discussion due to the insufficient SNR in this frequency range. The spectra are comprised of the three allowed ISBTs, $|1\rangle \rightarrow |2\rangle$, $|2\rangle \rightarrow |3\rangle$, and $|3\rangle \rightarrow |4\rangle$ without any sign of additional absorption processes, such as due to the two-photon transition $|1\rangle \rightarrow |3\rangle$. As has been mentioned earlier, the broad feature associated to the nonlinear refractive index is absent in the absorption spectra. There are three aspects worth noting. First, the absorption peak associated to the $|1\rangle \rightarrow |2\rangle$ transition is shifted to

⁶Under the stated assumptions, this equation is equivalent to $\alpha = -(2/L) \ln(|E_{\text{sig}}|/|E_{\text{ref}}|)$, where the sample length is taken as unity, $L \equiv 1$ (see for example [314]).

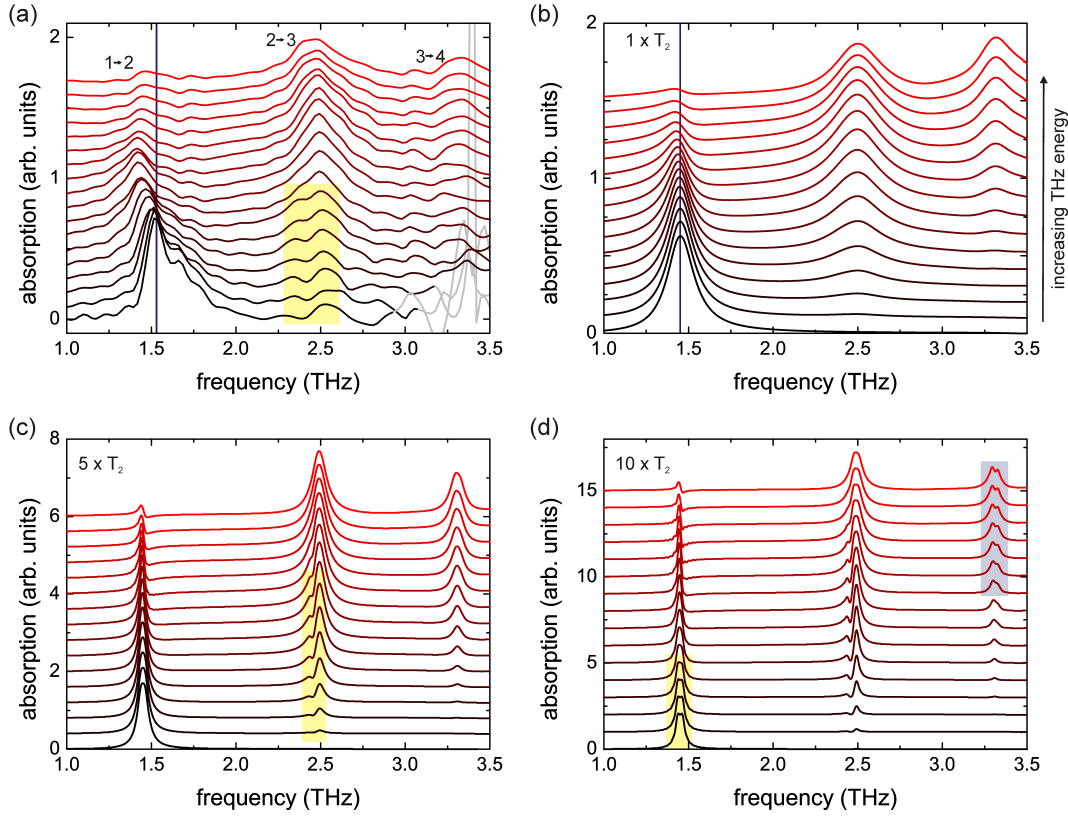


Figure 5.6: (a) Measured absorption spectrum for different THz pulse energies showing the three lowest ISBTs. The first absorption peak is red-shifted for higher driving fields (blue line). The second transition appears as a doublet for lower pump powers (yellow area). The curves are offset for clarity. Part of the spectra is shaded in gray due to the limited SNR. Adopted from [305]. (b) Simulated absorption spectrum for dephasing times extracted from Fig. 5.3. The red-shift of the first transition is absent (blue line). (c) Same for five times longer dephasing times. The second absorption peak shows a splitting for lower THz energies (yellow area). (d) Same for ten times longer dephasing times. In addition to the second absorption peak, both the first and third transition show a splitting (yellow and gray areas).

lower frequencies for higher pump powers (indicated by blue line). Second, the $|2\rangle \rightarrow |3\rangle$ absorption peak seems to be splitted for lower pump energies (yellow area). The splitting then disappears for THz fields above ≈ 6 kV/cm incident on the sample. And third, the relative amplitudes of the three absorption peaks vary with the incident THz field strength.

Figure 5.6b shows simulated absorption spectra with the dephasing parameters as derived using the iterative procedure discussed above (see Fig. 5.3). The center frequency of the first absorption peak is thereby independent of the incident THz field. This indicates that the experimentally observed redshift has to be attributed to a collective effect of the two-dimensional electron gas, which cannot be described in the single electron picture used in the FDTD

simulations. This effect has first been predicted in 1993 by Załuźny [315], and is related to an undressing of the collective ISB excitation which is causing the depolarization shift of the bare ISBT frequencies (see Chap. 3.1). According to theory, the depolarization shift is proportional to the population difference in the participating energy levels, $N_1 - N_2$ [316]. Thus, an intuitive explanation for the observed redshift is based on the transfer of population from the ground state to higher lying states. The experimental observation has till now been possible only using intense THz radiation from free-electron lasers with peak powers of 1 kW and several μs long pulses [317,318]. These high intensities have been necessary to transfer sufficient electrons to the excited state. The fact that we can observe the undressing of the collective excitation with comparatively weak THz pulses is a further indication for the coherent transfer of population within the pulse duration (see above).

Another signature for coherent driving is the observed frequency splitting of the $|2\rangle \rightarrow |3\rangle$ transition (yellow area in Fig. 5.6a). According to the level scheme shown in Fig. 5.1e, this splitting would be a consequence of the dressing of the $|1\rangle \rightarrow |2\rangle$ transition under intense THz irradiation. The frequency splitting of the dressed states is given by the generalized Rabi frequency [319]

$$\Omega = \sqrt{\Omega_{12} + \Delta}, \quad (5.4)$$

where Ω_{12} is the on-resonance Rabi frequency and Δ the detuning between the driving field and the transition frequency. The experimental observation of the Autler-Townes effect is in general based on nearly monochromatic pump fields, which lead to a well defined energy separation of the dressed states (see for example [297,302,303]). Thus, one important issue to clarify is whether the observation of these coherence effects is possible with broadband THz pulses, as are used in our experiment.

In regard of the quality of the data it is difficult to clearly identify the Autler-Townes effect and we can only give qualitative arguments. In addition, the disappearance of the level splitting for higher driving fields is counterintuitive, and, despite the fact that the dressing of the states is included in the Maxwell-Bloch model, the splitting cannot be observed in the simulated absorption spectra shown in Fig. 5.6b. These issues will be addressed shortly in the following.

As has been discussed above, the dephasing parameters have been derived from the data obtained at 1 mJ optical pump power, thereby assuming the dephasing to be power-independent. From a comparison of the linewidths of the first transition for low pump energies, however, it seems as if the values used in the simulations would overestimate the dephasing for low pump powers. Therefore, we have conducted FDTD simulations for five and ten times lower dephasing rates. The results are shown in Figs. 5.6c and 5.6d, respectively. For five times longer coherence times, the absorption peak of the $|2\rangle \rightarrow |3\rangle$ transition exhibits a similar doublet structure as in the experiment (yellow

area in Fig. 5.6c). For increasing THz peak fields, the splitting again vanishes. Thus, there is a qualitative agreement between the *idealized* FDTD simulations and our experimental results. For ten times longer coherence times, there appears even a level splitting of the absorption peak associated to the $|3\rangle \rightarrow |4\rangle$ transition (gray area in Fig. 5.6d). The frequency splitting in this case increases with increasing pump energy, as would be expected for the Autler-Townes effect. In addition, the first absorption peak shows a complicated structure, which is probably related to the Mollow triplet (yellow area in Fig. 5.6d). We conclude that the system is capable of showing coherent driving effects for low enough dephasing rates despite the broadband nature of the THz pulse.

Furthermore, the disappearance of the level splitting with increasing THz energies is also present in the simulation (see Fig. 5.6c), where the pure dephasing rate is kept constant. One possible explanation could be additional dephasing induced by power broadening [63]. However, we propose another explanation which is again related to the efficient transfer of population from the ground state to higher lying states. The Rabi frequency, Ω_{12} , in an ensemble of two-level systems, scales as $\Omega_{12} \propto \sqrt{n_{2d}}$, where n_{2d} is the areal density of carriers participating in the coherent superposition of states $|1\rangle$ and $|2\rangle$ [145,319]. In the present system, the electrons have to be shared among all levels. Thus, for increasing THz pulse energy, more and more electrons are excited to higher lying states and are thus no longer available for the Rabi oscillations. As a consequence, the level splitting gradually disappears.

Based on the above arguments, it might be possible that the observed level splitting is indeed a signature for the Autler-Townes effect. However, a clear identification would require a more detailed experimental investigation.

5.5 Quasi-Thermalization between a QW and a Photon Bath

In the discussion so far, the coherent population transfer between the ground and excited states has been mentioned several times. To investigate this aspect further, we have plotted in Fig. 5.7a the absorption strength

$$A_{ij} = \frac{1}{\omega_+ - \omega_-} \int_{\omega_-}^{\omega_+} \alpha(\omega) d\omega, \quad (5.5)$$

averaged over the frequency interval $\omega_- < \omega_{ij} < \omega_+$, versus the THz pulse energy

$$U_{\text{THz}} \propto \int_{-\infty}^{\infty} |E_{\text{ref}}(t)|^2 dt \quad (5.6)$$

normalized to the maximum value appearing in the measurement series. The experimental data is shown as dots.

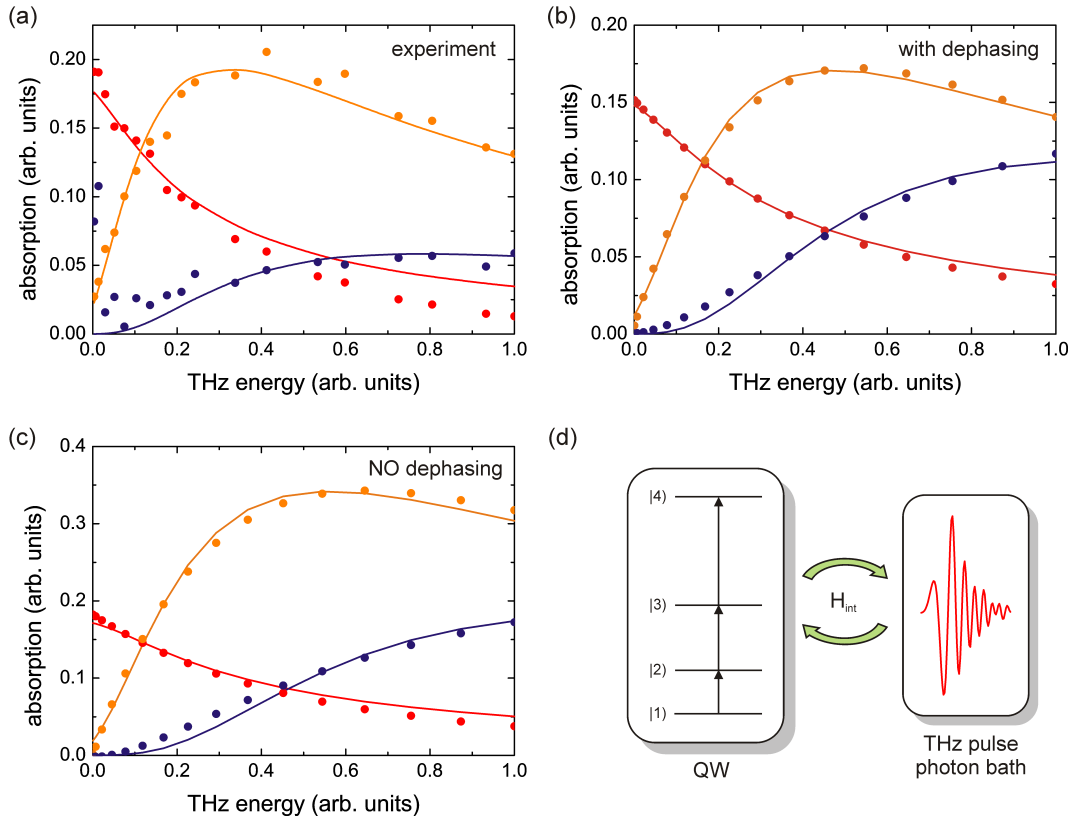


Figure 5.7: Integrated absorption strength of the lowest three transitions as function of the (normalized) THz energy (red = $|1\rangle \rightarrow |2\rangle$, orange = $|2\rangle \rightarrow |3\rangle$, blue = $|3\rangle \rightarrow |4\rangle$). The solid lines are fit results of Eq. (5.7) to the data (dots). (a) Experimental data. (b) FDTD results with dephasing. (c) FDTD results without dephasing. (d) The level occupation may thermalize by energy exchange via the interaction Hamiltonian with a photon bath provided by the broadband THz pulse.

At nearly zero THz energy, only the first transition (red) shows significant absorption, whereas the higher transitions $|2\rangle \rightarrow |3\rangle$ (orange) and $|3\rangle \rightarrow |4\rangle$ (blue) show almost no absorption. As the absorption strength is proportional to the population difference between the upper and the lower energy level (see Chap. 3.1), all electrons can be assumed to be in the ground state when no THz pulse is incident. For increasing pulse energy, the $|1\rangle \rightarrow |2\rangle$ absorption decreases towards zero. The second transition steeply increases and shows a maximum absorption strength around $U_{\text{THz}} \approx 0.3$. For higher pulse energies, the absorption decreases again. The absorption associated to the third transition, $|3\rangle \rightarrow |4\rangle$, sets in much slower and saturates for the highest investigated pulse energies. This behavior is due to the transfer of electrons from the ground state to the higher lying states.

As the relative distribution of the absorption strengths resembles a thermal electron population in the different subbands, we have attempted to fit the

data with an expression of the form

$$\tilde{A}_{ij} = A_{ij}^0 \ln \left(\frac{1 + e^{\hbar\omega_i/k_B T}}{1 + e^{\hbar\omega_j/k_B T}} \right). \quad (5.7)$$

Thereby, A_{ij}^0 is a scaling factor, $\hbar\omega_i$ and $\hbar\omega_j$ are the energies of levels $|i\rangle$ and $|j\rangle$ relative to the ground state and

$$T = aU_{THz} + b \quad (5.8)$$

is the effective electron temperature with a scaling parameter a and an offset b . The latter is essentially the substrate temperature. Equation (5.7) is based on the temperature dependence of the ISB absorption coefficient (3.13) with the Fermi energy set equal to the ground state energy⁷.

For the fitting procedure, we have assumed the energies of the QW levels to be known. Thus, the three absorption curves have been fitted using three independent amplitudes A_{ij}^0 , which take into account the different oscillator strengths, damping rates, etc. and a common parameter set, a and b , for the temperature. There is an excellent agreement between the experimental data and the fit results, which are shown as solid lines in Fig. 5.7a. We found the values $a = 235$ K, and $b = 19$ K. Thus, the electron population for the highest pump energy corresponds to the thermal population obtained for a lattice temperature as high as 255 K. However, this effective temperature is not the real temperature of the sample, as the width of the absorption lines is barely changed for higher pump powers⁸.

To investigate the microscopic origin of this quasi-thermalization of the level occupations, we have performed FDTD simulations with the dephasing parameters derived from the 1 mJ data, shown in Fig. 5.7b, as well as without any dephasing or energy relaxation processes (shown in Fig. 5.7c). In both cases, we observe a similar behavior with almost equal scaling parameters $a = 163$ K (139 K) and $b = 18$ K (16 K) for the case with (without) dephasing⁹. In both cases, the agreement between the fitted model and the data is excellent. Thus, we can safely eliminate elastic and inelastic scattering processes as reason for the observed energy dependence.

A possible explanation is sketched in Fig. 5.7d. The level occupations of the QW system may *thermalize* by exchanging energy with a photon bath, similar to a heat bath. The reservoir is in this case represented by the broadband THz pulse, and the coupling between the two systems is provided by the interaction

⁷The linear dependence on T , however, is omitted, as the number of electrons is conserved in the present experiment.

⁸The linewidth should strongly increase due to enhanced scattering with phonons and hot electrons.

⁹Note that the scaling of the x axis between the experimental and the simulated data is different due to the different energy intervals probed.

Hamiltonian H_{int} (see Chap. 3.1). Within the pulse duration, the electrons in the QW absorb and emit several photons until a kind of equilibrium distribution has been established. Thereby, the frequency distribution in the THz pulse does not have to be thermal, i.e. correspond to a blackbody spectrum. A different spectrum would just lead to different amplitude factors. Rather, the necessary condition is that the pulse duration is longer than the typical timescale for photon absorption and emission, which is set by the Rabi frequency. In the experiment, the pulse duration is shorter than the involved scattering times. Therefore, the occupation thermalization takes place within the decoherence time and results in a fully coherent quasi-thermal electron distribution.

Alternatively, the observed distribution may be a consequence of the coherent driving of the electronic transitions by the few-cycle THz pulse. In this case, the excellent correspondence between the thermal distribution and the observed occupations would be purely coincidental. To clarify which process is the dominating one, a further experimental and theoretical investigation is necessary.

To summarize, we have successfully demonstrated the direct observation of non-equilibrium dynamics of ISBTs subject to intense few-cycle THz pulses. Based on the excellent agreement between one-dimensional FDTD simulations utilizing multi-level Maxwell-Bloch equations, we could identify some of the intriguing effects that are accessible in the experiment. Thereby, the experiment revealed also collective dynamics that are not captured in a one-electron picture. The full treatment of the entire experimental results, however, goes beyond the scope of this thesis. The present study of the complex interaction of ISBT and intense THz pulses is rather intended to open the field for numerous further experiments and theoretical concepts aimed to study and utilize nonlinear light-matter interaction on THz time scales.

Chapter 6

Conclusions

The general aim of this thesis has been the investigation of the interaction of THz radiation with semiconductor heterostructures in a regime that goes beyond the usual linear description.

Two different pathways to reach this ambitious goal have been presented. For the first one we have borrowed concepts from cavity QED. By coupling the quantum wells to a nearby resonator, their radiative properties can be modified in a way that leads to the creation of a new class of light-matter-states very similar to ISB cavity polaritons [145].

The second approach has been based on the extension of a conventional THz TDS setup to use broadband THz pulses with high field strengths. These pulses could then be used directly to induce and probe nonlinear ISB dynamics in QWs on picosecond timescales.

The conclusions of the individual parts of the presented work are given in the following.

6.1 Cavity QED with THz Metamaterials

At the beginning of Chap. 3, the basic optical properties of ISBTs in semiconductor quantum wells have been introduced. Due to the polarization selection rules, electromagnetic radiation can couple to ISBTs only when the electric field is oriented parallel to the growth direction of the QW. This represents a tight constraint on experimental geometries aiming to investigate ISB excitations by free space radiation. Furthermore, many body effects modify the optical response. A single photon does not couple to a single electron, but rather to a collective mode of the two-dimensional electron gas, the ISB plasmon.

In the following, THz MMs have been introduced as an excellent way of coupling (normally incident) free space THz radiation to ISBTs. Thereby, the resonance frequency and Q-factor can almost entirely be determined by the right choice of geometry of the meta-atom. The influence of the most relevant parameters on the optical response of THz MMs has been discussed using the

example of the SRR, which is certainly the most prominent MM building block. Furthermore, by combination with collective excitations of the MM array, the radiative linewidth of dipolar resonances can be significantly reduced. The resonant mode of such a meta-atom can be represented by a localized plasmon showing an exponentially decaying electric field into the substrate, which is polarized perpendicular to the MM plane.

This field component can be used to efficiently couple the localized plasmon resonances of the meta-atoms to the ISB plasmons in the QW underneath the MM layer. The combination of these two concepts has thus enabled a range of intriguing experiments on coupled quantum systems. Using a single parabolic QW and a dSRR geometry, we found a coupling strength that has been sufficient to reach the strong coupling regime. The experimental proof has been a line splitting of the bare MM resonance. By etching away part of the substrate, the effective refractive index of the surrounding medium is changed, which leads to a blue shift of the bare MM resonance frequency. Thus, we could measure the polariton dispersion on the very same sample. By fitting a theoretical model to the data [146], we found a vacuum Rabi frequency of 0.17 THz, which makes almost 8% of the ISBT frequency.

The observed effects are thereby reminiscent of cavity QED with atoms in optical cavities [320], or excitons in dielectric microcavities [321]. The latter has lately been extended to ISB plasmons in metallic microcavities where the interaction strength has been shown to reach the ultrastrong coupling regime [148, 149]. A consequence of the strong interaction of the light in the cavity with the ISB plasmons is the formation of so-called ISB cavity polaritons as a new type of elementary excitation [145]. These polaritons are subject to intense research worldwide as they may enable lasing without inversion and the generation of quantum vacuum radiation in the THz and sub-THz even at room temperature [145, 206].

The system used in our work shows many similarities to the above cavity QED experiments. The photon field in the optical cavity has been replaced by the electromagnetic near-field of the localized plasmons as the fundamental MM excitations. Due to the near field interaction, the MM plasmons couple directly to the ISB plasmons giving rise to a similar Hamiltonian as in the cavity polariton experiments. Thus, we expect the dynamics of our system to be governed by the same physics. This includes also the possibility of emission of quantum vacuum radiation. The planar MM thereby constitutes an ideal way of coupling this radiation to free space in a controlled way.

Thus, triggered by the initial experiments conducted during this thesis, there will be a strong interest in further research in this direction. One intermediate goal will be the time resolved observation of strong coupling in a THz TDS spectrometer. To this end, a special emphasis will have to be paid to the right choice of meta-atom geometry featuring a high Q-factor. Apart from room temperature THz sources, these devices can also be used as efficient spatial

light modulators for pulse shaping and compressive imaging applications. In combination with the high nonlinearities achievable in especially designed QWs, the huge field enhancement in the vicinity of the MM might lead to the realization of THz nonlinear optical elements such as frequency doublers [313], and parametric mixers for heterodyne detection schemes [322].

6.2 High Field THz Time-Domain Spectroscopy

An alternative way to achieve high electric field strengths for spectroscopy has been presented in Chap. 4, where we have introduced the high field THz TDS setup that has been developed during this thesis. The core building block is a regenerative Ti:Sapphire amplifier capable of delivering sub-100 fs pulses with 4 mJ of energy. These amplifiers usually suffer from increased pulse-to-pulse fluctuations of the energy, which leads to signal-to-noise ratios on the order of 1:100 to 1:200. In order to use the setup for spectroscopy of ISBTs in QWs, a key issue has been the improvement of the noise figures.

To this end, the amplifier is seeded from an Er-doped fiber laser, which features two output ports. The two pulses have been derived from the same oscillator pulse and are therefore inherently stable with respect to each other. The second output at 1.56 μm is used for electro-optic detection of the THz pulses, which have been generated using the 780 nm pulses from the amplifier. Due to this separation of pump and probe wavelengths, the influence of stray light is minimized and a background free detection is possible. Furthermore, the all-electronic pulse picking allows to use the full repetition rate of the amplifier, which further increases the achievable SNR by $\sqrt{2}$.

For the generation of the THz pulses, various methods have been investigated. The requirements thereby have been a broad spectrum (> 5 THz) and an as high as possible electric field strength in the focus. During the work, we have also devised several ways of enhancing either the achievable field strength or the bandwidth of known emission concepts.

Area scaling has proven useful to circumvent saturation in all solid state THz emitters. Especially, we could apply this concept successfully to surface plasmon emitters, which constitute one of the first THz sources used for TDS. The achievable peak field strength has been on the order of 5 kV/cm with a large dynamic range even at high frequencies (> 4 THz).

Optical rectification in nonlinear crystals has been known for a long time to be capable of generating very high field strengths. However, phase matching between the optical pump and the THz pulses is a general problem. In this work, we have presented a novel type of phase-matching based on the dynamic modification of the THz refractive index of a large area GaP crystal by the strong pump pulse. This technique allows the use of thicker crystals without loosing bandwidth.

Furthermore, area sectioning has been shown as a technological step enabling the fabrication of large area interdigitated photoconductive antennas with a high yield of functioning devices. The emission spectrum from the antenna has been mainly focused to frequencies below 1 THz. However, this emitter delivered both the highest peak field strength (40 kV/cm) and the highest THz pulse energy (3 nJ).

The use of amplified pulses allows to explore novel techniques for THz generation, which are not possible with oscillator based setups. The most impressive one is the generation of THz radiation using the nonlinearity of ambient air by mixing the optical pump pulse with its second-harmonic in a laser induced filament. We have investigated THz emission both under tight and loose focusing conditions. In the latter regime, the THz yield could be further increased by 40% in terms of detected field and a factor 4.3 in terms of pulse energy by using a THz slot waveguide.

There are essentially two ways to further improve the achievable THz field strengths. The first one is to test different materials with higher nonlinearities. The second one would be to abandon the requirement of a huge bandwidth, thus, enabling the use of specialized techniques, such as quasi-phase matching or narrowband mixing of linearly chirped pulses.

Nevertheless, the achieved pulse parameters in this thesis are already sufficient for nonlinear spectroscopy on QW ISBTs. Due to its ease of use and the excellent stability of the generated THz pulses, the large area GaP crystal has proven the workhorse for this kind of experiments.

6.3 Quantum Optics Toy Box

The experiments presented in Chapter 5 are yet another proof of the fruitful combination of the THz spectral range with semiconductor heterostructures. Using the intense single-cycle THz pulses generated by dynamically phase-matched optical rectification in the large area GaP crystal [252], we have been able to perform THz TDS on ISBTs in a modulation doped multiple QW sample. In combination with a depletion-modulation technique [159], we could selectively measure the induced ISB polarization with an excellent SNR as function of the THz field amplitude of the driving pulse.

The measured THz field dependence of the optical response of the QWs showed intriguing features, which are clear indications of THz induced non-equilibrium dynamics. The main results of our experiments include the undressing of collective excitations and nonlinear wave mixing of the incident THz pulse with the induced ISB polarization. Such effects have been observed so far only with narrowband radiation from free electron lasers [313, 317, 318].

Further results have been the coherent population transfer to higher lying states and a line splitting of the $|2\rangle \rightarrow |3\rangle$ transition reminiscent of the Autler-

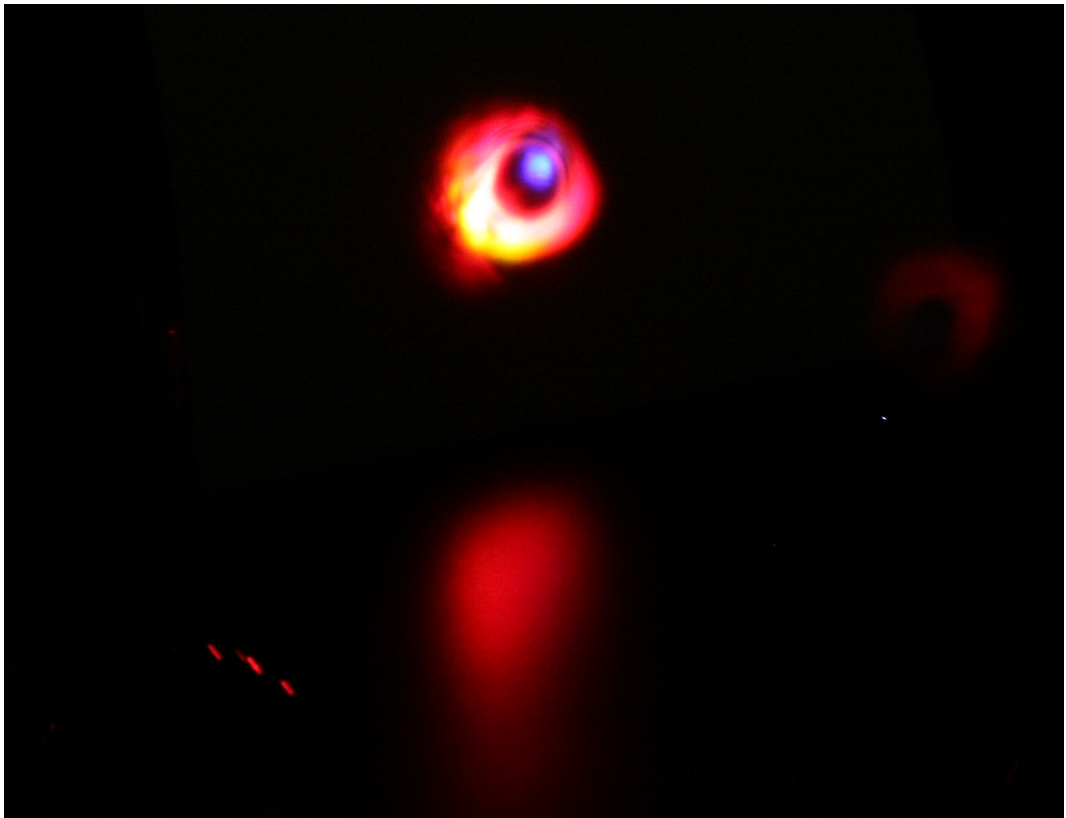
Townes effect [307]. Thereby, the ultrashort duration of the single-cycle pulses has been a key aspect enabling the observation of signatures of quantum coherence despite the fast dephasing times usually found in solid state systems [211].

With the excellent stability and high intensity of the pulses available in the developed THz TDS setup together with the high degree of control over the ISB system, we have an ideal quantum optics toy box at hand, which gives us the unique opportunity to test quantum optics theories beyond the standard textbook models. In combination with beam shaping, for example using THz MMs, coherent control schemes can be tested easily and non-equilibrium states can be created in a controlled way. This allows a detailed study of dephasing and energy loss channels in more complicated heterostructures, such as THz QCLs, and might open a route towards room temperature operation of these devices.

Further applications include the design and testing of parametric frequency converters based on QW nonlinearities for monolithic integration into QCL active regions. This helps to extend the range of frequencies accessible with solid state THz sources and might also serve as a way to increase the gain bandwidth, thereby enabling the mode-locked operation of THz QCLs.

The progress of scientific development is, in effect, a continual flight from wonder.

Albert Einstein



Supercontinuum generation in a short plasma filament.

List of Abbreviations

ABC	absorbing boundary condition
ABCD	air-biased-coherent-detection
ADE	auxiliary differential equation
AFM	atomic-force microscope
ASOPS	asynchronous optical sampling
dSRR	doubly-split-ring resonator
DTGS	deuterated triglycine sulfate
ECOPS	electronically controlled optical sampling
EIT	electromagnetically induced transparency
EOC	electro-optic crystal
EOD	electro-optic detection
FDTD	finite-difference time-domain
FFT	fast Fourier transformation
FIR	far-infrared
FTIR	Fourier transform infrared spectroscopy / spectrometer
FWHM	full width at half maximum
GVM	group velocity mismatch
ISB	intersubband
ISBT	intersubband transition
LO	longitudinal optical
LT-GaAs	low-temperature grown GaAs
MBE	molecular beam epitaxy

MCT	mercury cadmium telluride
MIR	mid-infrared
MM	metamaterial
MP	microscopic polarization
NIR	near-infrared
PBC	periodic boundary condition
PQW	parabolic quantum well
PVD	physical vapor deposition
Q factor	quality factor
QED	quantum electrodynamics
QW	quantum well
RIE	reactive ion etching
rms	root-mean square
RWA	rotating wave approximation
SI-GaAs	semi-insulating GaAs
SNR	signal-to-noise ratio
SRR	split-ring resonator
SVE	slowly-varying envelope approximation
SWG	slot waveguide
TDS	time-domain spectroscopy
THz	terahertz
TO	transverse optical

Appendix A

Growth Sheets

H727 - THz Plasmon Emitter

Layer (substrate → surface)	x (%)	Thickness (Å)	Doping (cm ⁻³)
SI GaAs substrate (100)		≈ 500 μm	
GaAs		20000	1.5 × 10 ¹⁶
LT GaAs @ 230 °C		500	

This sample is a regrowth of G567. Growth is followed by a 10 min in situ annealing step at 600 °C. The substrate diameter is 3".

H728 - THz Plasmon Emitter

Layer (substrate → surface)	x (%)	Thickness (Å)	Doping (cm ⁻³)
SI GaAs substrate (100)		≈ 500 μm	
GaAs		5000	3 × 10 ¹⁸
GaAs		1700	
LT GaAs @ 230 °C		700	

Growth is followed by a 10 min in situ annealing step at 600 °C. The substrate diameter is 3".

G234 - Ten Asymmetric Coupled Quantum Wells

Layer (substrate → surface)	x (%)	Thickness (Å)	Doping (cm ⁻³)
SI GaAs substrate (100)		508 μm ± 20 μm	
GaAs		500	
loop 20x			
AlAs		20	
GaAs		20	
endloop			
GaAs		3000	
AlGaAs	30	2000	
loop 10x			
<i>loop 4x</i>			
AlGaAs	30	5	1 × 10 ¹⁸
AlGaAs	30	10	
<i>end loop</i>			
AlGaAs	30	300	
GaAs		83	
AlGaAs	30	25	
GaAs		95	
AlGaAs	30	300	
<i>loop 4x</i>			
AlGaAs	30	5	1 × 10 ¹⁸
AlGaAs	30	10	
<i>end loop</i>			
end loop			
AlGaAs	30	5	1 × 10 ¹⁸
AlGaAs	30	2000	
GaAs		50	1 × 10 ¹⁵

G318 - Parabolic Quantum Well

Layer (substrate → surface)	x (%)	Thickness (Å)	Doping (cm ⁻³)
SI GaAs substrate (100)		508 μm ± 20 μm	
GaAs		1000	
loop 10x			
AlAs		6	
GaAs		14	
endloop			
AlGaAs	30	2000	
loop 10x			
AlGaAs	30	10	1.2 × 10 ¹⁹
AlGaAs	30	20	
end loop			
AlGaAs	30	300	
PQW GaAs/AlGaAs	0/30	1200	
AlGaAs	30	300	
loop 10x			
AlGaAs	30	10	1.2 × 10 ¹⁹
AlGaAs	30	20	
end loop			
AlGaAs	30	1000	
AlGaAs	30	100	1 × 10 ¹⁸
AlGaAs	30	800	
GaAs		50	

Parabolic quantum well is formed by digital alloying.

G334 - Parabolic Quantum Well

Layer (substrate → surface)	x (%)	Thickness (Å)	Doping (cm ⁻³)
SI GaAs substrate (100)		508 μm ± 20 μm	
GaAs		1000	
loop 50x			
AlAs		6	
GaAs		14	
endloop			
AlGaAs	30	2000	
loop 18x			
AlGaAs	30	10	1.8 × 10 ¹⁹
AlGaAs	30	20	
end loop			
AlGaAs	30	150	
PQW GaAs/AlGaAs	0/30	1400	
AlGaAs	30	150	
loop 18x			
AlGaAs	30	10	1.2 × 10 ¹⁹
AlGaAs	30	20	
end loop			
AlGaAs	30	200	
AlGaAs	30	110	1 × 10 ¹⁸
AlGaAs	30	800	
GaAs		50	

Parabolic quantum well is formed by digital alloying.

G424 - Parabolic Quantum Well

Layer (substrate → surface)	x (%)	Thickness (Å)	Doping (cm ⁻³)
SI GaAs substrate (100)		508 μm ± 20 μm	
GaAs		5000	
loop 50x			
AlAs		6	
GaAs		14	
endloop			
AlGaAs	30	2700	
PQW GaAs/AlGaAs	0/30	1400	
AlGaAs	30	1800	
GaAs		50	

Structure is a regrowth of G334 but undoped. Parabolic quantum well is formed by digital alloying.

UKQW - Multiple Quantum Wells

Layer (substrate → surface)	x (%)	Thickness (Å)	Doping (cm ⁻³)
SI GaAs substrate (100)			
AlGaAs	30.6	2000	
AlGaAs	Si δ -doping 72 s, 1×10^{12} cm ⁻²		
AlGaAs	30.6	7800	
loop 100x			
GaAs		14	
AlAs		5	
endloop			
AlGaAs	30.6	200	
loop 10x			
GaAs		15	
GaAs	Si δ -doping 1.5 s, 2×10^{10} cm ⁻²		
GaAs		15	
AlGaAs	30.6	300	
GaAs		520	
AlGaAs	30.6	300	
GaAs		15	
GaAs	Si δ -doping 1.5 s, 2×10^{10} cm ⁻²		
GaAs		15	
AlGaAs	30.6	1000	
endloop			
AlGaAs	30.6	9000	
AlGaAs	Si δ -doping 72 s, 1×10^{12} cm ⁻²		
AlGaAs	30.6	2000	
GaAs		100	

The sample has been fabricated at the University of California in Santa Barbara in 1994.

H797 - Multiple Quantum Wells

Layer (substrate → surface)	x (%)	Thickness (Å)	Doping (cm ⁻³)
SI GaAs substrate (100)		625 μm	
AlGaAs	30	2000	
AlGaAs	Si δ-doping, 1 × 10 ¹² cm ⁻²		
AlGaAs	30	7800	
loop 100x			
GaAs		14	
AlAs		5	
endloop			
AlGaAs	30	200	
loop 10x			
GaAs		15	
GaAs	Si δ-doping, 3 × 10 ¹⁰ cm ⁻²		
GaAs		15	
AlGaAs	30	300	
GaAs		520	
AlGaAs	30	300	
GaAs		15	
GaAs	Si δ-doping, 3 × 10 ¹⁰ cm ⁻²		
GaAs		15	
AlGaAs	30	1000	
endloop			
AlGaAs	30	9000	
AlGaAs	Si δ-doping, 1 × 10 ¹² cm ⁻²		
AlGaAs	30	2000	
GaAs		200	

The sample is a modified regrowth of UKQW.

H824 - Multiple Quantum Wells

Layer (substrate → surface)	x (%)	Thickness (Å)	Doping (cm ⁻³)
SI GaAs substrate (100)		625 μm	
AlGaAs	30	2000	
AlGaAs		Si δ-doping, 1 × 10 ¹² cm ⁻²	
AlGaAs	30	7800	
loop 100x			
GaAs		14	
AlAs		5	
endloop			
AlGaAs	30	200	
loop 10x			
GaAs		15	
GaAs		Si δ-doping, 3 × 10 ¹⁰ cm ⁻²	
GaAs		15	
AlGaAs	30	300	
GaAs		520	
AlGaAs	30	300	
GaAs		15	
GaAs		Si δ-doping, 3 × 10 ¹⁰ cm ⁻²	
GaAs		15	
AlGaAs	30	1000	
endloop			
AlGaAs	30	9000	
AlGaAs		Si δ-doping, 1 × 10 ¹² cm ⁻²	
AlGaAs	30	2000	
GaAs		200	

The sample is a regrowth of H797 with 1/3 less doping in the well part by using 2/3 of shutter opening time.

Appendix B

Analytic Expression for Polarizability of a Split-Ring Resonator

The SRR is one of the few meta-atom geometries for which a closed analytical expression for the polarizability tensor can be derived. This appendix gives a rough sketch of the procedure based on the so-called wire-and-loop model [162, 164].

Figure B.1a shows the geometry of the SRR. The center radius of the loop is R , the width of the wire strip is d , and the slit has a width of s . The SRR is assumed to be made of lossless metal. The validity of the model is further restricted to moderately sized rings with small wire diameter [323]:

$$kR \leq 1.3, \text{ and } d \ll R, \quad (\text{B.1})$$

where $k = \omega\sqrt{\varepsilon\mu}$ is the wavevector of the incident wave with the effective permittivity and permeability of the material as given by Eq. (3.23). Under these assumptions, the SRR can be modeled as a loaded loop antenna, where the slit represents a capacitive load.

The current distribution for a loop antenna driven by a delta-like voltage source V_0 at the azimuthal position $\phi_0 = 0$ can be expressed in form of a Fourier series [323]

$$I^T(\phi) = -i\frac{V_0}{\pi}\sqrt{\frac{\varepsilon}{\mu}}\left(\frac{1}{A_0} + 2\sum_1^{\infty}\frac{\cos n\phi}{A_n}\right). \quad (\text{B.2})$$

Under the assumptions (B.1), it is sufficient to keep only the first three terms

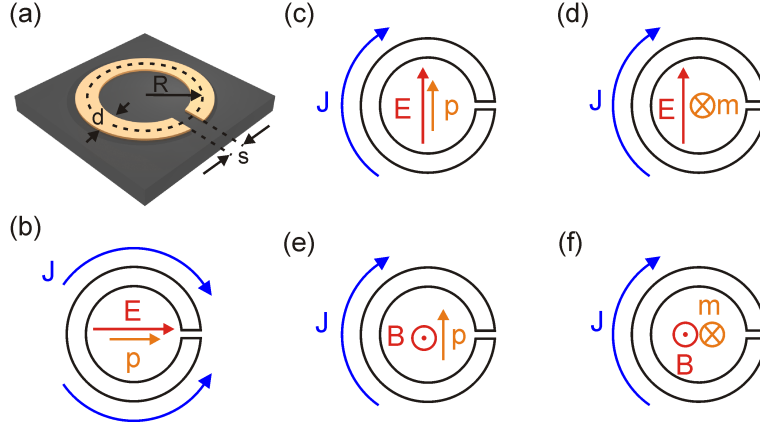


Figure B.1: (a) SRR geometry with wire thickness d , average ring diameter R , and slit width s . (b) Incident electric field E oriented parallel to slit induces a current density J flowing on both sides of the ring, leading to an electric dipole p oriented in the same direction. (c) Same for field perpendicular to slit. (d) In the same configuration, the asymmetric current gives rise to a magnetic dipole m pointing into the paper plane. (e) A varying magnetic field B pointing out of the paper plane gives also rise to an electric dipole. (f) In the same configuration, a magnetic dipole with opposite polarity is induced (Lenz' rule).

in the Fourier expansion (B.2) and only terms up to the order $(kr)^6$ [323]:

$$A_0 = \frac{kR}{\pi} \left[\ln \left(\frac{8R}{r_0} \right) - 2 \right] + \frac{1}{\pi} [0.667(kR)^3 - 0.267(kR)^5] - i [0.167(kR)^4 - 0.033(kR)^6] \quad (\text{B.3})$$

$$A_1 = \left(kR - \frac{1}{kR} \right) \frac{1}{\pi} \left[\ln \left(\frac{8R}{r_0} \right) - 2 \right] + \frac{1}{\pi} [-0.667(kR)^3 + 0.207(kR)^5] - i [0.333(kR)^2 - 0.133(kR)^4 + 0.026(kR)^6] \quad (\text{B.4})$$

$$A_2 = \left(kR - \frac{4}{kR} \right) \frac{1}{\pi} \left[\ln \left(\frac{8R}{r_0} \right) - 2.667 \right] - i [0.050(kR)^4 - 0.012(kR)^6] + \frac{1}{\pi} [-0.400(kR) + 0.210(kR)^3 - 0.086(kR)^5]. \quad (\text{B.5})$$

When the loop acts as receiving antenna, the antenna current I^R is obtained by integrating the generated electromotive force over the whole antenna.

For a plane wave with amplitude E_{in} , incident under an angle θ with the surface normal (z axis) and with electric field polarized at an angle ψ with respect to the y axis, the antenna current distribution is given as [323, 324]:

$$I_L^R(\phi) = E_{in} \left[J^R(\phi) - \frac{J^R(\phi_0)}{Y_{in} + Y_L} J^T(\phi - \phi_0) \right], \quad (\text{B.6})$$

where $J^T(\phi) = I^T(\phi)/V_0$ with I^T given by Eq. (B.2), and $J^R(\phi) = I^R(\phi)/E_{in}$ with [323]

$$I^R(\theta, \phi) = 2Ri\sqrt{\frac{\varepsilon}{\mu}}E_{in} \left[\cos\psi \left(\frac{J'_0(kR\sin\theta)}{iA_0} - \frac{2J'_1(kR\sin\theta)}{A_1} \cos\phi \right) - \frac{2J_1(kR\sin\theta)}{A_1kR\sin\theta} \sin\phi \sin\psi \cos\theta \right]. \quad (\text{B.7})$$

being the closed loop receiver current. Thereby, J_0 and J_1 are the Bessel functions of first kind with the primed versions denoting their derivatives. The azimuthal angle of incidence is taken as $\phi_0 = 0$ without loss of generality, which means that the plane wave is incident in the x - z plane.

Figures B.1b to B.1f list all possible combinations of incident electric and magnetic fields and the respective induced dipoles that have to be considered. The presence of the slit breaks the rotational symmetry of the loop and, hence, the SRR can be left or right handed. In the following, the left handed case is attributed to the upper sign and the other case to the lower sign.

Substitution of (B.2) and (B.7) in (B.6) gives

$$I_L^R(\phi) = 2Ri\sqrt{\frac{\varepsilon}{\mu}}E_{in} \left\{ \cos\psi \left(\frac{J'_0(kR\sin\theta)}{iA_0} - \frac{2J'_1(kR\sin\theta)}{A_1} \cos\phi \right) - \frac{2J_1(kR\sin\theta)}{A_1kR\sin\theta} \sin\phi \sin\psi \cos\theta + \frac{i}{\pi} \sqrt{\frac{\varepsilon}{\mu}} \frac{1}{Y_{in} + Y_L} \cos\psi \times \left(\frac{J'_0(kR\sin\theta)}{iA_0} \mp \frac{2J'_1(kR\sin\theta)}{A_1} \right) \left(\frac{1}{A_0} \pm \frac{2\cos\phi}{A_1} \right) \right\}, \quad (\text{B.8})$$

where only the first two terms of the Fourier expansion have been kept, as only these contribute to the electric and magnetic dipoles. If the gap would be closed, the admittance of the gap, Y_L , would become infinity and (B.8) would equal (B.7), as expected.

Excitation Due to Magnetic Field

For pure magnetic excitation, we choose $\theta = \pi/2$ and $\psi = 0$. We can identify the terms due to the magnetic field by comparison with the case $\theta = 0$ and $\psi = 0$, which only yields the terms due to E_y . The receiver current due to B_z is then

$$I_L^R(\phi)_{\pm} = -\frac{2RJ_1(kR)}{\mu A_0} B_z \left(1 + \frac{i}{Y_{in} + Y_L} \sqrt{\frac{\varepsilon}{\mu}} \frac{1}{A_0\pi} \right) \mp \frac{i}{Y_{in} + Y_L} \sqrt{\frac{\varepsilon}{\mu}} \frac{4RJ_1(kR)}{\pi\mu A_0 A_1} B_z \cos\phi, \quad (\text{B.9})$$

where we have used

$$E_y = \frac{1}{\mu} \sqrt{\frac{\mu}{\varepsilon}} B_z, \quad (\text{B.10})$$

and $J'_0(z) = -J_1(z)$.

The current consists of a uniform part which is responsible for the magnetic dipole moment and additionally, a "cos ϕ " part, which creates an electric dipole. Substitution of the uniform part into

$$\mathbf{m} = \frac{1}{2} \int \mathbf{r} \times \mathbf{j}(\mathbf{r}) d^3r \quad (\text{B.11})$$

yields the magnetic polarizability tensor element

$$\alpha_{zz}^{mm} = -\frac{2\pi R^3 J_1(kR)}{\mu A_0} \left(1 + \frac{i}{Y_{in} + Y_L} \sqrt{\frac{\varepsilon}{\mu}} \frac{1}{A_0 \pi} \right). \quad (\text{B.12})$$

The sign is independent of the handedness of the particle, as the induced current always flows according to Lenz' rule (see Fig. B.1f).

The remaining "cos ϕ " term of (B.9) yields the cross-polarizability element α_{yz}^{em} . We rewrite this in the form $I_L^R(\phi) = I_1 \cos \phi$ with

$$I_1 = \mp \frac{i}{Y_{in} + Y_L} \sqrt{\frac{\varepsilon}{\mu}} \frac{4R J_1(kR)}{\pi \mu A_0 A_1} B_z \quad (\text{B.13})$$

and substitute into

$$\mathbf{p} = \frac{I_1 R}{i\omega} \int_0^{2\pi} \begin{pmatrix} \cos \phi \sin \phi \\ \sin^2 \phi \\ 0 \end{pmatrix} d\phi = \frac{I_1 R}{i\omega} \begin{pmatrix} 0 \\ \pi \\ 0 \end{pmatrix} = \frac{I_1 \pi R}{i\omega} \hat{e}_y, \quad (\text{B.14})$$

which immediately yields

$$\alpha_{yz,\pm}^{em} = \mp \frac{4R^2 J_1(kR)}{\omega \mu A_0 A_1} \sqrt{\frac{\varepsilon}{\mu}} \frac{1}{Y_{in} + Y_L}. \quad (\text{B.15})$$

The situation is sketched in Fig. B.1e. Due to the geometry, there is no α_{xz}^{em} component of the polarizability tensor.

Excitation Due to Electric Field

Also in the case of electric excitation of the ring, we have to consider two distinct cases. First, we treat the excitation due to an electric field polarized

along the x axis. Substituting the values for $\psi = -pi/2$ and $\theta = 0$ into the "cos ϕ " term of (B.8) yields

$$I^R(\phi) = -\frac{2Ri}{A_1} \sqrt{\frac{\varepsilon}{\mu}} E_x \cos \phi =: I_1 \cos \phi, \quad (\text{B.16})$$

where we made use of

$$J_1'(0) = \frac{1}{2}. \quad (\text{B.17})$$

Equation (B.16) can be written in terms of a current density \mathbf{j} by using the fact that the current flows only on a ring with radius R and negligible thickness. Using the continuity equation and the divergence in cylindrical coordinates [289],

$$\nabla \mathbf{v} = \frac{1}{r} \left[\frac{\partial}{\partial r} (rv_r) + \frac{\partial}{\partial \phi} v_\phi + \frac{\partial}{\partial z} (rv_z) \right], \quad (\text{B.18})$$

gives the corresponding charge distribution

$$\rho(\mathbf{r}) = \frac{I_1}{i\omega} \frac{1}{r} \delta(r - R) \delta(z) \sin \phi. \quad (\text{B.19})$$

The electric dipole moment is then obtained by integrating over the position vector

$$\mathbf{p} = \int \mathbf{r} \rho(\mathbf{r}) d^3r. \quad (\text{B.20})$$

After re-substituting I_1 from (B.16), we find

$$p_x = -\frac{2\pi R^2}{\omega A_1} \sqrt{\frac{\varepsilon}{\mu}} E_x \quad (\text{B.21})$$

and also the desired polarization tensor element

$$\alpha_{xx}^{ee} = -\frac{2\pi R^2}{\omega A_1} \sqrt{\frac{\varepsilon}{\mu}}. \quad (\text{B.22})$$

Therefore, the response of the SRR to the incident field is not affected by the presence of the slit (see Fig. B.1b).

This changes for y polarization of the electric field. Substitution of $\psi = 0$ and $\theta = 0$ into (B.8) yields

$$\begin{aligned} I_L^R(\phi)_\pm &= -\frac{2Ri}{A_1} \sqrt{\frac{\varepsilon}{\mu}} \left(1 + \frac{i}{Y_{in} + Y_L} \sqrt{\frac{\varepsilon}{\mu}} \frac{2}{\pi A_1} \right) E_y \cos \phi \\ &\pm \frac{2\varepsilon R}{\pi \mu A_0 A_1} \frac{1}{Y_{in} + Y_L} E_y \end{aligned} \quad (\text{B.23})$$

where we again used (B.17). The first term is proportional to $\cos \phi$ and therefore responsible for the electric dipole moment. By identifying

$$I_1 = -\frac{2Ri}{A_1} \sqrt{\frac{\varepsilon}{\mu}} \left(1 + \frac{i}{Y_{in} + Y_L} \sqrt{\frac{\varepsilon}{\mu}} \frac{2}{\pi A_1} \right) E_y, \quad (\text{B.24})$$

and using (B.21), we can right away write down the polarizability tensor element

$$\alpha_{yy}^{ee} = -\frac{2\pi R^2}{\omega A_1} \sqrt{\frac{\varepsilon}{\mu}} \left(1 + \frac{i}{Y_{in} + Y_L} \sqrt{\frac{\varepsilon}{\mu}} \frac{2}{\pi A_1} \right). \quad (\text{B.25})$$

The situation is sketched in Fig. B.1c. The second part of (B.23) is a uniform current distribution that generates a magnetic dipole according to (B.11). The cross-polarized polarizability tensor element thus reads

$$\alpha_{zy,\pm}^{me} = \pm \frac{2\varepsilon R^3}{\mu A_0 A_1} \frac{1}{Y_{in} + Y_L}. \quad (\text{B.26})$$

A sketch is shown in Fig. B.1d. It is easy to check that (B.22) and (B.26) fulfill the symmetry relation $\alpha_{yz}^{em} = -\alpha_{zy}^{me}$ for small kR and $k = \omega\sqrt{\varepsilon\mu}$, as then $J_1(kR) \approx \frac{1}{2}kR = \omega\sqrt{\varepsilon\mu}R/2$.

Calculation of Load Admittance

The load admittance is given by the capacitance of the gap

$$Y_L = i\omega C_{\text{gap}}. \quad (\text{B.27})$$

In a first approximation, we can calculate C_{gap} as the capacitance of a parallel plate capacitor and add corrections due to the fringe fields [325]:

$$C_{\text{gap}} = \varepsilon \frac{\pi r_0^2}{s} + \varepsilon r_0 \left[\log \frac{16\pi r_0}{s} - 1 \right], \quad (\text{B.28})$$

where r_0 is the equivalent wire radius. According to [326], a strip of width d and thickness h can be replaced by a wire of radius r_0 where this equivalent radius is given as [323, 326]

$$r_0 \approx \frac{d+h}{4} \approx \frac{d}{4}, \quad (\text{B.29})$$

as typically $h \ll d$. The total capacitance of a split-ring has previously been calculated in [327, 328] as sum of the gap capacitance and the surface capacitance of the split ring

$$C_{\text{surf}} = \frac{2\varepsilon(h+w)}{\pi} \log \frac{4R}{s}. \quad (\text{B.30})$$

Thereby, they found in general a good agreement between FDTD simulations and their analytical formulation. In our picture, the surface capacitance is approximately that of the closed ring and already contained in the expression for the input admittance Y_{in} . Thus, the load capacitance should be approximated reasonably well by the parallel plate capacitance of the gap alone.

Appendix C

Coupled Pendulums

This appendix is devoted to the mechanical motion of two coupled pendulums. Despite its simplicity, the coupled pendulum model can give considerable insight into the physics underlying more complicated phenomena [185]. Examples include two-level atoms [329], stimulated resonance Raman interaction [330], or electromagnetically induced transparency [331]. The following derivations can be found in many textbooks (for example [332]).

The geometry is depicted in Fig. C.1. The pendulum consists of two particles of mass m that are connected via springs to the two sidewalls. The two springs have the spring constants k_1 and k_2 . A third spring with spring constant κ connects the two particles and is responsible for the coupling of the two pendulums. Motion is assumed to be possible only along the x axis. The displacement of the two particles from their equilibrium positions is denoted by x_1 and x_2 , respectively. To simplify the treatment, any damping is neglected.

The equations of motion of this system can be derived from Newton's laws. Thereby, the force, a spring is exerting on a particle, is given by the spring constant times the displacement from equilibrium (Hooke's law). This yields a set of coupled differential equations for x_1 and x_2 :

$$m \frac{\partial^2 x_1}{\partial t^2} = -k_1 x_1 - \kappa(x_1 - x_2), \quad (\text{C.1})$$

$$m \frac{\partial^2 x_2}{\partial t^2} = -k_2 x_2 - \kappa(x_2 - x_1). \quad (\text{C.2})$$

When we remove the coupling spring, i.e. set $\kappa = 0$, the equations simplify to

$$m \frac{\partial^2 x_1}{\partial t^2} = -k_1 x_1, \quad \text{and} \quad m \frac{\partial^2 x_2}{\partial t^2} = -k_2 x_2, \quad (\text{C.3})$$

which describe a simple harmonic motion with a characteristic frequency

$$\omega_i = \sqrt{\frac{k_i}{m}}. \quad (\text{C.4})$$

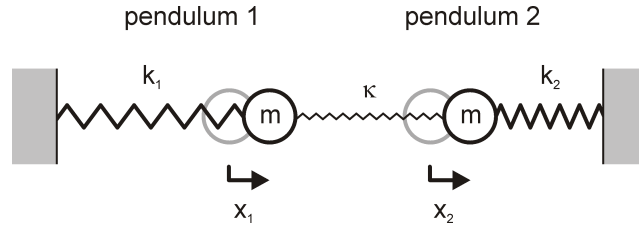


Figure C.1: Mechanical model of a coupled pendulum.

If $\kappa \neq 0$, but one of the pendulums is kept fixed at its origin, the equation of motion for the other pendulum is reduced to

$$m \frac{\partial^2 x_1}{\partial t^2} = -(k_1 + \kappa)x_1, \quad \text{and} \quad m \frac{\partial^2 x_2}{\partial t^2} = -(k_2 + \kappa)x_2, \quad (\text{C.5})$$

respectively. Thus, the coupling leads to a renormalization of the eigenfrequency of the unperturbed pendulum¹. The frequency shift is thereby the same for both pendulums and can be absorbed into the single pendulum frequency

$$\tilde{\omega}_i = \sqrt{\frac{k_i + \kappa}{m}}. \quad (\text{C.6})$$

The system of coupled equations is conveniently solved by making a harmonic analysis, i.e. using the Ansatz

$$x_i = a_i \cos(\omega t), \quad (\text{C.7})$$

with amplitude a_i and angular frequency ω . Following this procedure yields a homogeneous set of coupled linear equations for the two amplitudes a_1 and a_2 :

$$(k_1 + \kappa - m\omega^2)a_1 - \kappa a_2 = 0, \quad (\text{C.8})$$

$$-\kappa a_1 + (k_2 + \kappa - m\omega^2)a_2 = 0, \quad (\text{C.9})$$

which can be written in matrix notation as

$$\mathbf{M} \begin{pmatrix} a_1 \\ a_2 \end{pmatrix} = 0. \quad (\text{C.10})$$

To have non-trivial solutions for a_1 and a_2 , the determinant of \mathbf{M} has to vanish, i.e. $\det \mathbf{M} = 0$. Solving the resulting characteristic equation

$$(k_1 + \kappa - m\omega^2)(k_2 + \kappa - m\omega^2) - \kappa^2 = 0, \quad (\text{C.11})$$

¹In the case of a two-level system coupled to an electric field, this frequency pulling would be mediated through the diagonal terms of the interaction Hamiltonian, which are in general zero due to the electric-dipole selection rules.

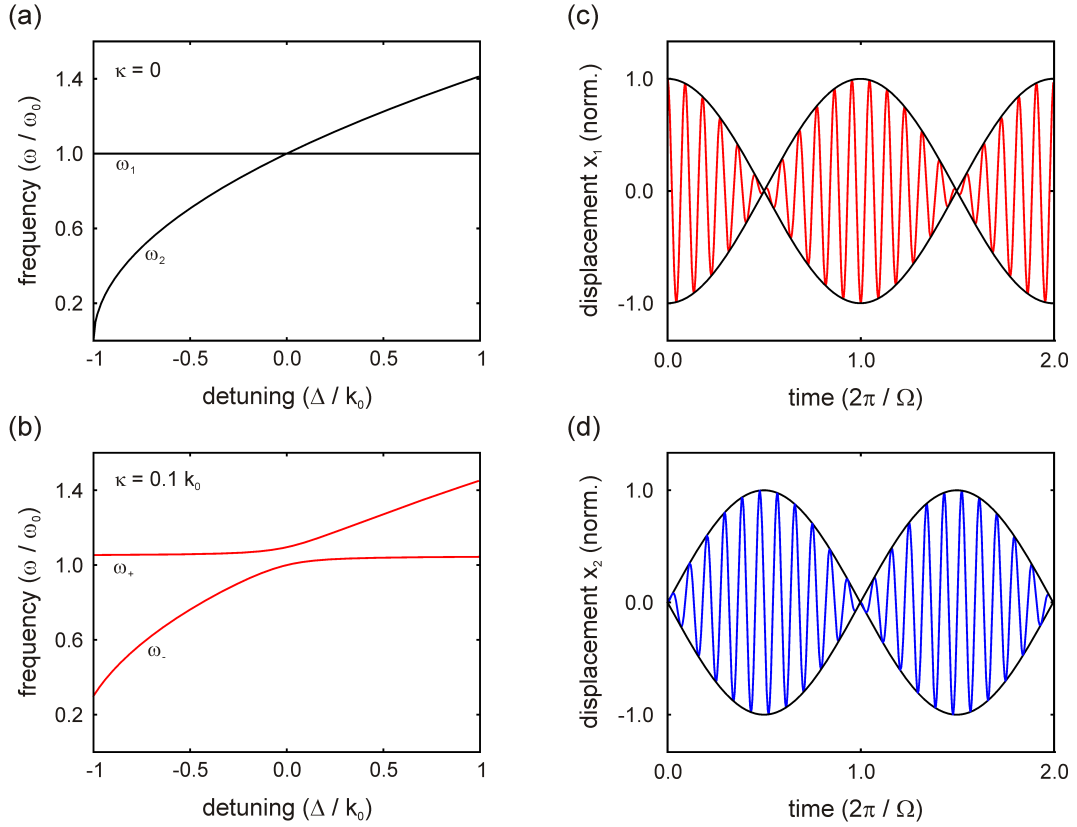


Figure C.2: (a, b) Frequencies of the eigenmodes of the two pendulums in the case of (a) zero coupling, $\kappa = 0$, and (b) non-zero coupling, $\kappa = 0.1k_0$, as function of the detuning Δ . The frequency axis is scaled to $\omega_0 = \sqrt{k_0/m}$. (c, d) Displacement of (c) pendulum 1 and (d) pendulum 2 as function of time for $\kappa = 0.1k_0$.

yields the two solutions

$$\omega_{\pm}^2 = \frac{1}{2m}(k_1 + k_2 + 2\kappa) \pm \frac{1}{2m}\sqrt{(k_1 - k_2)^2 + 4\kappa^2} \quad (\text{C.12})$$

for the new eigenfrequencies of the coupled system. The eigenstates associated with these frequencies are called normal modes.

To illustrate the effect of the coupling on the eigenfrequencies, ω_{\pm} is plotted in Fig. C.2 as function of a detuning Δ for two different values of κ . The detuning is introduced by setting $k_1 = k_0$ and $k_2 = k_0 + \Delta$. The characteristic frequency of pendulum 2 scales with $\sqrt{\Delta}$ according to (C.4), while the frequency of pendulum 1 remains constant.

When no coupling is present in the system (Fig. C.2a), the two frequency branches evolve independently and cross at $\Delta = 0$. However, for $\kappa \neq 0$, the two branches are repelled from each other, leading to a so-called anticrossing of the two modes. Additionally, the frequencies for both pendulums are shifted to higher values according to Eq. (C.6). The minimal frequency splitting occurs

at $\Delta = 0$ and, for $\kappa \ll \omega_0$ is given by

$$[\omega_+ - \omega_-]_{\Delta=0} \approx \frac{\kappa}{m\omega_0} \equiv \Omega. \quad (\text{C.13})$$

This normal mode splitting is a clear indication of strong coupling between the two pendulums. As $\Omega \propto \kappa$, the splitting is increased by increasing coupling strength. In addition, Ω gives the rate at which energy is exchanged between the two pendulums (see below).

In the following, we set $\Delta = 0$. In this simple case $k_1 = k_2 = k$, for which (C.12) yields the two solutions

$$\omega_- = \sqrt{\frac{k}{m}} \quad \text{and} \quad \omega_+ = \sqrt{\frac{k+2\kappa}{m}}. \quad (\text{C.14})$$

Substitution of Eq. (C.14) into (C.8) and (C.9) immediately yields that $a_1 = a_2$ for $\omega = \omega_-$, and $a_1 = -a_2$ for $\omega = \omega_+$. Thus, the two pendulums oscillate with equal amplitudes either in phase or out of phase by 180° . The general solution consists of a superposition of these two eigenmodes,

$$x_1 = c_1 \cos(\omega_- t + \phi_1) + c_2 \cos(\omega_+ t + \phi_2), \quad (\text{C.15})$$

$$x_2 = c_1 \cos(\omega_- t + \phi_1) - c_2 \cos(\omega_+ t + \phi_2), \quad (\text{C.16})$$

where c_1 , c_2 , ϕ_1 and ϕ_2 are integration constants, that have to be determined depending on the initial conditions. When only one pendulum is initially displaced from its equilibrium position and both are at rest, the initial conditions $x_1(0) = A$, and $x_2(0) = (\partial x_1 / \partial t)(0) = (\partial x_2 / \partial t)(0) = 0$ lead to

$$c_1 = c_2 = \frac{A}{2} \quad \text{and} \quad \phi_1 = \phi_2 = 0, \quad (\text{C.17})$$

and the final solution:

$$\begin{aligned} x_1 &= \frac{A}{2} [\cos(\omega_- t) + \cos(\omega_+ t)] \\ &= A \cos\left(\frac{\omega_+ - \omega_-}{2} t\right) \cos\left(\frac{\omega_+ + \omega_-}{2} t\right), \end{aligned} \quad (\text{C.18})$$

$$\begin{aligned} x_2 &= \frac{A}{2} [\cos(\omega_- t) - \cos(\omega_+ t)] \\ &= A \sin\left(\frac{\omega_+ - \omega_-}{2} t\right) \sin\left(\frac{\omega_+ + \omega_-}{2} t\right). \end{aligned} \quad (\text{C.19})$$

Both pendulums oscillate with the average frequency $\bar{\omega} = (\omega_+ + \omega_-)/2$ and slowly varying amplitudes $\propto \cos(\Omega/2t)$ and $\propto \sin(\Omega/2t)$, respectively. As the energy stored in each of the two pendulums is proportional to the square of the amplitude envelopes, there is a periodic exchange of energy at a rate Ω

according to Eq. (C.13). The displacement of two coupled pendulums is plotted in Figs. C.2c and C.2d as function of time for a coupling strength of $\kappa = 0.1k_0$. Initially, only pendulum 1 has been displaced from its equilibrium position.

In the discussion so far, we have neglected any damping effects. These can be easily incorporated in the model by adding the friction terms $-\gamma_1(\partial x_1/\partial t)$ and $-\gamma_2(\partial x_2/\partial t)$ to the equations of motion (C.1) and (C.2), respectively [185]. The harmonic analysis then yields complex eigenvalues, $\hat{\omega}_\pm$, whose real parts are again the normal mode frequencies. The imaginary parts are responsible for the damping of the oscillatory motion and represent the normal mode linewidths γ_\pm . To resolve the splitting of the normal mode frequencies in a system with damping, the frequency difference between the two modes has to be larger than the individual linewidths, respectively:

$$\Omega \geq \frac{\gamma_+}{m}, \frac{\gamma_-}{m}. \quad (\text{C.20})$$

For zero detuning, the two linewidths are given in first order by the average of the uncoupled pendulum damping rates, $\gamma_\pm = (\gamma_1 + \gamma_2)/2$.

Equation (C.20) poses important constraints on the experimental realization of strongly coupled systems. Equivalently, in the time domain, the energy exchange between the two pendulums has to be faster than the time it takes to dissipate the energy

$$T_\Omega = \frac{2\pi}{\Omega} < \tau = \left(\frac{\gamma_1}{2m} + \frac{\gamma_2}{2m} \right)^{-1}. \quad (\text{C.21})$$

Otherwise, the beating of the two pendulums would not be observable and, thus, both pendulums would appear to oscillate at the average frequency $\bar{\omega}$. Similarly, the same argument applies to the minimum length of the temporal window that is necessary to observe strong coupling. If the scan length T is chosen to be smaller than T_Ω , the splitting of the modes cannot be resolved, even if there would be no damping at all.

Appendix D

Quantum Well Models for FDTD Simulations

The finite-difference implementations of the quantum well models are based on the auxiliary differential equation (ADE) method [167]. Due to the polarization selection rules of ISBTs, the models apply only to the grid cells for the z component of the electric field. In the 3d FDTD simulations, the QW is taken to occupy a single layer underneath the MM. In the case of 1d FDTD calculations, the QW model is applied to the entire sample. The description of the FDTD code is found in Chap. 3.2.

D.1 Lorentz Model

The Lorentz oscillator is a popular model for the interaction of light with atomic systems [32, 89]. It is also well suited for the description of intersubband transitions in quantum wells when treated in a one-electron picture [40]. The starting point is the intersubband polarization density

$$P_z(\omega) = \frac{f_{12}n_0e^2/m_{\text{eff}}}{\omega_{12}^2 - \omega^2 + i\gamma\omega} E_z \quad (\text{D.1})$$

induced by the z component of the electric field. Thereby, ω_{12} is the transition frequency, f_{12} the oscillator strength, n_0 the carrier density, m_{eff} the effective electron mass, and γ the damping rate. The latter is related to the exponential decay time τ of the free induction decay via $\gamma = 2/\tau$. The thickness of the QW is half a grid cell. Thus, the volume electron density n_0 is calculated from the areal density n_{2d} via $n_0 = 2n_{2d}/\Delta z$.

For the finite-difference model, we make use of the ADE method. To this end, Eq. (D.1) is converted into a partial differential equation for the current density J_z via [167]

$$J_z(t) = \frac{\partial}{\partial t} P_z(t) \leftrightarrow J_z(\omega) = i\omega P_z(\omega). \quad (\text{D.2})$$

Substitution of (D.1) yields

$$\omega_{12}^2 J_z + \frac{\partial^2}{\partial t^2} J_z + \gamma \frac{\partial}{\partial t} J_z = \frac{f_{12} n_0 e^2}{m_{\text{eff}}} \frac{\partial}{\partial t} E_z. \quad (\text{D.3})$$

To derive a second-order finite difference equation, the derivatives are expanded around time step n :

$$\begin{aligned} \frac{1}{\Delta t^2} \left(J_z|_{i,j,k}^{n+1} - 2 J_z|_{i,j,k}^n + J_z|_{i,j,k}^{n-1} \right) + \frac{\gamma}{2\Delta t} \left(J_z|_{i,j,k}^{n+1} - J_z|_{i,j,k}^{n-1} \right) \\ + \omega_{12}^2 J_z|_{i,j,k}^n = \frac{f_{12} n_0 e^2}{m_{\text{eff}}} \left(\frac{E_z|_{i,j,k}^{n+1} - E_z|_{i,j,k}^{n-1}}{2\Delta t} \right). \end{aligned} \quad (\text{D.4})$$

Thereby, the current density and the electric field are centered on the same grid coordinates. Solving for the new time step $n + 1$ yields the ADE

$$J_z|_{i,j,k}^{n+1} = A J_z|_{i,j,k}^n + B J_z|_{i,j,k}^{n-1} + C \left(\frac{E_z|_{i,j,k}^{n+1} - E_z|_{i,j,k}^{n-1}}{2\Delta t} \right) \quad (\text{D.5})$$

with

$$A = \frac{4 - 2\omega_{12}^2 \Delta t^2}{2 + \gamma \Delta t} \quad (\text{D.6})$$

$$B = \frac{\gamma \Delta t - 2}{\gamma \Delta t + 2} \quad (\text{D.7})$$

$$C = \frac{2\varepsilon_0 f_{12} \omega_p^2 \Delta t^2}{2 + \gamma \Delta t}, \quad (\text{D.8})$$

and the plasma frequency

$$\omega_p^2 = \frac{n_0 e^2}{m_{\text{eff}} \varepsilon_0}. \quad (\text{D.9})$$

The final step is to solve

$$\nabla \times \mathbf{H} = \varepsilon_0 \varepsilon_\infty \frac{\partial}{\partial t} \mathbf{E} + \mathbf{J} \quad (\text{D.10})$$

for $\mathbf{E}|_{i,j,k}^{n+1}$ after substituting the current density $\mathbf{J} = J_z \hat{z}$ with Eq. (D.5). This yields the modified update equation for the electric field

$$\mathbf{E}|_{i,j,k}^{n+1} = D \mathbf{E}|_{i,j,k}^n + E \mathbf{E}|_{i,j,k}^{n-1} + F [\nabla \times \mathbf{H}]^{n+1/2} - G \mathbf{J}|_{i,j,k}^n - H \mathbf{J}|_{i,j,k}^{n-1} \quad (\text{D.11})$$

with

$$D = \frac{4\varepsilon_0\varepsilon_\infty}{C + 4\varepsilon_0\varepsilon_\infty} \quad (\text{D.12})$$

$$E = \frac{C}{C + 4\varepsilon_0\varepsilon_\infty} \quad (\text{D.13})$$

$$F = \frac{4\Delta t}{C + 4\varepsilon_0\varepsilon_\infty} \quad (\text{D.14})$$

$$G = \frac{2\Delta t(1 + A)}{C + 4\varepsilon_0\varepsilon_\infty} \quad (\text{D.15})$$

$$H = \frac{2\Delta tB}{C + 4\varepsilon_0\varepsilon_\infty}. \quad (\text{D.16})$$

D.2 Maxwell-Bloch Model

The following derivation is a summary of the seminal paper by Ziolkowski [209] but using the discretization scheme proposed by Bidégaray [333]. The complex interaction of single-cycle THz pulses with quantum mechanical two-level systems, such as QWs, is best modeled in a semi-classical approach. The electromagnetic fields are treated classically via the set of Maxwell's equations in a non-magnetic medium with dielectric constant ε .

The two-level system is generally defined by a state vector $|\psi\rangle$, whose time evolution is given by the time-dependent Schrödinger equation

$$i\hbar \frac{\partial}{\partial t} |\psi\rangle = H |\psi\rangle, \quad (\text{D.17})$$

where H is the Hamiltonian of the combined system of unperturbed quantum system and perturbation due to the external electromagnetic field:

$$H_{\text{int}} = er_{12}E_z, \quad (\text{D.18})$$

with r_{12} being the transition matrix element with respect to the quantum state $|\psi\rangle$ and $-e$ the electron charge. Ziolkowski has shown that Eq. (D.17) can be transformed to [209]:

$$\begin{aligned} \frac{\partial}{\partial t} \begin{pmatrix} \rho_1 \\ \rho_2 \\ \rho_3 \end{pmatrix} &= \begin{pmatrix} 0 & \omega_0 & 0 \\ -\omega_0 & 0 & 2\Omega_R \\ 0 & -2\Omega_R & 0 \end{pmatrix} \begin{pmatrix} \rho_1 \\ \rho_2 \\ \rho_3 \end{pmatrix} \\ &- \begin{pmatrix} 1/T_2 & 0 & 0 \\ 0 & 1/T_2 & 0 \\ 0 & 0 & 1/T_1 \end{pmatrix} \begin{pmatrix} \rho_1 \\ \rho_2 \\ \rho_3 - \rho_{30} \end{pmatrix}, \end{aligned} \quad (\text{D.19})$$

where ω_0 is the ISBT frequency, $\Omega_R = (er_{12}/\hbar)|E_z|$ the so-called Rabi frequency, T_1 the excited state lifetime, T_2 the dephasing time and ρ_{30} the population difference in the system at equilibrium. The three dimensionless parameters ρ_1, ρ_2 , and ρ_3 thereby satisfy the relations $-1 \leq \rho_1, \rho_2, \rho_3 \leq +1$ and $\rho_1^2 + \rho_2^2 + \rho_3^2 = 1$ and represent the dispersive (in-phase) component of the polarization, the absorptive (quadrature) component of the polarization and the fractional difference in populations of the two states ($\rho_3 = -1$ for the ground state and $\rho_3 = +1$ for the excited state). In this formulation, all parameters are real valued. Using the ISBT polarization density

$$P_z = -ner_{12}\rho_1 \quad (\text{D.20})$$

yields the coupled set of Maxwell-Bloch equations [209]:

$$\nabla \times \mathbf{E} = -\mu_0 \frac{\partial}{\partial t} \mathbf{H}, \quad (\text{D.21})$$

$$\nabla \times \mathbf{H} = \varepsilon_0 \varepsilon \frac{\partial}{\partial t} \mathbf{E} + \frac{ner_{12}}{T_2} \rho_1 \hat{\mathbf{z}} - ner_{12} \omega_0 \rho_2 \hat{\mathbf{z}}, \quad (\text{D.22})$$

and

$$\frac{\partial}{\partial t} \rho_1 = -\frac{1}{T_2} \rho_1 + \omega_0 \rho_2, \quad (\text{D.23})$$

$$\frac{\partial}{\partial t} \rho_2 = -\omega_0 \rho_1 - \frac{1}{T_2} \rho_2 + 2 \frac{er_{12}}{\hbar} E_z \rho_3, \quad (\text{D.24})$$

$$\frac{\partial}{\partial t} \rho_3 = -2 \frac{er_{12}}{\hbar} E_z \rho_2 - \frac{1}{T_1} (\rho_3 - \rho_{30}). \quad (\text{D.25})$$

The final step is to derive a finite-difference scheme of the Maxwell-Bloch equations.

The important point in deriving a discretized formulation of the Maxwell-Bloch equations is to choose the right time for discretizing ρ . As is suggested by the form of the Maxwell equations, it is good to have the electric field and the material parameters located on the same space grid and the magnetic field offset by a half-cell. The electric field is, as usual, discretized at time steps n , etc. and the magnetic field at time steps $n + 1/2$, etc.

Before we make the discretization, we analytically manipulate the Bloch equations to be more amenable for numerical integration, as has been done in [209]. The exponential decay terms and the constant ρ_{30} make the differential equations stiff and may cause problems. Ziolkowski therefore proposed to introduce new variables u_i through the definitions

$$\rho_1 = e^{-t/T_2} u_1, \quad \rho_2 = e^{-t/T_2} u_2, \quad \text{and} \quad \rho_3 = \rho_{30} + e^{-t/T_1} u_3. \quad (\text{D.26})$$

Substitution of (D.26) into (D.21) to (D.25) gives

$$\nabla \times \mathbf{E} = -\mu_0 \frac{\partial}{\partial t} \mathbf{H}, \quad (\text{D.27})$$

$$\nabla \times \mathbf{H} = \varepsilon_0 \varepsilon \frac{\partial}{\partial t} \mathbf{E} + A(t)u_1 \hat{\mathbf{z}} - B(t)u_2 \hat{\mathbf{z}}, \quad (\text{D.28})$$

$$\frac{\partial}{\partial t} u_1 = \omega_0 u_2, \quad (\text{D.29})$$

$$\frac{\partial}{\partial t} u_2 = -\omega_0 u_1 + C_p(t)E_z u_3 + D(t)E_z, \quad (\text{D.30})$$

$$\frac{\partial}{\partial t} u_3 = -C_m(t)E_z u_2, \quad (\text{D.31})$$

where

$$A(t) = \frac{ner_{12}}{T_2} e^{-t/T_2}, \quad (\text{D.32})$$

$$B(t) = ner_{12}\omega_0 e^{-t/T_2}, \quad (\text{D.33})$$

$$C_p(t) = 2 \frac{er_{12}}{\hbar} e^{-t(1/T_1 - 1/T_2)}, \quad (\text{D.34})$$

$$C_m(t) = 2 \frac{er_{12}}{\hbar} e^{-t(1/T_2 - 1/T_1)}, \quad (\text{D.35})$$

$$D(t) = 2 \frac{er_{12}}{\hbar} \rho_{30} e^{t/T_2}. \quad (\text{D.36})$$

For the time discretization of the Bloch equations, there are basically two possibilities. The first one has been originally proposed by Ziolkowski, where ρ is discretized at time step n and the Bloch equations are expanded around $n + 1/2$. In this case, there is a mixing between the current and next time step which makes it necessary to use a predictor-corrector or fixed-point iteration scheme [209]. The second possibility has been proposed by Bidégaray [333], where ρ is discretized at time step $n + 1/2$ and the Bloch equations consequently at time step n . At least in the one-dimensional case, this procedure leads to a fully explicit integration scheme and we will make use of it in the following. The time and space discretized variables are written using the notation $A(n\Delta t, i\Delta x, j\Delta y, k\Delta z) = A|_{ijk}^n$, where Δt , Δx , Δy , and Δz are the cell sizes in the four dimensions. Expansion of Ampère's law (D.28) around $n + 1/2$ yields

$$\begin{aligned} \mathbf{E}|_{ijk}^{n+1} &= \mathbf{E}|_{ijk}^n - \frac{\Delta t}{\varepsilon_0 \varepsilon} A(n + \frac{1}{2}) u_1|_{ijk}^{n+1/2} \hat{\mathbf{z}} \\ &+ \frac{\Delta t}{\varepsilon_0 \varepsilon} B(n + \frac{1}{2}) u_2|_{ijk}^{n+1/2} \hat{\mathbf{z}} + \frac{\Delta t}{\varepsilon_0 \varepsilon} [\nabla \times \mathbf{H}]^{n+1/2}. \end{aligned} \quad (\text{D.37})$$

Note that the state vectors u_1 and u_2 at time step $n + 1/2$ are already known when the new value of the electric field at time step $n + 1$ is to be calculated. Therefore, the Maxwell-Bloch equations have been successfully decoupled. The

final step is the discretization of the Bloch equations (D.29) to (D.31) by expanding them around time step $n + 1$ (and the state vector around $n + 1/2$). This leads to

$$\begin{aligned} u_2|_{ijk}^{n+3/2} &= \frac{F_-}{F_+} u_2|_{ijk}^{n+1/2} + \frac{4\Delta t}{F_+} \left(D(n+1) E_z|_{ijk}^{n+1} - \omega_0 u_1|_{ijk}^{n+1/2} \right) \\ &+ \frac{4\Delta t}{F_+} C_p(n+1) E_z|_{ijk}^{n+1} u_3|_{ijk}^{n+1/2}, \end{aligned} \quad (\text{D.38})$$

where

$$F_+ = 4 - \Delta t^2 \omega_0^2 - \Delta t^2 C \left(E_z|_{ijk}^{n+1} \right)^2, \quad (\text{D.39})$$

$$F_- = 4 + \Delta t^2 \omega_0^2 + \Delta t^2 C \left(E_z|_{ijk}^{n+1} \right)^2, \quad (\text{D.40})$$

$$C = C_m(t)C_p(t) = \frac{4e^2 r_{12}^2}{\hbar^2}, \quad (\text{D.41})$$

and

$$u_1|_{ijk}^{n+3/2} = u_1|_{ijk}^{n+1/2} + \frac{\Delta t \omega_0}{2} \left(u_2|_{ijk}^{n+3/2} + u_2|_{ijk}^{n+1/2} \right), \quad (\text{D.42})$$

$$\begin{aligned} u_3|_{ijk}^{n+3/2} &= u_3|_{ijk}^{n+1/2} \\ &- \frac{\Delta t C_m(n+1)}{2} E_z|_{ijk}^{n+1} \left(u_2|_{ijk}^{n+3/2} + u_2|_{ijk}^{n+1/2} \right). \end{aligned} \quad (\text{D.43})$$

Finally, we have arrived at a fully explicit integration scheme for the coupled Maxwell-Bloch equations for a two-level model.

D.3 Multilevel Maxwell-Bloch Model

In the following, we will summarize the derivation of a set of coupled differential equations for multilevel quantum well systems. The discussion is based on the textbook by Milonni and Eberly [89], unless otherwise stated. The derivation of the Maxwell-Bloch equations is generally three dimensional, but the discretization for the FDTD method will focus on a one-dimensional quantum well system. We begin with the Hamiltonian of an atomic system in an external field

$$H = H_0 + V_{\text{ext}}, \quad (\text{D.44})$$

and the time-dependent Schrödinger equation

$$i\hbar \frac{\partial \Psi}{\partial t} = H\Psi. \quad (\text{D.45})$$

The Hamiltonian of the quantum system is thereby assumed to be time-independent, leading to a complete set of eigenstates Φ_n and eigenvalues E_n which fulfill

$$H_0 \Phi_n = E_n \Phi_n. \quad (\text{D.46})$$

As the Φ_n constitute a complete set, any state Ψ of the quantum system, which is a solution to (D.45), can be written as a superposition

$$\Psi = \sum_n a_n \Phi_n, \quad (\text{D.47})$$

where the expansion coefficients a_n are called probability amplitudes.

The coupling of the QW to an applied electric field $E_z(t)$ is given in the dipole approximation as

$$V_{\text{ext}} = -\hat{d}E_z(t) = erE_z(t), \quad (\text{D.48})$$

where $\hat{d} = -er$ is the dipole moment, $-e$ the electron charge and r the displacement of the electron from its equilibrium position. We have assumed that the electric field is oriented parallel to the dipole's axis. With (D.48), the matrix elements associated with the optical transition $n \rightarrow m$ can be written as

$$V_{nm}(t) = er_{nm}E_z(t), \quad (\text{D.49})$$

where

$$r_{nm} = \langle \Phi_n | r | \Phi_m \rangle = \int \Phi_n^* r \Phi_m d^3r = r_{mn}^* \quad (\text{D.50})$$

is the transition dipole element. To include the effects of scattering, we introduce the so-called density matrix ρ via

$$\rho_{nm} = a_n a_m^*. \quad (\text{D.51})$$

Thereby, the density matrix fulfills the von Neumann equation

$$i\hbar \frac{\partial \rho}{\partial t} = i\hbar \dot{\rho} = [H, \rho], \quad (\text{D.52})$$

where the square brackets denote the commutator $[a, b] = ab - ba$, or equivalently [334]

$$i\hbar \dot{\rho}_{nm} = (E_n - E_m)\rho_{nm} + \sum_k V_{nk}\rho_{km} - \sum_l V_{lm}\rho_{nl}. \quad (\text{D.53})$$

The total rate of change of the matrix elements is equal to the sum over the individual rates of change, i.e.

$$\dot{\rho}_{nm} = (\dot{\rho}_{nm})_{\text{Schrödinger}} + (\dot{\rho}_{nm})_{\text{elastic}} \quad (\text{D.54})$$

for the off-diagonal elements and

$$\dot{\rho}_{nn} = (\dot{\rho}_{nn})_{\text{Schrödinger}} + (\dot{\rho}_{nn})_{\text{inelastic}} + (\dot{\rho}_{nn})_{\text{spontaneous emission}} \quad (\text{D.55})$$

for the diagonal elements. The terms denoted by *Schrödinger* are those in Eq. (D.53), *elastic* stands for elastic collisions, which just lead to dephasing,

inelastic stands for collisions that change the level occupations in an irreversible way, i.e. lead to loss of population and, finally, *spontaneous emission* stands for transfer of population from the upper to the lower state without being coupled to the external radiation field. In particular, the terms are given by

$$(\dot{\rho}_{nm})_{\text{elastic}} = -\frac{1}{\tau_{nm}}\rho_{nm}, \quad (\text{D.56})$$

$$(\dot{\rho}_{nn})_{\text{inelastic}} = -\Gamma_n\rho_{nn}, \quad (\text{D.57})$$

$$(\dot{\rho}_{nn})_{\text{spontaneous emission}} = -\sum_{m<n} A_{nm}\rho_{nn} + \sum_{m>n} A_{mn}\rho_{mm}. \quad (\text{D.58})$$

The coefficient A_{nm} describes population transfer between levels n and m by spontaneous emission or non-radiative scattering channels. To preserve positiveness of the density matrix, $A_{nm} \geq 0$ [210]. The relaxation of the population to thermal equilibrium can be modeled by setting [210]

$$A_{nm} = A_{mn}e^{(E_n-E_m)/(k_B T)} = A_{mn}e^{-(\hbar\omega_{mn})/(k_B T)}, \quad (\text{D.59})$$

where k_B is the Boltzmann constant and T the temperature. If only spontaneous emission is responsible for the population relaxation, then A_{nm} is given by the Einstein A coefficient

$$A_{mn} = \frac{e^2|r_{mn}|^2\omega_{mn}^3}{3\pi\epsilon_0\hbar c}, \quad m > n \quad (\text{D.60})$$

with the transition frequency

$$\omega_{nm} = \frac{1}{\hbar}(E_n - E_m) \equiv -\omega_{mn}. \quad (\text{D.61})$$

It can be shown that the effect of inelastic collisions on the off-diagonal elements ρ_{nm} is to add an additional term to the dephasing rate $1/\tau_{nm}$. The total relaxation rate is given by

$$\beta_{nm} = \frac{1}{\tau_{nm}} + \frac{1}{2}(\Gamma_n + \Gamma_m + A_{nm}) \equiv \beta_{mn}. \quad (\text{D.62})$$

With these additional terms and (D.49) inserted into (D.53), the final set of equations reads

$$\begin{aligned} \dot{\rho}_{nm} &= -(\beta_{nm} + i\omega_{nm})\rho_{nm} \\ &\quad - \frac{ie}{\hbar}E_z(t) \left(\sum_k r_{nk}\rho_{km} - \sum_l r_{lm}\rho_{nl} \right), \end{aligned} \quad (\text{D.63})$$

$$\begin{aligned} \dot{\rho}_{nn} &= -\frac{ie}{\hbar}E_z(t) \left(\sum_k r_{nk}\rho_{kn} - \sum_l r_{ln}\rho_{nl} \right) \\ &\quad - \Gamma_n\rho_{nn} - \sum_{m \neq n} A_{nm}\rho_{nn} + \sum_{m \neq n} A_{mn}\rho_{mm}. \end{aligned} \quad (\text{D.64})$$

The material equations are completed by the polarization density,

$$\mathbf{P}(\mathbf{r}, t) = P(\mathbf{r}, t)\hat{z} = -Ne \sum_{n,m} r_{nm} \rho_{mn}(\mathbf{r}, t), \quad (\text{D.65})$$

and Ampère's law

$$\nabla \times \mathbf{H}(\mathbf{r}, t) = \varepsilon_\infty \varepsilon_0 \frac{\partial \mathbf{E}}{\partial t}(\mathbf{r}, t) + \frac{\partial P}{\partial t}(\mathbf{r}, t)\hat{z}. \quad (\text{D.66})$$

Note that while the density matrix elements are complex, the polarization density and, thus, the electric field are real valued.

For the discretization, it is beneficial to have the electric field and the material parameters located at the same space grid cell. To indicate the discretized variables on the Yee grid, we use the notation $A(n\Delta t) \equiv A|^n$. Expanding Eq. (D.66) around time step $n - 1/2$ yields

$$\mathbf{E}|^n = \mathbf{E}|^{n-1} + \frac{\Delta t}{\varepsilon_\infty \varepsilon_0} [\nabla \times \mathbf{H}]^{n-1/2} - \frac{\Delta t}{\varepsilon_\infty \varepsilon_0} \dot{P} \Big|^{n-1/2} \hat{z}. \quad (\text{D.67})$$

The important point in deriving a discretized formulation of the Maxwell-Bloch equations is to choose the right time discretization the density matrix ρ . The mostly used method has been proposed by Ziolkowski [209]. The density matrix is thereby discretized at time step n and the Bloch equations are therefore expanded around $n + 1/2$. This leads to a very efficient and stable formulation, but needs a predictor-corrector scheme to solve the coupled Ampère and Bloch equations. Another approach has been given by Bidégaray [333], where ρ is discretized at intermediate time steps, $n + 1/2$, and, hence, the Bloch equations around n . In one dimension, this approach decouples the Bloch equations from the Maxwell equations and the predictor-corrector scheme has only to be used for the Bloch equations. Therefore, this method is also termed weakly-coupled scheme. We will use this discretization in the following. However, both integration schemes suffer from non-conservation of positiveness of the density matrix [210]. The solution is to split Eqs. (D.63) and (D.64) into a relaxation-nutation part

$$\dot{\rho}_{nm} = -(\beta_{nm} + i\omega_{nm}) \rho_{nm}, \quad (\text{D.68})$$

$$\dot{\rho}_{nn} = -\left(\Gamma_n + \sum_{m \neq n} A_{nm}\right) \rho_{nn} + \sum_{m \neq n} A_{mn} \rho_{mm} \quad (\text{D.69})$$

and a Hamiltonian part

$$\dot{\rho}_{nm} = -\frac{ie}{\hbar} E_z(t) \left(\sum_k r_{nk} \rho_{km} - \sum_l r_{lm} \rho_{nl} \right), \quad (\text{D.70})$$

which are separately solvable and each conserve positiveness [210]. The operations that advance $\boldsymbol{\rho}$ by one time step as a solution to the above equations are labeled by $S_R(\Delta t)$ for (D.68) and (D.69), and $S_H(E, \Delta t)$ for (D.70), respectively. It has been found by Bidégaray *et al.* [333], that the first order scheme

$$|\boldsymbol{\rho}|^{n+1/2} = S_R(\Delta t)S_H(E|^{n}, \Delta t) |\boldsymbol{\rho}|^{n-1/2} \quad (\text{D.71})$$

is already sufficient to being nonlinearly stable and to preserve positiveness. Equation (D.71) indicates that, first, the Hamiltonian part is solved and the result of the calculation has then to be inserted into the relaxation-nutation part. According to [333], the relaxation-nutation part is numerically stiff and therefore has to be computed last in order to ensure accuracy.

To solve the relaxation-nutation part, we rewrite Eqs. (D.68) and (D.69) in terms of a linear operator \mathcal{R} [210],

$$\dot{\boldsymbol{\rho}} = \mathcal{R}\boldsymbol{\rho}, \quad (\text{D.72})$$

where

$$(\mathcal{R}\boldsymbol{\rho})_{nm} = -(\beta_{nm} + i\omega_{nm})\rho_{nm}, \quad (\text{D.73})$$

$$(\mathcal{R}\boldsymbol{\rho})_{nn} = -\left(\Gamma_n + \sum_{m \neq n} A_{nm}\right)\rho_{nn} + \sum_{m \neq n} A_{mn}\rho_{mm}. \quad (\text{D.74})$$

Equation (D.72) is solved by

$$|\boldsymbol{\rho}|^{n+1/2} = e^{\mathcal{R}\Delta t} |\boldsymbol{\rho}|^{n-1/2}, \quad (\text{D.75})$$

where $\exp(\mathcal{R}\Delta t)$ is a constant matrix and can be, once calculated at the beginning of the simulation, applied to each time step.

The first step is to recognize that (D.73) and (D.74) constitute actually two independent operators, which we term \mathcal{R}_{off} and \mathcal{R}_{on} in the following. The first one, \mathcal{R}_{off} , defined via (D.73), just contains diagonal elements. The exponential is therefore easily calculated by taking the exponential element-wise, i.e.

$$e^{\mathcal{R}_{off}\Delta t}\rho_{nm} = e^{-(\beta_{nm}+i\omega_{nm})\Delta t}\rho_{nm}. \quad (\text{D.76})$$

The second operator, \mathcal{R}_{on} , defined by (D.74), can be written as a $L \times L$ matrix, where L is the number of levels. The matrix elements are then given by

$$(\mathcal{R}_{on})_{ij} = \begin{cases} -\left(\Gamma_i + \sum_{k \neq i} A_{ik}\right) & \text{for } i = j, \\ A_{ji} & \text{for } i \neq j, \end{cases} \quad (\text{D.77})$$

Due to (D.59), the matrix is in general neither symmetric nor sparse. Thus, the easiest way to tackle the problem is to calculate the exponential directly via the series expansion of the exponential [335],

$$\exp A = \sum_{n=0}^{\infty} \frac{1}{n!} A^n. \quad (\text{D.78})$$

The summation stops when the series has converged to any desired degree. As this calculation is performed just once at the beginning of the computation, it is easily extended to machine precision ϵ . The convergence criterion is in this case

$$\max_{ij} \left| \frac{(A^n)_{ij}}{n!} \right| \leq \epsilon. \quad (\text{D.79})$$

In general, the series converges after few iterations. Finally, we end up with the expression

$$e^{\mathcal{R}_{on}\Delta t} \rho_{nn} = (e^{\mathcal{R}_{on}\Delta t})_{nn} \rho_{nn} + \sum_{m \neq n} (e^{\mathcal{R}_{on}\Delta t})_{nm} \rho_{mm} \quad (\text{D.80})$$

for updating the diagonal elements of ρ .

Next, the Hamiltonian part is solved by expanding the equation around time step n using the conventional second-order finite differences,

$$\begin{aligned} \frac{1}{\Delta t} \left(\rho_{nm}|^{n+1/2} - \rho_{nm}|^{n-1/2} \right) &= -\frac{ie}{2\hbar} E|^{n-1} \left[\sum_k r_{nk} \left(\rho_{km}|^{n+1/2} + \rho_{km}|^{n-1/2} \right) \right. \\ &\quad \left. - \sum_l r_{lm} \left(\rho_{nl}|^{n+1/2} + \rho_{nl}|^{n-1/2} \right) \right]. \quad (\text{D.81}) \end{aligned}$$

Using the property $r_{nn} \equiv 0$, we state that the sums do not contain any terms $\propto \rho_{nm}|^{n+1/2}$. Thus, we can directly give the update equation for the Hamiltonian part

$$\begin{aligned} \rho_{nm}|^{n+1/2} &= \rho_{nm}|^{n-1/2} - \frac{ie\Delta t}{2\hbar} E|^{n-1} \left[\sum_k r_{nk} \left(\rho_{km}|^{n+1/2} + \rho_{km}|^{n-1/2} \right) \right. \\ &\quad \left. - \sum_l r_{lm} \left(\rho_{nl}|^{n+1/2} + \rho_{nl}|^{n-1/2} \right) \right]. \quad (\text{D.82}) \end{aligned}$$

There is still a coupling of new and old values of the state variables. However, the equations in the given form are amenable for the predictor-corrector method [209]. To this end, the equations are written in the form

$$\rho_{nm}|^{\text{new}} = \rho_{nm}|^{n-1/2} + \Delta t F_{nm} \left(\rho|^{n-1/2}, \rho|^{\text{new}} \right), \quad (\text{D.83})$$

where $F_{nm}()$ is the right hand side of the respective equation up to the old value and the bold face symbol indicates the state vector consisting of all Bloch elements. In the first iteration, $\rho|^{\text{new}}$ is set equal to the old values $\rho|^{n-1/2}$. The calculated values of $\rho|^{\text{new}}$ are then re-inserted into (D.83) until the relative change is below some threshold value. According to [209], three to five iterations are sufficient to reach a relative variation below 0.001%. The result is the

new value of the Bloch vector, $\boldsymbol{\rho}|^{n+1/2} = \boldsymbol{\rho}|^{\text{new}}$. To enhance the speed of the computation, use can be made of the relation $\rho_{nm} = \rho_{mn}^*$.

The final step is the calculation of the time derivative of the polarization density at time step $n + 1/2$. Following [333], we recognize first, that the polarization density (D.65) is equivalently written in the form

$$P(r, t) = -eN\text{Tr}(\mathbf{r}_{mn}\boldsymbol{\rho}), \quad (\text{D.84})$$

where $\text{Tr}(\cdot)$ is the trace operation and \mathbf{r}_{mn} is the dipole element matrix with coefficients given by (D.50). Furthermore, Eqs. (D.63) and (D.64) can be written in the form

$$\dot{\boldsymbol{\rho}} = (\mathcal{R}\boldsymbol{\rho}) - \frac{ie}{\hbar}E_z(t)[\mathbf{r}_{mn}, \boldsymbol{\rho}], \quad (\text{D.85})$$

with the relaxation-nutation operator \mathcal{R} introduced earlier and the commutator $[a, b]$. The time derivative of P is in this notation given by

$$\dot{P}(r, t) = -eN\text{Tr}(\mathbf{r}_{mn}(\mathcal{R}\boldsymbol{\rho})). \quad (\text{D.86})$$

where we have used the one-dimensional geometry in which $E_z(t)$ is just a scalar factor and can be pulled out of the trace. Writing Eq. (D.86) for time step $n + 1/2$ yields the result

$$\dot{P}|^{n+1/2} = -eN \sum_{n,m} r_{nm} \mathcal{R}(\boldsymbol{\rho}|^{n+1/2})_{mn}, \quad (\text{D.87})$$

which together with (D.73) and (D.74) closes the FDTD cycle.

Appendix E

Description of Laser Systems

As has been mentioned at the beginning of Chap. 4, a specialized laser system is necessary to provide the required pump pulse energies for high-power THz TDS. The setup developed during this thesis is based on a regenerative Ti:Sapphire amplifier combined with an Er:Fiber laser as seed source. The working principle of the two lasers is explained in the following.

E.1 Er:Fiber Laser

At the heart of the laser system is a commercially available fiber laser (C-Fiber Sync 780 Custom from Menlo Systems) based on Er^{3+} doped silica fibers as gain medium (see Fig. E.1 for an overview). The whole assembly consists of three parts, the passively mode-locked fiber ring oscillator with two outputs, a frequency doubling stage and a fiber amplifier stage. The fiber laser acts both as seed source for the regenerative amplifier and as probe laser for detecting the THz field. As the cavity lengths of both the fiber amplifier and the Ti:Sapphire amplifier are unknown, it is not possible to derive pump and probe pulses from the same source pulse. Rather, the probe pulse closest in time to the amplified pump pulse has to be utilized. A crucial parameter in this sense is a stable repetition rate, i.e. a constant cavity length, of the seed source. Fiber lasers are among the most stable laser sources to date, both in terms of repetition rate and pulse-to-pulse energy fluctuations. The main contribution to timing jitter comes from fluctuations of the cavity length due to thermal expansion [336]. This can be easily reduced by proper packaging of the fiber laser. The C-Fiber Sync is additionally equipped with a cavity length stabilization, which would allow synchronization with another laser source.

The working principle of a passively mode-locked fiber ring oscillator is illustrated in Fig. E.2. The necessary gain is provided by Er^{3+} ions that are introduced as dopants in conventional silica fibers. The level scheme of Er^{3+} is shown in Fig. E.2a. At room temperature, the only transition that provides sufficient gain is ${}^4\text{I}_{13/2} \rightarrow {}^4\text{I}_{15/2}$ with an emission band centered around 1535 nm.

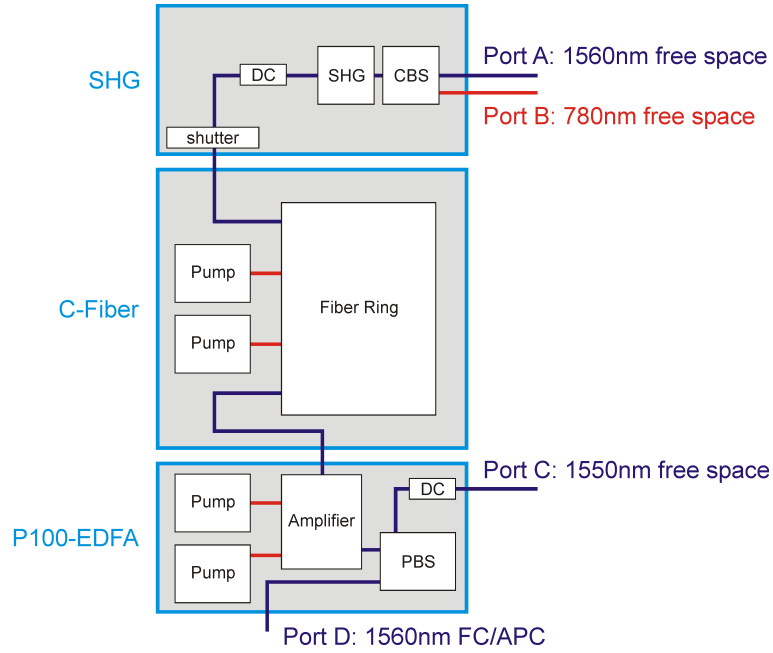


Figure E.1: Schematic of the fiber laser assembly. The output of a passively mode-locked fiber ring laser (C-Fiber) is split in two parts. One part is frequency doubled using a periodically poled LiNbO₃ crystal (SHG). The generated 780 nm light is separated from the pump beam by a chromatic beam splitter (CBS). The other part of the oscillator pulse is amplified using a fiber amplifier (P100-EDFA). By controlling the polarization of the amplified pulse, the output power ratio between a free space port (Port C) and a fiber coupled port (Port D) can be freely adjusted. Further elements are the pump laser diodes (Pump), a dispersion control (DC), an electronically controlled shutter (shutter) and a polarization sensitive beam splitter with polarization control (PBS). Figure adapted from Menlo Systems test report.

The upper laser state ${}^4I_{13/2}$ is a meta-stable state with a lifetime on the order of 10 ms [336]. Electrons are pumped into the higher lying state ${}^4I_{11/2}$ by a 980 nm pump laser. In general, master oscillator power amplifier (MOPA) diode lasers are used for this purpose due to their small footprint and low power consumption [339]. The population transfer from state ${}^4I_{11/2}$ to the upper laser level ${}^4I_{13/2}$ happens efficiently by nonradiative relaxation. In a three level laser, such as the Er³⁺ fiber laser, reabsorption of the emitted laser light by ions in the ground state plays a major role and limits the achievable gain bandwidth. However, the absorption spectrum is slightly offset from the emission spectrum, and by a proper choice of fiber length, a gain bandwidth of up to 40 nm can be achieved [336].

To get a working laser, the gain fiber has to be integrated into a cavity. The scheme of a typical passively mode-locked fiber laser ring cavity is displayed in Fig. E.2b. Passively mode-locked fiber lasers feature a low component count and yield higher pulse energies at shorter pulse durations [336]. Mode-locking

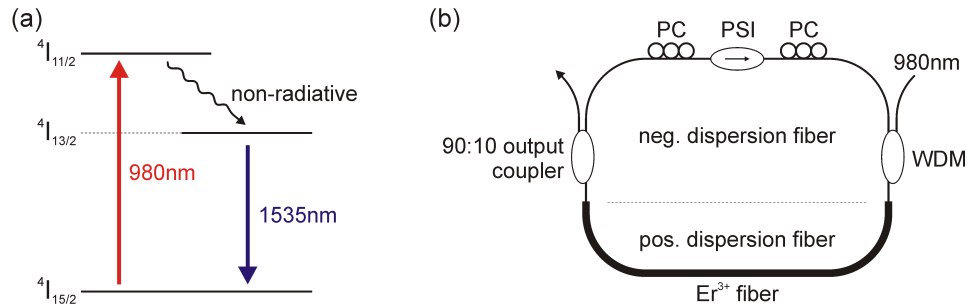


Figure E.2: (a) Level scheme of Er^{3+} ions in silica host [32]. The lasing transition is from the state $4I_{13/2}$ to $4I_{15/2}$. (b) Schematic of a ring cavity of a passively mode-locked fiber laser based on nonlinear polarization rotation [337, 338]. Unidirectional operation of the cavity is achieved by a polarization sensitive isolator (PSI). The polarization is adjusted before and after the PSI by a polarization controller (PC). The pump light is coupled in by a wavelength division multiplexer (WDM) and the laser pulses are finally coupled out by a 90:10 output coupler.

is thereby achieved either by an intracavity all-optical switch or an external saturable absorber, which exhibit reduced losses for higher intensities and therefore favor pulsed operation [336].

The cavity shown in Fig. E.2b, uses an all-fiber optical switch based on nonlinear polarization rotation [337, 338]. The polarization of the laser light traveling in the cavity is adjusted using two polarization controllers (PC) before and after a polarization sensitive isolator [340]. This element ensures both unidirectional propagation of the light and a certain polarization state. Single mode fibers are in general not isotropic and support two orthogonal polarizations, i.e. can be considered as slightly birefringent. Owing to the small core diameter, the light intensities traveling in the fiber can reach sufficiently high values to enable self- and cross-phase modulation. These two effects cause a rotation of the pulse polarization, an effect known as ellipse rotation [341]. The amount of change in polarization is thereby a function of the peak intensity. By carefully adjusting the polarization controllers, stable and self-starting mode-locked laser operation can be achieved with pulse lengths well below 100 fs [337, 338, 342].

For such short pulse lengths, dispersion is an important aspect and the minimization of the group velocity dispersion (GVD) is a key to ultrashort pulses. In fiber lasers, the GVD can be controlled by the geometry of the fiber, i.e. the core diameter and the thickness of the cladding, and to some extent by the material used. In the example shown in Fig. E.2b, two types of fiber with positive and negative dispersion are used. This serves, first, to compensate the dispersion in the cavity and, second, to reduce the nonlinearity in the fibers by using stretched pulses [337, 338].

The laser pulses are extracted by using an 90:10 output coupler just after the positive dispersion fiber. The minimum pulse length is then achieved by an

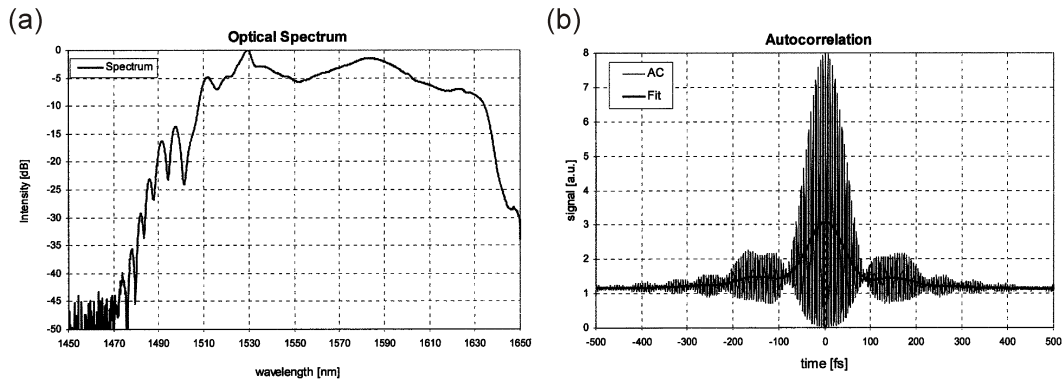


Figure E.3: (a) Spectrum and (b) autocorrelation of the 1560 nm free space port D (taken from Menlo Systems test report).

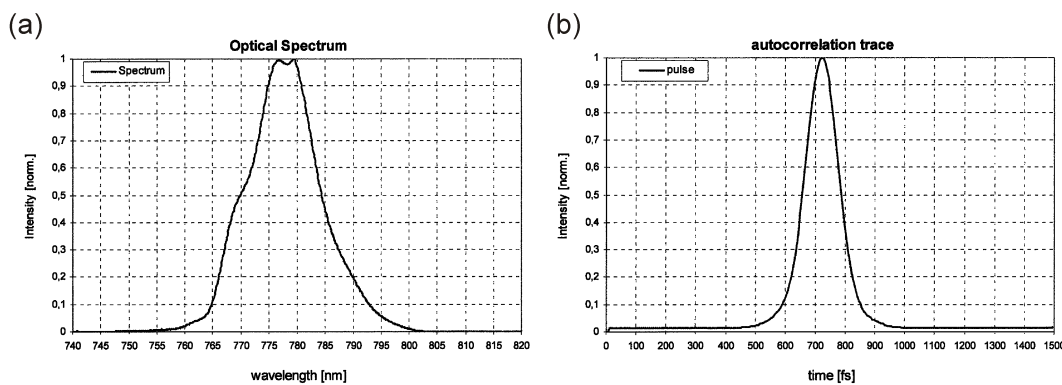


Figure E.4: (a) Spectrum and (b) autocorrelation of the 780 nm free space port B (taken from Menlo Systems test report).

external dispersion control (DC), for example, using the right length of negative dispersion fiber. The pulses are further split in two parts, one for frequency doubling (SHG) and the other one for amplification in an Er:Fiber amplifier (P100-EDFA) (see Fig. E.1). The working principle of the latter is similar to the fiber oscillator and details can be found in textbooks (see for example [336]). The P100-EDFA has two outputs, one free-space and one fiber-coupled port. The laser power can be continuously distributed among the two exit ports by using a polarization controller and a polarization sensitive fiber beam splitter. However, the shortest possible pulses at the free-space port (which is used for the setup) are achieved only for maximum power settings. The pulses have an average power of 310 mW at a pulse duration of 69 fs and a repetition rate of 80 MHz. The spectrum and the autocorrelation as given in the Menlo Systems test report are shown in Figs. E.3a and E.3b, respectively. The autocorrelation data has been confirmed by measurements with a self-built autocorrelator (not shown).

Only 20 mW of the oscillator output is fed into the Er:Fiber amplifier. The

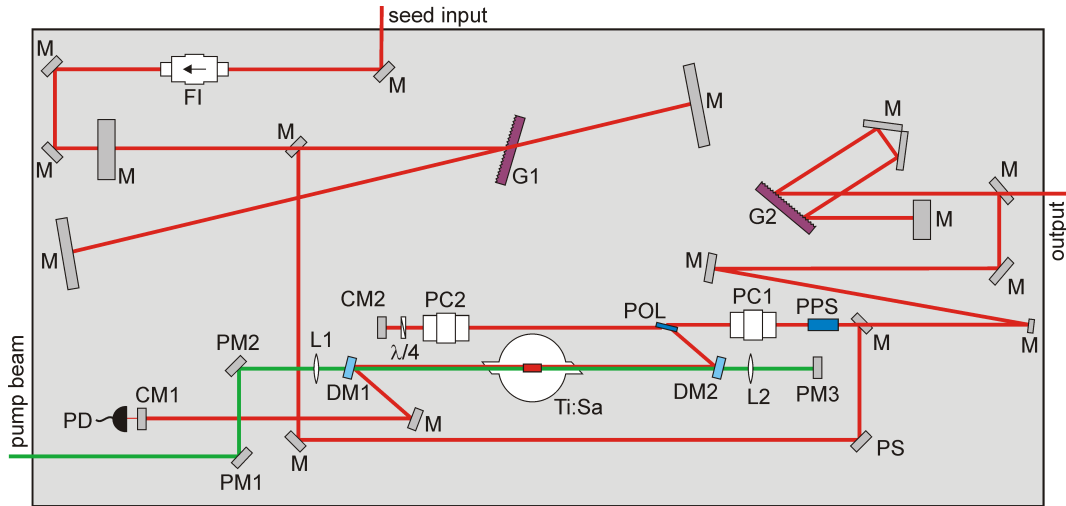


Figure E.5: Seed (red) and pump (green) beam paths in the regenerative amplifier. The optical elements are (M) mirror, (PS) periscope, (FI) Faraday isolator, (G1) stretcher grating, (G2) compressor grating, (PC1) and (PC2) Pockels cells, (CM1) and (CM2) cavity end-mirrors, (PM1) to (PM3) pump mirrors, (DM1) and (DM2) dichroic mirrors, (L1) and (L2) focusing lenses for pump beam, (Ti:Sa) Ti:Sapphire crystal in sealed chamber, (POL) thin film polarizer, (PPS) polarizing periscope, ($\lambda/4$) quarter-wave plate, and (PD) photodiode. Elements with reflected and transmitted beam indicate two different beam heights. For details see text.

main part is used for generation of frequency doubled pulses with a center wavelength of 780 nm. The schematic of the doubling stage (SHG) is shown in Fig. E.1. The SHG assembly is entirely consisting of free-space optical components. The oscillator and the SHG unit are separated by an electronically controlled optical shutter, which closes once the laser loses its mode-lock position. This is a safety measure to protect the doubling crystal from giant Q-switched pulses that may occur during the search for a new mode-lock state. The pulse is then focused into a periodically poled LiNbO_3 crystal for quasi-phase matched frequency doubling [343]. Efficiencies up to 95%/nJ are possible [336]. The remaining pump light at 1560 nm and the 780 nm pulses are spatially separated by a dichroic mirror (CBS) and are available from ports A and B, respectively. In the experiment, only the 780 nm light is used. The spectrum and the autocorrelation are shown in Figs. E.4a and E.4b, respectively. The pulses have a length of 86 fs and a spectral width of 14 nm. From an average power of 81 mW, the pulse energy is calculated to 1 nJ, which is just above the minimum value needed for seeding the regenerative amplifier.

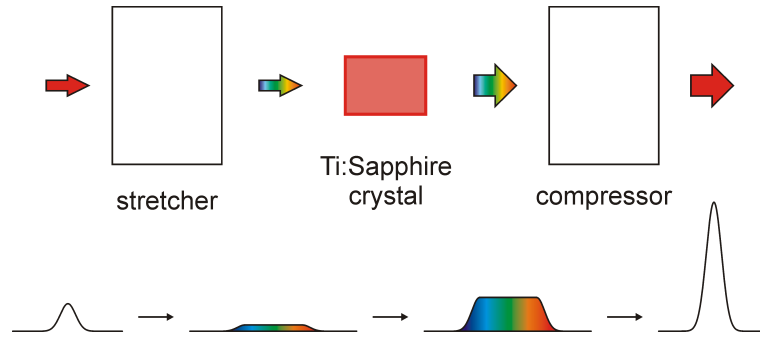


Figure E.6: Principle of stretched pulse amplification. The short seed pulse is strongly dispersed in a grating or prism stretcher to pulse lengths of several picoseconds. After amplification in the Ti:Sapphire crystal, the peak intensity is still far below the damage threshold. The pulse is finally recompressed to sub-100 fs pulse lengths in a grating compressor, for instance.

E.2 Regenerative Ti:Sapphire Amplifier

In order to increase the pump pulse energy from 1 nJ to several mJ, a commercially available regenerative Ti:Sapphire amplifier has been used (Spectra Physics Spitfire XP 4W). The beam paths of the seed, pump and amplified pulses are shown in Fig. E.5.

Due to its high saturation fluence (1 J/cm^2 [344]) and the long lifetime of the upper laser state at room temperature ($3.15 \mu\text{s}$ [345]), Ti:Sapphire is the ideal amplifier gain material. Additionally, the emission and absorption bands are spectrally well separated with their maxima centered around 800 nm and 500 nm, respectively [345]. To minimize spurious reflections, the crystal facets are coated with a high-quality anti-reflection coating that can withstand the high pump fluences. Compared to the more commonly used method of cutting the facets under the Brewster angle, this method has the advantage of easier alignment and better beam profile, leading to a higher quality of the amplified pulse. The crystal is sealed in a chamber filled with dry air ($< 1\%$ humidity) and cooled to -10°C to reduce the heat load to the crystal and the associated thermal lensing effects.

The necessary energy for pumping the amplifier crystal is delivered by a frequency doubled Q-switched Nd:YLF laser (Spectra Physics Empower30) with a center wavelength of 527 nm. The repetition rate of the pump laser is 1 kHz with an average power of 18 W. The pulse energy of 18 mJ is deposited in the crystal over several nanoseconds, giving the circulating seed pulse enough time to reach saturation. The crystal is primarily pumped from one side with the transmitted part of the pump pulse being reflected back into the crystal from the other side. This pump geometry features an easy alignment and yields a good gain profile. Compared to a two-sided pumping geometry, the number of optics is reduced, again improving the performance.

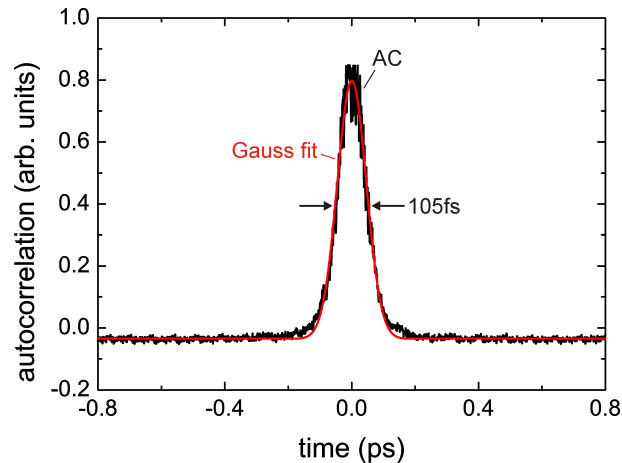


Figure E.7: Autocorrelation trace (black) of the amplified pulse for the compressor adjusted for the shortest pulse length. From a least-squares fit of a Gaussian to the autocorrelation trace (red) the pulse FWHM-length is estimated to 75 fs.

There are two basic schemes for amplification of the seed pulse, regenerative amplification and multipass amplification [344]. While, in the latter, the seed pulse experiences less absorption and dispersion due to a lower component count, it is much more difficult to achieve a good overlap with the pump region and to maintain stable operation. In the regenerative amplification scheme, a seed pulse is picked by the first Pockels cell (PC1) and is inserted into the cavity. Thereby, the 80 MHz repetition rate of the seed laser is reduced to the 1 kHz repetition rate of the amplifier. After typically 12 to 15 passes through the crystal, the pulse energy has saturated and the pulse is ejected by the second Pockels cell (PC2). The beam paths of both seed and pump pulses are collinear in the crystal which yields a good overlap of the seed pulse with the gain region. Additionally, the beams are normally incident on the crystal which helps to further minimize thermal lensing effects.

An important aspect limiting the amplification of ultrashort laser pulses are the extremely high fluences involved. The damage threshold of most optical materials is on the order of a few GW/cm^2 while typical peak powers easily reach two to three orders of magnitude higher values [344]. The solution is the so-called chirped pulse amplification (CPA). The principle is sketched in Fig. E.6. The ultrashort seed pulse is first stretched to a pulse length around 100 ps using a 4-pass grating stretcher (G1). The peak intensity of the pulse is therefore reduced by three orders of magnitude. The grating stretcher delays different frequency components by a different amount of time, resulting in a strongly chirped pulse (therefore the name).

The stretched pulse can now safely be amplified without damaging the crystal. The regenerative amplifier can reach amplification levels on the order of 10^6 . After the amplification, the pulse is recompressed to 75 fs using a 4-pass grating

compressor (G2). The autocorrelation of the compressed pulse is shown in Fig. E.7 together with a least-squares fit of a Gaussian. The output pulses have a pulse energy of 4 mJ at a repetition rate of 1 kHz and a center wavelength of 780 nm. To avoid any self-focusing effects during propagation in ambient air, the beam $1/e^2$ -diameter is 8 mm.

Bibliography

- [1] W. Schmidt, *Optical Spectroscopy in Chemistry and Life Sciences: An Introduction* (Wiley, New York, 2005).
- [2] Y.-S. Lee, *Principles of Terahertz Science and Technology* (Springer, New York, 2009).
- [3] C. Kittel, *Einführung in die Festkörperphysik* (Oldenbourg, München, 2002).
- [4] H. Harde, S. Keiding, and D. Grischkowsky, THz commensurate echoes: Periodic rephasing of molecular transitions in free-induction decay, *Phys. Rev. Lett.* **66**, 1834–1837 (1991).
- [5] M. C. Nuss, K. W. Goossen, J. P. Gordon, P. M. Mankiewich, and M. L. O'Malley, Terahertz time-domain measurement of the conductivity and superconducting band gap in niobium, *J. Appl. Phys.* **70**, 2238–2241 (1991).
- [6] R. Ulbricht, E. Hendry, J. Shan, T. F. Heinz, and M. Bonn, Carrier dynamics in semiconductors studied with time-resolved terahertz spectroscopy, *Rev. Mod. Phys.* **83**, 543–586 (2011).
- [7] A. Tackeuchi, S. Muto, T. Inata, and T. Fujii, Direct observation of picosecond spin relaxation of excitons in GaAs/AlGaAs quantum wells using spin-dependent optical nonlinearity, *Appl. Phys. Lett.* **56**, 2213–2215 (1990).
- [8] T. C. Damen, K. Leo, J. Shah, and J. E. Cunningham, Spin relaxation and thermalization of excitons in GaAs quantum wells, *Appl. Phys. Lett.* **58**, 1902–1904 (1991).
- [9] A. Tackeuchi, O. Wada, and Y. Nishikawa, Electron spin relaxation in InGaAs/InP multiple-quantum wells, *Appl. Phys. Lett.* **70**, 1131–1133 (1997).
- [10] J. F. Federici, B. Schulkin, F. Huang, D. Gary, R. Barat, F. Oliveira, and D. Zimdars, THz imaging and sensing for security applications - explosives, weapons and drugs, *Semicond. Sci. Technol.* **20**, S266–S280 (2005).
- [11] C. Jördens and M. Koch, Detection of foreign bodies in chocolate with pulsed terahertz spectroscopy, *Opt. Eng.* **47**, 037003 (2008).
- [12] K. Fukunaga, Y. Ogawa, S. Hayashi, and I. Hosako, Terahertz spectroscopy for art conservation, *IEICE Electronics Express* **4**, 258–263 (2007).

- [13] A. J. Fitzgerald, E. Berry, N. N. Zinovev, G. C. Walker, M. A. Smith, and J. M. Chamberlain, An introduction to medical imaging with coherent terahertz frequency radiation, *Phys. Med. Biol.* **47**, R67–R84 (2002).
- [14] J. M. Chamberlain, Where optics meets electronics: recent progress in decreasing the terahertz gap, *Phil. Trans. R. Soc. Lond. A* **362**, 199–213 (2004).
- [15] D. H. Auston, K. P. Cheung, and P. R. Smith, Picosecond photoconductive Hertzian dipoles, *Appl. Phys. Lett.* **45**, 284–286 (1984).
- [16] W. S. Benedict, M. A. Pollack, and W. J. Tomlinson, III, The water-vapor laser, *IEEE J. Quantum Electron.* **QE-5**, 108–124 (1969).
- [17] K. Johnson, M. Price-Gallagher, O. Mamer, A. Lesimple, C. Fletcher, Y. Chen, X. Lu, M. Yamaguchi, and X.-C. Zhang, Water vapor: An extraordinary terahertz wave source under optical excitation, *Phys. Lett. A* **372**, 6037–6040 (2008).
- [18] J. Horvat and R. A. Lewis, Peeling adhesive tape emits electromagnetic radiation at terahertz frequencies, *Opt. Lett.* **34**, 2195–2197 (2009).
- [19] B. Ferguson and X.-C. Zhang, Materials for terahertz science and technology, *Nat. Mater.* **1**, 26–33 (2002).
- [20] P. H. Siegel, Terahertz technology, *IEEE Trans. Microwave Theory Tech.* **50**, 910–928 (2002).
- [21] M. F. Kimmitt, Reststrahlen to T-Rays - 100 years fo terahertz radiation, *J. Biol. Phys.* **29**, 77–85 (2003).
- [22] D. Dragoman and M. Dragoman, Terahertz fields and applications, *Prog. Quantum Electron.* **28**, 1–66 (2004).
- [23] K. Sakai (Ed.), *Terahertz Optoelectronics* (Springer, New York, 2004).
- [24] O. Manasreh, *Semiconductor Heterojunctions and Nanostructures* (McGraw-Hill, New York, 2005).
- [25] P. R. Smith, D. H. Auston, A. M. Johnson, and W. M. Augustyniak, Picosecond photoconductivity in radiation-damaged silicon-on-sapphire films, *Appl. Phys. Lett.* **38**, 47–50 (1981).
- [26] D. H. Auston, Subpicosecond electro-optic shock waves, *Appl. Phys. Lett.* **43**, 713–715 (1983).
- [27] A. Y. Cho and J. R. Arthur, Molecular beam epitaxy, *Prog. Solid State Chem.* **10**, 157–191 (1975).
- [28] F. W. Smith, A. R. Calawa, C.-L. Chen, M. J. Manfra, and L. J. Mahoney, New MBE buffer used to eliminate backgating in GaAs MESFETs, *IEEE Electron Device Lett.* **9**, 77–80 (1988).

-
- [29] S. Gupta, M. Y. Frankel, J. A. Valdmanis, J. F. Whitaker, G. A. Mourou, F. W. Smith, and A. R. Calawa, Subpicosecond carrier lifetime in GaAs grown by molecular beam epitaxy at low temperatures, *Appl. Phys. Lett.* **59**, 3276–3278 (1991).
- [30] G. Bastard, *Wave Mechanics Applied to Semiconductor Heterostructures* (Wiley, New York, 1991).
- [31] L. C. West and S. J. Eglash, First observation of an extremely large-dipole infrared transition within the conduction band of a GaAs quantum well, *Appl. Phys. Lett.* **46**, 1156–1158 (1985).
- [32] A. Yariv, *Optical electronics in modern communications* (Oxford University Press, 1997).
- [33] G. L. Hansen, J. L. Schmit, and T. N. Casselman, Energy gap versus alloy composition and temperature in $\text{Hg}_{1-x}\text{Cd}_x\text{Te}$, *J. Appl. Phys.* **53**, 7099–7101 (1982).
- [34] Y. Zhang, T.-T. Tang, C. Girit, Z. Hao, M. C. Martin, A. Zettl, M. F. Crommie, Y. R. Shen, and F. Wang, Direct observation of a widely tunable bandgap in bilayer graphene, *Nature* **459**, 820–823 (2009).
- [35] A. A. Andronov, I. V. Zverev, V. A. Kozlov, Y. N. Nozdrin, S. A. Pavlov, and V. N. Shastin, Stimulated emission in the long-wavelength IR region from hot holes in Ge in crossed electric and magnetic fields, *JETP Letters* **40**, 804–807 (1984).
- [36] J. Faist, F. Capasso, D. L. Sivco, C. Sirtori, A. L. Hutchinson, and A. Y. Cho, Quantum cascade laser, *Science* **22**, 553–556 (1994).
- [37] R. Köhler, A. Tredicucci, F. Beltram, H. E. Beere, E. H. Linfield, A. G. Davies, D. A. Ritchie, R. C. Iotti, and F. Rossi, Terahertz semiconductor-heterostructure laser, *Nature* **417**, 156–159 (2002).
- [38] B. S. Williams, Terahertz quantum-cascade lasers, *Nat. Photonics* **1**, 517–525 (2007).
- [39] P. Dean, Y. L. Lim, A. Valavanis, R. Kliese, M. Nikolić, S. P. Khanna, M. Lachab, D. Indjin, Z. Ikonić, P. Harrison, A. D. Rakić, E. H. Linfield, and A. G. Davies, Terahertz imaging through self-mixing in a quantum cascade laser, *Opt. Lett.* **36**, 2587–2589 (2011).
- [40] M. Helm, *The Basic Physics of Intersubband Transitions* (Academic Press, San Diego, 2000) vol. 62 of *Semiconductors and Semimetals*.
- [41] B. F. Levine, R. J. Malik, J. Walker, K. K. Choi, C. G. Bethea, D. A. Kleinman, and J. M. Vandenberg, Strong $8.2\mu\text{m}$ infrared intersubband absorption in doped GaAs/AlAs quantum well waveguides, *Appl. Phys. Lett.* **50**, 273–275 (1987).

- [42] F. Keilmann, Critical-incidence coupling to intersubband excitations, *Solid State Commun.* **92**, 223–226 (1994).
- [43] D. Heitmann, J. P. Kotthaus, and E. G. Mohr, Plasmon dispersion and intersubband resonance at high wavevectors in Si(100) inversion layers, *Solid State Commun.* **44**, 715–718 (1982).
- [44] V. G. Veselago, The electrodynamics of substances with simultaneously negative values of ϵ and μ , *Sov. Phys. Usp.* **10**, 509–514 (1968), (original publication *Usp. Fiz. Nauk* 92, 517–526 (1964)).
- [45] J. B. Pendry, Negative refraction makes a perfect lens, *Phys. Rev. Lett.* **85**, 3966–3969 (2000).
- [46] J. W. Strutt (Lord Rayleigh), On the influence of obstacles arranged in rectangular order upon the properties of a medium, *Phil. Mag. Series 5* **34**, 481–502 (1892).
- [47] W. E. Kock, Metallic delay lenses, *Bell System Tech. J.* **27**, 58–82 (1948).
- [48] R. E. Collin, *Field Theory of Guided Waves* (McGraw-Hill, New York, 1960).
- [49] W. Weber, Ueber den Zusammenhang der Lehre vom Diamagnetismus mit der Lehre von dem Magnetismus und der Elektrizität, *Ann. Phys.* **87**, 145–189 (1852).
- [50] S. A. Schelkunoff and H. T. Friis, *Antennas. Theory and Practice* (Wiley, New York, 1952).
- [51] N. Fang, H. Lee, C. Sun, and X. Zhang, Sub-diffraction-limited optical imaging with a silver superlens, *Science* **308**, 534–537 (2005).
- [52] R. Ulrich, Interference filters for the far infrared, *Appl. Opt.* **7**, 1987–1996 (1968).
- [53] S. T. Chase and R. D. Joseph, Resonant array bandpass filters for the far infrared, *Appl. Opt.* **22**, 1775–1779 (1983).
- [54] H. Tao, N. I. Landy, C. M. Bingham, X. Zhang, R. D. Averitt, and W. J. Padilla, A metamaterial absorber for the terahertz regime: Design, fabrication and characterization, *Opt. Express* **16**, 7181–7188 (2008).
- [55] N. I. Landy, S. Sajuyigbe, J. J. Mock, D. R. Smith, and W. J. Padilla, Perfect metamaterial absorber, *Phys. Rev. Lett.* **100**, 207402 (2008).
- [56] J. B. Pendry, D. Schurig, and D. R. Smith, Controlling electromagnetic fields, *Science* **312**, 1780–1782 (2006).
- [57] U. Leonhardt, Optical conformal mapping, *Science* **312**, 1777–1780 (2006).
- [58] R. Liu, C. Ji, J. J. Mock, J. Y. Chin, T. J. Cui, and D. R. Smith, Broadband ground-plane cloak, *Science* **323**, 366–369 (2009).

-
- [59] S. Zhang, D. A. Genov, Y. Wang, M. Liu, and X. Zhang, Plasmon-induced transparency in metamaterials, *Phys. Rev. Lett.* **101**, 047401 (2008).
- [60] N. Verellen, Y. Sonnefraud, H. Sobhani, F. Hao, V. V. Moshchalkov, P. Van Dorpe, P. Nordlander, and S. A. Maier, Fano resonances in individual coherent plasmonic nanocavities, *Nano Lett.* **9**, 1663–1667 (2009).
- [61] F. Capolino, *Theory and Phenomena of Metamaterials* (CRC Press, Boca Raton, 2009).
- [62] M. A. Seo, H. R. Park, S. M. Koo, D. J. Park, J. H. Kang, O. K. Suwal, S. S. Choi, P. C. M. Planken, G. S. Park, N. K. Park, Q. H. Park, and D. S. Kim, Terahertz field enhancement by a metallic nano slit operating beyond the skin-depth limit, *Nat. Photonics* **3**, 152–156 (2009).
- [63] R. W. Boyd, *Nonlinear Optics* (Academic Press, San Diego, 2008) 3rd ed.
- [64] M. W. Klein, C. Enkrich, M. Wegener, and S. Linden, Second-harmonic generation from magnetic metamaterials, *Science* **313**, 502–504 (2006).
- [65] M. W. Klein, M. Wegener, N. Feth, and S. Linden, Experiments on second- and third-harmonic generation from magnetic metamaterials, *Opt. Express* **15**, 5238–5247 (2007).
- [66] H. Merbold, A. Bitzer, and T. Feurer, Second harmonic generation based on strong field enhancement in nanostructured THz materials, *Opt. Express* **19**, 7262–7273 (2011).
- [67] A. Mayer and F. Keilmann, Far-infrared nonlinear optics. II. $\chi^{(3)}$ contributions from the dynamics of free carriers in semiconductors, *Phys. Rev. B* **33**, 6962–6968 (1986).
- [68] H. Shichijo and K. Hess, Band-structure-dependent transport and impact ionization in GaAs, *Phys. Rev. B* **23**, 4197–4207 (1981).
- [69] Y. Shi, Q.-I. Zhou, C. Zhang, and B. Jin, Ultrafast high-field carrier transport in GaAs measured by femtosecond pump-terahertz probe spectroscopy, *Appl. Phys. Lett.* **93**, 121115 (2008).
- [70] M. C. Hoffmann, J. Hebling, H. Y. Hwang, K.-L. Yeh, and K. A. Nelson, THz-pump / THz-probe spectroscopy of semiconductors at high field strengths, *J. Opt. Soc. Am. B* **26**, A29–A34 (2009).
- [71] W. Kuehn, P. Gaal, K. Reimann, M. Woerner, T. Elsaesser, and R. Hey, Coherent ballistic motion of electrons in a periodic potential, *Phys. Rev. Lett.* **104**, 146602 (2010).
- [72] L. Razzari, F. H. Su, G. Sharma, F. Blanchard, A. Ayesheshim, H.-C. Bandulet, R. Morandotti, J.-C. Kieffer, T. Ozaki, M. Reid, and F. A. Hegmann, Nonlinear ultrafast modulation of the optical absorption of intense few-cycle terahertz pulses in n-doped semiconductors, *Phys. Rev. B* **79**, 193204 (2009).

- [73] F. H. Su, F. Blanchard, G. Sharma, L. Razzari, A. Ayesheshim, T. L. Cocker, L.V. Titova, T. Ozaki, J.-C. Kieffer, R. Morandotti, M. Reid, and F. A. Hegmann, Terahertz pulse induced intervalley scattering in photoexcited GaAs, *Opt. Express* **17**, 9620–9629 (2009).
- [74] I.-C. Ho and X.-C. Zhang, Driving intervalley scattering and impact ionization in InAs with intense terahertz pulses, *Appl. Phys. Lett.* **98**, 241908 (2011).
- [75] R. Mickevičius and A. Reklaitis, Electron intervalley scattering in gallium arsenide, *Semicond. Sci. Technol.* **5**, 805–812 (1990).
- [76] T. Löffler, M. Kreß, M. Thomson, T. Hahn, N. Hasegawa, and H. G. Roskos, Comparative performance of terahertz emitters in amplifier-laser-based systems, *Semicond. Sci. Technol.* **20**, S134–S141 (2005).
- [77] M. C. Hoffmann and J. A. Fülöp, Intense ultrashort terahertz pulses: generation and applications, *J. Phys. D* **44**, 083001 (2011).
- [78] J. Hebling, K.-L. Yeh, M. C. Hoffmann, B. Bartal, and K. A. Nelson, Generation of high-power terahertz pulses by tilted-pulse-front excitation and their application possibilities, *J. Opt. Soc. Am. B* **25**, B6–B19 (2008).
- [79] J. A. Fülöp, L. Pálfalvi, M. C. Hoffmann, and J. Hebling, Towards generation fo mJ-level ultrashort THz pulses by optical rectification, *Opt. Express* **19**, 15090–15097 (2011).
- [80] H. Hirori, A. Doi, F. Blanchard, and K. Tanaka, Single-cycle terahertz pulses with amplitudes exceeding 1MV/cm generated by optical rectification in LiNbO₃, *Appl. Phys. Lett.* **98**, 091106 (2011).
- [81] A. Sell, A. Leitenstorfer, and R. Huber, Phase-locked generation and field-resolved detection of widely tunable terahertz pulses with amplitudes exceeding 100MV/cm, *Opt. Lett.* **33**, 2767–2769 (2008).
- [82] F. Junginger, A. Sell, O. Schubert, B. Mayer, D. Brida, M. Marangoni, G. Cerullo, A. Leitenstorfer, and R. Huber, Single-cycle multiterahertz transients with peak fields above 10MV/cm, *Opt. Lett.* **35**, 2645–2647 (2010).
- [83] A. A. Michelson, On the application of interference-methods to spectroscopic measurements, *Philos. Mag.* **31** (5), 338–346 (1891).
- [84] E. D. Palik, A far infrared bibliography, *J. Opt. Soc. Am.* **50**, 1329–1336 (1960).
- [85] P. B. Fellgett, Spectromètre interférentiel multiplex pour mesures infra-rouges sur les étoiles, *J. Phys. Radium* **19**, 237–240 (1958).
- [86] G. Grüner (Ed.), *Millimeter and Submillimeter Wave Spectroscopy of Solids* (Springer, New York, 1998).

-
- [87] M. Born and E. Wolf, *Principles of Optics* (Cambridge University Press, 1999) 7th ed.
- [88] P. R. Griffiths and J. A. de Haseth, *Fourier Transform Infrared Spectroscopy* (Wiley, New York, 2007).
- [89] P. W. Milonni and J. H. Eberly, *Lasers* (Wiley, New York, 1988).
- [90] S. P. Langley, The bolometer, *Nature* **25**, 14–16 (1881).
- [91] D. H. Auston, K. P. Cheung, J. A. Valdmanis, and D. A. Kleinman, Cherenkov radiation from femtosecond optical pulses in electro-optic media, *Phys. Rev. Lett.* **53**, 1555–1558 (1984).
- [92] C. Fattering and D. Grischkowsky, Point source terahertz optics, *Appl. Phys. Lett.* **53**, 1480–1482 (1988).
- [93] M. van Exter, C. Fattering, and D. Grischkowsky, High-brightness terahertz beams characterized with an ultrafast detector, *Appl. Phys. Lett.* **55**, 337–339 (1989).
- [94] J. Xu and X.-C. Zhang, Circular involute stage, *Opt. Lett.* **29**, 2082–2084 (2004).
- [95] G.-J. Kim, S.-G. Jeon, J.-I. Kim, and Y.-S. Jin, Terahertz pulse detection using rotary optical delay line, *Jpn. J. Appl. Phys.* **46**, 7332–7335 (2007).
- [96] P. A. Elzinga, R. J. Kneisler, F. E. Lytle, Y. Jiang, G. B. King, and N. M. Laurendeau, Pump/probe method for fast analysis of visible spectral signatures utilizing asynchronous optical sampling, *Appl. Opt.* **26**, 4303–4309 (1987).
- [97] C. Janke, M. Först, M. Nagel, H. Kurz, and A. Bartels, Asynchronous optical sampling for high-speed characterization of integrated resonant terahertz sensors, *Opt. Lett.* **30**, 1405–1407 (2005).
- [98] T. Yasui, E. Saneyoshi, and T. Araki, Asynchronous optical sampling terahertz time-domain spectroscopy for ultrahigh spectral resolution and rapid data acquisition, *Appl. Phys. Lett.* **87**, 061101 (2005).
- [99] G. Sucha, M. E. Fermann, D. J. Hartner, and M. Hofer, A new method for rapid temporal scanning of ultrafast lasers, *IEEE J. Sel. Top. Quantum Electron.* **2**, 605–621 (1996).
- [100] F. Tauser, C. Rausch, J. H. Posthumus, and F. Lison, Electronically controlled optical sampling using 100MHz repetition rate fiber lasers, *Proc. SPIE* **6881**, 68810O (2008).
- [101] L. Duvillaret, F. Garet, and J.-L. Coutaz, A reliable method for extraction of material parameters in terahertz time-domain spectroscopy, *IEEE J. Sel. Top. Quantum Electron.* **2**, 739–746 (1996).

- [102] W. Sha, A. L. Smirl, and W. F. Tseng, Coherent plasma oscillations in bulk semiconductors, *Phys. Rev. Lett.* **74**, 4273–4276 (1995).
- [103] R. Kersting, K. Unterrainer, G. Strasser, H. F. Kauffmann, and E. Gornik, Few-cycle THz emission from cold plasma oscillations, *Phys. Rev. Lett.* **79**, 3038–3041 (1997).
- [104] R. Kersting, J. N. Heyman, G. Strasser, and K. Unterrainer, Coherent plasmons in n-doped GaAs, *Phys. Rev. B* **58**, 4553–4559 (1998).
- [105] J. Darmo, G. Strasser, T. Müller, R. Bratschitsch, and K. Unterrainer, Surface-modified GaAs terahertz plasmon emitter, *Appl. Phys. Lett.* **81**, 871–873 (2002).
- [106] R. Atanasov, A. Heché, J. L. P. Hughes, H. M. van Driel, and J. E. Sipe, Coherent control of photocurrent generation in bulk semiconductors, *Phys. Rev. Lett.* **76**, 1703–1706 (1996).
- [107] D. Côté, J. M. Fraser, M. DeCamp, P. H. Bucksbaum, and H. M. van Driel, THz emission from coherently controlled photocurrents in GaAs, *Appl. Phys. Lett.* **75**, 3959–3961 (1999).
- [108] H. Hamster, A. Sullivan, S. Gordon, W. White, and R. W. Falcone, Subpicosecond, electromagnetic pulses from intense laser-plasma interaction, *Phys. Rev. Lett.* **71**, 2725–2728 (1993).
- [109] D. J. Cook and R. M. Hochstrasser, Intense terahertz pulses by four-wave rectification in air, *Opt. Lett.* **25**, 1210–1212 (2000).
- [110] T. Löffler, T. Hahn, M. Thomson, F. Jacob, and H. G. Roskos, Large-area electro-optic ZnTe terahertz emitters, *Opt. Express* **13**, 5353–5362 (2005).
- [111] K. K. Williams, Z. D. Taylor, J. Y. Suen, H. Lu, R. S. Singh, A. C. Gossard, and E. R. Brown, Toward a 1550nm InGaAs photoconductive switch for terahertz generation, *Opt. Lett.* **34**, 3068–3070 (2009).
- [112] H. Roehle, R. J. B. Dietz, H. J. Hensel, J. Böttcher, H. Künzel, D. Stanze, M. Schell, and B. Sartorius, Next generation 1.5 μ m terahertz antennas: mesa-structuring of InGaAs/InAlAs photoconductive layers, *Opt. Express* **18**, 2296–2301 (2010).
- [113] D. E. Aspnes and A. A. Studna, Dielectric functions and optical parameters of Si, Ge, GaP, GaAs, GaSb, InP, InAs, and InSb from 1.5 to 6.0 eV, *Phys. Rev. B* **27**, 985–1009 (1983).
- [114] D. Krökel, D. Grischkowsky, and M. B. Ketchen, Subpicosecond electrical pulse generation using photoconductive switches with long carrier lifetimes, *Appl. Phys. Lett.* **54**, 1046–1047 (1989).

-
- [115] N. Katzenellenbogen and D. Grischowsky, Efficient generation of 380fs pulses of THz radiation by ultrafast laser pulse excitation of a biased metal-semiconductor interface, *Appl. Phys. Lett.* **58**, 222–224 (1990).
- [116] J. Kröll, *High performance terahertz time-domain spectroscopy: Application, control and amplification of few cycle terahertz radiation*, PhD thesis, Vienna University of Technology (2007).
- [117] P. U. Jepsen, R. H. Jacobsen, and S. R. Keiding, Generation and detection of terahertz pulses from biased semiconductor antennas, *J. Opt. Soc. Am. B* **13**, 2424–2436 (1996).
- [118] I. A. Stegun and M. Abramowitz, *Handbook of Mathematical Functions* (Dover, 1965).
- [119] J. D. Jackson, *Klassische Elektrodynamik* (Walter de Gruyter, Berlin, 2002).
- [120] W. Sha, J.-K. Rhee, T. B. Norris, and W. J. Schaff, Transient carrier and field dynamics in quantum-well parallel transport: From the ballistic to the quasi-equilibrium regime, *IEEE J. Quantum Electron.* **28**, 2445–2455 (1992).
- [121] J. E. Pedersen, V. G. Lyssenko, J. M. Hvam, P. U. Jepsen, S. R. Keiding, C. B. Sørensen, and P. E. Lindelof, Ultrafast local field dynamics in photoconductive THz antennas, *Appl. Phys. Lett.* **62**, 1265–1267 (1993).
- [122] S. D. Brorson, J. Zhang, and S. R. Keiding, Ultrafast carrier trapping and slow recombination in ion-bombarded silicon on sapphire measured via THz spectroscopy, *Appl. Phys. Lett.* **64**, 2385–2387 (1994).
- [123] G. C. Loata, M. D. Thomson, T. Löffler, and H. G. Roskos, Radiation field screening in photoconductive antennae studied via pulsed terahertz emission spectroscopy, *Appl. Phys. Lett.* **91**, 232506 (2007).
- [124] S. Kono, M. Tani, and K. Sakai, Coherent detection of mid-infrared radiation up to 60THz with an LT-GaAs photoconductive antenna, *IEE Proc.: Optoelectron.* **149**, 105–109 (2002).
- [125] J. A. Valdmanis, G. Mourou, and C. W. Gabel, Picosecond electro-optic sampling system, *Appl. Phys. Lett.* **41**, 211–212 (1982).
- [126] J. A. Valdmanis and G. Mourou, Subpicosecond electrooptic sampling: Principles and applications, *IEEE J. Quantum Electron.* **QW-22**, 69–78 (1986).
- [127] Y. Cai, I. Brener, J. Lopata, J. Wynn, L. Pfeiffer, J. B. Stark, Q. Wu, X.-C. Zhang, and J. F. Federici, Coherent terahertz radiation detection: Direct comparison between free-space electro-optic sampling and antenna detection, *Appl. Phys. Lett.* **73**, 444–446 (1998).
- [128] Q. Wu and X.-C. Zhang, Design and characterization of traveling-wave electrooptic terahertz sensors, *IEEE J. Sel. Top. Quantum Electron.* **2**, 693–700 (1996).

- [129] Q. Wu and X.-C. Zhang, 7 terahertz broadband GaP electro-optic sensor, *Appl. Phys. Lett.* **70**, 1784–1786 (1997).
- [130] P. C. M. Planken, H.-K. Nienhuys, H. J. Bakker, and T. Wenckebach, Measurement and calculation of the orientation dependence of terahertz pulse detection in ZnTe, *J. Opt. Soc. Am. B* **18**, 313–317 (2001).
- [131] J. Kröll, J. Darmo, and K. Unterrainer, Metallic wave-impedance matching layers for broadband terahertz optical systems, *Opt. Express* **15**, 6552–6560 (2007).
- [132] W. L. Faust and C. H. Henry, Mixing of visible and near-resonance infrared light in GaP, *Phys. Rev. Lett.* **17**, 1265–1268 (1966).
- [133] A. Leitenstorfer, S. Hunsche, J. Shah, M. C. Nuss, and W. H. Knox, Detectors and sources for ultrabroadband electro-optic sampling: Experiment and theory, *Appl. Phys. Lett.* **74**, 1516–1518 (1999).
- [134] D. J. Lockwood, G. Yu, and N. L. Rowell, Optical phonon frequencies and damping in AlAs, GaP, GaAs, InP, InAs and InSb studied by oblique incidence infrared spectroscopy, *Solid State Commun.* **136**, 404–409 (2005).
- [135] W. L. Faust, C. H. Henry, and R. H. Eick, Dispersion in the nonlinear susceptibility of GaP near the Reststrahl band, *Phys. Rev.* **173**, 781–786 (1968).
- [136] W. D. Johnston, Jr. and I. P. Kaminow, Contributions to optical nonlinearity in GaAs as determined from Raman scattering efficiencies, *Phys. Rev.* **188**, 1209–1211 (1969).
- [137] D. F. Nelson and E. H. Turner, Electro-optic and piezoelectric coefficients and refractive index of gallium phosphide, *J. Appl. Phys.* **39**, 3337–3343 (1968).
- [138] F. L. Madarasz, J. O. Dimmock, N. Dietz, and K. J. Bachmann, Sellmeier parameters for ZnGaP₂ and GaP, *J. Appl. Phys.* **87**, 1564–1565 (2000).
- [139] H. H. Li, Refractive index of ZnS, ZnSe, and ZnTe and its wavelength and temperature derivatives, *J. Phys. Chem. Ref. Data* **13**, 103–150 (1984).
- [140] E. Palik, *Handbook of Optical Constants of Solids* (Academic Press, San Diego, 1998) vol. IV.
- [141] M. Schall, M. Walther, and P. U. Jepsen, Fundamental and second-order phonon processes in CdTe and ZnTe, *Phys. Rev. B* **64**, 094301 (2001).
- [142] B. Pödör and V. P. Izvekov, Far-infrared lattice absorption in gallium phosphide, *Revue Phys. Appl.* **18**, 737–739 (1983).
- [143] K. Saito, T. Tanabe, Y. Oyama, K. Suto, T. Kimura, and J. Nishizawa, Terahertz-wave absorption in GaP crystals with different carrier densities, *J. Phys. Chem. Solids* **69**, 597–600 (2008).

-
- [144] R. H. Stolen, Far-infrared absorption in high resistivity GaAs, *Appl. Phys. Lett.* **15**, 74–75 (1969).
- [145] C. Ciuti, G. Bastard, and I. Carusotto, Quantum vacuum properties of the intersubband cavity polariton field, *Phys. Rev. B* **72**, 115303 (2005).
- [146] Y. Todorov and C. Sirtori, Intersubband polaritons in the electrical dipole gauge, *Phys. Rev. B* **85**, 045304 (2012).
- [147] G. Günter, A. A. Anappara, J. Hees, A. Sell, G. Biasiol, L. Sorba, S. De Liberato, C. Ciuti, A. Tredicucci, A. Leitenstorfer, and R. Huber, Sub-cycle switch-on of ultrastrong light-matter interaction, *Nature* **458**, 178–181 (2009).
- [148] P. Jouy, A. Vasanelli, Y. Todorov, A. Delteil, G. Biasiol, L. Sorba, and C. Sirtori, Transition from strong to ultrastrong coupling regime in mid-infrared metal-dielectric-metal cavities, *Appl. Phys. Lett.* **98**, 231114 (2011).
- [149] M. Geiser, F. Castellano, G. Scalari, M. Beck, L. Nevou, and J. Faist, Ultrastrong coupling regime and plasmon polaritons in parabolic semiconductor quantum wells, *Phys. Rev. Lett.* **108**, 106402 (2012).
- [150] G. Scalari, C. Maissen, D. Turčinková, D. Hagenmüller, S. De Liberato, C. Ciuti, C. Reichl, D. Schuh, W. Wegscheider, M. Beck, and J. Faist, Ultrastrong coupling of the cyclotron transition of a 2d electron gas to a THz metamaterial, *Science* **335**, 1323–1326 (2012).
- [151] R. Dingle, W. Wiegmann, and C. H. Henry, Quantum states of confined carriers in very thin $\text{Al}_x\text{Ga}_{1-x}\text{As}$ -GaAs- $\text{Al}_x\text{Ga}_{1-x}\text{As}$ heterostructures, *Phys. Rev. Lett.* **33**, 827–830 (1974).
- [152] S. Adachi, GaAs, AlAs, and $\text{Al}_x\text{Ga}_{1-x}\text{As}$: Material parameters for use in research and device applications, *J. Appl. Phys.* **58**, R1–R29 (1985).
- [153] M. O. Watanabe, J. Yoshida, M. Mashita, T. Nakanisi, and A. Hojo, Band discontinuity for GaAs / AlGaAs heterojunction determined by $C - V$ profiling technique, *J. Appl. Phys.* **57**, 5340–5344 (1985).
- [154] P. A. M. Dirac, The quantum theory of the emission and absorption of radiation, *Proc. R. Soc. Lond. A* **114**, 243–265 (1927).
- [155] B. Jonsson and S. T. Eng, Solving the Schrödinger equation in arbitrary quantum-well potential profiles using the transfer matrix method, *IEEE J. Quantum Electron.* **26**, 2025–2035 (1990).
- [156] M. Fox, *Optical Properties of Solids* (Oxford University Press, 2001).
- [157] B. Gelmont, V. Gorfinkel, and S. Luryi, Theory of the spectral line shape and gain in quantum wells with intersubband transitions, *Appl. Phys. Lett.* **68**, 2171–2173 (1996).

- [158] S. K. Chun, D. S. Pan, and K. L. Wang, Intersubband transitions in a p -type δ -doped SiGe/Si quantum well, *Phys. Rev. B* **47**, 15638–15647 (1993).
- [159] J. N. Heyman, R. Kersting, and K. Unterrainer, Time-domain measurement of intersubband oscillations in a quantum well, *Appl. Phys. Lett.* **72**, 644–646 (1998).
- [160] E. F. Kuester, M. A. Mohamed, M. Piket-May, and C. L. Holloway, Averaged transition conditions for electromagnetic fields at a metafilm, *IEEE Trans. Antennas Propag.* **51**, 2641–2651 (2003).
- [161] S. A. Tretyakov, A. J. Viitanen, S. I. Maslovski, and I. E. Saarela, Impedance boundary conditions for regular dense arrays of dipole scatterers, *IEEE Trans. Antennas Propag.* **51**, 2073–2078 (2003).
- [162] S. A. Tretyakov, F. Mariotte, C. R. Simovski, T. G. Kharina, and J.-P. Heliot, Analytical antenna model for chiral scatterers: Comparison with numerical and experimental data, *IEEE Trans. Antennas Propag.* **44**, 1006–1014 (1996).
- [163] R. Marqués, F. Medina, and R. Rafi-El-Idrissi, Role of bianisotropy in negative permeability and left-handed metamaterials, *Phys. Rev. B* **65**, 144440 (2002).
- [164] B. Sauviac, C. R. Simovski, and S. A. Tretyakov, Double split-ring resonators: Analytical modelling and numerical simulations, *Electromagnetics* **24**, 317–338 (2004).
- [165] D. R. Jackson and N. G. Alexópoulos, Analysis of planar strip geometries in a substrate-superstrate configuration, *IEEE Trans. Antennas Propag.* **AP-34**, 1430–1438 (1986).
- [166] D. R. Smith and J. B. Pendry, Homogenization of metamaterials by field averaging, *J. Opt. Soc. Am. B* **23**, 391–403 (2006).
- [167] A. Taflove and S. C. Hagness, *Computational Electrodynamics: The Finite-Difference Time-Domain Method* (Artech House, Boston, 2000) 2nd ed.
- [168] Y. Hao and R. Mittra, *FDTD Modeling of Metamaterials: Theory and Applications* (Artech House, Boston, 2009).
- [169] B. Engquist and A. Majda, Absorbing boundary conditions for numerical simulation of waves, *Proc. Natl. Acad. Sci. USA* **74**, 1765–1766 (1977).
- [170] G. Mur, Absorbing boundary conditions for the finite-difference approximation of the time-domain electromagnetic-field equations, *IEEE Trans. Electromagn. Compat.* **EMC-23**, 377–382 (1981).
- [171] K. Umashankar and A. Taflove, A novel method to analyze electromagnetic scattering of complex objects, *IEEE Trans. Electromagn. Compat.* **24**, 397–405 (1982).

-
- [172] K. S. Yee, Numerical solution of initial boundary value problems involving Maxwell's equations in isotropic media, *IEEE Trans. Antennas Propag.* **14**, 302–307 (1966).
- [173] J. B. Pendry, A. J. Holden, D. J. Robbins, and W. J. Stewart, Magnetism from conductors and enhanced nonlinear phenomena, *IEEE Trans. Microwave Theory Tech.* **47**, 2075–2084 (1999).
- [174] S. Tretyakov, *Analytical Modeling in Applied Electromagnetics* (Artech House, Boston, 2003).
- [175] M. A. Ordal, L. L. Long, R. J. Bell, S. E. Bell, R. R. Bell, R. W. Alexander, Jr., and C. A. Ward, Optical properties of the metals Al, Co, Cu, Au, Fe, Pb, Ni, Pd, Pt, Ag, Ti and W in the infrared and far infrared, *Appl. Opt.* **22**, 1099–1119 (1983).
- [176] M. A. Ordal, R. J. Bell, R. W. Alexander, Jr., L. L. Long, and M. R. Querry, Optical properties of fourteen metals in the infrared and far infrared: Al, Co, Cu, Au, Fe, Pb, Mo, Ni, Pd, Pt, Ag, Ti, V, and W, *Appl. Opt.* **24**, 4493 (1985).
- [177] V. J. Logeeswaran, N. P. Kobayashi, M. S. Islam, W. Wu, P. Chaturvedi, N. X. Fang, S. Y. Wang, and R. S. Williams, Ultrasoother silver thin films deposited with a germanium nucleation layer, *Nano Lett.* **9**, 178–182 (2009).
- [178] N. Laman and D. Grischkowsky, Terahertz conductivity of thin metal films, *Appl. Phys. Lett.* **93**, 051105 (2008).
- [179] M. Walther, D. G. Cooke, C. Sherstan, M. Hajar, M. R. Freeman, and F. A. Hegmann, Terahertz conductivity of thin gold films at the metal-insulator percolation transition, *Phys. Rev. B* **76**, 125408 (2007).
- [180] G. Acuna, S. F. Heucke, F. Kuchler, H.-T. Chen, A. J. Taylor, and R. Kersting, Surface plasmons in terahertz metamaterials, *Opt. Express* **16**, 18745–18751 (2008).
- [181] A. Bitzer, J. Wallauer, H. Helm, H. Merbold, T. Feurer, and M. Walther, Lattice modes mediate radiative coupling in metamaterial arrays, *Opt. Express* **17**, 22108–22113 (2009).
- [182] R. Singh, C. Rockstuhl, and W. Zhang, Strong influence of packing density in terahertz metamaterials, *Appl. Phys. Lett.* **97**, 241108 (2010).
- [183] V. A. Fedotov, M. Rose, S. L. Prosvirnin, N. Papasimakis, and N. I. Zheludev, Sharp trapped-mode resonances in planar metamaterials with a broken structural symmetry, *Phys. Rev. Lett.* **99**, 147401 (2007).
- [184] W. H. Louisell, Correspondence between Pierce's coupled mode amplitudes and quantum operators, *J. Appl. Phys.* **33**, 2435–2436 (1962).
- [185] L. Novotny, Strong coupling, energy splitting, and level crossings: A classical perspective, *Am. J. Phys.* **78**, 1199–1202 (2010).

- [186] V. Savona, L. C. Andreani, P. Schwendimann, and A. Quattropani, Quantum well excitons in semiconductor microcavities: Unified treatment of weak and strong coupling regimes, *Solid State Commun.* **93**, 733–739 (1995).
- [187] Y. Todorov, A. M. Andrews, R. Colombelli, S. De Liberato, C. Ciuti, P. Klang, G. Strasser, and C. Sirtori, Ultrastrong light-matter coupling regime with polariton dots, *Phys. Rev. Lett.* **105**, 196402 (2010).
- [188] G. Khitrova, H. M. Gibbs, F. Jahnke, M. Kira, and S. W. Koch, Nonlinear optics of normal-mode-coupling semiconductor microcavities, *Rev. Mod. Phys.* **71**, 1591–1639 (1999).
- [189] H. M. Gibbs, G. Khitrova, and S. W. Koch, Exciton-polariton light-semiconductor coupling effects, *Nat. Photonics* **5**, 275–282 (2011).
- [190] C. Weisbuch, M. Nishioka, A. Ishikawa, and Y. Arakawa, Observation of the coupled exciton-photon mode splitting in a semiconductor quantum microcavity, *Phys. Rev. Lett.* **69**, 3314–3317 (1992).
- [191] Y. Todorov, A. M. Andrews, I. Sagnes, R. Colombelli, P. Klang, G. Strasser, and C. Sirtori, Strong light-matter coupling in subwavelength metal-dielectric microcavities at terahertz frequencies, *Phys. Rev. Lett.* **102**, 186402 (2009).
- [192] M. Geiser, C. Walther, G. Scalari, M. Beck, M. Fischer, L. Nevou, and J. Faist, Strong light-matter coupling at terahertz frequencies at room temperature in electronic LC resonators, *Appl. Phys. Lett.* **97**, 191107 (2010).
- [193] D. J. Shelton, I. Brener, J. C. Ginn, M. B. Sinclair, D. W. Peters, K. R. Coffey, and G. D. Boreman, Strong coupling between nanoscale metamaterials and phonons, *Nano Lett.* **11**, 2104–2108 (2011).
- [194] R. C. Miller, A. C. Gossard, D. A. Kleinman, and O. Munteanu, Parabolic quantum wells with the GaAs-Al_xGa_{1-x}As system, *Phys. Rev. B* **29**, 3740–3743 (1984).
- [195] L. Brey, N. F. Johnson, and B. I. Halperin, Optical and magneto-optical absorption in parabolic quantum wells, *Phys. Rev. B* **40**, 10647–10649 (1989).
- [196] J. Ulrich, R. Zobl, K. Unterrainer, G. Strasser, E. Gornik, K. D. Maranowski, and A. C. Gossard, Temperature dependence of far-infrared electroluminescence in parabolic quantum wells, *Appl. Phys. Lett.* **74**, 3158–3160 (1999).
- [197] W. Kohn, Cyclotron resonance and de Haas-van Alphen oscillations of an interacting electron gas, *Phys. Rev.* **123**, 1242–1244 (1961).
- [198] A. M. Andrews priv. comm.
- [199] R. Bratschitsch, T. Müller, R. Kersting, G. Strasser, and K. Unterrainer, Coherent terahertz emission from optically pumped intersubband plasmons in parabolic quantum wells, *Appl. Phys. Lett.* **76**, 3501–3503 (2000).

-
- [200] R. Kersting, R. Bratschitsch, G. Strasser, K. Unterrainer, and J. N. Heyman, Sampling a terahertz dipole transition with subcycle time resolution, *Opt. Lett.* **25**, 272–274 (2000).
- [201] D. Dietze, A. Benz, G. Strasser, K. Unterrainer, and J. Darmo, Terahertz meta-atoms coupled to a quantum well intersubband transition, *Opt. Express* **19**, 13700–13706 (2011).
- [202] C. W. Luo, K. Reimann, M. Woerner, T. Elsaesser, R. Hey, and K. H. Ploog, Phase-resolved nonlinear response of a two-dimensional electron gas under femtosecond intersubband excitation, *Phys. Rev. Lett.* **92**, 047402 (2004).
- [203] N. Meinzer, M. Ruther, S. Linden, C. M. Soukoulis, G. Khitrova, J. Hendrickson, J. D. Oritzky, H. M. Gibbs, and M. Wegener, Arrays of Ag split-ring resonators coupled to InGaAs single-quantum-well gain, *Opt. Express* **18**, 24140–24151 (2010).
- [204] A. Gabbay, J. Reno, J. R. Wendt, A. Gin, M. C. Wanke, M. B. Sinclair, E. Shaner, and I. Brener, Interaction between metamaterial resonators and intersubband transitions in semiconductor quantum wells, *Appl. Phys. Lett.* **98**, 203103 (2011).
- [205] A. Gabbay and I. Brener, Theory and modeling of electrically tunable metamaterial devices using inter-subband transitions in semiconductor quantum wells, *Opt. Express* **20**, 6584–6597 (2012).
- [206] S. De Liberato and C. Ciuti, Quantum vacuum radiation spectra from a semiconductor microcavity with a time-modulated vacuum rabi frequency, *Phys. Rev. Lett.* **98**, 103602 (2007).
- [207] A. A. Anappara, S. De Liberato, A. Tredicucci, C. Ciuti, G. Biasiol, L. Sorba, and F. Beltram, Signatures of the ultrastrong light-matter coupling regime, *Phys. Rev. B* **79**, 201303(R) (2009).
- [208] M. F. Faggin and M. A. Hines, Improved algorithm for the suppression of interference fringe in absorption spectroscopy, *Rev. Sci. Instrum.* **75**, 4547–4553 (2004).
- [209] R. W. Ziolkowski, The incorporation of microscopical material models into the FDTD approach for ultrafast optical pulse simulations, *IEEE Trans. Antennas Propag.* **45**, 375–391 (1997).
- [210] B. Bidégaray, A. Bourgeade, and D. Reignier, Introducing physical relaxation terms in Bloch equations, *J. Comput. Phys.* **170**, 603–613 (2001).
- [211] S. Hughes, Breakdown of the area theorem: Carrier-wave Rabi flopping of femtosecond optical pulses, *Phys. Rev. Lett.* **81**, 3363–3366 (1998).
- [212] K. Raimann, R. P. Smith, A. M. Weiner, T. Elsaesser, and M. Woerner, Direct field-resolved detection of terahertz transients with amplitudes of megavolts per centimeter, *Opt. Lett.* **28**, 471–473 (2003).

- [213] M. D. Thomson, M. Kress, T. Loeffler, and H. G. Roskos, Broadband THz emission from gas plasmas induced by femtosecond optical pulses: From fundamentals to applications, *Laser & Photon. Rev.* **1**, 349–368 (2007).
- [214] M. Reid and R. Fedosejevs, Quantitative comparison of terahertz emission from (100) InAs surfaces and a GaAs large-aperture photoconductive switch at high fluences, *Appl. Opt.* **44**, 149–153 (2005).
- [215] X.-C. Zhang, B. B. Hu, J. T. Darrow, and D. H. Auston, Generation of femtosecond electromagnetic pulses from semiconductor surfaces, *Appl. Phys. Lett.* **56**, 1011–1013 (1990).
- [216] S. M. Sze, *Physics of Semiconductor Devices* (Wiley, New York, 1981) 2nd ed.
- [217] W. E. Spicer, Z. Liliental-Weber, E. Weber, N. Newman, T. Kendelewicz, R. Cao, C. McCants, P. Mahowald, K. Miyano, and I. Lindau, The advanced unified defect model for Schottky barrier formation, *J. Vac. Sci. Technol. B* **6**, 1245–1251 (1988).
- [218] H. C. Casey, D. D. Sell, and K. W. Wecht, Concentration dependence of the absorption coefficient for n and p type GaAs between 1.3 and 1.6eV, *J. Appl. Phys.* **46**, 250–257 (1975).
- [219] H. R. Philipp and H. Ehrenreich, Optical properties of semiconductors, *Phys. Rev.* **129**, 1550–1560 (1963).
- [220] T. Dekorsy, T. Pfeifer, W. Kütt, and H. Kurz, Subpicosecond carrier transport in GaAs surface-space-charge fields, *Phys. Rev. B* **47**, 3842–3849 (1993).
- [221] T. Dekorsy, H. Auer, H. J. Bakker, H. G. Roskos, and H. Kurz, THz electromagnetic emission by coherent infrared-active phonons, *Phys. Rev. B* **53**, 4005–4014 (1996).
- [222] H. Dember, Über eine photoelektrische Kraft in Kupferoxydul-Kristallen, *Phys. Z.* **32**, 554–556 (1931).
- [223] J. N. Heyman, N. Coates, A. Reinhardt, and G. Strasser, Diffusion and drift in terahertz emission at GaAs surfaces, *Appl. Phys. Lett.* **83**, 5476–5478 (2003).
- [224] A. Reklaitis, Comparison of efficiencies of GaAs-based pulsed terahertz emitters, *J. Appl. Phys.* **101**, 116104 (2007).
- [225] Gregory Snider. www.nd.edu/~gsnider/.
- [226] I. H. Tan, G. L. Snider, L. D. Chang, and E. L. Hu, A selfconsistent solution of Schrödinger-Poisson equations using a nonuniform mesh, *J. Appl. Phys.* **68**, 4071–4076 (1990).
- [227] A. Leitenstorfer, S. Hunsche, J. Shah, M. C. Nuss, and W. H. Knox, Femtosecond charge transport in polar semiconductors, *Phys. Rev. Lett.* **82**, 5140–5143 (1999).

-
- [228] J. S. Hwang, H. C. Lin, K. I. Lin, and X.-C. Zhang, Terahertz radiation from InAlAs and GaAs surface intrinsic-N⁺ structures and the critical electric field of semiconductors, *Appl. Phys. Lett.* **87**, 121107 (2005).
- [229] A. Lisauskas, A. Reklaitis, R. Venckevičius, I. Kašalynas, G. Valušis, G. Gri-galiūnaitė-Vonsevičienė, H. Maestre, J. Schmidt, V. Blank, M. D. Thomson, H. G. Roskos, and K. Köhler, Experimental demonstration of efficient pulsed terahertz emission from a stacked GaAs/AlGaAs p-i-n-i heterostructure, *Appl. Phys. Lett.* **98**, 091103 (2011).
- [230] S. L. Chuang, S. Schmitt-Rink, B. I. Greene, P. N. Saeta, and A. F. J. Levi, Optical rectification at semiconductor surfaces, *Phys. Rev. Lett.* **68**, 102–105 (1992).
- [231] M. Reid and R. Fedosejevs, Terahertz emission from (100) InAs surfaces at high excitation fluences, *Appl. Phys. Lett.* **86**, 011906 (2005).
- [232] K. H. Yang, P. L. Richards, and Y. R. Shen, Generation of far-infrared radiation by picosecond light pulses in LiNbO₃, *Appl. Phys. Lett.* **19**, 320–323 (1971).
- [233] M. Bass, P. A. Franken, J. F. Ward, and G. Weinreich, Optical rectification, *Phys. Rev. Lett.* **9**, 446–448 (1962).
- [234] X. F. Ma and X.-C. Zhang, Determination of ratios between nonlinear-optical coefficients by using subpicosecond optical rectification, *J. Opt. Soc. Am. B* **10**, 1175–1179 (1993).
- [235] B. B. Hu, X.-C. Zhang, D. H. Auston, and P. R. Smith, Free-space radiation from electro-optic crystals, *Appl. Phys. Lett.* **56**, 506–508 (1990).
- [236] X.-C. Zhang and D. H. Auston, Optoelectronic measurement of semiconductor surfaces and interfaces with femtosecond optics, *J. Appl. Phys.* **71**, 326–338 (1992).
- [237] A. Rice, Y. Jin, X. F. Ma, X.-C. Zhang, D. Bliss, J. Larkin, and M. Alexander, Terahertz optical rectification from ⟨110⟩ zinc-blende crystals, *Appl. Phys. Lett.* **64**, 1324–1326 (1994).
- [238] A. Bonvalet, M. Joffre, J. L. Martin, and A. Migus, Generation of ultrabroad-band femtosecond pulses in the mid-infrared by optical rectification of 15fs light pulses at 100MHz repetition rate, *Appl. Phys. Lett.* **67**, 2907–2909 (1995).
- [239] Q. Wu and X.-C. Zhang, Free-space electro-optics sampling of mid-infrared pulses, *Appl. Phys. Lett.* **71**, 1285–1286 (1997).
- [240] P. Y. Han and X.-C. Zhang, Coherent, broadband midinfrared terahertz beam sensors, *Appl. Phys. Lett.* **73**, 3049–3051 (1998).
- [241] J. Hebling, G. Almási, I. Z. Kozma, and J. Kuhl, Velocity matching by pulse front tilting for large-area THz-pulse generation, *Opt. Express* **10**, 1161–1166 (2002).

- [242] F. Blanchard, L. Razzari, H.-C. Bandulet, G. Sharma, R. Morandotti, J.-C. Kieffer, T. Ozaki, M. Reid, H. F. Tiedje, H. K. Haugen, and F. A. Hegmann, Generation of 1.5 μ J single-cycle terahertz pulses by optical rectification from a large aperture ZnTe crystal, *Opt. Express* **15**, 13212–13220 (2007).
- [243] P. H. Borchers, K. Kunc, G. F. Alfrey, and R. L. Hall, The lattice dynamics of gallium phosphide, *J. Phys. C* **12**, 4699–4705 (1979).
- [244] E. W. Van Stryland, M. A. Woodall, H. Vanherzeele, and M. J. Soileau, Energy band-gap dependence of two-photon absorption, *Opt. Lett.* **10**, 490–492 (1985).
- [245] J. Faure, J. Van Tilborg, R. A. Kaindl, and W. P. Leemans, Modelling laser-based table-top THz sources: Optical rectification, propagation and electro-optic sampling, *Opt. Quantum Electron.* **36**, 681–697 (2004).
- [246] J. T. Darrow, X.-C. Zhang, and D. H. Auston, Power scaling of large-aperture photoconducting antennas, *Appl. Phys. Lett.* **58**, 25 (1991).
- [247] A. S. Barker, Jr., Dielectric dispersion and phonon line shape in gallium phosphide, *Phys. Rev.* **165**, 917–922 (1968).
- [248] D. F. Parsons and P. D. Coleman, Far infrared optical constants of gallium phosphide, *Appl. Opt.* **10**, 1683–1685 (1971).
- [249] A. N. Pikhtin, V. T. Prokopenko, and A. D. Yas'kov, Dispersion of the refractive index of light and permittivity of gallium phosphide, *Sov. Phys. Semicond.* **10**, 1224–1226 (1976).
- [250] S. Casalbuoni, H. Schlarb, B. Schmidt, P. Schmüser, B. Steffen, and A. Winter, Numerical studies on the electro-optic detection of femtosecond electron bunches, *Phys. Rev. ST Accel. Beams* **11**, 072802 (2008).
- [251] P. U. Jepsen, D. G. Cooke, and M. Koch, Terahertz spectroscopy and imaging - modern techniques and applications, *Laser & Photon. Rev.* **5**, 124–166 (2011).
- [252] D. Dietze, K. Unterrainer, and J. Darmo, Dynamically phase-matched terahertz generation, *Opt. Lett.* **37**, 1047–1049 (2012).
- [253] G. A. Samara, Temperature and pressure dependences of the dielectric constants of semiconductors, *Phys. Rev. B* **27**, 3494–3505 (1983).
- [254] S. Ushioda, J. D. McMullen, and M. J. Delaney, Damping mechanism of polaritons in GaP, *Phys. Rev. B* **8**, 4634–4637 (1973).
- [255] F. Ganikhanov and F. Vallée, Coherent TO phonon relaxation in GaAs and InP, *Phys. Rev. B* **55**, 15614–15618 (1997).
- [256] J. Y. Yarnell, J. L. Warren, R. G. Wenzel, and P. J. Dean, *Neutron Inelastic Scattering* (International Atomic Energy Agency, Vienna, 1968) vol. 1, p. 301.

-
- [257] M. Y. Frankel, J. F. Whitaker, G. A. Mourou, F. W. Smith, and A. R. Calawa, High-voltage picosecond photoconductor switch based on low-temperature-grown GaAs, *IEEE Trans. Electron Devices* **37**, 2493–2498 (1990).
- [258] S. Verghese, K. A. McIntosh, and E. R. Brown, Optical and terahertz power limits in the low-temperature-grown GaAs photomixers, *Appl. Phys. Lett.* **71**, 2743–2745 (1997).
- [259] C. Ludwig and J. Kuhl, Studies of the temporal and spectral shape of terahertz pulses generated from photoconductive switches, *Appl. Phys. Lett.* **69**, 1194–1196 (1996).
- [260] D. You, R. R. Jones, P. H. Bucksbaum, and D. R. Dykaar, Generation of high-power sub-single-cycle 500-fs electromagnetic pulses, *Opt. Lett.* **18**, 290–292 (1993).
- [261] E. Budiarto, J. Margolies, S. Jeong, J. Son, and J. Bokor, High-intensity terahertz pulses at 1-kHz repetition rate, *IEEE J. Quantum Electron.* **32**, 1839–1846 (1996).
- [262] D. Bachmann, *Terahertz Matrix Emitter*, Master’s thesis, Vienna University of Technology (2011).
- [263] A. Dreyhaupt, S. Winnerl, T. Dekorsky, and M. Helm, High-intensity terahertz radiation from microstructured large-area photoconductor, *Appl. Phys. Lett.* **86**, 121114 (2005).
- [264] H. Hamster, A. Sullivan, S. Gordon, and R. W. Falcone, Short-pulse terahertz radiation from high-intensity-laser-produced plasmas, *Phys. Rev. E* **49**, 671–677 (1994).
- [265] A. Couairon and A. Mysyrowicz, Femtosecond filamentation in transparent media, *Phys. Rep.* **441**, 47–189 (2007).
- [266] T. Bartel, P. Gaal, K. Raimann, M. Woerner, and T. Elsaesser, Generation of single-cycle THz transients with high electric-field amplitudes, *Opt. Lett.* **30**, 2805–2807 (2005).
- [267] K. Y. Kim, A. J. Taylor, J. H. Glowina, and G. Rodriguez, Coherent control of terahertz supercontinuum generation in ultrafast laser-gas interactions, *Nat. Photonics* **2**, 605–609 (2008).
- [268] J. Dai, J. Liu, and X.-C. Zhang, Terahertz wave air photonics: Terahertz generation and detection with laser-induced gas plasma, *IEEE J. Sel. Top. Quantum Electron.* **17**, 183–190 (2011).
- [269] M. Kress, T. Loeffler, S. Eden, M. Thomson, and H. G. Roskos, Terahertz-pulse generation by photoionization of air with laser pulses composed of both fundamental and second-harmonic waves, *Opt. Lett.* **29**, 1120–1122 (2004).

- [270] D. Dietze, J. Darmo, S. Roither, A. Pugzlys, J. N. Heyman, and K. Unterrainer, Polarization of terahertz radiation from laser generated plasma filaments, *J. Opt. Soc. Am. B* **26**, 2016–2027 (2009).
- [271] F. Blanchard, G. Sharma, X. Ropagnol, L. Razzari, R. Morandotti, and T. Ozaki, Improved terahertz two-color plasma sources pumped by high intensity laser beam, *Opt. Express* **17**, 6044–6052 (2009).
- [272] D. Dietze, K. Unterrainer, and J. Darmo, Terahertz emission from a two-color plasma filament in a slot waveguide, *Appl. Phys. Lett.* **100**, 091113 (2012).
- [273] J. Dai and X.-C. Zhang, Terahertz wave generation from gas plasma using a phase compensator with attosecond phase-control accuracy, *Appl. Phys. Lett.* **94**, 021117 (2009).
- [274] J. Dai, N. Karpowicz, and X.-C. Zhang, Coherent polarization control of terahertz waves generated from two-color laser-induced gas plasma, *Phys. Rev. Lett.* **103**, 023001 (2009).
- [275] E. R. Peck and K. Reeder, Dispersion of air, *J. Opt. Soc. Am.* **62**, 958–962 (1972).
- [276] C. D’Amico, A. Houard, M. Franco, B. Prade, A. Mysyrowicz, and A. Couairon, Conical forward THz emission from femtosecond-laser-beam filamentation in air, *Phys. Rev. Lett.* **98**, 235002 (2007).
- [277] X. Xie, J. Dai, and X.-C. Zhang, Coherent control of THz wave generation in ambient air, *Phys. Rev. Lett.* **96**, 075005 (2006).
- [278] A. Houard, Y. Liu, B. Prade, and A. Mysyrowicz, Polarization analysis of terahertz radiation generated by four-wave mixing in air, *Opt. Lett.* **33**, 1195–1197 (2008).
- [279] K. Y. Kim, J. H. Glowina, A. J. Taylor, and G. Rodriguez, Terahertz emission from ultrafast ionizing air in symmetry-broken laser fields, *Opt. Express* **15**, 4577–4584 (2007).
- [280] P. B. Corkum, Plasma perspective on strong-field multiphoton ionization, *Phys. Rev. Lett.* **71**, 1994–1997 (1993).
- [281] M. Chen, A. Pukhov, X.-Y. Peng, and O. Willi, Theoretical analysis and simulations of strong terahertz radiation from the interaction of ultrashort laser pulses with gases, *Phys. Rev. E* **78**, 046406 (2008).
- [282] N. Karpowicz and X.-C. Zhang, Coherent terahertz echo of tunnel ionization in gases, *Phys. Rev. Lett.* **102**, 093001 (2009).
- [283] A. A. Silaev and N. V. Vvedenskii, Residual-current excitation in plasmas produced by few-cycle laser pulses, *Phys. Rev. Lett.* **102**, 115005 (2009).

-
- [284] L. D. Landau and E.M. Lifshitz, *Quantum Mechanics* (Pergamon, New York, 1965) 2nd ed.
- [285] P. B. Corkum, N. H. Burnett, and F. Brunel, Above-threshold ionization in the long-wavelength limit, *Phys. Rev. Lett.* **62**, 1259–1262 (1989).
- [286] D. W. Schumacher and P. H. Bucksbaum, Phase dependence of intense-field ionization, *Phys. Rev. A* **54**, 4271–4278 (1996).
- [287] A. Talebpour, J. Yang, and S. L. Chin, Semi-empirical model for the rate of tunnel ionization of N_2 and O_2 molecules in an intense Ti:sapphire laser pulse, *Opt. Commun.* **163**, 29–32 (1999).
- [288] A. D. Polyanin and V. F. Zaitsev, *Handbuch der linearen Differentialgleichungen* (Spektrum Akademischer Verlag, Heidelberg, 1994).
- [289] I. N. Bronstein, K. A. Semendjajew, G. Musiol, and H. Mühlig, *Taschenbuch der Mathematik* (Harri Deutsch, Frankfurt am Main, 2001).
- [290] Y. Liu, A. Houard, M. Durand, B. Prade, and A. Mysyrowicz, Maker fringes in the terahertz radiation produced by a 2-color laser field in air, *Opt. Express* **17**, 11480–11485 (2009).
- [291] X.-Y. Peng, C. Li, M. Chen, T. Toncian, R. Jung, O. Willi, Y.-T. Li, W.-M. Wang, S.-J. Wang, F. Liu, A. Pukhov, Z.-M. Sheng, and J. Zhang, Strong terahertz radiation from air plasmas generated by an aperture-limited Gaussian pump laser beam, *Appl. Phys. Lett.* **94**, 101502 (2009).
- [292] D. K. Cheng, *Field and Wave Electromagnetics* (Addison-Wesley, London, 1983).
- [293] B. E. A. Saleh and M. C. Teich, *Fundamentals of Photonics* (Wiley, New York, 1991).
- [294] H. Zhong, N. Karpowicz, and X.-C. Zhang, Terahertz emission profile from laser-induced air plasma, *Appl. Phys. Lett.* **88**, 261103 (2006).
- [295] H. Kogelnik and T. Li, Laser beams and resonators, *Appl. Opt.* **5**, 1550–1567 (1966).
- [296] I. I. Rabi, Space quantization in a gyrating magnetic field, *Phys. Rev.* **51**, 652–654 (1937).
- [297] G. B. Serapiglia, E. Paspalakis, C. Sirtori, K. L. Vodopyanov, and C. C. Phillips, Laser-induced quantum coherence in a semiconductor quantum well, *Phys. Rev. Lett.* **84**, 1019–1022 (2000).
- [298] F. Eickemeyer, M. Woerner, A. M. Weiner, T. Elsaesser, R. Hey, and K. H. Ploog, Coherent nonlinear propagation of ultrafast electric field transients through intersubband resonances, *Appl. Phys. Lett.* **79**, 165–167 (2001).

- [299] M. Wagner, M. Helm, M. S. Sherwin, and D. Stehr, Coherent control of THz intersubband polarization in a voltage controlled single quantum well, *Appl. Phys. Lett.* **99**, 131109 (2011).
- [300] S. G. Carter, V. Birkedal, C. S. Wang, L. A. Coldren, A. V. Maslov, D. S. Citrin, and M. S. Sherwin, Quantum coherence in an optical modulator, *Science* **310**, 651–653 (2005).
- [301] J. R. Danielson, Y.-S. Lee, J. P. Prineas, J. T. Steiner, M. Kira, and S. W. Koch, Interaction of strong single-cycle terahertz pulses with semiconductor quantum wells, *Phys. Rev. Lett.* **99**, 237401 (2007).
- [302] M. Wagner, H. Schneider, D. Stehr, S. Winnerl, A. M. Andrews, S. Schartner, G. Strasser, and M. Helm, Observation of the intraexcitonic Autler-Townes effect in GaAs/AlGaAs semiconductor quantum wells, *Phys. Rev. Lett.* **105**, 167401 (2010).
- [303] B. Zaks, D. Stehr, T.-A. Truong, P. M. Petroff, S. Hughes, and M. S. Sherwin, THz-driven quantum wells: Coulomb interactions and Stark shifts in the ultrastrong coupling regime, *New J. Phys.* **13**, 083009 (2011).
- [304] J. F. Dynes, M. D. Frogley, M. Beck, J. Faist, and C. C. Phillips, ac Stark splitting and quantum interference with intersubband transitions in quantum wells, *Phys. Rev. Lett.* **94**, 157403 (2005).
- [305] D. Dietze, J. Darmo, and K. Unterrainer, Phase-locked nonlinear dynamics of multi-level quantum systems, *in preparation* (2012).
- [306] E. F. Schubert, R. F. Kopf, J. M. Kuo, H. S. Luftman, and P. A. Garbinski, Spatial resolution of the capacitance-voltage profiling technique on semiconductors with quantum confinement, *Appl. Phys. Lett.* **57**, 497–499 (1990).
- [307] S. H. Autler and C. H. Townes, Stark effect in rapidly varying fields, *Phys. Rev.* **100**, 703–722 (1955).
- [308] B. R. Mollow, Power spectrum of light scattered by two-level systems, *Phys. Rev.* **188**, 1969–1975 (1969).
- [309] U. Fano, Effects of configuration interaction on intensities and phase shifts, *Phys. Rev.* **124**, 1866–1878 (1961).
- [310] D. Golde, M. Wagner, D. Stehr, H. Schneider, M. Helm, A. M. Andrews, T. Roch, G. Strasser, M. Kira, and S. W. Koch, Fano signatures in the intersubband terahertz response of optically excited semiconductor quantum wells, *Phys. Rev. Lett.* **102**, 127403 (2009).
- [311] J. B. Khurgin and S. Li, Two-photon absorption and nonresonant nonlinear index of refraction in the intersubband transitions in the quantum wells, *Appl. Phys. Lett.* **62**, 126–128 (1993).

-
- [312] R. W. Boyd, M. G. Raymer, P. Narum, and D. J. Harter, Four-wave parametric interactions in a strongly driven two-level system, *Phys. Rev. A* **24**, 411–423 (1981).
- [313] J. N. Heyman, K. Craig, B. Galdrikian, M. S. Sherwin, K. Campman, P. F. Hopkins, S. Fafard, and A. C. Gossard, Resonant harmonic generation and dynamic screening in a double quantum well, *Phys. Rev. Lett.* **72**, 2183–2186 (1994).
- [314] J. B. Williams, M. S. Sherwin, K. D. Maranowski, and A. C. Gossard, Dissipation of intersubband plasmons in wide quantum wells, *Phys. Rev. Lett.* **87**, 037401 (2001).
- [315] M. Zaluźny, Influence of the depolarization effect on the nonlinear intersubband absorption spectra of quantum wells, *Phys. Rev. B* **47**, 3995–3998 (1993).
- [316] M. Zaluźny, Saturation of intersubband absorption and optical rectification in asymmetric quantum wells, *J. Appl. Phys.* **74**, 4716–4722 (1993).
- [317] M. S. Sherwin, K. Craig, B. Galdrikian, J. Heyman, A. Markelz, K. Campman, S. Fafard, P. F. Hopkins, and A. Gossard, Nonlinear quantum dynamics in semiconductor quantum wells, *Physica D* **83**, 229–242 (1995).
- [318] K. Craig, B. Galdrikian, J. N. Heyman, A. G. Markelz, J. B. Williams, M. S. Sherwin, K. Campman, P. F. Hopkins, and A. C. Gossard, Undressing a collective intersubband excitation in a quantum well, *Phys. Rev. Lett.* **76**, 2382–2385 (1996).
- [319] C. Cohen-Tannoudji, *The Autler-Townes effect revisited* (Springer, New York, 1996) chapter 11 in *Amazing Light: A volume dedicated to Charles Hard Townes on his 80th Birthday*, pp. 109–124.
- [320] H. Walther, B. T. H. Varcoe, B.-G. Englert, and T. Becker, Cavity quantum electrodynamics, *Rep. Prog. Phys.* **69**, 1352–1382 (2006).
- [321] G. Khitrova, H. M. Gibbs, M. Kira, S. W. Koch, and A. Scherer, Vacuum Rabi splitting in semiconductors, *Nat. Phys.* **2**, 81–90 (2006).
- [322] J. Darmo, D. Dietze, M. Martl, and K. Unterrainer, Nonorthodox heterodyne electro-optic detection for terahertz optical systems, *Appl. Phys. Lett.* **98**, 161112 (2011).
- [323] Y. T. Lo and S. W. Lee, *Antenna Handbook: Antenna Theory* (Van Nostrand Reinhold, New York, 1993).
- [324] R. W. P. King and C. W. Harrison, *Antennas and Waves: A Modern Approach* (MIT Press, Cambridge, 1969).
- [325] L. D. Landau and E. M. Lifshitz, *Electrodynamics of Continuous Media* (Pergamon, New York, 1984).

- [326] S. Tretyakov, On geometrical scaling of split-ring and double-bar resonators at optical frequencies, *Metamaterials* **1**, 40–43 (2007).
- [327] O. Sydoruk, E. Tatartschuk, E. Shamonina, and L. Solymar, Analytical formulation for the resonant frequency of split rings, *J. Appl. Phys.* **105**, 014903 (2009).
- [328] A. Elhawil, J. Stiens, C. De Tandt, W. Ranson, and R. Vounckx, An equivalent circuit model of single circular open-ring resonators, *IEEE J. Sel. Top. Quantum Electron.* **16**, 380–385 (2010).
- [329] C. Cohen-Tannoudji, B. Diu, and F. Laloë, *Quantum-Mechanics, Vol. 1* (Wiley, New York, 1977).
- [330] P. R. Hemmer and M. G. Prentiss, Coupled-pendulum model of the stimulated resonance Raman effect, *J. Opt. Soc. Am. B* **5**, 1613–1623 (1988).
- [331] C. L. Garrido Alzar, M. A. G. Martinez, and P. Nussenzevig, Classical analog of electromagnetically induced transparency, *Am. J. Phys.* **70**, 37–41 (2002).
- [332] F. Kuypers, *Klassische Mechanik* (Wiley, New York, 1997) 5th. ed.
- [333] B. Bidégaray, Time discretizations for Maxwell-Bloch equations, *Numer. Methods for Partial Differential Eq.* **19**, 284–300 (2003).
- [334] S. Chang and V. Minogin, Density-matrix approach to dynamics of multilevel atoms in laser fields, *Phys. Rep.* **365**, 65–143 (2002).
- [335] M. W. Hirsch, S. Smale, and R. L. Devaney, *Differential Equations, Dynamical Systems, and an Introduction to Chaos* (Elsevier Academic Press, Amsterdam, 2004).
- [336] M. J. F. Digonnet (Ed.), *Rare-Earth-Doped Fiber Lasers and Amplifiers* (Marcel Dekker, New York, 2001).
- [337] K. Tamura, E. I. Ippen, H. A. Haus, and L. E. Nelson, 77-fs pulse generation from a stretched-pulse mode-locked all-fiber ring laser, *Opt. Lett.* **18**, 1080–1082 (1993).
- [338] K. Tamura, L. E. Nelson, H. A. Haus, and E. P. Ippen, Soliton versus nonsoliton operation of fiber ring lasers, *Appl. Phys. Lett.* **64**, 149–151 (1994).
- [339] L. E. Nelson, S. B. Fleischer, G. Lenz, and E. P. Ippen, Efficient frequency doubling of a femtosecond fiber laser, *Opt. Lett.* **21**, 1759–1761 (1996).
- [340] H. Shimizu, S. Yamazaki, T. Ono, and K. Emura, Highly practical fiber squeezer polarization controller, *IEEE J. Lightwave Technol.* **9**, 1217–1224 (1991).
- [341] G. P. Agrawal, *Nonlinear Fiber Optics* (Academic Press, San Diego, 2001) 3rd ed.

- [342] M. Hofer, M. E. Fermann, F. Haberl, M. H. Ober, and A. J. Schmidt, Mode locking with cross-phase and self-phase modulation, *Opt. Lett.* **16**, 502–504 (1991).
- [343] M. Yamada, N. Nada, M. Saitoh, and K. Watanabe, First-order quasi-phase matched LiNbO₃ waveguide periodically poled by applying an external field for efficient blue second-harmonic generation, *Appl. Phys. Lett.* **62**, 435–436 (1993).
- [344] G. D. Reid and K. Wynne, Ultrafast laser technology and spectroscopy, In *Encyclopedia of Analytical Chemistry* (Wiley, New York, 2006) pp. 13644–13670.
- [345] P. F. Moulton, Spectroscopic and laser characteristics of Ti:Al₂O₃, *J. Opt. Soc. Am. B* **3**, 125–133 (1986).

Curriculum Vitae

Personal

Name	Daniel Ronald Dietze
Date of Birth	28. August 1981
Place of Birth	Regensburg, Germany
Nationality	German
Family Status	married, one child
Current Address	Tivoligasse 65 / 12, 1120 Vienna, Austria
E-Mail	daniel.dietze@tuwien.ac.at

Education

since 2007	PhD at the Photonics Institute, Vienna University of Technology, Austria
2004 - 2007	Graduate studies in physics at the Technical University of Munich, Germany; (with highest honors)
2002 - 2004	Undergraduate studies in physics at the University of Regensburg
2001 - 2002	Civil service

Career History

since 2007	Research assistant at the Photonics Institute, Vienna University of Technology, Austria
2006	Diploma work at the Max-Planck-Institute for Quantum Optics, Garching, Germany
2006	Internship with Jena-Optronik GmbH, Jena, Germany
2005	Internship with the Max-Planck-Institute for Plasma Physics, Garching, Germany
2002 - 2007	Independent software developer

Career Related Activities

- Member of local organizing committee of the *International Quantum Cascade Laser School and Workshop 2012*, Baden, Austria; 02.09.2012 - 06.09.2012
- Member of local organizing committee of the *European Semiconductor Laser Workshop 2009*, Vienna, Austria; 25.09.2009 - 26.09.2009
- Co-founder and first president of the Vienna Student Chapter of the Optical Society of America
- Member of the Vienna Doctoral Program on Complex Quantum Systems (CoQuS)

Awards

1. *Student-Poster Award*, International Workshop on Optical Terahertz Science and Technology 2009, Santa Barbara, CA, USA

List of Publications

Journal Papers

1. D. Dietze, J. Darmo, K. Unterrainer, *Phase-locked nonlinear dynamics of multi-level quantum systems*, in preparation (2012)
2. D. Dietze, K. Unterrainer, J. Darmo, *Dynamically phase-matched terahertz generation*, Opt. Lett. **37**, 1047-1049 (2012)
3. D. Dietze, K. Unterrainer, J. Darmo, *Terahertz emission from a two-color plasma filament in a slot waveguide*, Appl. Phys. Lett. **100**, 091113 (2012)
4. J. Darmo, D. Dietze, M. Martl, K. Unterrainer, *Nonorthodox heterodyne electro-optic detection for terahertz optical systems*, Appl. Phys. Lett. **98**, 161112 (2011)
5. D. Dietze, A. Benz, G. Strasser, K. Unterrainer, J. Darmo, *Terahertz meta-atoms coupled to a quantum well intersubband transition*, Opt. Express **19**, 13700 - 13706 (2011)
6. D. Dietze, J. Darmo, K. Unterrainer, *Guided Modes in Layered Semiconductor Terahertz Structures*, IEEE J. Quantum Electron. **46**, 618 - 625 (2010)
7. M. Martl, J. Darmo, D. Dietze, K. Unterrainer, E. Gornik, *Terahertz waveguide emitter with subwavelength confinement*, J. Appl. Phys. **107**, 013110 (2010)
8. D. Dietze, J. Darmo, S. Roither, A. Pugzlys, J.N. Heyman, K. Unterrainer, *Polarization of terahertz radiation from laser generated plasma filaments*, J. Opt. Soc. Am. B **26**, 2016 - 2027 (2009)
9. N. Syassen, D. M. Bauer, M. Lettner, T. Volz, D. Dietze, J. J. García-Ripoll, J. I. Cirac, G. Rempe, S. Dürr, *Strong Dissipation Inhibits Losses and Induces Correlations in Cold Molecular Gases*, Science **320**, 1329 - 1331 (2008)
10. N. Syassen, D. M. Bauer, M. Lettner, D. Dietze, T. Volz, S. Dürr, G. Rempe, *Atom-Molecule Rabi Oscillations in a Mott Insulator*, Phys. Rev. Lett. **99**, 033201 (2007)

Conference Proceedings

1. S. Dürr, N. Syassen, D.M. Bauer, M. Lettner, T. Volz, D. Dietze, J.J. García-Ripoll, J. I. Cirac, G. Rempe, *A Dissipative Tonks-Girardeau Gas of Molecules*, Proceedings of the XXI International Conference on Atomic Physics, edited by R. Côté, P.L. Gould, M. Rozman, and W. W. Smith, World Scientific, London (2009), pp. 307-314 (arXiv:0810.2217)

Conference Contributions

1. D. Dietze, A. Benz, G. Strasser, K. Unterrainer, J. Darmo, *Strong Terahertz Light-Matter Coupling Between Metamaterials and Intersubband Transitions*; Talk: CLEO 2012, San Jose, USA; 06.05.2012 - 11.05.2012.
2. M. Martl, J. Darmo, D. Dietze, A. Benz, C. Deutsch, H. Detz, A. M. Andrews, G. Strasser, K. Unterrainer, *THz time domain spectroscopy of quantum cascade lasers*; Talk: SPIE Photonics West 2012, San Francisco, USA (invited); 21.01.2012 - 26.01.2012.
3. J. Darmo, M. Martl, D. Dietze, G. Strasser, K. Unterrainer, *THz Photonics for Non-destructive Testing*; Talk: International THz Conference, Villach, Austria (invited); 24.11.2011 - 25.11.2011.
4. D. Dietze, D. Bachmann, K. Unterrainer, J. Darmo, *Generation of Intense Broadband THz Pulses*; Poster: International THz Conference, Villach, Austria; 24.11.2011 - 25.11.2011.
5. J. Kristoferitsch, D. Dietze, K. Unterrainer, J. Darmo, *Perpendicular coupling in terahertz metamaterials*; Talk: 5. THz Frischlinge Treffen 2011, Regensburg, Germany; 06.06.2011 - 08.06.2011.
6. J. Darmo, D. Dietze, M. Martl, K. Unterrainer, *New Generation of the Electro-Optic Terahertz Detectors*; Poster: CLEO Europe 2011, Munich, Germany; 22.05.2011 - 26.05.2011.
7. J. Darmo, K. Serita, D. Dietze, H. Murakami, I. Kawayama, K. Unterrainer, M. Tonouchi, *Frequency and Time Mapping of Terahertz Meta-Atoms*; Talk: CLEO Europe 2011, Munich, Germany; 22.05.2011 - 26.05.2011.
8. D. Dietze, J. Darmo, G. Strasser, K. Unterrainer, *Metasurfaces Coupled to Terahertz Intersubband Transitions*; Talk: CLEO Europe 2011, Munich, Germany; 22.05.2011 - 26.05.2011.
9. M. Martl, J. Darmo, D. Dietze, C. Deutsch, M. Brandstetter, A. Benz, A. M. Andrews, P. Klang, W. Schrenk, G. Strasser, K. Unterrainer, *THz Time Domain Spectroscopy of Coupled Cavity THz Quantum Cascade Lasers with Metal-Metal Waveguide*; Talk: CLEO Europe 2011, Munich, Germany; 22.05.2011 - 26.05.2011.
10. J. Darmo, D. Dietze, M. Martl, K. Unterrainer, *Prospects of Heterodyning in Electro-Optic Detector*; Poster: CLEO 2011, Baltimore, USA; 01.05.2011 - 06.05.2011.
11. K. Serita, J. Darmo, D. Dietze, H. Murakami, I. Kawayama, K. Unterrainer, M. Tonouchi, *Time- and Frequency-Domain Imaging of Dynamics in Terahertz Meta-Atoms*; Poster: CLEO 2011, Baltimore, USA; 01.05.2011 - 06.05.2011.

12. M. Martl, D. Dietze, J. Darmo, C. Deutsch, A. Benz, M. Brandstetter, K. Unterrainer, P. Klang, A. M. Andrews, W. Schrenk, G. Strasser, E. Gornik, *Investigation of Double Metal THz Quantum Cascade Lasers by Terahertz Time-Domain Spectroscopy*; Poster: GMe Forum 2011, Vienna, Austria; 14.04.2011 - 15.04.2011.
13. D. Dietze, J. Darmo, G. Strasser, K. Unterrainer, *Terahertz Intersubband Transitions Coupled to Metasurfaces*; Talk: OTST 2011, Santa Barbara, USA; 13.03.2011 - 17.03.2011.
14. J. Kristoferitsch, J. Darmo, D. Dietze, K. Unterrainer, *Permittivity tuning of terahertz metamaterial using a genetic algorithm*; Poster: OTST 2011, Santa Barbara, USA; 13.03.2011 - 17.03.2011.
15. T. Balciunas, D. Lorenc, M. Ivanov, O. Smirnova, A. Pugzlys, A.M. Zheltikov, D. Dietze, J. Darmo, K. Unterrainer, T. Rathje, G. Paulus, A. Baltuska, *Tunable THz generation with a CEP-stable multicolor OPA*; Poster: 2011 OSA Optics and Photonics Congress, Istanbul, Turkey; 13.02.2011 - 18.02.2011.
16. D. Dietze, J. Darmo, M. Martl, K. Unterrainer, *Terahertz Artificial Resonant Interface Layers*; Poster: EOS Annual Meeting 2010, Paris, France; 26.10.2010 - 29.10.2010.
17. M. Martl, J. Darmo, D. Dietze, C. Deutsch, A. Benz, M. Brandstetter, K. Unterrainer, P. Klang, A. M. Andrews, W. Schrenk, G. Strasser, E. Gornik, *Broadband Terahertz Pulse Propagation in Subwavelength Size Quantum Cascade Laser Waveguides*; Talk: EOS Annual Meeting 2010, Paris, France; 26.10.2010 - 29.10.2010.
18. J. Darmo, M. Martl, D. Dietze, K. Unterrainer, *THz Quantum Cascade Lasers Based Systems for Remote Sensing*; Talk: 20th International Conference on Applied Electromagnetics and Communications, Dubrovnik, Croatia (invited); 20.09.2010 - 23.09.2010.
19. D. Dietze, J. Darmo, M. Martl, K. Unterrainer, *Terahertz Resonant Artificial Interface Layers*; Talk: IRMMW-THz 2010, Rome, Italy; 05.09.2010 - 10.09.2010.
20. M. Martl, J. Darmo, D. Dietze, C. Deutsch, A. Benz, M. Brandstetter, K. Unterrainer, P. Klang, A. M. Andrews, W. Schrenk, G. Strasser, E. Gornik, *Terahertz Spectroscopy of Double Metal Quantum Cascade Structures*; Talk: IRMMW-THz 2010, Rome, Italy; 05.09.2010 - 10.09.2010.
21. M. Martl, D. Dietze, J. Darmo, C. Deutsch, A. Benz, M. Brandstetter, K. Unterrainer, P. Klang, A. M. Andrews, W. Schrenk, G. Strasser, E. Gornik, *Investigation of Double Metal THz Quantum Cascade Lasers by Terahertz Time-domain Spectroscopy*; Poster: IQCLSW 2010, Florence, Italy; 30.08.2010 - 03.09.2010.

22. W. Parz, D. Dietze, C. Deutsch, A. Benz, J. Darmo, T. Müller, G. Fasching, A. M. Andrews, G. Strasser, K. Unterrainer, *Phase-resolved time domain studies of quantum cascade lasers*; Talk: IQCLSW 2010, Florence, Italy (invited); 30.08.2010 - 03.09.2010.
23. T. Balciunas, D. Lorenc, A. Pugzlys, D. Dietze, J. Darmo, K. Unterrainer, A. Baltuska, *Tunability of THz emission in a laser induced plasma*; Talk: ICONO 2010, Kazan, Russia (invited); 23.08.2010 - 26.08.2010.
24. J. Darmo, M. Martl, D. Dietze, K. Unterrainer, *THz Quantum Cascade Laser Based System for Remote Sensing*; Talk: 14th International Symposium on Ultrafast Phenomena in Semiconductors, Vilnius, Lithuania (invited); 23.08.2010 - 25.08.2010.
25. M. Martl, D. Dietze, W. Parz, C. Deutsch, A. Benz, J. Darmo, T. Müller, G. Fasching, A. M. Andrews, G. Strasser, K. Unterrainer, *Phase-resolved THz spectroscopy*; Talk: ICONO 2010, Kazan, Russland (invited); 23.08.2010 - 26.08.2010.
26. M. Martl, D. Dietze, W. Parz, C. Deutsch, A. Benz, J. Darmo, T. Müller, G. Fasching, A. M. Andrews, G. Strasser, K. Unterrainer, *Phase-resolved THz time domain studies of quantum cascade lasers*; Talk: 10th International Workshop on Nonlinear Optics and Excitation Kinetics in Semiconductors, Paderborn, Germany (invited); 16.08.2010 - 19.08.2010.
27. T. Balciunas, D. Lorenc, M. Ivanov, O. Smirnova, A. Pugzlys, A. M. Zheltikov, D. Dietze, J. Darmo, K. Unterrainer, Rathje T., G. Paulus, A. Baltuska, *Tunability of THz Emission Originating from Sub-Cycle Electron Bursts in a Laser Induced Plasma*; Talk: Ultrafast Phenomena 2010, Colorado, USA; 18.07.2010 - 23.07.2010.
28. D. Dietze, J. Darmo, K. Unterrainer, *Terahertz Plasmon Dispersion Relations in layered Semiconductor Structures*; Poster: DPG Spring Meeting, Regensburg, Germany; 21.03.2010 - 26.03.2010.
29. D. Dietze, J. Darmo, K. Unterrainer, *Calculation of Terahertz Plasmon Dispersion Relations in layered Semiconductor Structures*; Poster: 16th International Winterschool Mauterndorf "New Developments in Solid State Physics", Mauterndorf, Austria; 22.02.2010 - 26.02.2010.
30. M. Martl, J. Darmo, D. Dietze, K. Unterrainer, C. Deutsch, P. Klang, A. M. Andrews, W. Schrenk, G. Strasser, *Studies of Terahertz Quantum Cascade Lasers by Terahertz Microchip Emitters*; Poster: 16th International Winterschool Mauterndorf "New Developments in Solid State Physics", Mauterndorf, Austria; 22.02.2010 - 26.02.2010.
31. J. Darmo, M. Martl, D. Dietze, A. Urich, K. Unterrainer, *Terahertz detector with optical readout*; Poster: 2nd International Workshop TeraTech, Osaka, Japan; 30.11.2009 - 03.12.2009.

32. J. Darmo, W. Parz, M. Martl, D. Dietze, T. Müller, G. Strasser, K. Unterrainer, *Few-cycle THz studies of quantum cascade laser active regions and resonators*; Keynote Lecture: 2nd International Workshop TeraTech, Osaka, Japan (invited); 30.11.2009 - 03.12.2009.
33. J. Darmo, M. Martl, D. Dietze, K. Unterrainer, *Amplification of THz pulses in quantum cascade laser*; Keynote Lecture: Japan Science and Technology Agency, Osaka, Japan, JST Osaka, Japan (invited); 30.11.2009.
34. A. Urich, J. Darmo, D. Dietze, M. Martl, K. Unterrainer, *Optical Properties of Graphene in the THz Range*; Talk: CoQuS Retreat 2009, Traunkirchen, Austria; 04.09.2009 - 09.09.2009.
35. J. Darmo, M. Martl, D. Dietze, A. Urich, K. Unterrainer, *Far-infrared power detector with optical readout*; Talk: CLEO Europe 2009, Munich, Germany; 14.06.2009 - 19.06.2009.
36. D. Dietze, J. Darmo, J.N. Heyman, A. Urich, K. Unterrainer, *Polarization of THz Radiation from Laser Generated Plasma Filaments*; Talk: CLEO Europe 2009, Munich, Germany; 14.06.2009 - 19.06.2009.
37. A. Urich, J. Darmo, D. Dietze, M. Martl, K. Unterrainer, *Towards THz Spectroscopy of Graphene*; Talk: THz Frischlinge Meeting Berlin 2009, Berlin, Germany; 07.06.2009 - 10.06.2009.
38. D. Dietze, M. Martl, J. Darmo, S. Roither, A. Pugzlys, J.N. Heyman, K. Unterrainer, *Polarization of THz Radiation from Laser Generated Plasma Filaments*; Poster: CLEO 2009, Baltimore, USA; 31.05.2009 - 05.06.2009.
39. D. Dietze, J. Darmo, K. Unterrainer, *Polarization Dependence of THz Radiation Generated in Laser Induced Plasmas*; Talk: OTST 2009, Santa Barbara, USA; 07.03.2009 - 11.03.2009.
40. D. Dietze, J. Darmo, K. Unterrainer, *Polarization of THz Radiation from Laser Generated Plasma Filaments*; Talk: 5th ADLIS Workshop, Munich, Germany; 02.03.2009 - 04.03.2009.
41. J. Darmo, G. Fasching, A. Benz, W. Parz, M. Martl, D. Dietze, A. M. Andrews, G. Strasser, K. Unterrainer, *Terahertz quantum-cascade lasers: phase resolved dynamics and micro cavity effects*; Talk: SPIE Photonics West, San Jose, USA (invited); 24.01.2009 - 29.01.2009.
42. J. Darmo, J. Kröll, M. Martl, D. Dietze, W. Parz, C. Barbieri, C. Sirtori, K. Unterrainer, *Phase-resolved study of lasing in THz quantum cascade lasers*; Talk: EOS Annual Meeting 2008, Paris, France (invited); 29.09.2008 - 02.10.2008.
43. D. Dietze, J. Darmo, K. Unterrainer, *Terahertz time-domain spectroscopy of a two-dimensional electron gas in GaAs/AlGaAs heterostructures*; Poster: EOS Annual Meeting 2008, Paris, France; 29.09.2008 - 02.10.2008.

44. D. Dietze, J. Darmo, K. Unterrainer, *Terahertz time-domain spectroscopy of a two-dimensional electron gas in GaAs/AlGaAs heterostructures*; Poster: 58. Jahrestagung der Österreichischen Physikalischen Gesellschaft, Leoben, Austria; 22.09.2008 - 26.09.2008.
45. J. Darmo, G. Fasching, A. Benz, J. Kröll, M. Martl, D. Dietze, S. Barbieri, C. Sirtori, A. M. Andrews, W. Schrenk, G. Strasser, K. Unterrainer, *Terahertz Quantum-Cascade Lasers: Time Domain Spectroscopy and Micro Cavity Effects*; Keynote Lecture: IRMMW-THz 2008, Pasadena, USA; 15.09.2008 - 19.09.2008.
46. D. Dietze, D. Kelly, J. Darmo, K. Unterrainer, *THz Ellipsometry in Theory and Experiment*; Poster: IRMMW-THz 2008, Pasadena, USA; 15.09.2008 - 19.09.2008.
47. J. Darmo, J. Kröll, M. Martl, W. Parz, D. Dietze, S. Barbieri, C. Sirtori, K. Unterrainer, *Time Domain Spectroscopy of Gain, Loss and Coherence in Quantum Cascade Lasers*; Talk: IQCLSW 2008, Monte Verita, Ascona, Switzerland (invited); 14.09.2008 - 19.09.2008.
48. J. Darmo, J. Kröll, M. Martl, D. Dietze, S. Barbieri, C. Sirtori, K. Unterrainer, *Terahertz Semiconductor Gain Medium: Static Properties and Dynamic Behavior*; Talk: CLEO 2008, San Jose, USA (invited); 04.05.2008 - 09.05.2008.
49. J. Darmo, J. Kröll, M. Martl, D. Dietze, S. Barbieri, C. Sirtori, K. Unterrainer, *Quantum cascade laser: between device physics and quantum optics*; Talk: 15th International Winterschool on New Developments in Solid State Physics, Bad Hofgastein, Austria (invited); 18.02.2008 - 22.02.2008.
50. J. Darmo, J. Kröll, M. Martl, W. Parz, D. Dietze, K. Unterrainer, C. Barbieri, C. Sirtori, *Phase and amplitude resolved time domain study of terahertz quantum cascade lasers*; Talk: 402nd Wilhelm und Else Heraeus-Seminar, Obergurgl, Austria (invited); 03.02.2008 - 09.02.2008.

Acknowledgements

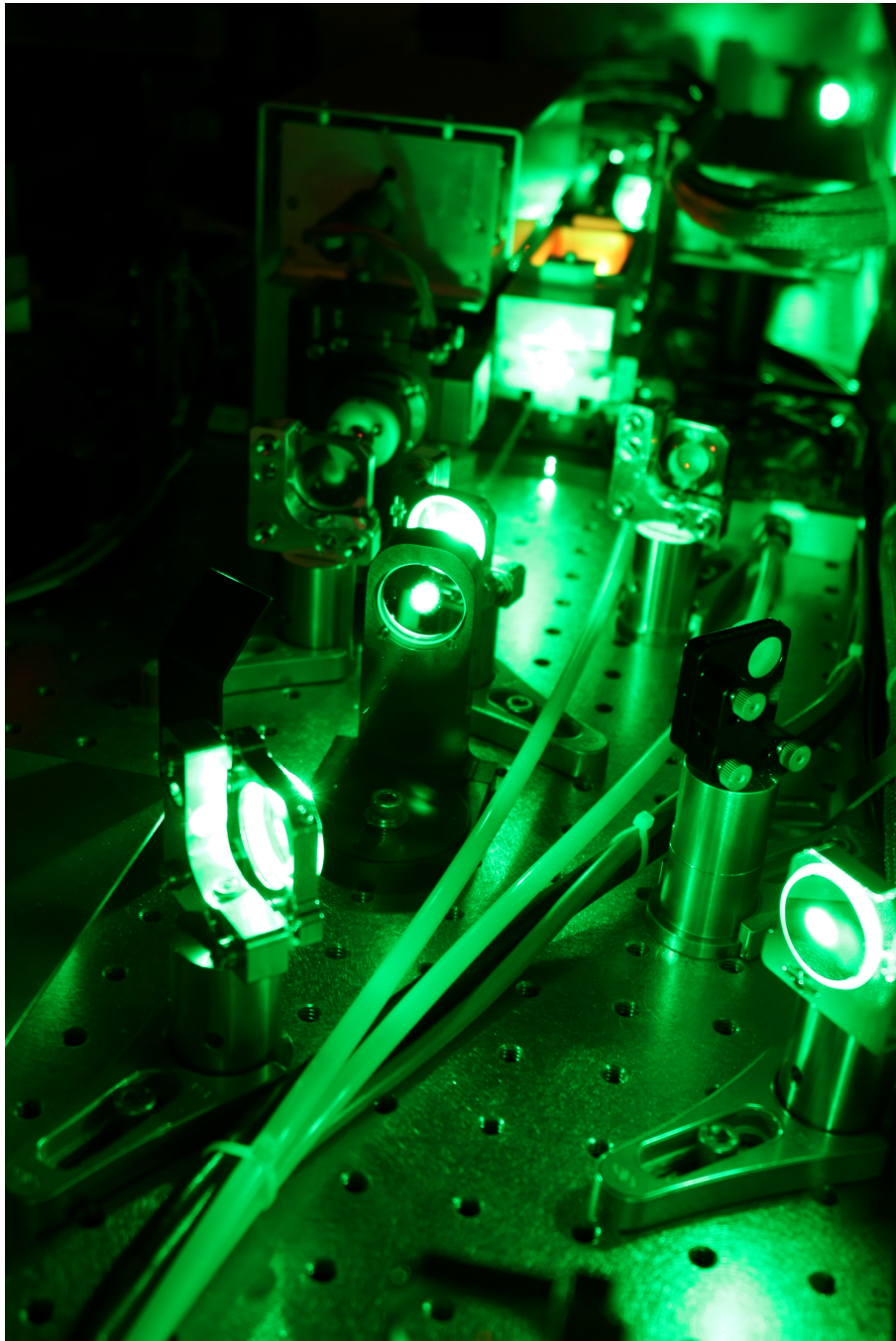
Finally, I would like to take the opportunity to express my gratitude to all the people who have supported me throughout my PhD thesis.

First of all, I would like to thank Karl Unterrainer for giving me the opportunity of writing my PhD thesis as a part of his research team, for his valuable advice and of course his generosity. Furthermore, I am very thankful to my supervisor Juraj Darmo who has always been generous with excellent ideas and with whom I had many fruitful discussions over the past years. In addition, I would like to thank him for keeping me clear of most of the tedious work involved with sample preparation in the cleanroom.

My gratitude also goes to the members of the THz lab, Martin Brandstetter, Gernot Fasching, Marco Furchi, Thomas Gebbhard, Martin Janitz, Michael Krall, Jakob Kristoferitsch, Govinda Lilley, Michael Martl, Thomas Moldaschl, Thomas Müller, Wolfgang Parz, Andreas Pospischil, and Stefan Schwarz for the friendly atmosphere which makes life at the university so comfortable. Special thanks go to Alexander Urich and my room mates Alexander Benz and Elisabeth Magerl for proof reading of the thesis (AU, EM), many priceless discussions and amusing distractions when work was once again going tough. Thanks to Christoph Deutsch who helped me out with the RIE in the cleanroom. Thanks also to Dominic Bachmann who did an excellent job building the large area photoconductive emitter antenna array.

Valuable support also came from Gottfried Strasser, Werner Schrenk, Max Andrews, and Hermann Detz from the Institute for Solid State Electronics, who spent countless hours at the MBE and in the cleanroom to provide excellently grown samples. I would like to thank James Heyman from the Macalester College, St. Paul, Minnesota, USA for helping me build the first version of the high power THz setup based on two-color laser generated plasma filaments. For technical and scientific support during the very first plasma emission experiments, I would also like to thank Andrius Baltuska, Audrius Pugzlys, and Stefan Roither from the Photonics Institute who have not only provided a Ti:Sapphire amplifier, but have also managed to keep it in a decent shape.

Thanks to my parents and my sister who have always believed in me. For home always feeling like home, no matter where. Special thanks to my wife Michèle who has never lost her faith in me finally graduating. Thanks for bearing all my tempers when work once again was not going as intended. Finally, I would like to thank my son Nicolas, who gave me an excellent reason to eventually finish my thesis.



The SpitfireXP cavity.

